frontiers | Research Topics

AI-driven zero carbon cyber-energy system

Edited by
Yushuai Li, Jianhua Zhang, Rui Fan and Bonan Huang

Published in
Frontiers in Energy Research

ISSN 1664-8714
ISBN 978-2-83251-963-9
DOI 10.3389/978-2-83251-963-9

About Frontiers

Frontiers is more than just an open access publisher of scholarly articles: it is a pioneering approach to the world of academia, radically improving the way scholarly research is managed. The grand vision of Frontiers is a world where all people have an equal opportunity to seek, share and generate knowledge. Frontiers provides immediate and permanent online open access to all its publications, but this alone is not enough to realize our grand goals.

Frontiers journal series

The Frontiers journal series is a multi-tier and interdisciplinary set of open-access, online journals, promising a paradigm shift from the current review, selection and dissemination processes in academic publishing. All Frontiers journals are driven by researchers for researchers; therefore, they constitute a service to the scholarly community. At the same time, the *Frontiers journal series* operates on a revolutionary invention, the tiered publishing system, initially addressing specific communities of scholars, and gradually climbing up to broader public understanding, thus serving the interests of the lay society, too.

Dedication to quality

Each Frontiers article is a landmark of the highest quality, thanks to genuinely collaborative interactions between authors and review editors, who include some of the world's best academicians. Research must be certified by peers before entering a stream of knowledge that may eventually reach the public - and shape society; therefore, Frontiers only applies the most rigorous and unbiased reviews. Frontiers revolutionizes research publishing by freely delivering the most outstanding research, evaluated with no bias from both the academic and social point of view. By applying the most advanced information technologies, Frontiers is catapulting scholarly publishing into a new generation.

What are Frontiers Research Topics?

Frontiers Research Topics are very popular trademarks of the *Frontiers journals series*: they are collections of at least ten articles, all centered on a particular subject. With their unique mix of varied contributions from Original Research to Review Articles, Frontiers Research Topics unify the most influential researchers, the latest key findings and historical advances in a hot research area.

Find out more on how to host your own Frontiers Research Topic or contribute to one as an author by contacting the Frontiers editorial office: frontiersin.org/about/contact

AI-driven zero carbon cyber-energy system

Topic editors

Yushuai Li — University of Oslo, Norway
Jianhua Zhang — Clarkson University, United States
Rui Fan — University of Denver, United States
Bonan Huang — Northeastern University, China

Citation

Li, Y., Zhang, J., Fan, R., Huang, B., eds. (2023). *AI-driven zero carbon cyber-energy system*. Lausanne: Frontiers Media SA. doi: 10.3389/978-2-83251-963-9

Table of contents

frontiers | Frontiers in Energy Research

TYPE Editorial
PUBLISHED 01 February 2023
DOI 10.3389/fenrg.2023.1141013

OPEN ACCESS

EDITED AND REVIEWED BY
ZhaoYang Dong,
Nanyang Technological University,
Singapore

*CORRESPONDENCE
Yushuai Li,
lysise@126.com

SPECIALTY SECTION
This article was submitted to Smart Grids, a section of the journal Frontiers in Energy Research

RECEIVED 09 January 2023
ACCEPTED 26 January 2023
PUBLISHED 01 February 2023

CITATION
Li Y, Zhang J, Fan R and Huang B (2023), Editorial: AI-Driven zero carbon cyber-energy system.
Front. Energy Res. 11:1141013.
doi: 10.3389/fenrg.2023.1141013

Editorial: AI-Driven zero carbon cyber-energy system

Yushuai Li[1]*, Jianhua Zhang[2], Rui Fan[3] and Bonan Huang[4]

[1]Department of Informatics, University of Oslo, Oslo, Norway, [2]Department of Electrical and Computer Engineering, Clarkson University, Potsdam, NY, United States, [3]Department of Electrical and Computer Engineering, University of Denver, Denver, CO, United States, [4]School of Information Science and Engineering, Northeastern University, Shenyang, China

KEYWORDS

artificial intelligence, cyber-energy system, zero carbon, machine learning, renewable energy sources

Editorial on the Research Topic
AI-Driven zero carbon cyber-energy system

The increasing pressure from the energy crisis and environment pollution has led to the urgency of energy structure and technology upgrades. As a future energy development trend, Cyber-Energy System (CES) focuses on deeply integrating multiple types of energy resources (including electricity power, heat, cooling, and gas, etc.) and advanced communication technology to improve the energy utilization efficiency, reduce the costs and emissions, and increase the proportion of renewable energy resources. Since AI technology is both suitable for solving model-driven and data-driven research problems, it fits well with the features of CES such as diversified information date and interdependent infrastructures. By reasonably utilizing AI and multi-energy conversion technology, it is entirely possible for CES to achieve low (even zero) operation in the processes of energy generation, conversion, transmission, distribution, and consumption. Meanwhile, zero carbon in CES requires innovation in many aspects, including policy, markets, modeling, planning, control, and operation, which brings many new challenges.

The aim of this Research Topic is to address and disseminate state-of-the-art research and opportunities regarding the application of AI and multi-energy conversion technology to achieve low/zero system operation for CES. Through a rigorous peer-review process, 10 articles have been accepted, which are summarized as follows.

In the article "A Deep Learning Approach to the Transformer Life Prediction Considering Diverse Aging Factors," He et al. investigated the aging phenomenon of power system transformers, whose representative degeneration variables were extracted from real transformer operational data. Combined with the average life of the equipment, the extracted features were used as indicators for transformer reliability evaluations. A deep learning–based approach was developed by using a convolutional neural network for effective equipment life prediction. The performance of the transformer life prediction model was verified using field-test data.

In the article "Autonomous underwater vehicle docking system for energy and data transmission in cabled ocean observatory networks," Sun and Han presented an active landmark tracking framework to improve the accuracy and reliability of short-range docking between autonomous underwater vehicles (AUVs) and a docking station (DS) in cabled ocean observatory networks (COON). The proposed framework included a two-stage docking algorithm based on convolutional neural networks (CNN) to estimate the 3D relative position and orientation between the AUV and DS during docking, as well as an extended Kalman filter and Hungarian matching algorithm to improve the robustness of the system. The

effectiveness of the proposed framework was demonstrated through experiments in both a pool and a lake.

In the article "Distributed Low-Carbon Energy Management Method for Port Microgrid Based on We-Energies under Polymorphic Network," Teng et al. proposed a port microgrid based on we-energies and its polymorphic distributed low-carbon energy management. Firstly, a polymorphic energy management system was established for a port microgrid based on we-energies to guarantee information interaction between neighbors. Further, considering the characteristics of we-energies, the operating cost function was constructed. In addition, a port microgrid low-carbon energy management model was constructed. Finally, a distributed solution method was proposed to reduce port carbon emissions and to help the development of the green low-carbon port.

In the article "Green Polymorphic Cooperative Formation Strategy of Low-Carbon Unmanned Surface Vessels," Lu et al. constructed a multi-lateral cooperative control system for USVs in a polymorphic network to achieve topological scalability of multi-USVs. A multi-lateral distributed control protocol was proposed. With the help of a MAS (Multi-Agent System) model and an Ad-Hoc network, green, energy-saving, and scalable autonomous cooperative formation of the future USVs was structured.

In the article "Intelligent Decoupling Control Study of PMSM Based on the Neural Network Inverse System," Da-Wei et al. established a decoupling control system model of a permanent magnet synchronous motor neural network inverse system. The data collected from the analytical inverse system of the PMSM model was used to analyze and compare the prediction accuracy and running time of the neural network, so as to optimize the structure and parameters of the neural networks. The results showed that the permanent magnet synchronous motor decoupling control system based on an RBF neural network inverse system has better dynamic and static decoupling performance and robustness.

In the article "Polymorphic Distributed Energy Management for Low-Carbon Port Microgrid With Carbon Capture and Carbon Storage Devices," Shan et al. proposed a polymorphic distributed energy management method for a low carbon port microgrid with a carbon capture and carbon storage device. First, this paper presented a low carbon port microgrid in a polymorphic network environment to realize an information interaction among energy subjects in different modes and to improve the network communication performance. Further, an energy management model of the low-carbon port microgrid was constructed considering the additional carbon capture and carbon storage device in the port. In addition, a distributed energy management method was proposed for different port microgrid operation modes.

In the article "Energy Management Without Iteration—A Regional Dispatch Event-Triggered Algorithm for Energy Internet," Tan proposed a region scheduling event triggering algorithm (RDETA). With RDETA, the energy management does not need to iterate with each asynchronous communication and does not rely on a global synchronous clock. In addition, the RDETA is capable of using regional communications and regional energy dispatching. Therefore, the size of the dispatch area can be adjusted automatically according to the extent of the energy problem. Simulation results and theoretical analysis demonstrated the effectiveness of the proposed algorithm.

In the article "Intelligent Command Filter Design for Strict Feedback Unmodeled Dynamic MIMO Systems with Applications to Energy Systems," Feng et al. proposed a command-filtered control scheme for multi-input multi-output strict feedback non-linear unmodeled dynamical systems. Therein, a dynamic signal combined with radial basis function neural networks was considered, which enabled handling of the dynamic uncertainties. The command filter was further employed to prevent explosions. The authors showed that the proposed method possessed better suitability than single-input single-output strict feedback non-linear systems.

In the article "Low carbon economic dispatch of power system at multiple time scales considering GRU wind power forecasting and integrated carbon capture," Ding et al. proposed a three-stage economic dispatch framework, based on the Carbon Capture and Storage (CCS) technique and the multi-timescale Gated recurrent unit (GRU) wind power forecasting model. In the proposed framework, the CCS plants were equipped with conventional thermal power plants to enable low carbon emission and flexible regulation capability. Meanwhile, the AI-based GRU forecasting technique with higher accuracy and less training time efficiently facilitated optimal system dispatches. Based on the corresponding 3-stage GRU wind power forecasting, a three-stage dispatch modeling with day-ahead, intra-day, and dynamic stages was developed for the power system with large integration of CCS and wind plants to improve the system operation and control, further achieving low wind curtailment, load loss, and dispatching costs.

In the article "Measurement Error Estimation for Distributed Smart Meters Through a Modified BP Neural Network," Xia et al. presented a measurement error estimation method for distributed smart meters by using a modified BP neural network. The considered BP neural network was designed by reasonably combining the internal activation function, iterative step size, and other relevant parameters. Several experiments were considered to demonstrate the feasibility and effectiveness of the constructed distributed smart electricity meter system.

Author contributions

YL, JZ, RF, and BH are responsible to summarize articles 1–3, 4–5, 6-7, and 8–10, respectively. YL is also responsible to write and check the whole paper.

Acknowledgments

We thank all authors who submitted their high-quality articles to the Research Topic, and all reviewers who went to great efforts to accomplish their review tasks.

Conflict of interest

The authors declare that the research was conducted in the absence of any commercial or financial relationships that could be construed as a potential conflict of interest.

Publisher's note

frontiers | Frontiers in Energy Research

ORIGINAL RESEARCH
published: 13 May 2022
doi: 10.3389/fenrg.2022.908199

Energy Management Without Iteration—A Regional Dispatch Event-Triggered Algorithm for Energy Internet

*Jiaming Tan**

Faculty of Electrical and Control Engineering, Liaoning Technical University, Huludao, China

Centralized algorithms and distributed algorithms have gained great attention on the energy Internet nowadays. The centralized algorithm presses too much communication and numeration load to its control center in large-scale and neterogeny EI. The distributed algorithm requests too many times of iteration, and the performance and convergence speed is quite slow. The current literature presents a regional dispatch event-triggered algorithm (RDETA). Energy management in RDETA can transform between a centralized model and distributed model. With the effort, the energy management does notrequire iteration times in quantity. And due to event-triggered asynchronous communication, energy management not only relieson a global synchronous clock but also decreasecommunication frequency in most cases and increasecommunication frequency in exigency. In addition, RDETA adopts regional communication and regional energy dispatch, which can automatically modulate the scale of dispatch area by the degree of the energy problem. Finally, simulation results and theoretical demonstration show the aforementioned contributions of the proposed algorithm.

Keywords: asynchronous communication, centralized algorithm, distributed algorithm, energy internet, energy management, multi-agent system, renewable energy source, zone control

OPEN ACCESS

Edited by:
Yushuai Li,
University of Oslo, Norway

Reviewed by:
Ning Zhang,
Anhui University, China
Wei Gao,
University of Denver, United States

***Correspondence:**
Jiaming Tan
m15124403461@163.com

Specialty section:
This article was submitted to Smart Grids, a section of the journal Frontiers in Energy Research

Received: *30 March 2022*
Accepted: *11 April 2022*
Published: *13 May 2022*

Citation:
Tan J (2022) Energy Management Without Iteration—A Regional Dispatch Event-Triggered Algorithm for Energy Internet. Front. Energy Res. 10:908199. doi: 10.3389/fenrg.2022.908199

INTRODUCTION

Energy is a fundamental guarantee to industrial engineering and human society. With the much more frequent appearance of the fossil energy crisis, global environmental pollution, and multiple energy loads in industry, agriculture, and the daily life of humanity in recent years, it is imperative to create a better strategy to utilize multi-energy in higher efficiency, lower pollution, and more sustainable methods. Energy Internet (EI) and multi-energy systems rise in response to the proper time and conditions (Huang et al., 2010; Sun et al., 2017; Abdella et al., 2021). The key contributions of EI are to realize cooperation (Wang et al., 2020), optimization (Lu et al., 2019), management (Zhang et al., 2017), control (Zhang et al., 2020a), and complementation (Qin et al., 2019) among multiple energy subsystems. Furthermore, EI also contributes greatly in absorbing unstable renewable energy resources through the complex energy networks, enhancing the utilization rate of energy and accelerating energy sustainable development.

However, different from traditional fuel-based centralized power systems, EI is called for effectively coupling various neterogeny energy with different speeds and costs of the manufacture, transmission, and conversion and simultaneously managing large-scale energy systems. In consequence, how to cooperatively allocate energy generation resources including

renewable resources that are incapable to control, complex energy conversion among various energy, and satisfying changeable and unpredictable energy loads tends into an exceedingly serious challenge in EI. For handling these issues, recent investigations adopt two main methods. One is centralized algorithms, and another is distributed algorithms.

The centralized algorithm can be subdivided into analytical algorithms (Lin and Viviani, 1984; Lin et al., 1992; Wright, 1997) and heuristic algorithms (Sun et al., 2013; Moeini-Aghtaie et al., 2014). Centralized algorithms have a high quality of performance and a high speed. They can settle small-scale energy trading with no need for iteration. However, the centralized algorithms rely on a strongly centralized communication and control center, are sensitive to single-point failures and modeling errors (Yile et al., 2017), are hard to protect users' privacy (Pourbabak et al., 2017), *etc*. To sum up, the centralized algorithm is suitable for small-scale systems, whereas is unfit for large and complex systems in EI. To overcome the aforementioned drawbacks, the distributed algorithm becomes a burgeoning and effective substitute methodology to replace the centralized algorithm to deal with large and complex systems in EI. Demystified by multi-agent systems (Liang et al., 2021), distributed algorithms divide EI into subsystems and subdivide subsystems into energy devices. So Sun (2019) named subsystems in EI we-energy, and defined we-energy as basic energy units with the functions of the multi-energy manufacture, multi-energy consumption, multi-energy conversation, and multi-energy storage. This we-energy has high quality compared with other recent researches in the author's view, so this study chooses we-energy as a model of energy subsystems.

The distributed algorithm in EI mainly includes four species of rudimentary theoretical knowledge containing price-guide algorithms (Yuang et al., 2022), alternating direction method of multipliers (ADMM) (Zhang et al., 2017), Newton descent algorithms (Li et al., 2020), and consensus-based methods (Sun et al., 2019). Xu et al. (2018) adopted a quasi-Newton algorithm to address economic optimization issues in multi-area. Sun et al. (2015) applied consensus-based methods in multi-agent systems to EI on the first try. Despite distributed algorithms being much fitter to large and complex EI than the centralized algorithm, the synchronous clock bus line is still too long due to the scale of global systems. Therefore, Li et al. (2019) renovated communication strategy to asynchronous event-triggered communication and embedded it into the execution of traditional distributed algorithms. Through its effort, each energy body can asynchronously trigger information exchanging to the global system at discrete instants driven by serious conditions to remove unnecessary communication. Nevertheless, communication and calculation in each time of triggering are still too large to operate. By the way, Li et al. (2019) sacrificed energy balance under the circumstances that communication is not triggered whereas disadvantages of energy mismatch are far more serious than economic loss. So sacrificing economic optimization is a better choice. Huang et al. (2016) raised co-optimization among microgrids. Can et al. (2021) adopted a price-guiding algorithm in EI, whereas the price in it is the energy selling price. The research value of the selling price is much less than that of energy manufacturing and converting costs. Additionally, nonlinear cost functions make energy cost changeable, which greatly increase the difficulty of research.

To sum up, recent research on EI has disadvantages hereafter. First, the largest challenge in energy management is all current algorithms require iterations. As we all know, iteration press a great burden on communication and calculation. Communication and calculation times about algorithms with iterations are hundreds of thousands of magnification to that without iterations. So it is a serious matter to invent an algorithm without iteration in EI. Second, because of the large and complex scale of EI, the synchronous clock bus line and global communication consume too much operation cost. The asynchronous communication in the literature (Li et al., 2019) addressed that problem to a certain degree whereas the communication in (Li et al., 2019) was a global communication. Regional communication may be better. Third, price-guiding is an irreplaceable method to alloplastic energy flow issues, because energy price is the only way to estimate value among different types of energy. However, recent research only invests in the selling price. Compared with the selling price, energy cost is far more ponderable in energy conversation. Nevertheless, because of complex cost functions, energy cost is fickle and difficult to be modeled. Finally, distributed algorithms at present are too sensitive to initial values whereas some initial values are difficult to ensure.

These challenges about EI hereinbefore can be settled together. Herein, a regional dispatch event-triggered algorithm (RDETA) comes into being to address the aforementioned issues. Mainly contributions of this article are summarized as following:

1) RDETA does not require iterations. As we all know, iterations press too much burden on communication and calculation. Communication and calculation times about algorithms with iterations are hundreds of thousands of magnification to that without iterations. Therefore, RDETA could increasingly decrease communication and calculation costs in EI.
2) RDETA renovates the communication method to event-triggered asynchronous regional distributed parallel communication, which is exceedingly fit for large EI. Because of the scale of EI, global communication requires too many communicating times. RDETA upsteps communication scope by event-triggered strategy. Furthermore, asynchronous communication does not rely on the synchronous clock bus line. Meanwhile, it decreases communication frequency in most cases to reduce unnecessary costs and increases communication frequency in exigency to aggrandize algorithm adjusting performance to be answerable for emergency circumstances.
3) This study subdivides energy price into energy selling price, energy average cost price, and energy momentary cost price. With this effort, the price-guiding method is better in complex nonlinear cost functions in EI. It is worth noting that these concepts all hereinbefore are originally put forward in this study. They fit energy management whereas may not fit other economic management issues.

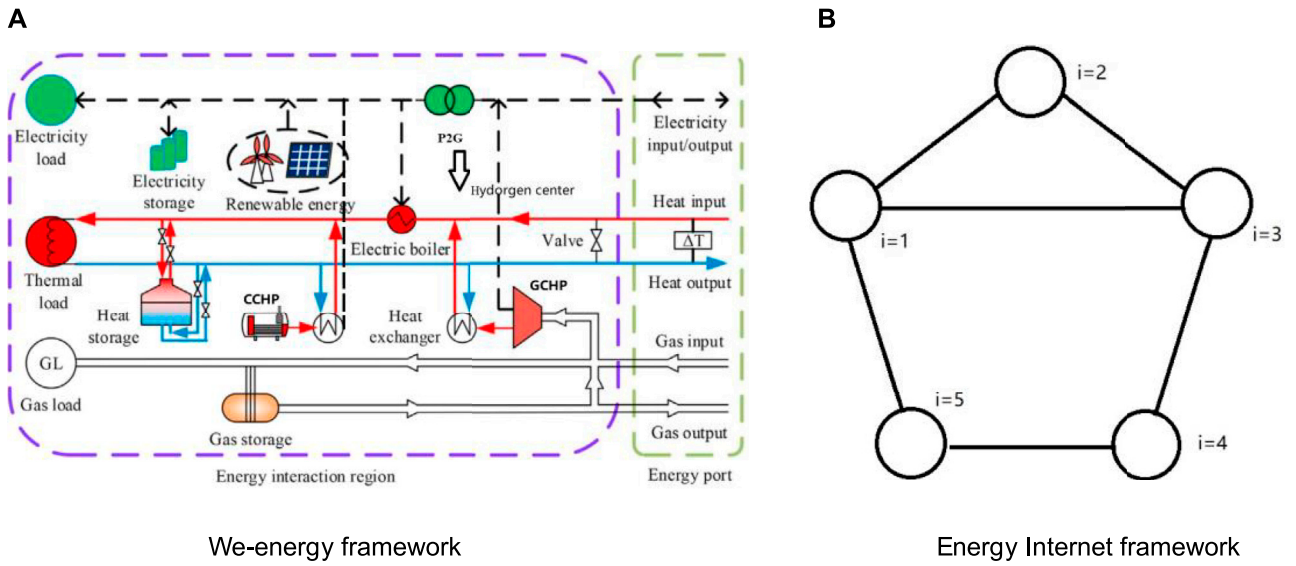

FIGURE 1 | (A) We-energy framework. **(B)** Energy Internet framework.

4) RDETA adopts high order partial differential equations to centralize dispatch in one or two we-energies. Each energy devices only transmit its partial differential formula and high order partial differential formulas to the control platform inside we-energy. The agents communicate nothing about operating conditions. Therefore, RDETA reinforced the protection of users' privacy. In addition, because of high order partial differential equations, RDETA is not sensitive to initial values.
5) Three secondary contributions. One is to replace day-ahead forecasting with communication-ahead forecasting to enhance forecasting accuracy. Another is that when the event-triggered system does not activate, RDETA chooses to sacrifice economic optimality rather than energy supply-demand balance because the detriment of energy mismatch is much greater than that of reducing economic earnings. The last contribution is that RDETA entirely handles the issue of energy conversion.

The rest of this study is as follows. **Section 2** introduces the proposed mathematical model of EI, we-energies, and energy devices. **Section 3** first introduces some fundamental knowledge. Then, it introduces the proposed RDETA. **Section 3** demonstrates the optimal performance and avoiding Zeno behavior of RDETA, too. **Section 4** analyses several illustrative case studies to show the proposed RDETA applied to a simulated EI. The conclusion drawn from this study is in **Section 5**.

MATHEMATICAL MODEL OF EI

An anticipated construction of single we-energy, employed to couple multiple energy components together, is depicted in **Figure 1A**. We can divide the energy devices of each we-energy into seven classes, i.e., including the energy manufacturer (EM), the energy transform devices (TD), the energy storage devices (SD), the energy load (EL), the energy transfer path (TP), the information communication path (ICP), and the we-energy control platform (CP). As a small but complex and consummate energy subsystem of the energy prosumer (the conception of prosumer was in (Kubli et al., 2018)), we-energies can play multitudinous roles of energy supplier, energy transformer, and energy terminal user by controlling orders from CP. CP controls its multi-energy generators, multi-energy transform devices, multi-energy storage devices, and multi-energy loads. e.g., each we-energy can sell the part of excess power flow to other we-energies to help we-energies under power shortage circumstances and earn an additional economic profit.

The we-energy is regarded as a power supplier at this moment. In the meantime, the we-energy shall purchase deficit heat energy flow from other we-energies if it is hard to reach its heat supply-demand balance, so it plays a role of the heat terminal user. As shown in **Figures 1A, B**, the dispatch inside we-energy is centralized dispatch controlled by CP whereas the cooperation among we-energies is implemented under a sparse and distributed communication network based on the theory of multi-agent systems that are topology structures with great promise in the future compositive energy systems. In this mode, each we-energy only needs to exchange information with its corresponding neighbors when an event triggers asynchronous communication to implement their co-management. We can obtain optimal operating conditions through RDETA. To this end, the interconnected EI cyber information structure and physical structure are far different from preceding energy hub models (Sheikhi et al., 2015; Bahrami and Sheikhi, 2016). The energy hub models in previous research are mainly devoted to the energy import side. Each energy hub

can reach its energy supply-demand balance. However, we-energies are integrated energy agents constituted of energy hubs and terminal energy users and their co-dispatch can reach further interconnection on both energy entrance sides and energy exit sides. Through these efforts, the system flexibility, scalability, and reliability of EI can be greatly improved. Additionally, it is necessary for energy in the EI network to be transmitted and transformed in easy means. So only power, heat, and gas frequently-used energy conform to the requirement from the network in EI. On this account, EI in this study is power-heat-gas EI. Other types of energy including coal are not discussed in this study. What is noteworthy is that, despite great promise about interconnection among we-energies, the large-scale and complex structure of it brings abundant serious challenges because of the frequency of communication, iterations, and calculations. To handle these issues, RDETA uses various methods such as regional communications, event-triggered asynchronous communications, transitions between distributed model and centralized model, and high-order partial differential equations. The purposes of these methods are to avoid global communications in large EI, reduce unnecessary superfluous communications and rely upon synchronous clock bus lines, settle complex and large EI with the performance-superior centralized algorithm in distributed multi-agent systems, and avoid iterations. In addition, RDETA replaces the day-ahead forecasting (Zhang et al., 2020b) with communication-ahead forecasting to enhance forecasting accuracy.

We-Energy Model

As seen in **Figure 1A**, at the energy entrance or export side, the received power flow (P^{in}), heat flow (H^{in}), and gas flow (G^{in}) enter into or depart from the we-energy *via* the solid-state transformers, the caliducts, and the natural gas pipelines. Inside the we-energy structure, the received generated power flow comes from the wind generators (WG) (P^{W}), the solar generators (SG) (P^{S}), and the power output of the CHP units including coal-based CHP units (CCHP) (P^{CC}) and gas-based CHP units (GCHP) (P^{GC}). The received dissolved power flow is split into two paths, i.e., the one consumed by the terminal power users and the other one transformed by the power conversion devices including electric boilers (EB) (P^{EB}) and power-to-gas devices (P2G) (P^{P2G}). The received generated heat flow comes from the heat output of CHP units incorporating solar heat devices (SH), CCHP (H^{CC}), GCHP units (H^{GC}), and EB (H^{EB}). The received consumption of heat flow is utilized by terminal users only because heat is difficult to transform. The received generated gas flow comes from the equivalent gas generators (EGG) and the gas output of P2G (G^{P2G}). The received dissolved gas flow is subdivided into two paths, i.e., the one consumed by the terminal gas users and the other one transformed by the gas-based CHP units (P^{GC}). In addition, the energy (i.e., power, heat, and gas) storage devices (PS, HS, and GS) can adjust their operating conditions of energy supply or demand of the we-energy, which are determined by the discharge/charge states (P^{SD}), (H^{SD}), and (G^{SD}). It is worth noting that, all the aforementioned energy flows are vectors. The positive values of the symbol of energy output, and vice-versa. The energy loads contain two parts including the utilization of terminal users and the transfer loads. The transfer loads mean one type of energy converses with another type of that, e.g., power flow converses to gas flow *via* P2G, by this method, certain gas load transfers to the power load.

From the preceding part of the study, we can get to know that, the EM includes five kinds of devices, i.e., the WG, the SG, the SH, the CCHP, and the EGG. The TD includes the P2G, the EB, and the GCHP. The SD contains PS, HS, and GS.

Energy flow in we-energies could be calculated as follows:

$$\begin{bmatrix} P^{\text{in}}_{i,t}-P^{\text{U}}_{i,t} \\ H^{\text{in}}_{i,t}-H^{\text{U}}_{i,t} \\ G^{\text{in}}_{i,t}-G^{\text{U}}_{i,t} \end{bmatrix} = \begin{bmatrix} \nu_{\text{PP}}{}^{\text{SST}}\eta_{\text{PP}}{}^{\text{SST}} & \nu_{\text{PH}}{}^{\text{EB}}\eta_{\text{PH}}{}^{\text{EB}} & \nu_{\text{PG}}{}^{\text{P2G}}\eta_{\text{PG}}{}^{\text{P2G}} \\ 0 & 1 & 0 \\ \nu_{\text{GP}}{}^{\text{GCHP}}\eta_{\text{GP}}{}^{\text{GCHP}} & \nu_{\text{GP}}{}^{\text{GCHP}}\eta_{\text{GP}}{}^{\text{GCHP}} & \nu_{\text{GG}}{}^{\text{EWC}} \end{bmatrix} \begin{bmatrix} P^{\text{in}}_{i,t}+P^{\text{EM}}_{i,t}+P^{\text{SD}}_{i,t} \\ H^{\text{in}}_{i,t}+H^{\text{EM}}_{i,t}+H^{\text{SD}}_{i,t} \\ G^{\text{in}}_{i,t}+G^{\text{EM}}_{i,t}+G^{\text{SD}}_{i,t} \end{bmatrix}, \tag{1}$$

i is the serial number of the we-energy; t is the time; superscript U is the terminal energy user; ν is the proportion of the energy converted from the corresponding energy carrier in the total energy flow; and η is the efficiency of energy conversion.

$$\begin{cases} P^{\text{EM}}_{i,t} = P^{\text{W}}_{i,t} + P^{\text{S}}_{i,t} + P^{\text{CCHP}}_{i,t} \\ H^{\text{EM}}_{i,t} = H^{\text{S}}_{i,t} + P^{\text{CCHP}}_{i,t} \\ G^{\text{EM}}_{i,t} = G^{\text{EGG}}_{i,t} \end{cases} \tag{2}$$

We consider an EI as a multi-agent system with n we-energy subsystems, including in each we-energy no more than ξ participants but not limited to energy devices and terminal users. For the simplification of notations, we adopt a three-dimensional vector $\{X_{i,j} \in R^3 | i = 1, ..., \varepsilon;\ j = 1, ..., \xi_i\}$ to represent the decision variables of controllable devices in EI and employ $x^m_{i,j}$ to represent the m th element of X_{ij}. The three elements $x^1_{i,j}$, $x^2_{i,j}$, and $x^3_{i,j}$ in X_{ij} express power, heat, and gas flow, respectively.

EM Devices Mathematical Model

Renewable Energy Devices Model

One of the main purpose is to promote the utilization of renewable resources because they are clean, environmentally friendly, and low-cost. However, renewable energy resources are scattered in the distribution of geographic position and unpredictable energy production in time. As for better absorbing them, the forecasting accuracy is exceedingly significant. Traditional researchers adopt day-ahead forecasting (Bahrami and Sheikhi, 2016) to predict renewable energy generators. Nevertheless, due to the long time scale (1 day), the accuracy of day-ahead forecasting is exceedingly hard to be assured. For heightening the predicted precision, this study presents communication-ahead forecasting using the day-ahead assist method as follows:

$$\left\{ \mu^m_{i,j,t_{k+1}} = x^m_{i,j,t_k} + sg^m_{i,j,t_k}(t_{k+1} - t_k) + \Delta r_{(t_{k+1}-t_k)} \middle| x^m_{i,j} \in RE \right\} \tag{3}$$

RE mean the set of renewable energy devices; t_k and t_{k+1} mean the present time and the next measuring time; sg^m_{i,j,t_k} is the day-ahead subgradient factor which expresses the tendency of x^m_{i,j,t_k} in t_k; $\Delta r_{(t_{k+1}-t_k)}$ is the day-ahead convex or nonconvex compensation from t_k to t_{k+1} because the trend of $x^m_{i,j}$ may not be linear; $\mu^m_{i,j,t_{k+1}}$ is

the mathematic expectation of $x^m_{i,j,t_{k+1}}$. Note that the accurate value may not be the mathematic expectation because of the forecast error. In this study, we assume that the forecasting error obeys the Gaussian distribution whose feasibility analysis has been introduced in the study by Wu et al. (2015). Then, the probability density function of $x^m_{i,j,t_{k+1}}$ can be modeled as:

$$f\left(x^m_{i,j,t_{k+1}}\right) = \frac{1}{\sqrt{2\pi}\sigma^m_{i,j,t_{k+1}}} e^{-\frac{\left(x^m_{i,j,t_{k+1}} - \mu^m_{i,j,t_{k+1}}\right)}{2\left(\sigma^m_{i,j,t_{k+1}}\right)^2}} \left| x^m_{i,j,t_{k+1}} \in RE \right. \quad (4)$$

$\sigma^m_{i,j,t_{k+1}}$ is the standard deviation of $x^m_{i,j,t_{k+1}}$, which shows the dispersed degree of accurate value. $\sigma^m_{i,j,t_{k+1}}$ is determined by day-ahead forecasting and measure frequency. It can be calculated as:

$$\sigma^m_{i,j,t_{k+1}} = I^m_{i,j}\left(t_{k+1} - t_k\right) \quad (5)$$

$I^m_{i,j}$ is the day-ahead disperse degree forecasting value.

In addition, the confidence intervals of $x^m_{i,j,t_{k+1}}$ can be solved as $[x^{m-down}_{i,j,t_{k+1}}, x^{m-up}_{i,j,t_{k+1}}]$ by the **Eq. 4** by the homologous method in probability theory in the confidence level $100(1-\partial)\%$. We choose ∂ as 0.05 in this study. In addition, we adopt TD, SD, and EL to absorb all renewable energies. Then the operating conditions of renewable energy devices can be:

$$\left\{ x^m_{i,j,t_{k+1}} \in \left[x^{m-down}_{i,j,t_{k+1}}, x^{m-up}_{i,j,t_{k+1}} \right] \middle| x^m_{i,j} \in RE \right\} \quad (6)$$

Based on the aforementioned reason, the cost of renewable energy devices can be the punishment for energy deficiency. So if we choose the forecasting result higher, the economic optimization will be better, whereas the dependability will be worse, and *vice-versa*. The cost functions of renewable energy devices can be as following:

$$C^{m-RE}_{i,j,t_{k+1}} = a^{RE}_{i,j}\left(x^m_{i,j,t_{k+1}} - x^{m-down}_{i,j,t_{k+1}}\right)^2 \quad (7)$$

$a^{RE}_{i,j}$ is a positive constant.

The limits of renewable energy devices are as follows:

$$\left\{ x^m_{i,j,t_{k+1}} \in \left[x^{m-down}_{i,j,t_{k+1}}, x^{m-up}_{i,j,t_{k+1}} \right] \middle| x^m_{i,j} \in RE \right\} \quad (8)$$

That is the same as **Eq. 6**.

By the way, $\Delta r_{(t_{k+1}-t_k)}$ and $\sigma^m_{i,j,t_{k+1}}$ have their trigger conditions. If the trigger condition of $\Delta r_{(t_{k+1}-t_k)}$ is not reached, the tendency of x^m_{i,j,t_k} will be regarded as linear. If the trigger condition of $\sigma^m_{i,j,t_{k+1}}$ is not reached, we will regard the mathematic expectation of $x^m_{i,j,t_{k+1}}$ as the accuracy of it and the equations including **Eqs 4–8** will be meaningless because the forecasting precision is enough. In this study, the trigger condition of them is that they are more than 4 and 50 s, respectively.

Fossil Fuel Burning Based EM Devices

First, the technology of co-generation combining heat and power has already matured recently. And because of the high-efficient performance, that technology is much better than fuel-based plants and fuel-based boilers in the purpose of environmentally friendly and economic optimal. To sum up, fuel-based plants and fuel-based boilers are all replaced by co-generation combined heat and power devices. Second, to handle and investigate the ramping rate constraints of CCHPs, its form in discrete shape is always modeled into a knapsack mathematical problem. It is worth noting that we only consider the ramping constrain of the bower but not of heat because the response speed of heat is exceedingly slow. That reason is also fit for GCHP. The cost function of CCHP is as follows:

$$\begin{aligned} C_{i,j,t_k} &= \mathrm{a}_{i,j}{x^1_{i,j}}^2 + \mathrm{b}_{i,j}x^1_{i,j,t_k} + \alpha_{i,j}{x^2_{i,j,t_k}}^2 \\ &+\beta_{i,j}x^2_{i,j,t_k} + \mathrm{c}_{i,j}x^1_{i,j,t_k}x^2_{i,j,t_k} + \chi_{i,j} + \\ &\left(x^1_{i,j} + x^2_{i,j,t_k}\right) \times \left(\eta_{i,j}\right)^{-1} \times prf \end{aligned} \quad (9)$$

where $\mathrm{a}_{i,j}$, $\mathrm{b}_{i,j}$, $\alpha_{i,j}$, $\beta_{i,j}$, $\mathrm{c}_{i,j}$, and $\chi_{i,j}$ express cost factors, which are controlled by the energy emission of the thermal unit. They are all constants and the second-order coefficients with a single variable are positive constants. $\eta_{i,j}$ is the energy conversion efficiency of CCHP. prf represents the price of coal. And the constraints of CCHP are as follows:

$$-P^{\mathrm{ramp}}_{i,j} \le x^1_{i,j,t_k} - x^2_{i,j,t_k} \le P^{\mathrm{ramp}}_{i,j} \quad (10)$$

$$\mathrm{d}_{i,j}x^1_{i,j,t_k} + \mathrm{e}_{i,j}x^2_{i,j,t_k} + \mathrm{f}_{i,j} \ge 0 \quad (11)$$

$$\mathrm{d}_{i,j}x^1_{i,j,t_k} + \mathrm{e}_{i,j}x^2_{i,j,t_k} \le \mathrm{g}_{i,j} \quad (12)$$

$P^{\mathrm{ramp}}_{i,j}$ is the ramp rate constraint. Other coefficients without introduction are constants.

EGG Devices

Natural gas is a kind of fossil fuel and there are not any devices that can produce it. The only way to get natural gas is to buy it from related departments. The only thing we need to consider is the natural gas price, which cannot be changed by EI but decided by other departments.

TD Devices Mathematical Model

P2G and EB Models

The model and cost function of P2G are as follows:

$$-x^3_{i,j,t_k} = \eta_{i,j,t_k}x^1_{i,j,t_k} \quad (13)$$

$$C_{i,j,t_k} = -\theta_{i,j,t_k}x^1_{i,j,t_k} \quad (14)$$

η_{i,j,t_k} is the energy transforming the efficiency of P2G. θ_{i,j,t_k} is a positive constant that expresses operating cost. The constraint of DP2G is as follows:

$$P^{\mathrm{P2G-min}}_{i,j} \le -x^1_{i,j,t_k} \quad (15)$$

$P^{\mathrm{P2G-min}}_{i,j}$ is the start-stop limit of P2G. Because power energy in the network of EI is limited and the capacity of P2G is very large, we do not consider the energy conversion upper constraint. There is a resemblance between P2G and EB in the model, the operating cost function, and the constraint. We only need to replace the energy type.

GCHP Models

The model and operating cost function of DGC are as follows:

$$C_{i,j,t_k} = \left(x^1_{i,j} + x^2_{i,j,t_k}\right) \times \left(\eta_{i,j}\right)^{-1} \times \left(prg + \theta_{i,j}\right) \tag{16}$$

Where $\theta_{i,j}$ is a positive constant that expresses operating cost. $\eta_{i,j}$ is the energy conversion efficiency of CCHP. prg represents the price of gas. By the way, some coefficients are shown in the same letters between CCHP and GCHP, whereas the significance of them is different because the subscripts change along with the types of device. The reason is also fit to conditions between other devices.

The constraints of GCHP are as follows:

$$-P^{\text{ramp}}_{i,j} \le x^1_{i,j,t_k} - x^2_{i,j,t_k} \le P^{\text{ramp}}_{i,j} \tag{17}$$

$$\mathrm{d}_{i,j}x^1_{i,j,t_k} + \mathrm{e}_{i,j}x^2_{i,j,t_k} + \mathrm{f}_{i,j} \ge 0 \tag{18}$$

$$\mathrm{d}_{i,j}x^1_{i,j,t_k} + \mathrm{e}_{i,j}x^2_{i,j,t_k} \le \mathrm{g}_{i,j} \tag{19}$$

$P^{\text{ramp}}_{i,j}$ is the ramp rate constraint. Other coefficients without introduction are constants.

SD Devices Mathematical Model

There is an optimal reserve in SD. If the stored energy is much less than the optimal reserve, it will press too much stress on SD devices. If things go on like this for too long, it may injure the capacity of SD devices. If the stored energy is much more than the optimal reserve, the stored energy will be under a risk of a leak. So the optimal condition function of SD is as follows:

$$O^m_{i,j,t_{ki,t}} = \mathrm{a}_{i,j}x^{m-S}_{i,j,t_k}\left(x^{m-S}_{i,j,t_k} - 2\mu^m_{i,j}\right) + \mathrm{b}_{i,j} \tag{20}$$

O is the optimal function of stored energy in SD, superscript m represents the type of energy, x^{m-S}_{i,j,t_k} is the stored energy in time, t_k. $\mu^m_{i,j}$ is the optimal reserve of energy in SD, $\mathrm{a}_{i,j}$ and $\mathrm{b}_{i,j}$ are invariable constants, and $\mathrm{a}_{i,j}$ is negative. The cost function of DPSD is as follows:

$$C_{i,j,t_k} = O^m_{i,j,t_k} - O^m_{i,j,t_{k-1}} + \theta_{i,j}\left\|x^m_{i,j,t_k}\right\|_2 \tag{21}$$

$\theta_{i,j}$ is a positive constant that expresses operating cost, and x^m_{i,j,t_k} is the energy flow from SD. So we can know the following:

$$x^m_{i,j,t_k} = x^{m-S}_{i,j,t_{k-1}} - x^{m-S}_{i,j,t_k} \tag{22}$$

The limits of SD are as follows:

$$-x^{\text{in}-\text{SD}}_{i,j} \le x^m_{i,j,t_k} \le x^{\text{out}-\text{SD}}_{i,j} \tag{23}$$

$$x^{m-\text{S}-\min}_{i,j} \le x^{m-S}_{i,j,t_k} \le x^{m-\text{S}-\max}_{i,j} \tag{24}$$

$x^{m}_{i,j}\text{in}-\text{SD}$ and $x^{m}_{i,j}\text{out}-\text{SD}$ are the maximum energy flow limits about energy input and output rate of DPSD, respectively. $x^{m-\text{S}-\min}_{i,j}$ and $x^{m-\text{S}-\max}_{i,j}$ are minimum and maximum values of energy capacity, respectively.

EL Mathematical Model

There are two essential challenges in EL. One is the randomness of terminal users, the other is load shifting. Load shifting is analyzed here. RDETA could absorb the randomness of terminal users in the large multi-agent system of EI by RDETA, which will be introduced in **Section IV**. In the multi-energy system of EI, different energy loads can transform between each other by energy conversion, e.g., power flow converses to gas flow *via* P2G, through this method certain gas load transfers to the power load. So the model of EL is as follows:

$$x^m_{i,j,t_k} = u^m_{i,j,t_k} + tr^m_{i,j,t_k} \tag{25}$$

$$tr^{n_1}_{i,j,t_k} + tr^{n_2}_{i,j,t_k} + tr^{n_3}_{i,j,t_k} + \ldots + tr^{n_N}_{i,j,t_k} = -\eta^{mn}_{i,j}tr^m_{i,j,t_k} \tag{26}$$

$\eta^{mn}_{i,j}$ is the energy conversion efficiency from energy m to energy n. m is a constant, while n is a set of various numbers because a kind of energy can change into more than one type of energy. By the way, the energy load can also be forecast predicted by communication-ahead forecasting which is similar to renewable energy resources. The only difference is that we regard the mathematic expectation of forecasting value as the accuracy value because the randomness of energy load is much lower than that of renewable energy resources.

ENERGY MANAGEMENT AND RDETA ALGORITHM

Proposes and Difficulties of Energy Management

Considering an EI with a number of we-energies, the expectation of energy management is to minimize the cost under the circumstance that the total energy demand in the whole society that covers is satisfied by the synergy among all participators. We can model it as a mathematical objective function as:

$$\min obj = \sum_{i=1,j=1}^{\varepsilon,\xi_i}\left(C_{i,j,t_k}\right)$$
$$\begin{cases} \sum_{i=1}^{\varepsilon}\sum_{j=1}^{\xi_i} I \times X_{i,j} = \sum_{i=1}^{\varepsilon}\sum_{j=1}^{\xi_i} U_{i,j} \\ \varphi\left(x^m_{i,j}\right) < 0 \end{cases} \tag{27}$$

The cost not only includes the visualized economic expenditure but also contains some invisible expenditure incorporating but not limited to the inaccurate forecasting of renewable energy resources, undertaking the risk of energy mutation, energy pour and energy shortage, and the like. $U_{i,j}$ is the matrix of terminal users' energy consumption. φ is a local closed convex set for $X_{i,j}$. The main difficulties of energy management are as follows:

First, the maximal challenge is too many iterations for the following reason. The complex mathematical issue of energy management is impossible to be solved by continuous math theory. So the only way to settle it is discrete mathematics based on supercomputers. However, that method brings hundreds of thousands of times of iterations. What is more, each time of iteration is accompanied by large communication. Second, the randomness of terminal users and the uncertainty of renewable energy resources cause a mass of trouble. Third, because of the complexity of energy management, recently parallel algorithms in computer math in embedded software

are incompatible with EI, which highly limits the high performance of supercomputers. Fourth, because of the large scale of EI, it is exceedingly difficult to build the synchronous clock bus line and global communication. Fifth, although a certain part of EI is uncertain, it does not change tempestuously moment by moment. When participators change a little, the dispatch earnings may be no more than the cost of computing and communicating. Sixth, the principle of multi-energy conversion is complex and multitudinous, and the iteration in the algorithm is incompatible with energy conversion. Seventh, the privacy of we-energies and devices is difficult to protect. Last but not least, the cost of energy generation and conversion is changeable, which causes certain trouble to economic optimization.

The Developing of Energy Management Algorithms

Energy management in a traditional power system adopts the centralized algorithm, which is nearly infeasible because of too much pressure on the control center and communication. So the distributed algorithm rises (Yuang et al., 2022). The distributed algorithm not only greatly reduces the pressure of the control center but also absorbs renewable energy resources in the huge system of EI. Moreover, the issue of privacy protection is half done in it (agents communicate with neighbor agents so their privacy is not entirely protected). Additionally, the incompatible issue is settled on its own. The distributed algorithm is great progress because it is at least a feasible method. However, other disadvantages hereinbefore still exist. What is more, the distributed algorithm requires an excess of iteration times and a large of communications at each time of iteration. What is worth noting is that the computing and communicating times in distributed algorithms are much more than that in centralized algorithms. Whereas the computing and communicating in distributed algorithm allocate to all we-energies, but that in the centralized algorithm are entirely undertaken by the control center. A large number of technology limits including the hardware structure, the size of the microcircuit, and the packaging technology impose certain restrictions on the performance of the supercomputer in the control center, so a centralized algorithm is impracticable. However, the number of the control platforms is not limited, so distributed algorithms can handle much more complex issues. So the distributed algorithm is doable in EI although the computing and communicating cost is large. Li et al. (2019) proposed the asynchronous distributed algorithm which reduces some meaningless communication and does not require the synchronous clock bus line. However, there are still various challenges in energy management, especially the iteration problem and the communicating and computing pressure it brings. Furthermore, the algorithm in the study by Li et al. (2019) sacrifices energy supply-demand balance under certain circumstances, which does great harm to EI. To this end, this study proposed that the RDETA algorithm can handle all aforementioned challenges. The difficulties of energy management, the contributions, and the greatest motivations of all these algorithms are in **Table 1** (✓ for entirely addressing, ✖ for not addressing, • for half addressing). RDETA adopts several technologies. Some are original, others are not original. **Table 2** shows all technologies and their contributions and their original circumstances (✓ for original, ✖ for not original).

Basic Knowledge of Graph Theory

Consider an EI system with ε we-energies, where i th we-energy has ξ_i participators. An undirected graph $Graph = (V, E, B)$ is adopted to model it, where $V = \{v_i | i = 1, 2, \cdots, n\}$ is a set of nodes representing agents in multi-agent systems and $E \subseteq V \times V$ is a set of undirected edges. Therein, the edge (v_i, v_j) denotes that v_i node and v_j node can communicate with each other if needed. The relationships between v_i and v_j is shown in $B = [b_{i,j}] \in R^{m \times n}$. The diagonal elements in that matrix are all zeros constantly. If a non-diagonal element $b_{i,j} > 0$, $(v_i, v_j) \in E$, they are neighbor agents. Whereas if$b_{i,j} = 0, (v_i, v_j) \notin E$, they are not neighbor agents. In the undirected graph, sides between nodes are not directed, so $(v_i, v_j) \in E$ equals to$(v_j, v_i) \in E$. In this study, we only study connected graph because non-connected graph represents two island energy system that need to be researched, respectively. If we replace a node the graph will be non-connected, that node is called cut-vertex.

RDETA Algorithm

In this study, the main purpose is to minimize all costs under the circumstance that all energy demands and all limits are satisfied. So we can model all participants in each we-energy as a vector space including a lot of vectors including the operating condition vector$\{X_{i,j} \in R^3 | i = 1, ..., \varepsilon; j = 1, ..., \xi_i\}$, their partial differential, and high-order differentials of cost functions. It is worth noting that, for polynomial functions, their high-order differentials will restrain to zero sooner or later. Whereas for other functions including but not limited to exponential functions, trigonometric functions and logarithmic functions, and their high-order differentials will never restrain. Additionally, some functions may have a too high order, which may greatly increase the computing pressure. So we should use an order supremum dd to avoid these troubles. If a vector is not zero after $(dd + 1)$ order differential, we adopt Chebyshev polynomials to lower the order to dd. We establish that in the original state all we-energies operate in the island model in a random condition and that all the energy supply-demand balances are satisfied. Then we will transmit the change value vector of energy resources and the energy loads to the control center inside the we-energy and the control center will solve the energy mismatch vector. Due to the different time scales between different types of energy, we deal with the forecasting results of a different energy in different ways for renewable energy devices and energy loads as follows:

$$x^1_{i,j,t_k} = 0.5 \times \left(z x^1_{i,j,t_k} + f x^1_{i,j,t_{k+1}} \right) \tag{28}$$

$$x^2_{i,j,t_k} = z x^2_{i,j,t_k} \tag{29}$$

$$x^3_{i,j,t_k} = f x^3_{i,j,t_k} \tag{30}$$

TABLE 1 | The development and contributions of an energy management algorithm.

Type of algorithm		Centralized algorithm	Distributed algorithm	Asynchronous distributed algorithm	Regional dispatch event-triggered algorithm (RDETA)
Greatest motivation		First algorithm in energy management	Disperse the pressure in the control center	No longer communicate meaninglessly	No longer need iterations
Feasibility analysis		Infeasible	Feasible	Feasible	Feasible
Difficulty in energy management and the addressing circumstances of the algorithms	Too many iterations	✖	✖	✖	✓
	Randomness of terminal users and renewable energy resources	✓	✓	✓	✓
	Incompatible parallel algorithms in computer	✖	✓	✓	✓
	Build the synchronous clock bus line	✖	✖	✓	✓
	Global communication	✖	✖	✖	✓
	Meaningless communications	✖	✖	✓	✓
	Energy conversion	✖	✖	✖	✓
	Privacy-protecting	✖	•	•	✓
	Changeable cost	✖	✖	✖	✓
Difficulty they bring and the addressing circumstance in later algorithms		Too much pressure to control center	✓	✓	✓
			Increase too many times of communications in each time of iteration	✖	✓
			The accuracy of astringency is poor	✖	✓
				Sacrifice energy supply-demand balance	✓

TABLE 2 | All technologies in RDETA and their contributions and original circumstances.

	High-order partial differential equation	Asynchronous communication	Coupling distributed model and centralized model	Regional communication	Communication -ahead forecasting	Concept of average cost and instantaneous cost	Sacrifice economic optimization to ensure energy balance
Contribution	Remove iterations, protect users' privacy	Remove synchronous bus line, avoid meaningless communication	Make infeasible centralized algorithms feasible	Remove global communication	Enhance the accuracy of forecasting	Handle the energy management issue at a changeable cost	Avoid the detriment of energy mismatch
Originality	✓	✖	✓	✓	✓	✓	✓

zx and fx are the present energy flow and the forecasting energy flow in the next measuring time. The responding speed of power is less than 1 ms and the inductor and capacitance can store or release some power in proper time. So we regard the power flow as the average value of the zx and fx so that the power flow in the time between two measurings will press close to the power demand.

The responding speed of gas may be several seconds or several seconds. We control gas at this time, and because of the slowly responding speed, the control may come into play in the next measuring time. So we regard the gas flow as fx in the next measuring time. . The responding time of heat is too long to consider. For this reason, the forecasting of it is meaningless. So we do not forecast it to reduce computing. Then each device transmits all their condition vectors, their partial differential and high-order partial differentials vectors of cost functions to the control center. Then, the control can solve the issues that all the first-order partial derivative values of the same independent values in EM are equal when the multi-energy balance is reached by high-order partial differential equations. The homologous independent values vector shows their optimal working conditions without TD

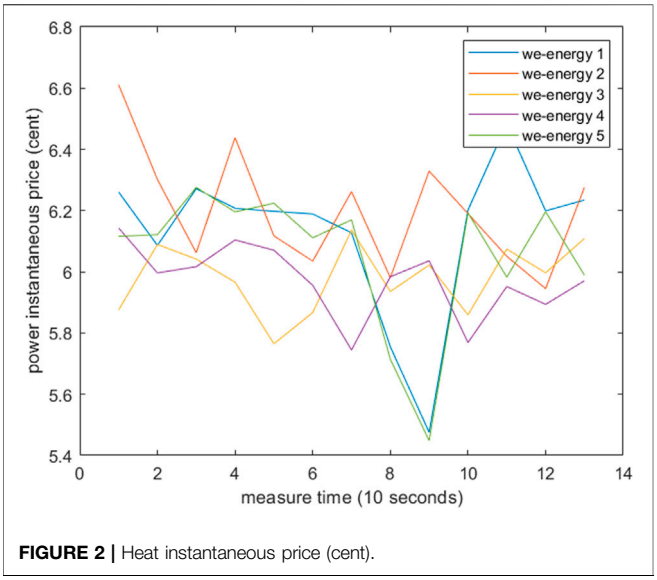

FIGURE 2 | Heat instantaneous price (cent).

devices. That first order is the instantaneous cost of the corresponding type of energy for the reason we will introduce in as follows. Then if the instantaneous cost of one type of energy is less than another type of energy and the cheap energy can change into the expensive energy by TD devices, the control center can solve another issue when the instantaneous cost of the expensive energy equals that of the conversion of the cheap energy when the multi-energy is balance. The instantaneous cost of conversion energy is the first-order partial differential of a composite function. The inside function is the cost function of the controllable EM devices of that energy (renewable energy devices are not controllable). The outside function is the cost function of TD. The new independent variable is the new operating conditions of relevant EM devices and the changeable of them is the opposite number of the operating conditions of TD devices. After that, the optimal work of island mode in each we-energy is finished. The next issue is the collaborative optimization among we-energies. First, we should solve all instantaneous costs of each energy and stack them into a price vector S_i with three elements. The instantaneous cost of energy whose load changes to another load is the partial differential of the energy generation about the controllable EM cost functions, while the instantaneous cost of energy whose load changes from another load is the partial differential of part of the energy generation which is utilized by terminal users about that. Then, the we-energy will transmit the energy price vector to neighbor we-energies and compute the trigger vector as follows:

$$\begin{aligned}
&\mathrm{T}^{i}{}_{1} = S_i \\
&\mathrm{T}^{i}{}_{2} = \mathrm{ave}\left\{\mathrm{T}^{i}{}_{1}, \mathrm{all}\left(\mathrm{T}^{i_2}{}_{1}\right) | i \sim i_2\right\} \\
&\mathrm{T}^{i}{}_{3} = \mathrm{ave}\left\{\mathrm{T}^{i}{}_{2}, \mathrm{all}\left(\mathrm{T}^{i_2}{}_{2}\right) | i \sim i_2\right\} \\
&\cdots\cdots \\
&\mathrm{T}^{i}{}_{k} = \mathrm{ave}\left\{\mathrm{T}^{i}{}_{k}, \mathrm{all}\left(\mathrm{T}^{i_2}{}_{k}\right) | i \sim i_2\right\}
\end{aligned} \tag{31}$$

The symbol ave means the average vector of all vectors in the set. The symbol ~ means that the two number we-energies between that symbol are neighbor-agents. The symbol all means a set of all elements under that circumstance. All we-energies will transmit their T_1^i to T_{q+1}^i to their neighbor-agents. q is the number of cut-vertex in the EI system. The reason for that is the low connected degree EI needs more control. If the difference value absolute of one of the element in T_1^i to T_{q+1}^i is larger than the homologous element in the trigger vector ℵ which is very small, the asynchronous communication between their two we-energies will be triggered. Then, two we-energies will be regarded as one big we-energy. They will share one control center and repeat the we-energy partial differential equation dispatch hereinbefore as follows:

$$\begin{aligned}
&\frac{d\left(C_{i,j,t_k}\right)}{x^m_{i,j,t_k}} = \frac{d\left(C_{i,j',t_k}\right)}{x^m_{i,j',t_k}} \\
&\frac{d\left(C_{i,j,t_k}\right)}{x^m_{i,j,t_k}} = k_1, \frac{d^2\left(C_{i,j,t_k}\right)}{\left(x^m_{i,j,t_k}\right)^2} = k_2, \frac{d^3\left(C_{i,j,t_k}\right)}{\left(x^m_{i,j,t_k}\right)^3} = k_3 \ldots \frac{d^n\left(C_{i,j,t_k}\right)}{\left(x^m_{i,j,t_k}\right)^n} = k_n \\
&\frac{d\left(C_{i,j',t_k}\right)}{x^m_{i,j',t_k}} = kk_1, \frac{d^2\left(C_{i,j',t_k}\right)}{\left(x^m_{i,j',t_k}\right)^2} = kk_2, \frac{d^3\left(C_{i,j',t_k}\right)}{\left(x^m_{i,j',t_k}\right)^3} = kk_3 \ldots \frac{d^n\left(C_{i,j',t_k}\right)}{\left(x^m_{i,j',t_k}\right)^n} = kk_n
\end{aligned} \tag{32}$$

The partial derivative values are the energy prices for the reason that is expressed hereinafter. *k* and *kk* are constants. There are three advantages of this operation. First, this operation is centralized in the two we-energies but is distributed in the whole EI for the reason that the two we-energies are very small to the whole large system of EI. It is worth noting that the method of partial differential equations is unfit for big systems but is fit for small systems. A big we-energy including two we-energies is a small system that is very fit to the method of the partial differential equations. Second, the partial differential equations can solve the issue of energy management without iteration. However, it is unfit for large systems because of the pressure of communication and computing. The RDETA adopts the partial differential equations in two we-energies which not only avoid iteration but also avoid too much computing and communicating pressure.

So the price vector in the two we-energies will be the same. Then, the control center will compute how much energy should be transmitted from one we-energy to another and stack it into an energy flow vector. After that, the asynchronous communication will be cut off, while the energy transmitting value will be reserved in a transmitting vector and the we-energies will transmit energy according to that. There are some points which should be emphasized. First, a we-energy can only asynchronously communicate to only one we-energy at a time. If the price difference still exists between it and another we-energy, that we-energy may communicate to it after it finished the asynchronous communication before. Second, after the asynchronous communication, if another asynchronous communication between them does not appear, the energy transmitting between them will be invariant even if the operating conditions of some energy devices change by the dispatch inside the own we-energy or the asynchronous communication between the we-energy and another we-energy. Third, when the next measuring time is

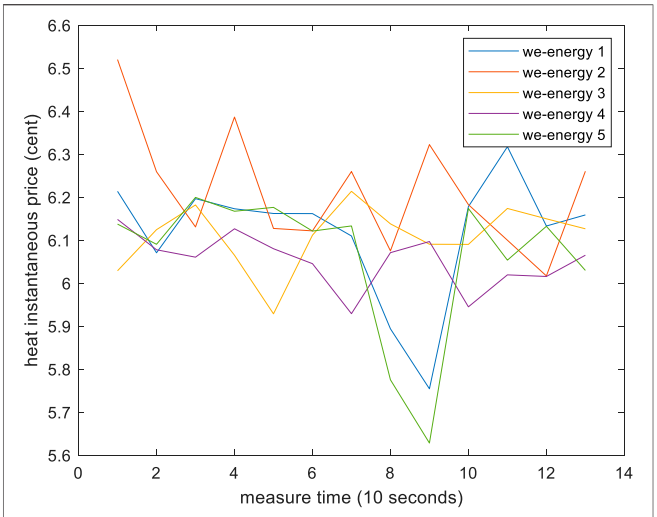

FIGURE 3 | Power instantaneous price (cent).

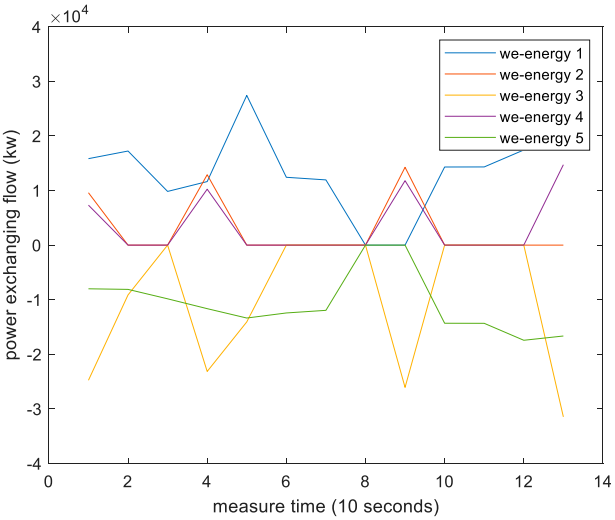

FIGURE 4 | Power exchanging flow (kw).

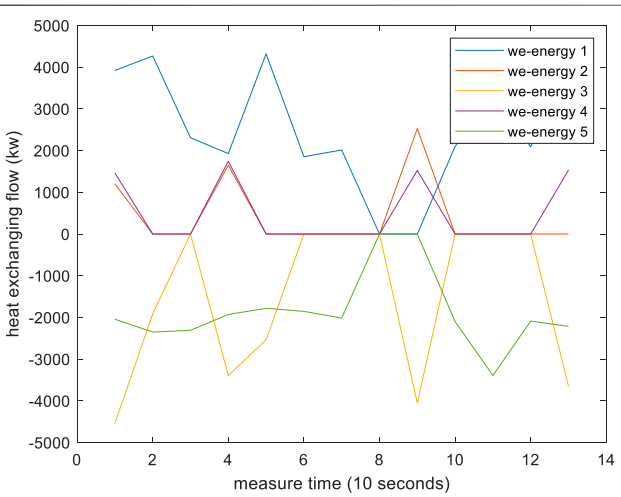

FIGURE 5 | Heat exchanging flow (kw).

reached, all we-energies will dispatch inside themselves by partial differential equations first, then they may asynchronously communicate and asynchronously dispatch. If one or two we-energies have the energy transmitting assignment between other we-energy, the asynchronous energy dispatch should consider the energy transmitting assignment. Fourth, if one we-energy should asynchronously communicate to two or more we-energies, whose we-energy will be communicated first may be random because there is not an asynchronous clock bus line in EI, so the trigger time may not be same in different we-energies. We cannot control which two we-energies will trigger early. Fifth, if the operating condition of a device is out of its in equation constraint, we will adjust it to a value on the constraint boundary. Then, we will adjust other values to reach the energy balance. By these methods, the energy management of RDETA will be realized. What is more, if the energy conversion efficiency and the operating cost factor of TD devices are all under a trigger condition, we can regard the transmitted load as the terminal users' load to simplify the computing pressure. In this study, that condition is 70% for energy conversion and 2 cent for the operating cost factor. It is worth noting that, RDETA cannot adopt KKT. The KKT is a good optimal method and good at handling optimal problems with in equation limits. However, KKT requires entire cost functions. If we adopt KKT, too much pressure will be given on communication and computing. To this end, RDETA adopts partial differential equations rather than KKT conditions. Devices only need to exchange partial differential vectors rather than all cost functions by this means. Generally, the communication needs to end when all the asynchronous communication is not triggered, while if the number of cut-vertex is less than 3, we can stop the communication when all we-energies communicate to all neighbors for one time.

Testification of Optimality and Avoiding Zeno Behaviors

As you can see, we do not prove the astringency of RDETA. The reason for that is there is not any iteration in RDETA, the astringency is obviously meaningless. The optimality is very easy to understand. However, what is the meaning of avoiding Zeno behaviors? The Zeno behavior means the trigger happens infinite times in a limited time. In this study, the Zeno behavior means the asynchronous communication is activated infinite times in one time of measuring.

The cost is changeable, which brings a serious challenge to energy management. For handling that issue, we propose several concepts including average cost, instantaneous cost, and finite difference cost.

The average cost is the specific value of the whole energy generation or conversion cost (can be solved by the cost function) and the energy flow. The finite difference cost is the specific value of a length of energy cost and the energy flow difference. The difference between the average cost and the finite difference cost is that the average cost is a specific value with the whole generation (conversion) energy, which is

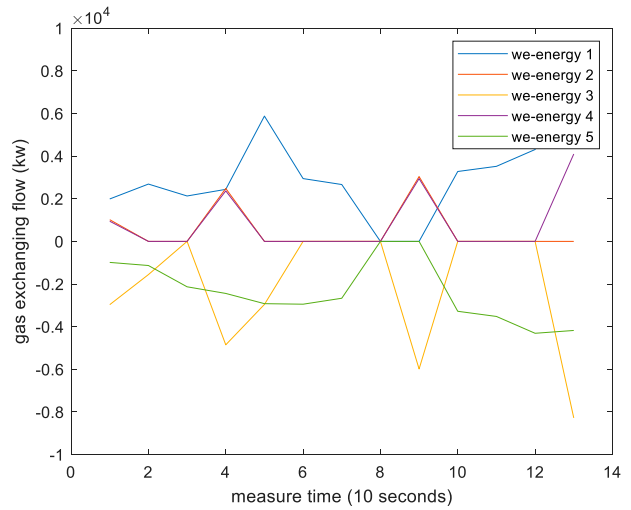

FIGURE 6 | Gas exchanging flow (kw).

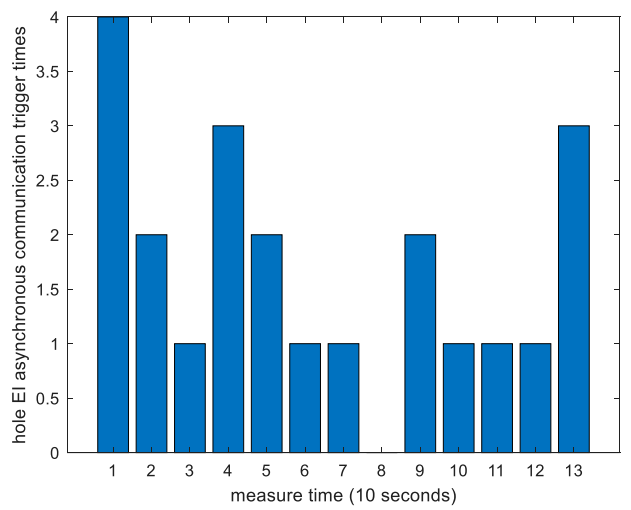

FIGURE 7 | WholeEI asynchronous communication trigger times.

from zero to an energy flow value. However, the finite difference cost is between energy flow a to energy flow$b$. That value can be solved by the difference value of the cost function value between a and b. If we choose a pair of values about a and b, in which a is exceedingly similar to$b$, the length finite difference cost can change into a point cost. The point cost is called the instantaneous cost.

Because the absolute value of $\aleph$ is exceedingly small, we can assume it as zero. Only if all trigger vectors are the same, the asynchronous communication will stop. Obviously, if all price vectors in each we-energy are the same, all trigger vectors will be the same, too. If price vectors are not all in the same value, T_1^i will trigger asynchronous communication. So the necessary and sufficient condition of asynchronous communication will stop is that all price vectors are in the same value.

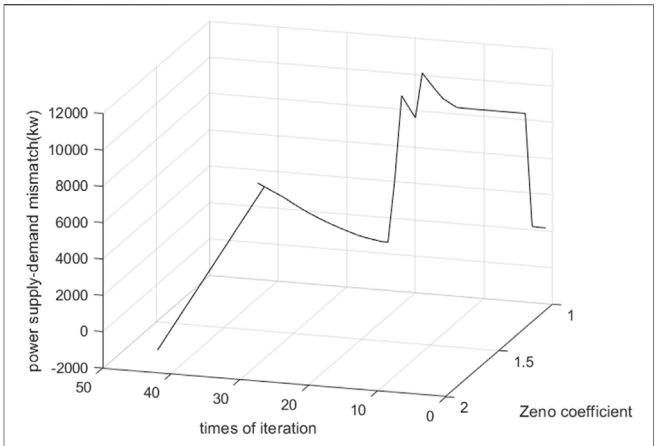

FIGURE 8 | Power supply-demand mismatch.

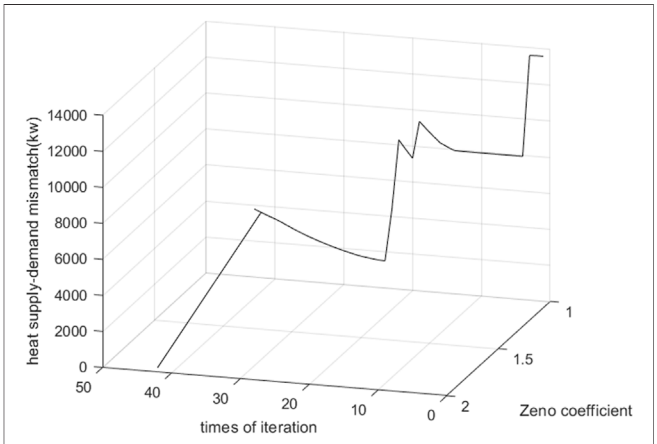

FIGURE 9 | Heat supply-demand mismatch.

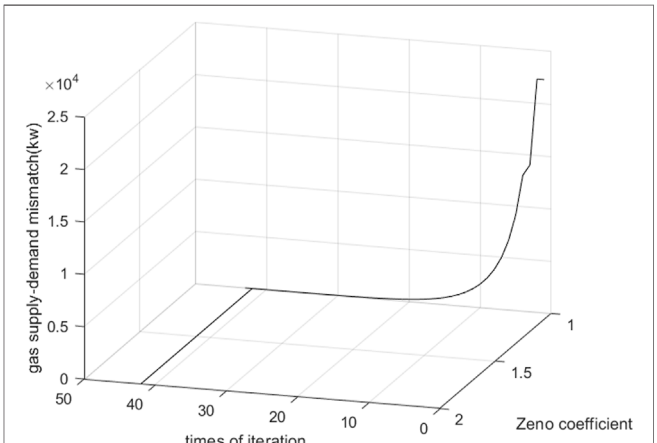

FIGURE 10 | A gas supply-demand mismatch.

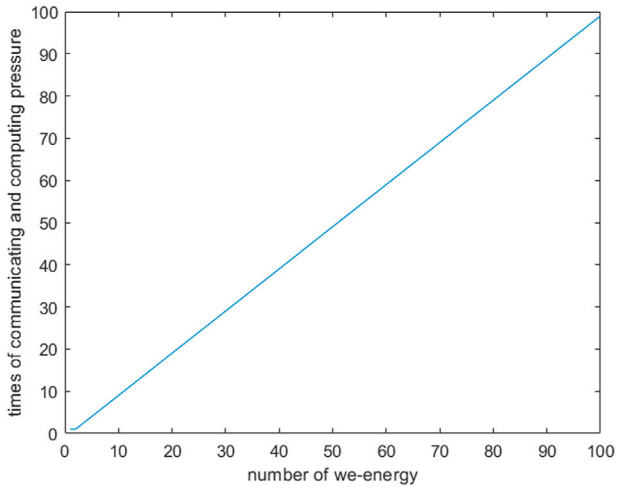

FIGURE 11 | Times of communicating and computing pressure.

If there are ε we-energies in EI, we can regard them as $\varepsilon - 1$ we-energies because we can regard two neighbor we-energies as one big we-energy. The neighbor we-energies of the big we-energy are all of the neighbor we-energies of them. The asynchronous communication can adjust their price vectors to the same. Even if another we-energy communicates to one of them, which leads their price vectors different, they can adjust themselves. What is worth noting is if a we-energy communicates to one of them for one time, the change of that we-energy which does not belong to the big we-energy is different from the change while the big we-energy is really one we-energy because that we-energy only communicates to one of them but not to both of them. However, after several times of adjusting inside the big we-energy and between the outside we-energy and one of the we-energy in the big we-energy, the dispatch will be the same of the big we-energy is a really we-energy because the big we-energy will adjust them to one we-energy sooner or later even if other we-energies disturb them. The two we-energies will undertake the perturbance together. Then, we can regard the big we-energy and a neighbor we-energy of it as a bigger we-energy for the same reason. So the big we-energy can enlarge over and over again until adsorbing the whole EI. So the price vectors of each we-energy will be the same after certain communication. The asynchronous communication will stop at the same time. The Zeno behavior of the asynchronous communication time is infinite and will never appear.

The optimization proof of the whole EI is the same as that of one we-energy because we can regard the whole EI as a big we-energy. In that big we-energy, all energy cost functions are convex functions, all price vectors are the same, and all energy conversion instantaneous costs are the same too. Under that circumstance, the energy balance is reached. If some energy devices operate in another condition, other devices also need to change the operating conditions to ensure the energy balance. The price of them will change. According to the theory of convex optimization, the increasing finite difference cost of the devices generating or transforming more energy is more than the decreasing finite difference cost of other devices because all functions are convex functions. (The cost functions of TD devices are also convex functions because they are composite functions.)

There are a large number of contributions of RDETA, which are summarized in **Figure 2**. Some are obvious while some are vague. We introduce some obscure contributions here. It is worth noting that there is not a relationship between the importance of the contributions and whether to introduce them here. The only reason to introduce them is that they are difficult to understand.

The reason RDETA can enhance privacy protection is that each we-energy only needs to exchange their T_1^i to T_{q+1}^i to other neighbor agents when the asynchronous communication is not triggered. The information in them is very less. Their operating conditions and a lot of important information do not need to exchange. The reason RDETA can make infeasible centralized algorithms feasible is that centralized algorithms are unsuitable for large systems, while RDETA only adopts it in one or two we-energy. The reason

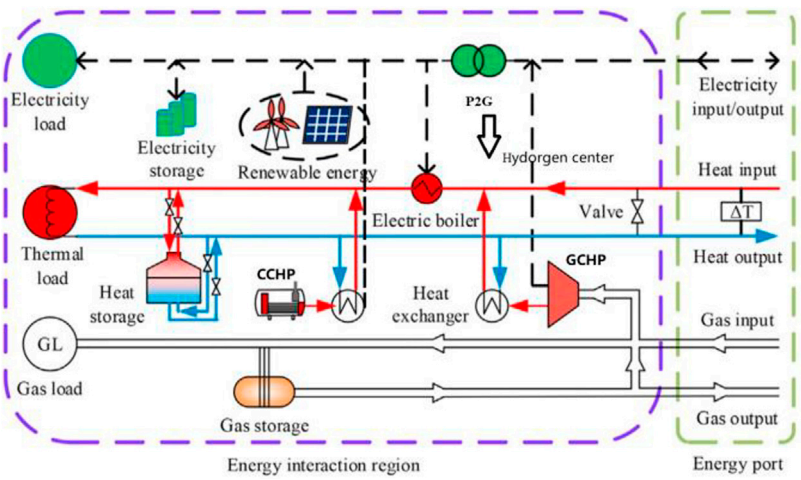

FIGURE 12 | We-energy framework.

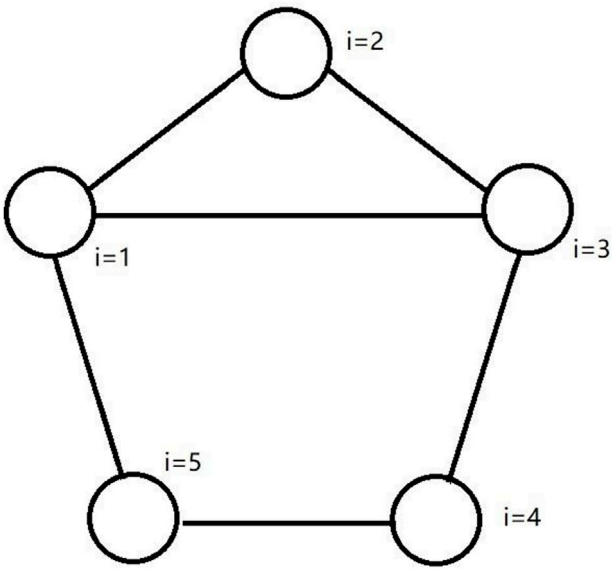

FIGURE 13 | Energy Internet framework.

RDETA can remove global communication is that RDETA only communicates in two we-energies at one time.

SIMULATION RESULTS

The performance of the proposed RDETA algorithm is tested on an EI system with five we-energies. The simulation platform and all data are shown in the **Supplementary Appendix**. The measurement interval time is 10 s. The simulation results are as follows.

Figures 2, **3** are the instantaneous price of power and heat (the gas price never changes). **Figures 4–6** are energy exchanging between each we-energy and others. **Figure 7** is the asynchronous communication times in whole EI. What is worth noting is that the communication order is randomized to a certain degree because there is not a synchronous clock bus line. For comparing with the traditional distributed algorithm, we give a distributed Newton algorithm result. Most data and models for the distributed Newton algorithm are the same as that in RDETA, while the gas production cost function is different because without the changing price of gas, the traditional algorithm cannot run. The cost function is as follows:

$$C_{i,t}^{\mathrm{DGP}} = \mathrm{a}_{i,t}^{\mathrm{DGP}} G_{i,t}^{\mathrm{DGP}\,2} + \mathrm{b}_{i,t}^{\mathrm{DGP}} G_{i,t}^{\mathrm{DGP}} + \mathrm{c}_{i,t}^{\mathrm{DGP}}$$

To differentiate, that device is called DGP in the distributed Newton algorithm but called EGG in RDETA.

Figures 8–10 are the power-heat-gas mismatch. The Zeno coefficient is the decrease times of the Newton downhill factor. The traditional Newton distributed algorithm goes by 43 times of iteration with global communication to make all types of energy mismatch less than500kw. However, RDETA adopts four times of iterations with regional communication (the communication workload of regional communication is one-sixth to that of global communication because there are six sides in the graph of EI in this study.) to make all types of energy match zero. Therefore, RDETA adopts a workload 64.5 times less than that of the traditional distributed algorithm to realize a better energy management result than that in the traditional distributed algorithm. Compared with traditional centralized algorithms, communicating and computing pressure of the control center about RDETA is much less. **Figure 11** is the times of communicating and computing pressure of the control center between traditional centralized algorithms and RDETA. As you can see, the communicating and computing pressure times between them are growing sharply with the growth of we-energy numbers. So RDETA is much more suitable for the large EI with lots of we-energies than traditional centralized algorithms.

Figure 12 is the we-energy framework. **Figure 13** is the EI framework. There are five we-energies in EI in this article. The price of gas is 8 cents per kwh . The price of coal is 6 cents per kwh . sg for power and gas is0.1 times the initial measure value. $k-1$ means the initial condition. Δ_r is all 2. I is all 4. sg of the energy load is 0.1 times its initial value. Other data is in the following big table. Some data is the same in CCHP and GCHP, so we only introduce it once. The heat load does not change the whole time.

CONCLUSION

In this study, an innovative asynchronous communication energy management framework without iterations has been introduced for the future EI. Along with five we-energies, the EI system can better address the features and requirements of EI in a way with much less workload. By the combination of distributed algorithms and centralized algorithms and the partial differential equations, the cost of RDETA greatly decreases and its performance of that is obviously increased. Simulation results and theoretical identifications have demonstrated the effectiveness of it. However, cyber attacks and nonconvex issues are out of consideration in this study. So they need to address this in future work.

DATA AVAILABILITY STATEMENT

The original contributions presented in the study are included in the article/**Supplementary Material**, further inquiries can be directed to the corresponding author.

AUTHOR CONTRIBUTIONS

The author has written the whole article by himself.

SUPPLEMENTARY MATERIAL

The Supplementary Material for this article can be found online at: https://www.frontiersin.org/articles/10.3389/fenrg.2022.908199/full#supplementary-material

REFERENCES

Abdella, J., Tari, Z., Anwar, A., Mahmood, A., and Han, F. (2021). An Architecture and Performance Evaluation of Blockchain-Based Peer-To-Peer Energy Trading. *IEEE Trans. Smart Grid* 12 (99), 1. doi:10.1109/TSG.2021.3056147

Bahrami, S., and Sheikhi, A. (2016). From Demand Response in Smart Grid Toward Integrated Demand Response in Smart Energy Hub. *IEEE Trans. Smart Grid* 7 (2), 650–658.

Can, W., Zhaohong, B., Qiuwei, W., Gengfeng, L., and Haipeng, X. (2021). Coordinated Post-Contingency Dispatch of Integrated Energy System With Multiple Participants Based on Distributed Energy Trading. *Int. J. Electr. Power & Energy Syst.* 130, 31. doi:10.1016/j.ijepes.2021.107011

Huang, A. Q., Crow, M. L., Heydt, G. T., Zheng, J. P., and Dale, S. J. (2010). The Future Renewable Electric Energy Delivery and Management (FREEDM) System: The Energy Internet. *Proc. IEEE* 99 (1), 133–148. doi:10.1109/JPROC.2010.2081330

Huang, B., Li, Y., Zhang, H., and Sun, Q. (2016). Distributed Optimal Co-Multi-Microgrids Energy Management for Energy Internet. *IEEE/CAA J. Automatica Sinica* 3 (4), 357. doi:10.1109/JAS.2016.7510073

Kubli, M., Loock, M., and Wüstenhagen, R. (2018). The Flexible Prosumer: Measuring the Willingness to Co-Create Distributed Flexibility. *Energy Policy* 114, 540–548. doi:10.1016/j.enpol.2017.12.044

Li, Y., Gao, D. W., Gao, W., Zhang, H., and Zhou, J. (2020). Double-Mode Energy Management for Multi-Energy System via Distributed Dynamic Event-Triggered Newton-Raphson Algorithm. *IEEE Trans. Smart Grid* 11 (99), 5339. doi:10.1109/TSG.2020.3005179

Li, Y., Zhang, H., Liang, X., and Huang, B. (2019). Event-Triggered-Based Distributed Cooperative Energy Management for Multienergy Systems. *IEEE Trans. Ind. Inf.* 15 (4), 2008–2022. doi:10.1109/tii.2018.2862436

Liang, H., Zhang, L., Sun, Y., and Huang, T. (2021). Containment Control of Semi-markovian Multiagent Systems With Switching Topologies. *IEEE Trans. Syst. Man, Cybern. Syst.* 51 (99), 1–11. doi:10.1109/TSMC.2019.2946248

Lin, C, E., and Viviani, G. L. (1984). Hierarchical Economic Dispatch for Piecewise Quadratic Cost Functions. *IEEE Power Eng. Rev.* 103, 1170. doi:10.1109/TPAS.1984.318445

Lin, C. E., Chen, S. T., and Huang, C.-L. (1992). A Direct Newton-Raphson Economic Dispatch. *IEEE Trans. Power Syst.* 7 (3), 1149–1154. doi:10.1109/59.207328

Lu, R., Hong, S. H., and Yu, M. (2019). Demand Response for Home Energy Management Using Reinforcement Learning and Artificial Neural Network. *IEEE Trans. Smart Grid* 10 (6), 6629–6639. doi:10.1109/tsg.2019.2909266

Moeini-Aghtaie, M., Dehghanian, P., Fotuhi-Firuzabad, M., and Abbaspour, A. (2014). Multiagent Genetic Algorithm: An Online Probabilistic View on Economic Dispatch of Energy Hubs Constrained by Wind Availability. *IEEE Trans. Sustain. Energy* 5 (2), 699–708. doi:10.1109/tste.2013.2271517

Pourbabak, H., Luo, J., Tao, C., and Su, W. (2017). A Novel Consensus-Based Distributed Algorithm for Economic Dispatch Based on Local Estimation of Power Mismatch. *IEEE Trans. Smart Grid* 9 (99), 1. doi:10.1109/TSG.2017.2699084

Qin, X., Sun, H., Shen, X., Guo, Y., Guo, Q., and Xia, T. (2019). A Generalized Quasi-Dynamic Model for Electric-Heat Coupling Integrated Energy System with Distributed Energy Resources. *Appl. Energy* 251, 113270. doi:10.1016/j.apenergy.2019.05.073

Sheikhi, A., Rayati, M., Bahrami, S., and Mohammad Ranjbar, A. (2015). Integrated Demand Side Management Game in Smart Energy Hubs. *IEEE Trans. Smart Grid* 6 (2), 675–683. doi:10.1109/tsg.2014.2377020

Sun, J., Palade, V., Wu, X. J., Fang, W., and Wang, Z. (2013). Solving the Power Economic Dispatch Problem With Generator Constraints by Random Drift Particle Swarm Optimization. *IEEE Trans. Industrial Inf.* 10 (1), 222–232. doi:10.1109/TII.2013.2267392

Sun, Q. (2019). *Energy Internet and we-energy*. Singapore: Springer-Verlag: Springer Nature.

Sun, Q., Fan, R., Li, Y., Huang, B., and Ma, D. (2019). A Distributed Double-Consensus Algorithm for Residential We-Energy. *IEEE Trans. industrial Inf.* 15, 4830. doi:10.1109/TII.2019.2921431

Sun, Q., Han, R., Zhang, H., Zhou, J., and Guerrero, J. M. (2015). A Multiagent-Based Consensus Algorithm for Distributed Coordinated Control of Distributed Generators in the Energy Internet. *IEEE Trans. Smart Grid* 6 (6), 3006–3019. doi:10.1109/tsg.2015.2412779

Sun, Q., Zhang, Y., He, H., Ma, D., and Zhang, H. (2017). A Novel Energy Function-Based Stability Evaluation and Nonlinear Control Approach for Energy Internet. *IEEE Trans. Smart Grid* 8, 1195–1210. doi:10.1109/tsg.2015.2497691

Wang, Y., Nguyen, T.-L., Xum, Y., Tran, Q. T., Xu, Y., Tran, Q.-T., et al. (2020). Peer-to-Peer Control for Networked Microgrids: Multi-Layer and Multi-Agent Architecture Design. *IEEE Trans. Smart Grid* 11 (6), 4688–4699. doi:10.1109/tsg.2020.3006883

Wright, S. J. (1997). *Primal-Dual Interior-Point Methods*. Philadelphia, PA: SIAM.

Wu, J., Zhang, B., Wang, K., Shao, J., Yao, J., Zeng, D., et al. (2015). Optimal Economic Dispatch Model Based on Risk Management for Wind-integrated Power System. *IET Generation, Transm. Distribution* 9 (15), 2152–2158. doi:10.1049/iet-gtd.2015.0209

Xu, T., Wu, W., Zheng, W., Sun, H., and Wang, L. (2018). Fully Distributed Quasi-Newton Multi-Area Dynamic Economic Dispatch Method for Active Distribution Networks. *IEEE Trans. Power Syst.* 33, 4253. doi:10.1109/TPWRS.2017.2771950

Yile, L., Liu, F., and Mei, S. (2017). Distributed Real-Time Economic Dispatch in Smart Grids: A State-Based Potential Game Approach. *IEEE Trans. Smart Grid* 9 (5), 4194–4208. doi:10.1109/TSG.2017.2652919

Yuang, X., Qingshan, X., Haiya, Q., and Li, C. (2022). Peer-to-Peer Energy Trading Considering the Output Uncertainty of Distributed Energy Resources. *Energy Rep.* 8, 567. doi:10.1016/j.egyr.2021.11.001

Zhang, H., Li, Y., Gao, D. W., and Zhou, J. (2017). Distributed Optimal Energy Management for Energy Internet. *IEEE Trans. Ind. Inf.* 13 (6), 3081–3097. doi:10.1109/tii.2017.2714199

Zhang, N., Sun, Q., Wang, J., and Yang, L. (2020a). Distributed Adaptive Dual Control via Consensus Algorithm in the Energy Internet. *IEEE Trans. Industrial Inf.* 17 (99), 1. doi:10.1109/TII.2020.3031437

Zhang, N., Sun, Q., and Yang, L. (2020b). A Two-Stage Multi-Objective Optimal Scheduling in the Integrated Energy System with We-Energy Modeling. *Energy* 215, 119121. doi:10.1016/j.energy.2020.119121

Conflict of Interest: The author declares that the research was conducted in the absence of any commercial or financial relationships that could be construed as a potential conflict of interest.

Publisher's Note: All claims expressed in this article are solely those of the authors and do not necessarily represent those of their affiliated organizations, or those of the publisher, the editors, and the reviewers. Any product that may be evaluated in this article, or claim that may be made by its manufacturer, is not guaranteed or endorsed by the publisher.

frontiers | Frontiers in Energy Research

ORIGINAL RESEARCH
published: 24 May 2022
doi: 10.3389/fenrg.2022.899732

Intelligent Command Filter Design for Strict Feedback Unmodeled Dynamic MIMO Systems With Applications to Energy Systems

Xuxiang Feng[1], *Lu Shi*[2,1] *and Yumeng Zhang*[1]*

[1]Aerospace Information Research Institute, Chinese Academy of Sciences, Beijing, China, [2]School of Electronics and Information, Northwestern Polytechnical University, Xi'an, China

This study presents a command filtered control scheme for multi-input multi-output (MIMO) strict feedback nonlinear unmodeled dynamical systems with its applications to power systems. To deal with dynamic uncertainties, a dynamic signal is introduced, together with radial basis function neural networks (RBFNNs) to overcome the influences of the dynamic uncertainties. Command filters (CFs) are used to prevent the explosion of complexity, where the compensating signals can eliminate the effect of filter errors. Compared with single-input single-output strict feedback nonlinear systems, the method proposed in this study has more suitability. In the end, the simulation experiments are carried out by applying the developed algorithm to power systems, where the simulation results verify the efficacy of the approach proposed.

Keywords: power system, dynamic uncertainty, command filter, MIMO system, strict feedback nonlinear system

OPEN ACCESS

Edited by:
Yushuai Li,
University of Oslo, Norway

Reviewed by:
Liqiang Tang,
University of Science and Technology Beijing, China
Yongshan Zhang,
University of Macau, China

****Correspondence:***
Yumeng Zhang
zhangym203409@aircas.ac.cn

Specialty section:
This article was submitted to Smart Grids, a section of the journal Frontiers in Energy Research

Received: *19 March 2022*
Accepted: *11 April 2022*
Published: *24 May 2022*

Citation:
Feng X, Shi L and Zhang Y (2022) Intelligent Command Filter Design for Strict Feedback Unmodeled Dynamic MIMO Systems With Applications to Energy Systems. Front. Energy Res. 10:899732. doi: 10.3389/fenrg.2022.899732

1 INTRODUCTION

In recent years, adaptive control has become a hotspot because of its strong disturbance-rejection property. Related theories, such as model reference control, robust adaptive control, and adaptive dynamic programming (Mukherjee et al., 2017; Yang et al., 2021b; Han and Liu, 2020; Yang et al., 2021d; L'Afflitto, 2018; Yang et al., 2021e), have been applied to many fields, including power systems, wind energy systems, and multi-agent systems (Li et al., 2020; Xu et al., 2018; Wu et al., 2017; Ghaffarzdeh and Mehrizi-Sani, 2020; Zou et al., 2020b; Ghosh and Kamalasadan, 2017; Namazi et al., 2018; Zou et al., 2020a). Moreover, applications of adaptive control on energy systems are also widely reported (Deese and Vermillion, 2021; Quan et al., 2020; Liu et al., 2022; Nascimento Moutinho et al., 2008; Liu et al., 2021). Among them, backstepping is a powerful tool since many energy systems can essentially be modeled as strict feedback systems, which can be analyzed through the backstepping technique.

The main idea of backstepping is to divide the whole system into a series of subsystems so that they can be analyzed individually. In this way, the control design and stability analysis can both be simplified, especially for large-scale systems (Yang et al., 2021a). Meanwhile, for unmodeled dynamical systems, if the unmodeled dynamics are ignored, the disturbance from dynamic uncertainties may result in unbounded evolution. Therefore, the dynamic uncertainties need to be paid enough attention, which is not considered in the aforementioned literatures. Zhao J. et al. (2021) presented a fuzzy adaptive control approach with an observer design for unmodeled dynamical systems. Xia et al. developed an output feedback control

design with quantized performance for dynamic uncertainties in Xia and Zhang (2018). Wang et al. (2017)investigated nonstrict feedback systems with unmodeled dynamics and dead zones through output feedback-based control methods. Although the aforementioned results can successfully tackle dynamic uncertainties, they are not able to deal with the explosion of complexity and avoid the influences of filter errors.

In the backstepping process, the explosion of complexity often occurs because the virtual control is repeatedly differentiated. Meanwhile, the computational complexity increases significantly, which results in the presented design not being suitable for applications (Yang et al., 2020). To deal with this issue, the dynamic surface control method is proposed (Wang and Huang, 2005). The dynamic surface control method uses first-order filters, where the virtual control is replaced by the filter states in each subsystem (Yang et al., 2021c). In this way, the repeated differentiation issue can be evaded. However, filter errors are introduced simultaneously, which degrades the control precision. Thus, command filters (CFs) are developed (Farrell et al., 2009). Based on the dynamic surface control approach, CFs additionally introduce compensating signals to compensate for the loss caused by filter errors, which further improves the control accuracy compared with the dynamic surface control method. Owing to this advantage, CFs are widely applied to many systems. For example, Zhu et al. (2018)investigated a command filtered robust adaptive neural network (NN) control for strict feedback nonlinear systems with input saturation. Zhao L. et al. (2021)presented an adaptive finite-time tracking control design with CFs. The adaptive fuzzy backstepping control approach of uncertain strict feedback nonlinear systems is developed by Wang et al. (2016). However, the applications of the backstepping technique in energy systems are not taken into consideration in these works. In addition, the systems of interest in these works are single-input single-output systems, which may give conservative results. Therefore, in this study, for multi-input multi-output (MIMO) strict feedback nonlinear unmodeled dynamical systems, a command filtered control method is developed and applied to energy systems.

The contributions of this study are two-fold. First, this study designs an adaptive backstepping control scheme for MIMO strict feedback nonlinear unmodeled dynamical systems with CFs, the compensating signal design and controller design are improved such that they can get higher tracking precision. Second, this study investigates the applications of the presented CF-based adaptive backstepping control approach on power systems, and a MIMO circuit system is used in the simulation experiments to verify the effectiveness of the method developed.

The rest of this article is organized as follows. **Section 2** provides the problem formulation and necessary assumptions. In **Section 3**, the control design is proposed. The stability analysis of the system with the presented design is carried out in **Section 4**. In **Section 5**, a voltage source converter-high voltage direct current transmission system is used to verify the efficacy of the proposed method. The conclusion is made in **Section 6**.

2 PROBLEM FORMULATION

In this study, the circuit system under consideration is modeled as

$$\begin{aligned} \dot{\varsigma} &= q(\varsigma, X), \\ \dot{X}_i &= F_i\left(\underline{X}_i\right) + G_i X_{i+1} + D_i + \Delta_i(\varsigma, X), \\ \dot{X}_i &= F_n(X) + G_n U + D_n + \Delta_n(\varsigma, X), \\ y &= X_1, \end{aligned} \tag{1}$$

where $X = \left[X_1 \ \ldots \ X_n\right]^{\mathrm{T}} \in \mathbb{R}^{nm}$, $y \in \mathbb{R}^m$, and $U \in \mathbb{R}^m$ are the system state, output, and the control input, respectively. $F_i(\cdot) : \mathbb{R}^{im} \to \mathbb{R}^m$ is a known continuous function, $q(\cdot,\cdot) : \mathbb{R} \times \mathbb{R}^{nm} \to \mathbb{R}$ is an unknown continuous function, $G_i \neq 0$ is a known constant, $D_i \in \mathbb{R}^m$ is an unknown constant vector, $\underline{X}_i = \left[X_1, \cdots, X_i\right]^{\mathrm{T}} \in \mathbb{R}^{im}$, $\varsigma \in \mathbb{R}$ is the unmeasured portion of the state, and $\Delta_i \in \mathbb{R}^m$ is the unmodeled dynamics.

In this study, the following assumptions are needed.

Assumption 1: Jiang and Praly (1998): The dynamic uncertainty Δ_i in **Eq. 1** is assumed to satisfy

$$\left\|\Delta_i(\varsigma, X)\right\| \leq \phi_{i1}\left(\left\|\underline{X}_i\right\|\right) + \phi_{i2}(\|\varsigma\|), \quad i = 1, \ldots, n \tag{2}$$

with unknown smooth functions $\phi_{i1}(\cdot) : \mathbb{R}_0^+ \to \mathbb{R}_0^+$ and $\phi_{i2}(\cdot) : \mathbb{R}_0^+ \to \mathbb{R}_0^+$. In addition, $\phi_{i2}(\cdot)$ is assumed to be strictly increasing.

Assumption 2: Jiang and Praly (1998): There exists an input-to-state practically stable Lyapunov function $V_\varsigma(\varsigma)$ for $\dot{\varsigma} = q(\varsigma, X)$ in **Eq. 1** such that

$$\begin{aligned} &\omega_1(\|\varsigma\|) \leq V_\varsigma(\varsigma) \leq \omega_2(\|\varsigma\|), \\ &\frac{\partial V_\varsigma}{\partial \varsigma} q(\varsigma, X) \leq -c_0 V_\varsigma(\varsigma) + \vartheta(\|X_1\|) + d_0, \end{aligned} \tag{3}$$

with ω_1 and ω_2 belonging to class $\mathcal{K}_\infty$ *functions,* $\vartheta(\cdot) : \mathbb{R}_0^+ \to \mathbb{R}_0^+$, and c_0 and d_0 being positive constants.

To deal with the dynamic uncertainty, a dynamic signal is designed with the following dynamics,

$$\dot{r} = -\bar{c} r + \bar{\vartheta}(\|X_1\|) + d_0, \qquad r(0) = r_0, \tag{4}$$

where $\bar{\vartheta}(X_1) \geq \vartheta(\|X_1\|)$, $\bar{c} \in (0, c_0)$, and $c_0 > 0$ and r_0 are constants.

Lemma 1: Hardy et al. (1952): For any $\xi_0 > 0$, one has

$$0 \leq \|\xi_0\| - \xi_0 \tanh\left(\frac{\xi_0}{\chi}\right) \leq 0.2785\chi,$$

where $\chi > 0$ is a constant.

Lemma 2: Jiang and Praly (1998):

For the unmeasured partial state $\varsigma(t)$ with initial state ς_0, $V_\varsigma(\varsigma)$ given in Assumption 2, the dynamic signal $r(t)$ in **Eq. 4**, and all $t \geq 0$, there is a non-negative function $B(t)$ *such that*

$$V_\varsigma(\varsigma) \leq r(t) + \Phi(t). \tag{5}$$

In addition, there is a limited time $T_0 = T_0\left(\bar{c}_0, r_0, \varsigma_0\right)$ such that $\Phi(t) = 0$ for all $t \geq T_0$.

With no loss of generality, choose $\overline{\Theta}(X_1)$ as $\overline{\Theta}(X_1) = X_1^2\Theta(X_1^2)$. Accordingly, the dynamic signal $r(t)$ is designed as

$$\dot{r} = -\bar{c}r + X_1^2\Theta(X_1^2) + d_0, \qquad r(0) = r_0. \tag{6}$$

The control objective of this study can be formulated as follows.

Control Objective: Consider the reference output X_d satisfying $\{X_d, \dot{X}_d, \ddot{X}_d\}$ are bounded. Under Assumptions 1–2, design a neuro-adaptive controller for the system (1), such that,

1. the system output X_1 can track the reference X_d asymptotically, and
2. all signals in the closed-loop system keep bounded.

3 NEURO-ADAPTIVE CONTROLLER DESIGN

First, the tracking errors E_i, filter errors Z_i, and the compensated tracking errors Λ_i are defined for each subsystem as

$$\begin{aligned} E_i &= X_i - A_{i-1},\ i = 1,2,3,\\ Z_i &= A_i - S_i,\ i = 1,2,\\ \Lambda_i &= E_i - B_i,\ i = 1,2,3, \end{aligned} \tag{7}$$

where A_i is the filter state, $A_0 = X_d$, S_i is the virtual control, and B_i is the compensating signal.

For the subsequent design and analysis, denote $\Theta_i = \|W_i^*\|^i$, $i = 1,\ldots,n$ with W_i^* being the ideal weight vector of the RBFNNs. In addition, denote $\hat{\Theta}_i(t)$ as the estimation of Θ_i with an estimation error $\tilde{\Theta}_i(t) = \Theta_i - \hat{\Theta}_i(t)$.

3.1 Adaptive Backstepping Design

3.1.1 Step 1

Based on **Eqs 1**, **7**, taking a derivative of E_1 yields

$$\begin{aligned} \dot{E}_1 &= F_1(X_1) + G_1X_2 + D_1 + \Delta_1 - \dot{X}_d\\ &= F_1(X_1) + G_1E_2 + G_1S_1 + G_1Z_1 + D_1 + \Delta_1 - \dot{X}_d. \end{aligned} \tag{8}$$

For the first subsystem, the virtual control S_1 is designed as

$$S_1 = \frac{1}{G_1}\left(-F_1 - K_1E_1 - \frac{\hat{\Theta}_1}{2\eta_1}\Lambda_1\varphi_1^{\mathrm{T}}\varphi_1 + \dot{X}_d\right), \tag{9}$$

with $K_1 = \mathrm{diag}\{K_{11}, \cdots, K_{1m}\}$ is a positive definite matrix, and $\eta_1 > 0$. To avoid repeated differentiation of the virtual control, a CF is designed as

$$\dot{A}_1 = \frac{S_1 - A_1}{\tau_1}, A_1(0) = S_1(0), \tag{10}$$

with a positive constant τ_1. To eliminate the effect of filter errors, the compensating signal is developed as

$$\dot{B}_1 = -K_1B_1 + G_1B_2 + G_1Z_1, B_1(0) = 0. \tag{11}$$

To compensate for the unknown dynamics, the adaptive law for Θ_1 is presented as

$$\dot{\hat{\Theta}}_1 = \frac{1}{2\eta_1}\Lambda_1^{\mathrm{T}}\Lambda_1\varphi_1^{\mathrm{T}}\varphi_1 - \gamma_1\hat{\Theta}_1, \hat{\Theta}_1(0) = 0, \tag{12}$$

where $\gamma_1 > 0$ is a constant.

3.1.2 Step i ($2 \le i \le n-1$)

From **Eqs 1**, **7**, differentiating E_i leads to

$$\begin{aligned} \dot{E}_i &= F_i + G_iX_{i+1} + D_i + \Delta_i - \dot{A}_{i-1}\\ &= F_i + G_iE_{i+1} + G_iS_i + G_iZ_i + D_i + \Delta_i - \dot{A}_{i-1}. \end{aligned} \tag{13}$$

The virtual control design S_i is developed as

$$S_i = \frac{1}{G_i}\left(-F_i - G_{i-1}E_{i-1} - K_iE_i - \frac{\hat{\Theta}_i}{2\eta_i}\Lambda_i\varphi_i^{\mathrm{T}}\varphi_i + \dot{A}_{i-1}\right), \tag{14}$$

where $K_i = \mathrm{diag}\{K_{i1}, \cdots, K_{im}\}$ is a positive definite matrix, and $\eta_i > 0$. To obviate repeated differentiation of the virtual control S_i, a CF is given as

$$\dot{A}_i = \frac{S_i - A_i}{\tau_i}, A_i(0) = S_i(0), \tag{15}$$

with a positive design parameter τ_i. To diminish the influences of filter errors, the compensating signal is proposed as

$$\dot{B}_i = -G_{i-1}B_{i-1} - K_iB_i + G_iB_{i+1} + G_iZ_i, B_i(0) = 0. \tag{16}$$

To deal with the parameter estimation, the adaptive law to estimate Θ_i is designed as

$$\dot{\hat{\Theta}}_i = \frac{1}{2\eta_i}\Lambda_i^{\mathrm{T}}\Lambda_i\varphi_i^{\mathrm{T}}\varphi_i - \gamma_i\hat{\Theta}_i, \hat{\Theta}_i(0) = 0, \tag{17}$$

with a constant $\gamma_i > 0$.

3.1.3 Step n

According to **Eqs 1**, **7**, the differentiation of E_n can be transformed as

$$\dot{E}_n = F_n + G_nU + D_n + \Delta_n - \dot{A}_{n-1}. \tag{18}$$

The controller design is given as

$$U = \frac{1}{G_n}\left(-F_n - G_{n-1}E_{n-1} - K_nE_n - \frac{\hat{\Theta}_n}{2\eta_n}\Lambda_n\varphi_n^{\mathrm{T}}\varphi_n + \dot{A}_{n-1}\right), \tag{19}$$

with design parameters $K_n = \mathrm{diag}\{K_{n1}, \cdots, K_{nm}\}$ is a positive definite matrix, and $\eta_n > 0$. The compensating signal for this step is presented as

$$\dot{B}_n = -G_{n-1}B_{n-1} - K_nB_n, B_n(0) = 0. \tag{20}$$

The adaptive law is developed as

$$\dot{\hat{\Theta}}_n = \frac{1}{2\eta_n}\Lambda_n^{\mathrm{T}}\Lambda_n\varphi_n^{\mathrm{T}}\varphi_n - \gamma_n\hat{\Theta}_n, \hat{\Theta}_n(0) = 0, \tag{21}$$

where $\gamma_n > 0$ is a constant.

4 STABILITY ANALYSIS

In this section, we analyze the stability of the closed-loop system (**Eq. 1**) with the presented design of the virtual control (**Eqs 9**, **14**), controller (**Eq. 19**), adaptive laws (**Eqs 12**, **17**, **21**), CFs (**Eq. 10**) and (**15**), and compensating signals (**Eqs 11**, **16**, **20**).

4.1 Step 1

Inserting **Eq. 9** into **Eq. 8**, we obtain

$$\dot{E}_1 = -K_1E_1 + G_1E_2 + G_1Z_1 - \frac{\hat{\Theta}_1}{2\eta_1}\Lambda_1\varphi_1^{\mathrm{T}}\varphi_1 + D_1 + \Delta_1. \tag{22}$$

From the aforementioned equation and **Eq. 11**, one has

$$\dot{\Lambda}_1 = -K_1\Lambda_1 + G_1\Lambda_2 - \frac{\hat{\Theta}_1}{2\eta_1}\Lambda_1\varphi_1^{\mathrm{T}}\varphi_1 + D_1 + \Delta_1. \tag{23}$$

The Lyapunov function is defined as $V_1\left(\Lambda_1, \tilde{\Theta}_1\right) = \frac{1}{2}\Lambda_1^{\mathrm{T}}\Lambda_1 + \frac{1}{2}\tilde{\Theta}_1^{\mathrm{T}}\tilde{\Theta}_1$. From Assumption 1, the term $\Lambda_1^{\mathrm{T}}\Delta_1$ satisfies

$$\Lambda_1^{\mathrm{T}}\Delta_1 \le \|\Lambda_1\|\phi_{11}(\|X_1\|) + \|\Lambda_1\|\phi_{12}(\|\varsigma\|). \tag{24}$$

For the term $\|\Lambda_1\|\phi_{11}(\|X_1\|)$ in the aforementioned equation, based on Lemma 1, one has

$$\|\Lambda_1\|\phi_{11}(X_1,\ \Lambda_1) \le \Lambda_1^{\mathrm{T}}\hat{\phi}_{11}(\|X_1\|) + \varepsilon'_{11},\ \varepsilon'_{11} = 0.2785\varepsilon_{11}, \tag{25}$$

with ε'_{11} and ε_{11} being positive constants and

$$\hat{\phi}_{11}(X_1,\ \Lambda_1) = \phi_{11}(\|X_1\|)\tanh\left(\frac{\Lambda_1^{\mathrm{T}}\phi_{11}(\|X_1\|)}{\varepsilon_{11}}\right).$$

Consider the term $\|\Lambda_1\|\phi_{12}(\|\varsigma\|)$ in **Eq. 24**, according to Lemma 2, we have

$$\|\Lambda_1\|\phi_{12}(\|\varsigma\|) \le \|\Lambda_1\|\phi_{12}\left(\omega_1^{-1}(r+\Phi)\right). \tag{26}$$

It is to be noted that $\phi_{12}(\cdot)$ is strictly increasing and non-negative from Assumption 1, together with the fact that $r + \Phi \le \max\{2r, 2\Phi\}$, one has

$$\begin{aligned}\|\Lambda_1\|\phi_{12}\left(\omega_1^{-1}(r+\Phi)\right) \le{}& \|\Lambda_1\|\phi_{12}\left(\omega_1^{-1}(2r)\right)\\ &+ \|\Lambda_1\|\phi_{12}\left(\omega_1^{-1}(2\Phi)\right).\end{aligned} \tag{27}$$

From Lemma 1, we can obtain

$$\|\Lambda_1\|\phi_{12}\left(\omega_1^{-1}(2r)\right) \le \Lambda_1^{\mathrm{T}}\hat{\phi}_{12}(\Lambda_1, r) + \varepsilon'_{12},\ \varepsilon'_{12} = 0.2785\varepsilon_{12}, \tag{28}$$

where ε'_{12} and ε_{12} are positive constants, and

$$\hat{\phi}_{12}(\Lambda_1, r)\phi_{12}\left(\omega_1^{-1}(2r)\right)\tanh\left(\frac{\Lambda_1\phi_{12}\left(\omega_1^{-1}(2r)\right)}{\varepsilon_{12}}\right),$$

$$\|\Lambda_1\|\phi_{12}\left\|\left(\omega_1^{-1}(2\Phi)\right)\right\| \le \frac{1}{4}\Lambda_1^{\mathrm{T}}\Lambda_1 + d_1(t), \tag{29}$$

where $d_1(t) = \phi_{12}^2\left(\omega_1^{-1}(2\Phi(t))\right)$. From **Eqs 23**–**29**, the derivative of V_1 can be expressed as

$$\begin{aligned}\dot{V}_1 &= \Lambda_1^{\mathrm{T}}\left(-K_1\Lambda_1 + G_1\Lambda_2 - \frac{\hat{\Theta}_1}{2\eta_1}\Lambda_1\varphi_1^{\mathrm{T}}\varphi_1 + D_1 + \Delta_1\right) - \tilde{\Theta}_1^{\mathrm{T}}\dot{\hat{\Theta}}_1\\ &\le -\Lambda_1^{\mathrm{T}}K_1\Lambda_1 - \frac{\hat{\Theta}_1}{2\eta_1}\Lambda_1^{\mathrm{T}}\Lambda_1\varphi_1^{\mathrm{T}}\varphi_1 + G_1\Lambda_1^{\mathrm{T}}\Lambda_2 + \frac{1}{2}\Lambda_1^{\mathrm{T}}\Lambda_1\\ &\quad + \frac{1}{2}D_1^{\mathrm{T}}D_1 - \tilde{\Theta}_1^{\mathrm{T}}\dot{\hat{\Theta}}_1 + \Lambda_1^{\mathrm{T}}\hat{\phi}_{11}(x_1,\ \Lambda_1) + \varepsilon'_{11} + \Lambda_1^{\mathrm{T}}\hat{\phi}_{12}(\Lambda_1, r)\\ &\quad + \varepsilon'_{12} + \frac{1}{4}\Lambda_1^{\mathrm{T}}\Lambda_1 + d_1(t).\end{aligned} \tag{30}$$

Using RBFNNs satisfies

$$\begin{aligned}\dot{V}_1 \le{}& -\Lambda_1^{\mathrm{T}}K_1\Lambda_1 - \frac{\hat{\Theta}_1}{2\eta_1}\Lambda_1^{\mathrm{T}}\Lambda_1\varphi_1^{\mathrm{T}}\varphi_1 + G_1\Lambda_1^{\mathrm{T}}\Lambda_2\\ &+ \Lambda_1 H_1(Y_1) + \frac{1}{2}D_1^{\mathrm{T}}D_1 + \varepsilon'_{11} + \varepsilon'_{12} + d_1(t) - \tilde{\Theta}_1^{\mathrm{T}}\dot{\hat{\Theta}}_1,\end{aligned} \tag{31}$$

where $H_1(Y_1) = \hat{\phi}_{11}(x_1, \Lambda_1) + \hat{\phi}_{12}(\Lambda_1, r) + \frac{3}{4}\Lambda_1$, $Y_1 = [X_1, \Lambda_1, r]^{\mathrm{T}}$. It is to be noted that $H_1(Y_1)$ is an unknown function. Then, according to the universal approximation theory, the unknown function $H_1(Y_1)$ can be approximated by the RBFNNs in the following form,

$$\hat{H}_1\left(Y_1 | W_1^*\right) = W_1^{*T}\varphi_1(Y_1), \tag{32}$$

with W_1^* being the ideal weight vector defined as

$$W_1^* = \arg\min_{W_1\in\Omega_{W_1}}\left[\sup_{Y_1\in\Omega_{Y_1}}\left\|\hat{H}_1\left(Y_1 | W_1\right) - H_1(Y_1)\right\|\right],$$

where Ω_{W_1} and Ω_{Y_1} are compact regions for W_1 and Y_1, respectively. The corresponding approximation error ε_1^* is defined as

$$\varepsilon_1^* = H_1(Y_1) - \hat{H}_1\left(Y_1 | W_1^*\right),$$

with $\|\varepsilon_1^*\| \le \varepsilon_1$ and a positive constant ε_1.

Based on the definition of Θ_1, combining with Young's inequality, we have

$$\Lambda_1^{\mathrm{T}}H_1(Y_1) \le \frac{\Theta_1}{2\eta_1}\Lambda_1^{\mathrm{T}}\Lambda_1\varphi_1^{\mathrm{T}}\varphi_1 + \frac{\eta_1}{2} + \frac{1}{2}\left(\Lambda_1^{\mathrm{T}}\Lambda_1 + \varepsilon_1^2\right). \tag{33}$$

Inserting **Eq. 33** into **Eq. 31** yields

$$\begin{aligned}\dot{V}_1 \le{}& -\Lambda_1^{\mathrm{T}}K_1\Lambda_1 - \frac{\Lambda_1\Lambda_i}{L_i} + \frac{\tilde{\Theta}_1}{2\eta_1}\Lambda_1^{\mathrm{T}}\Lambda_1\varphi_1^{\mathrm{T}}\varphi_1 + \frac{\eta_1}{2}\\ &+ \frac{1}{2}\left(\Lambda_1^{\mathrm{T}}\Lambda_1 + \varepsilon_1^2\right) + \varepsilon'_{11} + \varepsilon'_{12} + d_1(t) - \tilde{\Theta}_1^{\mathrm{T}}\dot{\hat{\Theta}}_1.\end{aligned} \tag{34}$$

4.2 Step i $(2 \le i \le n-1)$

Inserting the virtual control design **Eq. 14** into **Eq. 13**, we have

$$\dot{E}_i = -G_{i-1}E_{i-1} - K_iE_i + G_iE_{i+1} + G_iZ_i - \frac{\hat{\Theta}_i}{2\eta_i}\Lambda_i\varphi_i^{\mathrm{T}}\varphi_i + D_i + \Delta_i. \tag{35}$$

On the basis of **Eq. 16** and the aforementioned equation, one can obtain

$$\dot{\Lambda}_i = -G_{i-1}\Lambda_{i-1} - K_i\Lambda_i + G_i\Lambda_{i+1} - \frac{\hat{\Theta}_i}{2\eta_i}\Lambda_i\varphi_i^{\mathrm{T}}\varphi_i + D_i + \Delta_i. \tag{36}$$

To analyze the stability of the i-th subsystem through the Lyapunov theory, define the Lyapunov function for Λ_i and $\tilde{\Theta}_i$ as $V_i\left(\Lambda_i, \tilde{\Theta}_i\right) = \frac{1}{2}\Lambda_i^{\mathrm{T}}\Lambda_i + \frac{1}{2}\tilde{\Theta}_i^{\mathrm{T}}\tilde{\Theta}_i$. Based on Assumption 1, the term $\Lambda_i^{\mathrm{T}}\Delta_i$ satisfies

$$\Lambda_i^{\mathrm{T}}\Delta_i \le \|\Lambda_i\|\phi_{i1}\left(\left\|\underline{X}_i\right\|\right) + \|\Lambda_i\|\phi_{i2}(\|\varsigma\|). \tag{37}$$

Consider the term $\|\Lambda_i\|\phi_{i1}\left(\left\|\underline{X}_i\right\|\right)$ in **Eq. 37**, on account of Lemma 1, one has

$$\|\Lambda_i\|\phi_{i1}\left(\left\|\underline{X}_i\right\|\right) \le \Lambda_i^{\mathrm{T}}\hat{\phi}_{i1}\left(\underline{X}_i,\ \Lambda_i\right) + \varepsilon'_{i1},\ \varepsilon'_{i1} = 0.2785\varepsilon_{i1}, \quad (38)$$

with $\varepsilon'_{i1} > 0$, $\varepsilon_{i1} > 0$, and

$$\hat{\phi}_{i1}\left(\underline{X}_i,\ \Lambda_i\right) = \phi_{i1}\left(\left\|\underline{X}_i\right\|\right)\tanh\left(\frac{\Lambda_i\phi_{i1}\left(\left\|\underline{X}_i\right\|\right)}{\varepsilon_{i1}}\right).$$

For the term $\|\Lambda_i\|\phi_{i2}(\|\varsigma\|)$ in **(37)**, according to Lemma 2, we can obtain

$$\|\Lambda_i\|\phi_{i2}(\|\varsigma\|) \le \|\Lambda_i\|\phi_{i2}\left(\omega_1^{-1}(r+\Phi)\right). \quad (39)$$

Since ϕ_{i2} is strictly increasing and non-negative from Assumption 1, based on the fact $r + \Phi \le \max\{2r, 2\Phi\}$, one has

$$\begin{aligned}\|\Lambda_i\|\phi_{i2}\left(\omega_1^{-1}(r+\Phi)\right) \le{}& \|\Lambda_i\|\phi_{i2}\left(\omega_1^{-1}(2r)\right)\\ &+ \|\Lambda_i\|\phi_{i2}\left(\omega_1^{-1}(2\Phi)\right).\end{aligned} \quad (40)$$

On the basis of Lemma 1, we can obtain

$$\|\Lambda_i\|\phi_{i2}\left(\omega_1^{-1}(2r)\right) \le \Lambda_i^{\mathrm{T}}\hat{\phi}_{i2}(\Lambda_i, r) + \varepsilon'_{i2},\ \varepsilon'_{i2} = 0.2785\varepsilon_{i2}, \quad (41)$$

with $\varepsilon'_{i2} > 0$, $\varepsilon_{i2} > 0$, and

$$\hat{\phi}_{i2}(\Lambda_i, r) = \phi_{i2}\left(\omega_1^{-1}(2r)\right)\tanh\left(\frac{\Lambda_i\phi_{i2}\left(\omega_1^{-1}(2r)\right)}{\varepsilon_{i2}}\right).$$

Using Young's inequality, we have

$$\|\Lambda_i\|\phi_{i2}\left(\omega_1^{-1}(2\Phi)\right) \le \frac{1}{4}\Lambda_i^{\mathrm{T}}\Lambda_i + d_i(t), \quad (42)$$

where $d_i(t) = \phi_{i2}^2\left(\omega_1^{-1}(2\Phi(t))\right)$.

From **Eqs 36–42**, the derivative of V_i becomes

$$\begin{aligned}\dot{V}_i ={}& \Lambda_i\Bigg(-G_{i-1}\Lambda_{i-1} - K_i\Lambda_i + G_i\Lambda_{i+1}\\ &-\frac{\hat{\Theta}_i}{2\eta_i}\Lambda_i\varphi_i^{\mathrm{T}}\varphi_i + D_i + \Delta_i\Bigg) - \tilde{\Theta}_i^{\mathrm{T}}\dot{\hat{\Theta}}_i\\ \le{}& -G_{i-1}\Lambda_{i-1}^{\mathrm{T}}\Lambda_i - \Lambda_i^{\mathrm{T}}K_i\Lambda_i + G_i\Lambda_i^{\mathrm{T}}\Lambda_{i+1} - \frac{\hat{\Theta}_i}{2\eta_i}\Lambda_i^{\mathrm{T}}\Lambda_i\varphi_i^{\mathrm{T}}\varphi_i\\ &+ \frac{1}{2}\Lambda_i^{\mathrm{T}}\Lambda_i + \frac{1}{2}D_i^{\mathrm{T}}D_i + \Lambda_i^{\mathrm{T}}\hat{\phi}_{i1}\left(\underline{X}_i,\ \Lambda_i\right) + \varepsilon'_{i1} + \Lambda_i^{\mathrm{T}}\hat{\phi}_{i2}(\Lambda_i, r)\\ &+ \varepsilon'_{i2} + \frac{1}{4}\Lambda_i^{\mathrm{T}}\Lambda_i + d_i(t) - \tilde{\Theta}_i^{\mathrm{T}}\dot{\hat{\Theta}}_i.\end{aligned} \quad (43)$$

Applying RBFNNs yields

$$\begin{aligned}\dot{V}_i \le{}& -G_{i-1}\Lambda_{i-1}^{\mathrm{T}}\Lambda_i - \Lambda_i^{\mathrm{T}}K_i\Lambda_i + G_i\Lambda_i^{\mathrm{T}}\Lambda_{i+1} - \frac{\hat{\Theta}_i}{2\eta_i}\Lambda_i^{\mathrm{T}}\Lambda_i\varphi_i^{\mathrm{T}}\varphi_i\\ &+ \Lambda_i^{\mathrm{T}}H_i(Y_i) + \frac{1}{2}D_i^{\mathrm{T}}D_i + \varepsilon'_{i1} + \varepsilon'_{i2} + d_i(t) - \tilde{\Theta}_i^{\mathrm{T}}\dot{\hat{\Theta}}_i,\end{aligned} \quad (44)$$

where $H_i(Y_i) = \hat{\phi}_{i1}\left(\underline{X}_i,\ \Lambda_i\right) + \hat{\phi}_{i2}(\Lambda_i, r) + \frac{3}{4}\Lambda_i$, $Y_i = \left[\underline{X}_i^{\mathrm{T}},\ \Lambda_i,\ r\right]^{\mathrm{T}}$. The unknown function $H_i(Y_i)$ can be approximated in the following form:

$$\hat{H}_i(Y_i|W_i^*) = W_i^{*T}\varphi_i(Y_i), \quad (45)$$

where W_i^* is the ideal weight vector defined as

$$W_i^* = \underset{W_i\in\Omega_{W_i}}{\operatorname{argmin}}\left[\sup_{Y_i\in\Omega_{Y_i}}\left\|\hat{H}_i(Y_i|W_i) - H_i(Y_i)\right\|\right],$$

with Ω_{W_i} and Ω_{Y_i} being compact regions for W_i and Y_i, respectively. The approximation error ε_i^* is defined as

$$\varepsilon_i^* = H_i(Y_i) - \hat{H}_i(Y_i|W_i^*),$$

where $\|\varepsilon_i^*\| \le \varepsilon_i$ and $\varepsilon_i > 0$.

Based on the definition of Θ_i, using Young's inequality, one has

$$\Lambda_i^{\mathrm{T}}H_i(Y_i) \le \frac{\Theta_i}{2\eta_i}\Lambda_i^{\mathrm{T}}\Lambda_i\varphi_i^{\mathrm{T}}\varphi_i + \frac{\eta_i}{2} + \frac{1}{2}\left(\Lambda_i^{\mathrm{T}}\Lambda_i + \varepsilon_i^2\right). \quad (46)$$

Inserting **Eq. 46** into **Eq. 44**, one can obtain

$$\begin{aligned}\dot{V}_i \le{}& -G_{i-1}\Lambda_{i-1}^{\mathrm{T}}\Lambda_i - \Lambda_i^{\mathrm{T}}K_i\Lambda_i + G_i\Lambda_i^{\mathrm{T}}\Lambda_{i+1} + \frac{\tilde{\Theta}_i}{2\eta_i}\Lambda_i^{\mathrm{T}}\Lambda_i\varphi_i^{\mathrm{T}}\varphi_i\\ &+ \frac{\eta_i}{2} + \frac{1}{2}\left(\Lambda_i^{\mathrm{T}}\Lambda_i + \varepsilon_i^2\right) + \frac{1}{2}D_i^{\mathrm{T}}D_i + \varepsilon'_{i1} + \varepsilon'_{i2} + d_i(t)\\ &- \tilde{\Theta}_i^{\mathrm{T}}\dot{\hat{\Theta}}_i.\end{aligned} \quad (47)$$

4.3 Step n

Inserting **Eq. 19** into **Eq. 18** results in

$$\dot{E}_n = -G_{n-1}E_{n-1} - K_nE_n - \frac{\hat{\Theta}_n}{2\eta_n}\Lambda_n\varphi_n^{\mathrm{T}}\varphi_n + D_n + \Delta_n. \quad (48)$$

Based on the aforementioned equation and **Eq. 20**, we have

$$\dot{\Lambda}_n = -G_{n-1}\Lambda_{n-1} - K_n\Lambda_n - \frac{\hat{\Theta}_n}{2\eta_n}\Lambda_n\varphi_n^{\mathrm{T}}\varphi_n + D_n + \Delta_n. \quad (49)$$

To investigate system stability through the Lyapunov theory, the Lyapunov function is defined for Λ_n and $\tilde{\Theta}_n$ as $V_n(\Lambda_n, \tilde{\Theta}_n) = \frac{1}{2}\Lambda_n^{\mathrm{T}}\Lambda_n + \frac{1}{2}\tilde{\Theta}_n^2$. According to Assumption 1, the term $\Lambda_n^{\mathrm{T}}\Delta_n$ satisfies

$$\Lambda_n^{\mathrm{T}}\Delta_n \le \|\Lambda_n\|\phi_{n1}(\|X\|) + \|\Lambda_n\|\phi_{n2}(\|\varsigma\|). \quad (50)$$

For the term $\|\Lambda_n\|\phi_{n1}(\|x\|)$ in **Eq. 50**, one can obtain

$$\|\Lambda_n\|\phi_{n1}(\|X\|) \le \Lambda_n^{\mathrm{T}}\hat{\phi}_{n1}\left(X,\ \Lambda_n\right) + \varepsilon'_{n1},\ \varepsilon'_{n1} = 0.2785\varepsilon_{n1}, \quad (51)$$

with ε'_{n1} and ε_{n1} being positive constants and

$$\hat{\phi}_{n1}\left(X,\ \Lambda_n\right) = \phi_{n1}(\|X\|)\tanh\left(\frac{\Lambda_n\phi_{n1}(\|X\|)}{\varepsilon_{n1}}\right).$$

For the term $\|\Lambda_n\|\phi_{n2}(\|\varsigma\|)$, from Lemma 2, we have

$$\|\Lambda_n\|\phi_{n2}(\|\varsigma\|) \le \|\Lambda_n\|\phi_{n2}\left(\omega_1^{-1}(r+\Phi)\right). \quad (52)$$

Based on the facts that $\phi_{n2}(\cdot)$ is strictly increasing and non-negative from Assumption 1 and $r + \Phi \le \max\{2r, 2\Phi\}$, one has

$$\begin{aligned}\|\Lambda_n\|\phi_{n2}\left(\omega_1^{-1}(r+\Phi)\right) \le{}& \|\Lambda_n\|\phi_{n2}\left(\omega_1^{-1}(2r)\right)\\ &+ \|\Lambda_n\|\phi_{n2}\left(\omega_1^{-1}(2\Phi)\right).\end{aligned} \quad (53)$$

From Lemma 1, we can obtain

$$\|\Lambda_n\|\phi_{n2}\left(\omega_1^{-1}(2r)\right) \le \Lambda_n^{\mathrm{T}}\hat{\phi}_{n2}\left(\Lambda_n, r\right) + \varepsilon'_{n2},\ \varepsilon'_{n2} = 0.2785\varepsilon_{n2}, \quad (54)$$

where $\varepsilon'_{n2} > 0$ and $\varepsilon_{n2} > 0$ are constants and

$$\hat{\phi}_{n2}\left(\Lambda_n, r\right) = \phi_{n2}\left(\omega_1^{-1}(2r)\right)\tanh\left(\frac{\Lambda_n\phi_{n2}\left(\omega_1^{-1}(2r)\right)}{\varepsilon_{n2}}\right).$$

Applying Young's inequality, we have

$$\|\Lambda_n\|\phi_{n2}\left(\omega_1^{-1}(2\Phi)\right) \le \frac{1}{4}\Lambda_n^{\mathrm{T}}\Lambda_n + d_n(t), \quad (55)$$

with $d_n(t) = \phi_{n2}^2\left(\omega_1^{-1}(2\Phi(t))\right)$. From **Eqs 48–55**, the derivative of V_n becomes

$$\begin{aligned}\dot{V}_n &= \Lambda_n\Bigg(-G_{n-1}\Lambda_{n-1} - K_n\Lambda_n \\ &\quad -\frac{\hat{\Theta}_n}{2\eta_n}\Lambda_n\varphi_n^{\mathrm{T}}\varphi_n + D_n + \Delta_n\Bigg) - \tilde{\Theta}_n^{\mathrm{T}}\dot{\hat{\Theta}}_n \\ &\le -G_{n-1}\Lambda_{n-1}^{\mathrm{T}}\Lambda_n - \Lambda_n^{\mathrm{T}}K_n\Lambda_n - \frac{\hat{\Theta}_n}{2\eta_n}\Lambda_n^{\mathrm{T}}\Lambda_n\varphi_n^{\mathrm{T}}\varphi_n \\ &\quad + \frac{1}{2}D_n^{\mathrm{T}}D_n + \frac{1}{2}\Lambda_n^{\mathrm{T}}\Lambda_n + \Lambda_n^{\mathrm{T}}\hat{\phi}_{n1}\left(X,\ \Lambda_n\right) + \varepsilon'_{n1} \\ &\quad + \Lambda_n^{\mathrm{T}}\hat{\phi}_{n2}\left(\Lambda_n, r\right) + \varepsilon'_{n2} + \frac{1}{4}\Lambda_n^{\mathrm{T}}\Lambda_n + d_n(t) - \tilde{\Theta}_n^{\mathrm{T}}\dot{\hat{\Theta}}_n. \end{aligned} \quad (56)$$

Inserting **Eqs 19**, **51**, **52** into **Eq. 56** results in

$$\begin{aligned}\dot{V}_n &\le -G_{n-1}\Lambda_{n-1}^{\mathrm{T}}\Lambda_n - \Lambda_n^{\mathrm{T}}K_n\Lambda_n - \frac{\hat{\Theta}_n}{2\eta_n}\Lambda_n^{\mathrm{T}}\Lambda_n\varphi_n^{\mathrm{T}}\varphi_n \\ &\quad + \Lambda_n^{\mathrm{T}}H_n\left(Y_n\right) + \frac{1}{2}D_n^{\mathrm{T}}D_n + \varepsilon'_{n1} + \varepsilon'_{n2} + d_n(t) - \tilde{\Theta}_n^{\mathrm{T}}\dot{\hat{\Theta}}_n, \end{aligned} \quad (57)$$

where $H_n\left(Y_n\right) = \hat{\phi}_{n1}\left(X,\ \Lambda_n\right) + \hat{\phi}_{n2}\left(\Lambda_n, r\right) + \frac{3}{4}\Lambda_n$, $Y_n = \left[X,\ \Lambda_n,\ r\right]^{\mathrm{T}}$. The unknown function $H_n\left(Y_n\right)$ can be estimated as

$$\hat{H_n}\left(Y_n \middle| W_n^*\right) = W_n^{*T}\varphi_n\left(Y_n\right), \quad (58)$$

with W_n^* being the ideal weight vector defined as

$$W_n^* = \underset{W_n\in\Omega_{W_n}}{\operatorname{argmin}}\left[\sup_{Y_n\in\Omega_{Y_n}}\left\|\hat{H_n}\left(Y_n \middle| W_n\right) - H_n\left(Y_n\right)\right\|\right],$$

where Ω_{W_n} and Ω_{Y_n} are compact regions for W_n and Y_n, respectively, with the approximation error ε_n^* defined as

$$\varepsilon_n^* = H_n\left(Y_n\right) - \hat{H_1}\left(Y_n \middle| W_n^*\right),$$

with ε_n^* satisfying $\|\varepsilon_n^*\| \le \varepsilon_n$ and a positive constant ε_n.

From the definition of Θ_n, combining with Young's inequality, we can obtain

$$\Lambda_n H_n\left(Y_n\right) \le \frac{\Theta_n}{2\eta_n}\Lambda_n^{\mathrm{T}}\Lambda_n\varphi_n^{\mathrm{T}}\varphi_n + \frac{\eta_n}{2} + \frac{1}{2}\left(\Lambda_n^{\mathrm{T}}\Lambda_n + \varepsilon_n^2\right). \quad (59)$$

Applying Young's inequality, substituting **Eqs 21**, **59** into **Eq. 57** yields

$$\begin{aligned}\dot{V}_n &\le -G_{n-1}\Lambda_{n-1}^{\mathrm{T}}\Lambda_n - \Lambda_n^{\mathrm{T}}K_n\Lambda_n + \frac{\tilde{\Theta}_n}{2\eta_n}\Lambda_n^{\mathrm{T}}\Lambda_n\varphi_n^{\mathrm{T}}\varphi_n + \frac{\eta_n}{2} \\ &\quad + \frac{1}{2}\left(\Lambda_n^{\mathrm{T}}\Lambda_n + \varepsilon_n^2\right) + \frac{1}{2}D_n^{\mathrm{T}}D_n + \varepsilon'_{n1} + \varepsilon'_{n2} + d_n(t) \\ &\quad - \tilde{\Theta}_n\dot{\hat{\Theta}}_n. \end{aligned} \quad (60)$$

Theorem 1: Under Assumptions 1–2, with the virtual control (**Eqs 9**, **14**), the CF design (**Eqs 10**, **15**), the adaptive laws (**Eqs 12**, **17**, **21**), the compensating signals (**Eqs 11**, **16**, **20**), and the controller (**Eq. 19**), the following facts hold.

1. The tracking errors will converge to the neighborhood of the origin asymptotically.
2. The boundedness of all signals in the closed-loop system (**Eq. 1**) can be guaranteed.

Proof: Define $V = \sum_{i=1}^{n} V_i$, applying Young's inequality yields

$$\tilde{\Theta}_i^{\mathrm{T}}\hat{\Theta}_i \le \frac{1}{2}\Theta_i^{\mathrm{T}}\Theta_i - \frac{1}{2}\tilde{\Theta}_i^{\mathrm{T}}\tilde{\Theta}_i.$$

Based on **Eqs 34**, **47**, **60**, the overall Lyapunov function satisfies

$$\begin{aligned}\dot{V} &\le -\sum_{i=1}^{n}\Lambda_i^{\mathrm{T}}\left(K_i - \frac{1}{2}I_m\right)\Lambda_i - \sum_{i=1}^{n}\frac{\gamma_i}{2}\tilde{\Theta}_i^{\mathrm{T}}\tilde{\Theta}_i \\ &\quad + \frac{1}{2}\sum_{i=1}^{n}\left[\eta_i + \varepsilon_i^2 + D_i^{\mathrm{T}}D_i + \gamma_i + \Theta_i^{\mathrm{T}}\Theta_i + 2\varepsilon'_{i1}\right. \\ &\quad \left. + 2\varepsilon'_{i2} + 2d_i(t)\right] \\ &\le -aV + b, \end{aligned}$$

where I_m is the m-dimension identity matrix,

$$a = \min_{i=1,\ldots,n}\left\{\lambda_{\min}\left(2K_i - I_m\right),\ \gamma_i\right\},$$

$$b = \frac{1}{2}\sum_{i=1}^{n}\left[\eta_i + \varepsilon_i^2 + D_i^{\mathrm{T}}D_i + \gamma_i + \Theta_i^{\mathrm{T}}\Theta_i + 2\varepsilon'_{i1} + 2\varepsilon'_{i2} + 2d_i(t)\right].$$

Therefore, Λ_i, $\tilde{\Theta}_i$, and $\hat{\Theta}_i$ are bounded. Next, we investigate the boundedness of Z_i, and the dynamics of the filter error Z_i can be expressed as

$$\dot{Z}_i = \dot{A}_i - \dot{S}_i = -\frac{Z_i}{\tau_i} - \dot{S}_i, \quad (61)$$

where

$$\begin{aligned}\dot{s}_i &= \frac{1}{G_i}\Bigg(-\dot{F}_i - G_{i-1}\dot{E}_{i-1} - K_i\dot{E}_i - \frac{\dot{\hat{\Theta}}_i}{2\eta_i}\Lambda_i\varphi_i^{\mathrm{T}}\varphi_i - \frac{\hat{\Theta}_i}{2\eta_i}\dot{\Lambda}_i\varphi_i^{\mathrm{T}}\varphi_i \\ &\quad -\frac{\hat{\Theta}_i}{\eta_i}\Lambda_i\varphi_i^{\mathrm{T}}\dot{\varphi}_i + \ddot{A}_{i-1}\Bigg) \end{aligned}$$

is continuous on the compact set $\Omega_i \times \Omega_{X_d}$ with

$$\Omega_{X_d} = \left\{\left(X_d, \dot{X}_d, \ddot{X}_d\right) \middle| X_d^2 + \dot{X}_d^2 + \ddot{X}_d^2 \le R_0\right\},$$

$$\Omega_i = \left\{\left(E_i, Z_i, \tilde{\Theta}_i\right) \middle| E_i^2 + Z_i^2 + \tilde{\Theta}_i^2 \le R_i\right\},$$

and $R_0 > 0, R_i > 0$. Thus, $\dot{S}_i$ is bounded, which derives that Z_i is also bounded from **Eq. 61**. According to **Eqs 11**, **16**, **20**, B_i is bounded. Thus, E_i, A_i, S_i, U, and X_i are all bounded, which invokes ς, Δ, and r to be bounded based on Lemma 2 and **Eq. 6**. In the end, we can conclude that the boundedness of all the signals in the closed-loop system can be guaranteed. This completes the proof.

5 SIMULATION STUDY

The system considered in this section is a voltage source converter-high voltage direct current transmission system with the following dynamics (Hu et al. (2020)).

$$
\begin{aligned}
\dot{\varsigma} &= q(\varsigma, x),\\
\dot{x}_1 &= -b_2 x_1 - \frac{x_n}{L_2} + \omega x_2 + T_1 + \delta_1(\varsigma, x),\\
\dot{x}_2 &= -b_2 x_2 - \frac{x_4}{L_2} - \omega x_1 + \delta_2(\varsigma, x),\\
\dot{x}_3 &= \frac{x_1 - x_5}{C_2} + \omega x_4 + \delta_3(\varsigma, x),\\
\dot{x}_4 &= \frac{x_2 - x_6}{C_2} + \omega x_3 + \delta_4(\varsigma, x),\\
\dot{x}_5 &= -b_1 x_5 + \frac{x_3}{L_1} + \omega x_6 - \frac{u_d}{L_1} + \delta_5(\varsigma, x),\\
\dot{x}_6 &= -b_1 x_6 + \frac{x_4}{L_1} + \omega x_5 - \frac{u_q}{L_1} + \delta_6(\varsigma, x),
\end{aligned}
$$

where L_1 and L_2 are the electrical inductances, and C_1 and C_2 are the capacitances. Applying variable transformation $X_i = [x_{2i-1}, x_{2i}]^{\mathrm{T}}$, $\overline{X}_i = [x_{2i}, x_{2i-1}]^{\mathrm{T}}$, $X = [X_1, X_2, X_3]^{\mathrm{T}}$, $\overline{T} = [T_1, 0]^{\mathrm{T}}$, $c_1 = \mathrm{diag}\{1, -1\}$, and $U = \left[u_d, u_q\right]^{\mathrm{T}}$, the aforementioned equation becomes

$$
\begin{aligned}
\dot{\varsigma} &= q(\varsigma, X),\\
\dot{X}_1 &= -b_2 X_1 - \frac{X_2}{L_2} + \omega c_1 \overline{X}_1 + \overline{T} + \Delta_1(\varsigma, X),\\
\dot{X}_2 &= \frac{X_1 - X_3}{C_2} + \omega \overline{X}_2 + \Delta_2(\varsigma, X),\\
\dot{X}_3 &= -b_1 X_3 + \frac{X_2}{L_1} + \omega \overline{X}_3 - \frac{U}{L_1} + \Delta_3(\varsigma, X).
\end{aligned}
$$

By applying the presented control scheme, the control design is developed as

$$
\begin{aligned}
S_1 &= L_2\left(-b_2 X_1 + K_1 E_1 + \frac{\hat{\Theta}_1}{2\eta_1}\Lambda_1 \varphi_1^{\mathrm{T}}\varphi_1 + \omega c_1 \overline{X}_1 - \dot{X}_d\right),\\
S_2 &= C_2\left(\frac{X_1}{C_2} - \frac{E_1}{L_2} + K_2 E_2 + \omega \overline{X}_2 + \frac{\hat{\Theta}_2}{2\eta_2}\Lambda_2 \varphi_2^{\mathrm{T}}\varphi_2 - \dot{A}_1\right),\\
U &= L_1\left(-b_1 X_3 + \frac{X_2}{L_1} + \omega \overline{X}_3 - \frac{E_2}{C_2} + K_3 E_3 + \frac{\hat{\Theta}_3}{2\eta_3}\Lambda_3 \varphi_3^{\mathrm{T}}\varphi_3 - \dot{A}_2\right),
\end{aligned}
$$

with the compensating signal design

$$
\begin{aligned}
\dot{B}_1 &= -K_1 B_1 - \frac{B_2}{L_2} - \frac{Z_1}{L_2}, B_1(0) = 0.\\
\dot{B}_2 &= \frac{B_1}{L_2} - K_2 B_2 - \frac{B_3}{C_2} - \frac{Z_2}{C_2}, B_2(0) = 0.\\
\dot{B}_3 &= \frac{B_2}{C_2} - K_3 B_3, B_3(0) = 0.
\end{aligned}
$$

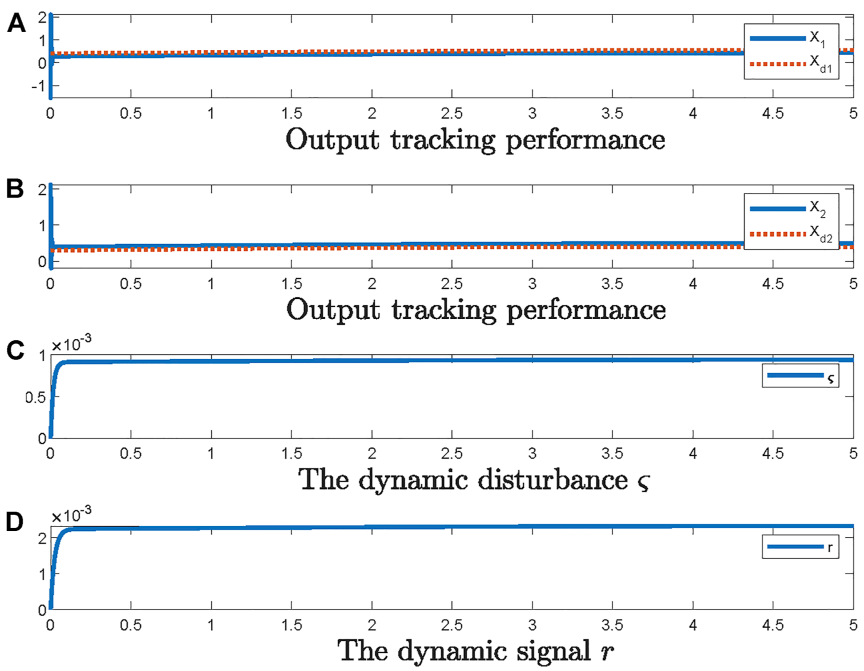

FIGURE 1 | Output tracking performance and evolution of dynamic uncertainties.

In addition, the CF design and adaptive law design are the same as **Eqs 10**, **11**, **15**, **16**, **20**.

The design parameters are given as $L_1 = 4$ mH, $L_2 = 8$ mH, $C_2 = 0.1\mu$F, $\overline{T} = [0.01, 0.02]^{\mathrm{T}}$, $\omega = 100\pi$ rad/s, $K_1 = \mathrm{diag}\{1258, 1646\}$, $K_2 = \mathrm{diag}\{124630, 161622\}$, $K_3 = \mathrm{diag}\{188539, 138474\}$, $\gamma_1 = 0.00085$, $\gamma_2 = 0.00066$, $\gamma_3 = 0.00059$, $\eta_1 = 0.00005$, $\eta_2 = 0.000003$, $\eta_3 = 0.000004$.

The RBFNNs are chosen in typical Gaussian form. To be specific, the RBFNN $\varphi_1(X_1, \Lambda_1, r)$ contains 32 nodes with the center and width being $[-2,2]\times[-2,2]\times[-2,2]\times[-2,2]\times[-2,2]$ and 2, respectively. RBFNN $\varphi_2\left(\underline{X}_2, \Lambda_2, r\right)$ contains 128 nodes and the center and width are distributed in $[-2,2]\times[-2,2]\times[-2,2]\times[-2,2]\times[-2,2]\times[-2,2]\times[-2,2]$ and 2. RBFNN $\varphi_3(X, \Lambda_3, r)$ contains 512 nodes with the center and width selected as $[-2,2]\times[-2,2]\times[-2,2]\times[-2,2]\times[-2,2]\times[-2,2]\times[-2,2]\times[-2,2]\times[-2,2]$ and 2, respectively.

The simulation results are shown in **Figure 1**. From **Figure 1**, it can be observed that the output tracking objective can be achieved and the system output can track the reference output asymptotically. The dynamic uncertainties can also converge with the convergence of system states.

6 CONCLUSION

In this study, a control approach for MIMO strict feedback nonlinear unmodeled dynamical systems with CFs is developed. The dynamic signal design introduced together with RBFNNs can efficiently prevent the effect of the dynamic uncertainties. The CFs employed in the controller design can not only prevent the explosion of complexity, but can also eliminate the effect of filter errors through the compensating signal design. Compared with single-input single-output strict feedback nonlinear systems, the approach proposed in this study is suitable for more general cases. Finally, in the simulation experiments, the presented method is applied to power systems, where the simulation results validate the effect of the scheme proposed.

DATA AVAILABILITY STATEMENT

The original contributions presented in the study are included in the article/Supplementary Material, further inquiries can be directed to the corresponding author.

AUTHOR CONTRIBUTIONS

XF, LS, and YZ contributed to conception and design of this study. XF investigated the theoretical analysis for the command filter design. LS performed the simulation study with application to an energy system. YZ organized the writing of the manuscript. XF, LS, and YZ collaborated to write all the sections of the manuscript. All authors contributed to manuscript revision, and read and approved the submitted version.

FUNDING

This work was supported by the Youth Innovation Promotion Association of Chinese Academy of Sciences under Grant 2020134.

REFERENCES

Deese, J., and Vermillion, C. (2021). Recursive Gaussian Process-Based Adaptive Control, with Application to a lighter-Than-air Wind Energy System. *IEEE Trans. Contr. Syst. Technol.* 29, 1823–1830. doi:10.1109/TCST.2020.3014159

Farrell, J. A., Polycarpou, M., Sharma, M., and Wenjie Dong, W. (2009). Command Filtered Backstepping. *IEEE Trans. Automat. Contr.* 54, 1391–1395. doi:10.1109/tac.2009.2015562

Ghaffarzdeh, H., and Mehrizi-Sani, A. (2020). Mitigation of Subsynchronous Resonance Induced by a Type Iii Wind System. *IEEE Trans. Sustain. Energ.* 11, 1717–1727. doi:10.1109/TSTE.2019.2938014

Ghosh, S., and Kamalasadan, S. (2017). An Integrated Dynamic Modeling and Adaptive Controller Approach for Flywheel Augmented Dfig Based Wind System. *IEEE Trans. Power Syst.* 32, 2161–2171. doi:10.1109/TPWRS.2016.2598566

Han, Q., and Liu, X. (2020). Robust I&I Adaptive Control for a Class of Quadrotors with Disturbances. *IEEE Access* 8, 216519–216528. doi:10.1109/ACCESS.2020.3041030

Hardy, G. H., Littlewood, J. E., and Pólya, G. (1952). *Inequalities*. Cambridge: Cambridge University Press.

Hu, C., Ma, Y., Yu, J., and Zhao, L. (2020). Dynamic Surface Backstepping Control for Voltage Source Converter-High Voltage Direct Current Transmission Grid Side Converter Systems. *Electronics* 9, 9020333. doi:10.3390/electronics9020333

Jiang, Z.-P., and Praly, L. (1998). Design of Robust Adaptive Controllers for Nonlinear Systems with Dynamic Uncertainties. *Automatica* 34, 825–840. doi:10.1016/s0005-1098(98)00018-1

L'Afflitto, A. (2018). Barrier Lyapunov Functions and Constrained Model Reference Adaptive Control. *IEEE Control. Syst. Lett.* 2, 441–446. doi:10.1109/LCSYS.2018.2842148

Li, C., Wu, Y., Sun, Y., Zhang, H., Liu, Y., Liu, Y., et al. (2020). Continuous Under-frequency Load Shedding Scheme for Power System Adaptive Frequency Control. *IEEE Trans. Power Syst.* 35, 950–961. doi:10.1109/TPWRS.2019.2943150

Liu, L., Liu, Y.-J., Tong, S., and Gao, Z. (2022). Relative Threshold-Based Event-Triggered Control for Nonlinear Constrained Systems with Application to Aircraft wing Rock Motion. *IEEE Trans. Ind. Inf.* 18, 911–921. doi:10.1109/TII.2021.3080841

Liu, L., Zhao, W., Liu, Y.-J., Tong, S., and Wang, Y.-Y. (2021). Adaptive Finite-Time Neural Network Control of Nonlinear Systems with Multiple Objective Constraints and Application to Electromechanical System. *IEEE Trans. Neural Netw. Learn. Syst.* 32, 5416–5426. doi:10.1109/TNNLS.2020.3027689

Mukherjee, S., Chowdhury, V. R., Shamsi, P., and Ferdowsi, M. (2017). Model Reference Adaptive Control Based Estimation of Equivalent Resistance and Reactance in Grid-Connected Inverters. *IEEE Trans. Energ. Convers.* 32, 1407–1417. doi:10.1109/TEC.2017.2710200

Namazi, M. M., Nejad, S. M. S., Tabesh, A., Rashidi, A., and Liserre, M. (2018). Passivity-based Control of Switched Reluctance-Based Wind System Supplying Constant Power Load. *IEEE Trans. Ind. Electron.* 65, 9550–9560. doi:10.1109/TIE.2018.2816008

Nascimento Moutinho, M., da Costa, C. T., Barra, W., and Augusto Lima Barreiros, J. (2008). Self-tunning Control Methodologies Applied to the Automatic Voltage Control of a Synchronous Generator. *IEEE Latin Am. Trans.* 6, 408–418. doi:10.1109/TLA.2008.4839110

Quan, X., Yu, R., Zhao, X., Lei, Y., Chen, T., Li, C., et al. (2020). Photovoltaic Synchronous Generator: Architecture and Control Strategy for a Grid-Forming Pv Energy System. *IEEE J. Emerg. Sel. Top. Power Electron.* 8, 936–948. doi:10.1109/JESTPE.2019.2953178

Wang, D., and Huang, J. (2005). Neural Network-Based Adaptive Dynamic Surface Control for a Class of Uncertain Nonlinear Systems in Strict-Feedback Form. *IEEE Trans. Neural Netw.* 16, 195–202. doi:10.1109/tnn.2004.839354

Wang, L., Li, H., Zhou, Q., and Lu, R. (2017). Adaptive Fuzzy Control for Nonstrict Feedback Systems with Unmodeled Dynamics and Fuzzy Dead Zone via Output Feedback. *IEEE Trans. Cybern.* 47, 2400–2412. doi:10.1109/TCYB.2017.2684131

Wang, Y., Cao, L., Zhang, S., Hu, X., and Yu, F. (2016). Command Filtered Adaptive Fuzzy Backstepping Control Method of Uncertain Non-linear Systems. *IET Control. Theor. & amp; Appl.* 10, 1134–1141. doi:10.1049/iet-cta.2015.0946

Wu, C., Chen, J., Xu, C., and Liu, Z. (2017). Real-time Adaptive Control of a Fuel Cell/battery Hybrid Power System with Guaranteed Stability. *IEEE Trans. Contr. Syst. Technol.* 25, 1394–1405. doi:10.1109/TCST.2016.2611558

Xia, X., and Zhang, T. (2018). Adaptive Quantized Output Feedback Dsc of Uncertain Systems with Output Constraints and Unmodeled Dynamics Based on Reduced-Order K-Filters. *Neurocomputing* 310, 236–245. doi:10.1016/j.neucom.2018.05.031

Xu, D., Liu, J., Yan, X.-G., and Yan, W. (2018). A Novel Adaptive Neural Network Constrained Control for a Multi-Area Interconnected Power System with Hybrid Energy Storage. *IEEE Trans. Ind. Electron.* 65, 6625–6634. doi:10.1109/TIE.2017.2767544

Yang, Y., Gao, W., Modares, H., and Xu, C.-Z. (2021a). Robust Actor-Critic Learning for Continuous-Time Nonlinear Systems with Unmodeled Dynamics. *IEEE Trans. Fuzzy Syst.* 2021, 1. doi:10.1109/TFUZZ.2021.3075501

Yang, Y., Kiumarsi, B., Modares, H., and Xu, C. (2021b). Model-Free λ-Policy Iteration for Discrete-Time Linear Quadratic Regulation. *IEEE Trans. Neural Netw. Learn. Syst.* 2021, 1–15. doi:10.1109/TNNLS.2021.3098985

Yang, Y., Liu, Z., Li, Q., and Wunsch, D. C. (2021c). Output Constrained Adaptive Controller Design for Nonlinear Saturation Systems. *Ieee/caa J. Autom. Sinica* 8, 441–454. doi:10.1109/JAS.2020.1003524

Yang, Y., Modares, H., Vamvoudakis, K. G., He, W., Xu, C.-Z., and Wunsch, D. C. (2021d). Hamiltonian-driven Adaptive Dynamic Programming with Approximation Errors. *IEEE Trans. Cybern.* 2021, 1–12. doi:10.1109/TCYB.2021.3108034

Yang, Y., Vamvoudakis, K. G., Modares, H., Yin, Y., and Wunsch, D. C. (2021e). Hamiltonian-driven Hybrid Adaptive Dynamic Programming. *IEEE Trans. Syst. Man. Cybern, Syst.* 51, 6423–6434. doi:10.1109/TSMC.2019.2962103

Yang, Y., Vamvoudakis, K. G., Modares, H., Yin, Y., and Wunsch, D. C. (2020). Safe Intermittent Reinforcement Learning with Static and Dynamic Event Generators. *IEEE Trans. Neural Netw. Learn. Syst.* 31, 5441–5455. doi:10.1109/TNNLS.2020.2967871

Zhao, J., Tong, S., and Li, Y. (2021a). Fuzzy Adaptive Output Feedback Control for Uncertain Nonlinear Systems with Unknown Control Gain Functions and Unmodeled Dynamics. *Inf. Sci.* 558, 140–156. doi:10.1016/j.ins.2020.12.092

Zhao, L., Yu, J., and Wang, Q.-G. (2021b). Finite-time Tracking Control for Nonlinear Systems via Adaptive Neural Output Feedback and Command Filtered Backstepping. *IEEE Trans. Neural Netw. Learn. Syst.* 32, 1474–1485. doi:10.1109/tnnls.2020.2984773

Zhu, G., Du, J., and Kao, Y. (2018). Command Filtered Robust Adaptive Nn Control for a Class of Uncertain Strict-Feedback Nonlinear Systems under Input Saturation. *J. Franklin Inst.* 355, 7548–7569. doi:10.1016/j.jfranklin.2018.07.033

Zou, W., Shi, P., Xiang, Z., and Shi, Y. (2020a). Consensus Tracking Control of Switched Stochastic Nonlinear Multiagent Systems via Event-Triggered Strategy. *IEEE Trans. Neural Netw. Learn. Syst.* 31, 1036–1045. doi:10.1109/tnnls.2019.2917137

Zou, W., Shi, P., Xiang, Z., and Shi, Y. (2020b). Finite-time Consensus of Second-Order Switched Nonlinear Multi-Agent Systems. *IEEE Trans. Neural Netw. Learn. Syst.* 31, 1757–1762. doi:10.1109/tnnls.2019.2920880

Conflict of Interest: The authors declare that the research was conducted in the absence of any commercial or financial relationships that could be construed as a potential conflict of interest.

Publisher's Note: All claims expressed in this article are solely those of the authors and do not necessarily represent those of their affiliated organizations, or those of the publisher, the editors, and the reviewers. Any product that may be evaluated in this article, or claim that may be made by its manufacturer, is not guaranteed or endorsed by the publisher.

frontiers | Frontiers in Energy Research

ORIGINAL RESEARCH
published: 27 June 2022
doi: 10.3389/fenrg.2022.936776

Intelligent Decoupling Control Study of PMSM Based on the Neural Network Inverse System

*Gong Da-Wei[1], Qiu Zhi-Qiang[2,3], Zheng Wei[2,3], Ke Zhi-Wu[2,3] and Liu Yang[1]**

[1]School of Mechanical and Electrical Engineering, University of Electronic Science and Technology of China, Chengdu, China, [2]Wuhan Second Ship Design and Research Institute, Wuhan, China, [3]Science and Technology on Thermal Energy and Power Laboratory, Wuhan, China

This study obtains the analytical inverse system of a permanent magnet synchronous motor (PMSM) model based on the traditional magnetic field orientation decoupling control mode by analyzing the inverse quality of the PMSM. Using the neural network's excellent approximation ability and well learning functions, a neural network inverse system (NNIS) of the decoupling control system was established by identifying and offline training the back propagation neural network (BPNN) and radial basis function neural network (RBFNN). The data collected from the analytical inverse system of the PMSM model are used to analyze and compare the prediction accuracy and running time of the neural network, so as to optimize the structure and parameters of the neural network. The simulation results of three PMSM decoupling control systems show that the PMSM decoupling control system based on RBF NNIS has good dynamic and static decoupling performance, and robustness.

Keywords: PMSM, neural network, inverse system, decoupling control, optimization

OPEN ACCESS

Edited by:
Bonan Huang,
Northeastern University, China

Reviewed by:
Shoulong Xu,
University of South China, China
Shenquan Wang,
Changchun University of Technology, China
Ran Duan,
Hong Kong Polytechnic University, China

****Correspondence:***
Liu Yang
ly2015@uestc.edu.cn

Specialty section:
This article was submitted to Process and Energy Systems Engineering, a section of the journal Frontiers in Energy Research

Received: *05 May 2022*
Accepted: *17 May 2022*
Published: *27 June 2022*

Citation:
Da-Wei G, Zhi-Qiang Q, Wei Z, Zhi-Wu K and Yang L (2022) Intelligent Decoupling Control Study of PMSM Based on the Neural Network Inverse System. Front. Energy Res. 10:936776. doi: 10.3389/fenrg.2022.936776

INTRODUCTION

PMSM is an efficient and energy-saving motor, and it is a nonlinear, multivariable, and strongly coupled control object (Bu et al., 2015; Sun et al., 2016; Bu et al., 2019a). The control effect of traditional motor control methods is not ideal. Various control methods of modern motors are essentially decoupling control. At present, the industry adopts field-oriented control to realize decoupling control through id = 0. This is a decoupling method based on an accurate mathematical model, which has good performance in steady-state decoupling. However, the system performance in the dynamic process and when the motor parameters change is not very ideal, and intelligent control is the development trend in the future. This kind of the control method does not have high requirements for the mathematical model. At present, it has many successful applications (Li et al., 2019a; Jie et al., 2020), such as NNIS. This method is an important branch of intelligent decoupling control of the PMSM.

In the decoupling strategy of the NNIS, the key is the design and construction of the neural network, but the relevant research and literature have not been discussed too much. A typical error in the back-propagation feed-forward neural network (BPNN) is selected in many documents to identify the inverse system (Bu et al., 2019b; Xie and Xie, 2020). There is no detailed description on how to select the parameters and algorithm in the BPNN. Similarly, RBFNN with good approximation and fitting ability has not been used to identify the inverse system, let alone compare the decoupling performance of two different neural network structures.

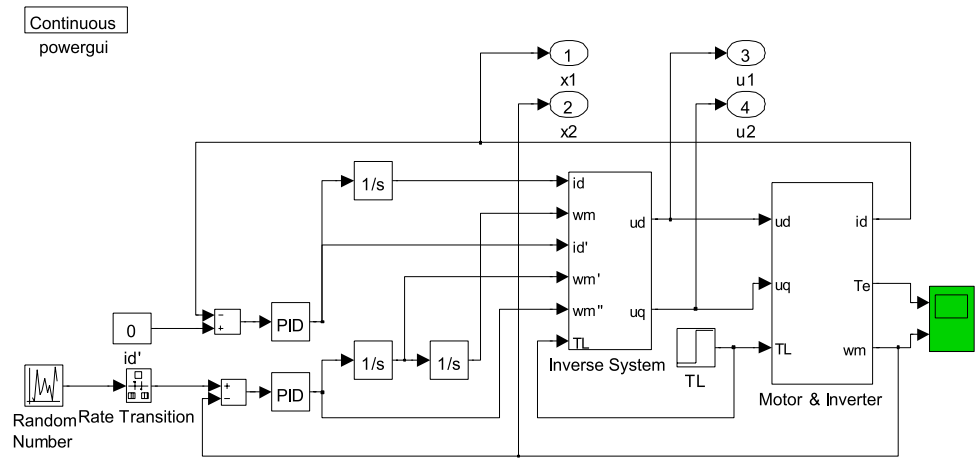

FIGURE 1 | PMSM inverse system sampling simulation diagram.

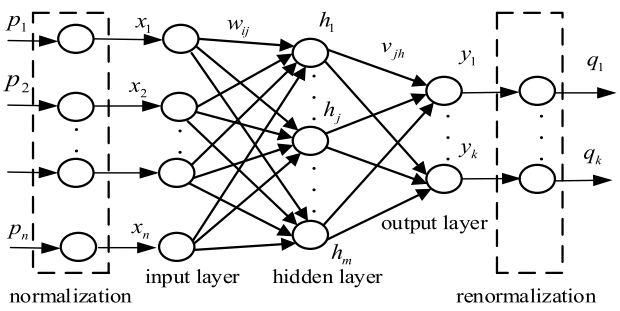

FIGURE 2 | BPNN structure.

This study deeply discusses the structural design of the BPNN, compares the decoupling effect between RBFNN and BPNN inverse systems, and finally obtains a PMSM decoupling system with excellent dynamic and static performance, and strong robustness when the parameters change and load disturbances occur.

NEURAL NETWORK IDENTIFICATION AND SAMPLE COLLECTION

The original training data of neural networks can be obtained through MATLAB simulation experiment of closed-loop analytical inverse decoupling control. Each group of training data of neural networks includes 5 input signals y_1, y_1, y_2, y_2', and y_2'', and 2 output signals u_d and u_q of the neural network (Wang et al., 2018; Bu and Li, 2019).

The stator current input is given as 0, the speed input is given as a random quantity with amplitude ranging from 40 *rad/s* to 140 *rad/s*, and the sampling system of the PMSM NNIS is shown in **Figure 1**.

TABLE 1 | Prediction error of BPNN with different hidden layer nodes.

Nodes	Percentage of maximum relative error (%)	Mean square error
10	9.405	8.31501e10-5
11	8.017	6.69010e10-5
12	1.623	1.12043e10-5
13	1.953	1.19563e10-5
14	20.361	2.01616e10-4
15	36.896	6.92855e10-4

DESIGN AND DECOUPLING OF BP NNIS FOR THE PERMANENT MAGNET SYNCHRONOUS MOTOR

BPNN (Back Propagation Neural Network)

BPNN is an error back propagation feedforward neural network. The structure of the BPNN is shown in **Figure 2**. The sample input vector $p=(p_1, p_2, \ldots, p_n)$ is normalized to obtain the input layer vector $x\in(x_1, x_2, \ldots, x_n)^T$. There are m neurons in the hidden layer, and the hidden layer output $h=(h_1, h_2, \ldots, h_m)^T$ is obtained. There are k neurons in the output layer, and the output $y=(y_1, y_2, \ldots, y_k)^T$ of the output layer is obtained. The output is de-normalized to obtain $q=(q_1, q_2, \ldots, q_k)^T$ sample training output. The weight between the input layer and the hidden layer is w_{ij}, and the threshold is θ_j. The weight between the hidden layer and the output layer is v_{jh}, and the threshold is τ_h.

The output of neurons in each layer meets the following requirements:

$$\begin{cases} h_j = f\left(\sum_{i=1}^{n} w_{ij}x_i - \theta_j\right) \\ y_h = f\left(\sum_{j=1}^{m} v_{jh}h_j - \tau_h\right) \end{cases} \quad (1)$$

TABLE 2 | Prediction error of BPNN with different hidden layer nodes.

Layer number	Percentage of maximum relative error (%)	Mean square error	Running time (s)
Single layer	1.623	1.12043e10-5	5238.44
Double layer	0.059	9.64101e10-7	9196.80

Number of Hidden Layer Nodes

There is a relationship among the number of hidden layer neurons *J*, the input vector dimension *n*, and the number of partitions *M* (Yin et al., 2004). Given the other two of them, one of the three parameters can be calculated. In the n-dimensional input space, the maximum number of linearly divisible J hidden layer neurons is

$$M(J,n) = \sum_{k=0}^{n} \binom{J}{k} \tag{2}$$

Now consider the case that the size of hidden layer nodes is small, when n ≥ J,

$$M = \binom{J}{0} + \binom{J}{1} + \cdots + \binom{J}{J} = 2^J \tag{3}$$

It is concluded that the hidden layer with 3 nodes will be able to provide classification, but when $J \geq$ n, the scale of the input vector must be larger than 3.

According to the above formula, *J* required to complete the classification as *M* in the *n*-dimensional pattern space can be found. This *M* constitutes the solution of the equation:

$$M = 1 + J + \frac{J(J-1)}{2!} + \cdots + \frac{J(J-1)\cdots(J-n+1)}{n!} \quad J > n \tag{4}$$

According to the previous section, the BPNN to be trained has 5 inputs and 2 outputs. Set the number of training iterations at net. trainparam. epochs: 2000, net. trainparam. goal: 10e-6 when using MATLAB training. The relationship between prediction error and the number of hidden layer nodes *M* is shown in **Table 1**.

The accuracy of neural network prediction decreases first and then increases with the number of nodes increasing. When the number of nodes is 12, the mean square error of prediction is minimum, so the number of nodes in the hidden layer is determined to be 12.

Hidden Layers of the Back Propagation Neural Network

According to Kolmoagorov's theorem (the representation theorem for continuous functions), given a continuous function:

$$\Phi: E^m \rightarrow R^n, \Phi(X) = Y \tag{5}$$

E^m is a unit cube, then Φ can be precisely realized by a three-layer neural network (Zhao and Wang, 2022a), the first layer of the neural network has 5 processing units, the middle layer has 12 processing units, and the third layer has 2 processing units. The continuity theorem guarantees that any continuous function and mapping can be implemented by a three-layer neural network (Ting, 2017).

TABLE 3 | Prediction error of BPNN with different activation functions.

Hidden layer transfer function	Tansig	Tansig
Transfer function of output layer	purelin	tansig
Percentage of maximum relative error	1.623%	0.160%
Mean square error	1.12043e10-5	2.38189e10-6
Running time	5238.44s	2919.85s

When using the single-layer hidden layer BPNN for training, the optimal number of hidden layer nodes is determined to be 12 (Zhao and Wang, 2022a). Now consider using the multi-layer hidden layer, and the prediction error of single-layer and dual-layer BPNN is shown in **Table 2**.

Compared with the single hidden layer, the multi-hidden layer has stronger generalization ability and higher prediction accuracy, but the training time is longer. When choosing the number of hidden layers, both network precision and training time should be considered. When the network precision meets the requirement, the single hidden layer can be selected to speed up the process (Li et al., 2021a). The comparative analysis not only verifies the reliability of the continuity theorem but also determines the use of the single hidden layer in training.

Back Propagation Neural Network Transfer Function

The transfer function is used to calculate the output of the hidden layer and the output layer, and logsig (S-shaped transfer function) is available:

$$f(x) = \frac{1}{1 + e^{-\alpha x_i}} \tag{6}$$

tansig (hyperbolic tangent S transfer function):

$$f(x_i) = \frac{1 - e^{-\alpha x_i}}{1 + e^{-\alpha x_i}} \tag{7}$$

purelin (linear transfer function):

$$f(x_i) = x_i \tag{8}$$

The default settings tansig and purelin are used for offline training using MATLAB/Simulink as shown earlier. After repeated comparison of different transfer functions, the prediction accuracy is greatly improved when tansig and tansig are used for the transfer functions of the hidden layer

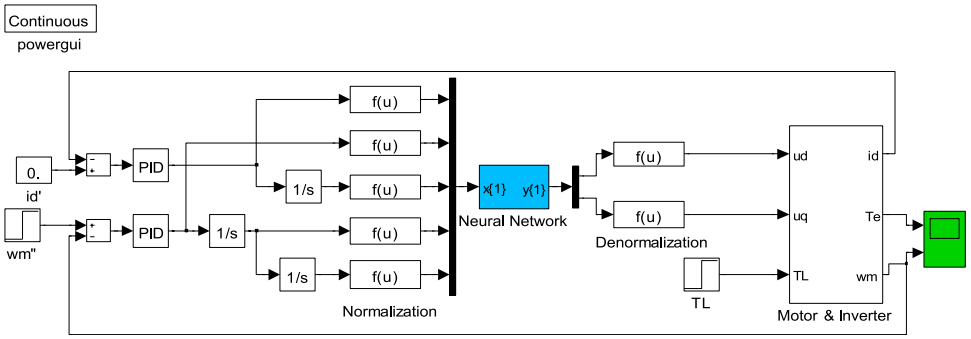

FIGURE 3 | NNIS of PMSM decoupling control system.

TABLE 4 | PID parameters of BP NNIS.

Regulator parameter	PI		PD	
	k_p	k_i	k_p	k_d
BPNN	0.03	0.01	1.143	0.0006

and output layer. The prediction errors of the BPNN with different activation functions are shown in **Table 3**.

Therefore, the BPNN is used to select the hyperbolic tangent S transfer function for function fitting approximation (Yin et al., 2004).

The Optimized Back Propagation Neural Network Module Is Generated

Repeated training is needed to determine the optimal parameters of the BPNN, and the neural network module generated by training is used to replace the inverse system for offline decoupling simulation of the BP NNIS of the PMSM (Yin et al., 2004; Pang et al., 2020). The main parameters of the program to generate BPNN are as follows:

net = newff (miN•max (pn) [122], {"tansig", "tansig"}, "trainlm", "learngdm"); net. trainPar.epochs = 2000; net. trainPar.show = 10; net. trainPar.goal = 10e-6; net. trainPar.min_grad = 1e-15;
net.trainPar.mu_dec = 0.1; net. trainPar.mu_inc = 7; net. trainPar.goal = 0.04; net. trainPar.lr = 0.5;
The PMSM decoupling control system based on the BP NNIS can be constructed by replacing the inverse system module with the generated BPNN module and adding normalization and inverse normalization modules before and after the neural network module, as shown in **Figure 3**.

The parameter setting of PI and PD regulator of BP NNIS is shown in **Table 4**.

At 0–0.2 s, the given load torque TL is 6 N m, and at 0.4 s, the load torque mutates to 12 N m; at 0–0.4 s, the given rotor speed ωr is 40 rad/s, in 0.4 s, ωr changes to 140 rad/s. Torque and speed response curves under inverse control mode are shown in **Figure 4**, and **Figure 5** shows the torque and speed response curves of the inverse system based on the BPNN under the same conditions (Zhang, 2010).

Comparing **Figure 4** and **Figure 5**, it can be found that when the set load torque changes suddenly, both controls can maintain the stability of load speed, but the inverse system control method has long torque response time and large peak value, and the peak value of torque reaches 17 *N m*. The overshoot is 41%, while the torque response time of BP NNIS is short and the peak value is small, and the overshoot is only 16%. When the set speed changes suddenly, the speed response of the two control modes is relatively fast, and there is basically no overshoot. However, in the inverse system control mode, the torque fluctuation is large and the adjustment time is long, while in the BP NNIS, the torque fluctuation is small and the recovery time is short.

In the test, the speed is kept at 90 *rad/s*, and the load has periodic step change between 6 *N m* and 12 *N m* rated load torque. The response curve of speed and torque under inverse control mode is shown in **Figure 6**. **Figure 7** shows the speed and torque response curves of the inverse system based on the BPNN under the same conditions.

Comparing **Figure 6** and **Figure 7**, it is not difficult to find that when the rated load torque changes periodically, the two control modes can maintain the speed stability, but under the inverse system control mode based on BPNN, the torque response overshoot is smaller and the adjustment time is shorter.

INVERSE SYSTEM DESIGN AND DECOUPLING OF RADIAL BASIS FUNCTION NEURAL NETWORK FOR PERMANENT MAGNET SYNCHRONOUS MOTOR

Radial Basis Function Neural Network

RBFNN as a feedforward network can approximate analytic nonlinear relations with arbitrary accuracy (Wang et al., 2022; Yang et al., 2020). It is a powerful tool to deal with complex nonlinear, uncertain, and coupling problems in MIMO systems. Now a PMSM decoupling control system based on the RBF NNIS

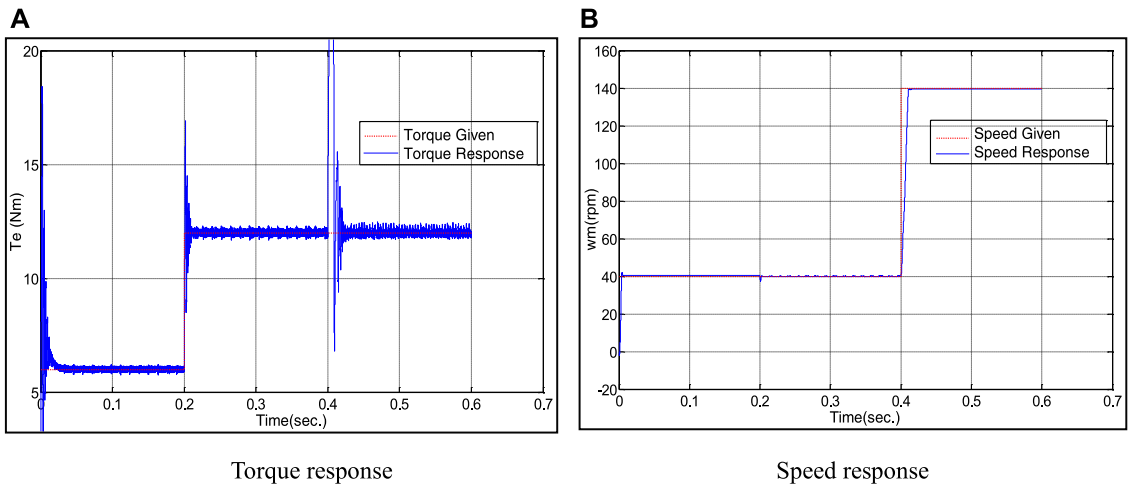

FIGURE 4 | Response curve of inverse system decoupling control.

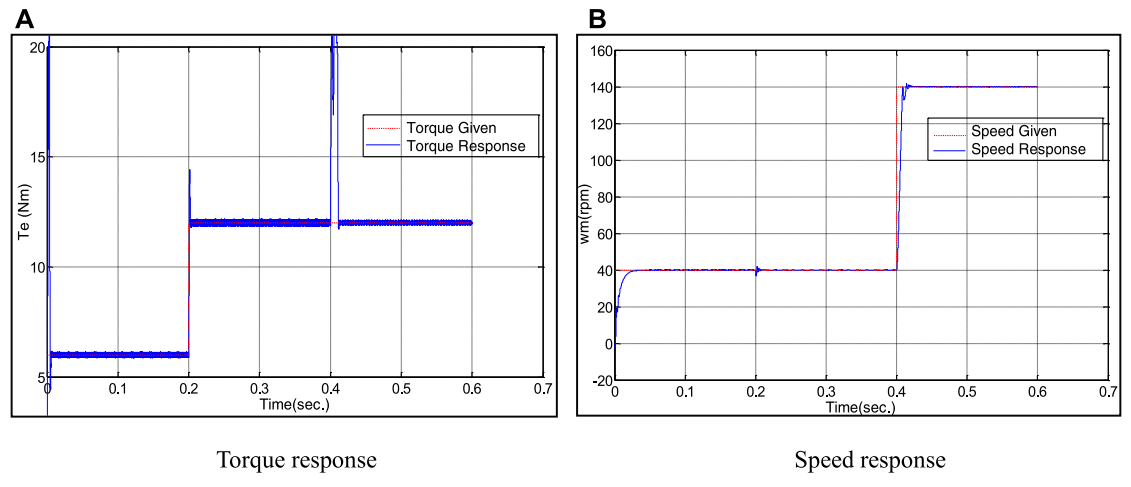

FIGURE 5 | Response curve of BPNN inverse system decoupling control.

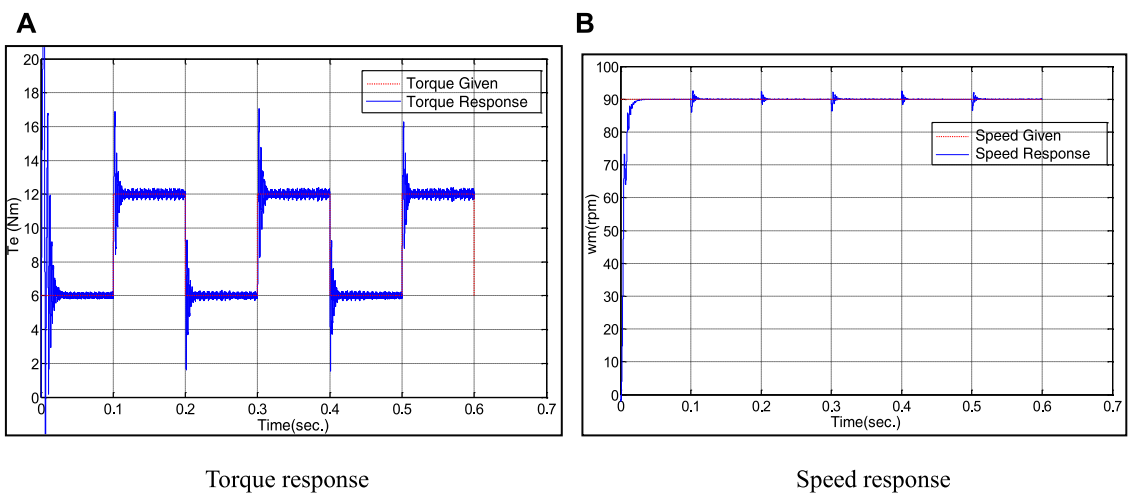

FIGURE 6 | Response curve of BPNN inverse system decoupling control when torque changes periodically.

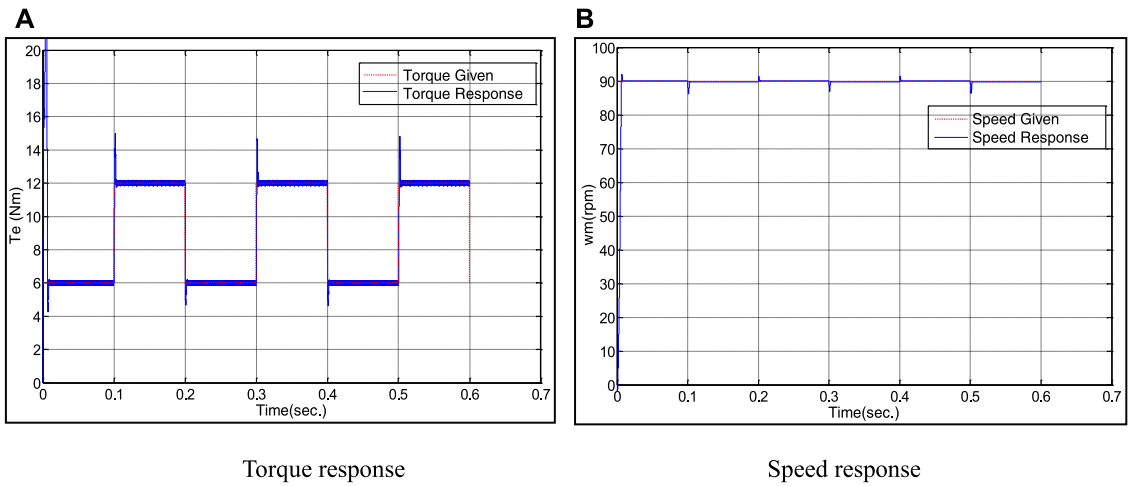

FIGURE 7 | Response curve of BPNN inverse system decoupling control when torque changes periodically.

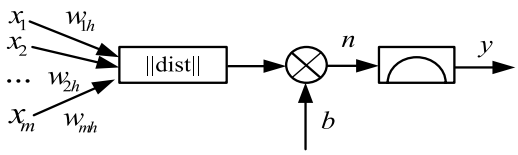

FIGURE 8 | RBF neural model. RBFNN structure as shown in **Figure 9**.

is established (Zhao and Wang, 2022b), which makes the system have good dynamic and static characteristics.

The RBF neural model is shown in **Figure 8**.

Before using the RBFNN, it is necessary to determine the number of hidden layer neurons, the center of transfer function, expansion constant, and a set of corresponding weights.

Structure of the Radial Basis Function Neural Network

The design methods of the RBFNN can be divided into two categories (Li et al., 2020; Li et al., 2021b; Huang et al., 2022).

1) The function center is randomly selected from the sample data and the center is fixed. After the RBF center is determined, the output of hidden layer is known (Chen, 2021).

Gaussian function is selected as radial basis function, so the transfer function of radial basis function neural network can be expressed as

$$R(X - c_i) = \exp\left(-\frac{M}{d_m^2}||X - c_i||^2 \right) \tag{9}$$

In the formula, M is the number of neurons in the hidden layer; d_m is the maximum distance between the selected centers. In this case, the mean square deviation of Gaussian RBF is fixed as

$$\sigma = \frac{d_m}{\sqrt{2M}} \tag{10}$$

The connection weight of the network can be directly calculated by the previous formula:

$$W = R^{+}d \tag{11}$$

In the formula, d is the desired response vector. R^{+} is the pseudo inverse of matrix R, and R is determined by

$$R = \{r_{ji}\} \tag{12}$$

$$g_{ji} = \exp\left(-\frac{M}{d_m^2}||X_j - c_i||^2 \right) \tag{13}$$

In the formula, X_j is the data quantity of the jth input sample, and the singular value decomposition method can be used to calculate the pseudo inverse of the matrix. This method corresponds to the MATLAB/newrb construction method.

2) In the dynamic adjustment method of function center, the center of RBF is moved, and its position is determined by self-

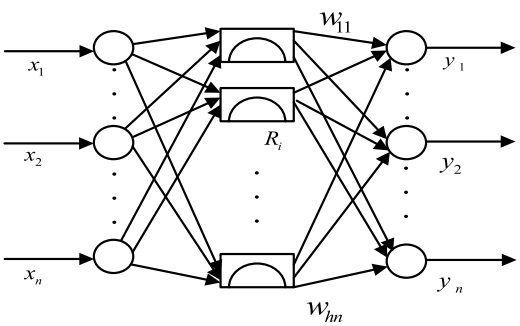

FIGURE 9 | RBF neural network.

TABLE 5 | Prediction error of different RBFNN structures.

RBFNN structures	Number of neurons	Square sum error	Running time (s)
Newrb	4000	0.23225	2310.65
Newrbe	258	3.29834	255.39

TABLE 6 | Prediction error of different RBF spread.

Spread	Number of neurons	Square sum error	Running time (s)
0.8	523	15.18543	613.22
1.0	258	3.29834	255.39
1.2	917	25.32467	1019.17

By comparison, when spread is set as the default value 1, the number and running time of neurons have advantages when the sum of square error requirements are met.

TABLE 7 | PID parameters of RBF NNIS.

Regulator parameter	PI		PD	
	k_p	k_i	k_p	k_d
RBFNN	0.003	0.001	14	0.01

organizing learning, while the linear weight of the output layer is calculated by supervised learning rules. The purpose of learning is to have the center of RBF located in the important area of input space. The specific steps are as follows:

1) Initialize the cluster center c_i. Generally, M samples are selected from the input sample X_i as the clustering center.
2) The input samples are grouped according to the nearest neighbor rule (Zuo et al., 2014); that is, M samples in Xi are assigned to the input sample cluster set θ_i with center c_i, that is, $X_j \in \theta_i$, and meet

$$d_i = \min \left\| X_j - c_i \right\| \tag{14}$$

where d_i represents the minimum Euclidean distance.

3) Calculate the mean value of samples in θ_i (i.e., clustering center c_i)

$$c_i = \frac{1}{M_i} \sum_{x_j \in \theta_j} X_j \tag{15}$$

where M_i is the number of input samples in θ_i. Calculate according to the aforementioned steps until the distribution of cluster center no longer changes. After the center of RBF is determined, if RBF is a Gaussian function, its mean square deviation σ can be calculated by Eq. 18. The output of the hidden layer can then be calculated. This method corresponds to the MATLAB/newrbe construction method.

Newrb and newrbe were, respectively, used to establish two kinds of RBFNNs. The error of the sum of squares was set as 10e-4 pairs of neurons. By comparing the sum of square error, the structure prediction error of different RBFNNs is shown in **Table 5**.

By comparison, it is concluded that newrbe can only be stopped when the number of neurons reaches the number of training samples. Although the required error precision is reached, the running time is too long. On the contrary, newrb can use fewer neurons to achieve the error precision, and the running time is shorter.

The Spread of the Radial Basis Function Neural Network

When applying the newrbe function to the design of the radial basis function neural network, the spread needs to cover as many input intervals as possible (Li et al., 2019b; Yang et al., 2019), so it needs to be

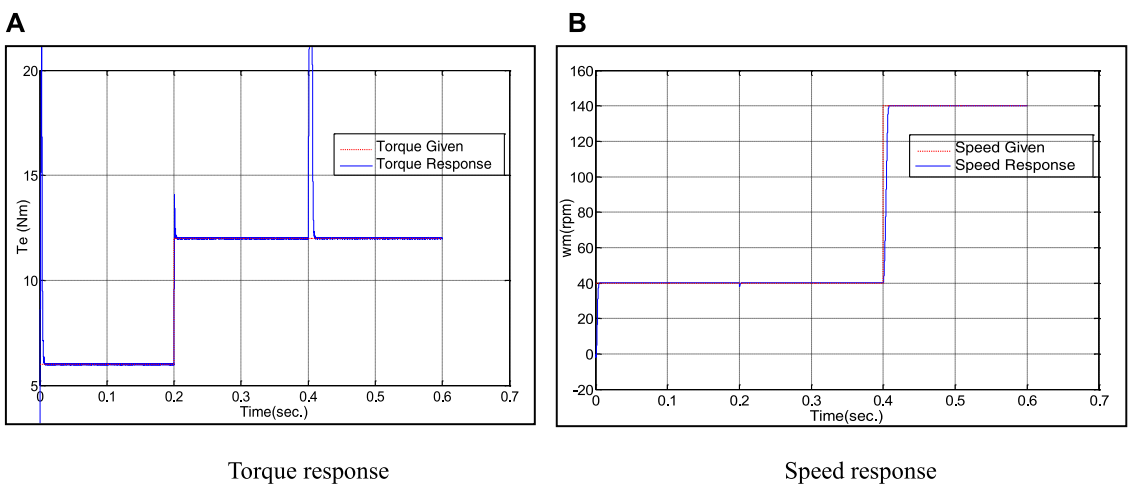

FIGURE 10 | Response curve of RBFNN inverse system decoupling control.

set as large as possible. However, too large spread will lead to the difficulty of numerical calculation, and the corresponding regions cross too much, which will reduce the accuracy. Reasonable selection of spread values has great influence on the prediction accuracy of the RBFNN. Newrb is used to construct the RBFNN and spread is set as different values for comparison (Wang and Xu, 2012; Pang et al., 2020). The prediction errors of different RBF spreads are shown in **Table 6**.

Generating Optimized Back Propagation Neural Network Module

In addition, the display interval was set as 1, the maximum number of neurons was set as 600, and the neural network module generated by training was used to replace the inverse system for the decoupling offline simulation of the inverse system of the RBFNN of the PMSM. The main parameters of the program to generate the RBFNN (Zuo et al., 2014) are as follows:

goal = 0.0001; spread = 1; MN = 600; DF = 1;

net = newrb (pn, tn, goal, spread, MN, DF);

By replacing the inverse system module with the generated RBFNN module, and adding the normalized and anti-normalized modules in the front and back to the neural network module, a PMSM decoupling control system based on the NNIS can be constructed, as shown in **Figure 3**.

The parameter setting of PI and PD regulator of RBF NNIS is shown in **Table 7**.

1) Static decoupling experiment under the same conditions as section 3:

Figure 10 shows the torque and speed response curves under the RBF NNIS control mode under the same conditions.

Comparing **Figure 10A** with **Figure 5A**, it can be found that when the speed remains unchanged and the torque changes suddenly, the control mode based on the RBF NNIS has faster response speed and shorter system stability time than BPNN. When the speed changes suddenly, the RBF NNIS also has a faster response speed.

2) Dynamic decoupling experiment against load disturbance under the same conditions as in Section 3:

Figure 11 shows the torque and speed response curves under the RBF NNIS control mode under the same conditions.

Comparing **Figure 7A** with **Figure 11A**, it can be found that when the set speed remains unchanged and the torque changes step periodically, the control method based on the RBF NNIS has faster response speed, smaller overshoot, and more stable torque in a steady state than BPNN torque regulation. Comparing **Figure 11B** with **Figure 7B**, it can be found that when the torque changes suddenly, the speed of the RBF NNIS is also more stable.

Decoupling Performance Analysis

The static decoupling test can verify the static decoupling performance of the system, that is, the stability of one variable when the other variable changes. It can be seen from **Figure 5** that the inverse decoupling control system based on the RBFNN has a very small overshoot, basically no oscillation, and the fastest response time when the speed and torque change.

The anti-load disturbance experiment can verify the dynamic decoupling performance of the system, and the dynamic decoupling performance is an important criterion for evaluating the advantages and disadvantages of the decoupling system. As can be seen from **Figure 7**, the inverse decoupling control system based on the RBFNN responds rapidly and is basically synchronized with the given load. The speed response under the control mode of the inverse system decoupling control system based on the RBFNN has no overshoot, the oscillation amplitude is very small, and the stability value is quickly restored. The speed response of the inverse system decoupling control system based on the BPNN has overshoot and large oscillation amplitude. Under the control mode of the inverse system decoupling control system (Bu et al., 2018), speed has a long-time jitter, and the recovery to the stable value is slow.

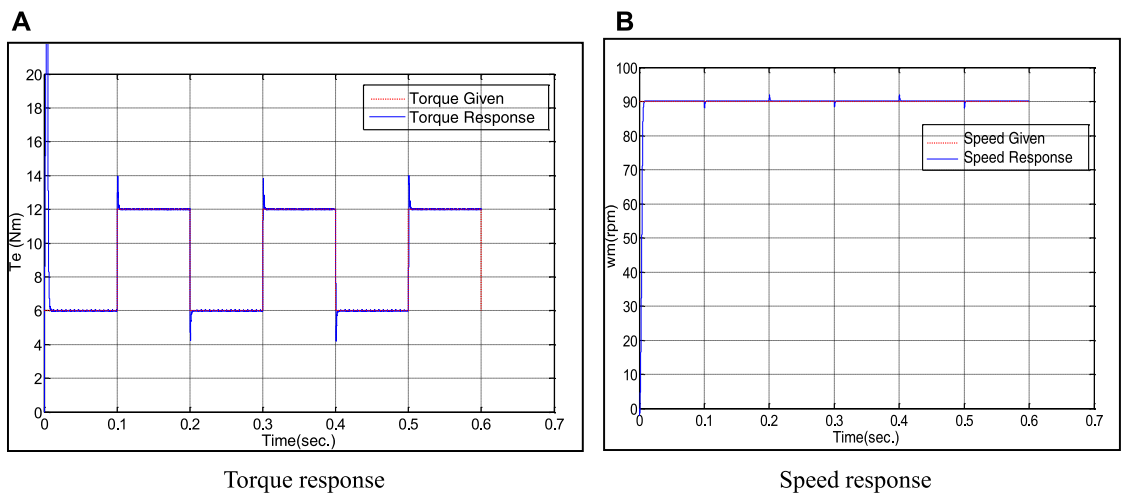

FIGURE 11 | Response curve of RBFNN inverse system decoupling control when torque changes periodically.

CONCLUSION

After verification and comparative analysis, it can be confirmed that the PMSM based on the RBF NNIS control mode has excellent static decoupling characteristics and better dynamic decoupling control performance. The simulation research based on RBF NNIS decoupling control has good robustness and stability compared with the other two decoupling controls. This is an optimized NNIS PMSM decoupling control system, which has a certain application value.

DATA AVAILABILITY STATEMENT

The original contributions presented in the study are included in the article/Supplementary Material. Further inquiries can be directed to the corresponding author.

AUTHOR CONTRIBUTIONS

GD-W is responsible for the MATLAB modeling of PMSM. QZ-Q, ZW, and KZ-W are responsible for theoretical derivation. LY is responsible for neural network inverse system simulation.

FUNDING

This work was supported by the National Defense Pre-Research Foundation of China (1126170104A, 1126180204B, 1126190508A, and 1126190508A).

ACKNOWLEDGMENTS

All data included in this study are available upon request by contact with the corresponding author.

REFERENCES

Bu, W., Chen, Y., and Zu, C. (2019). Stator Flux Orientation Inverse System Decoupling Control Strategy of Bearingless Inductionmotor Considering Stator Current Dynamics[J]. *IEEJ Trans. Electr. Electron. Eng.* 14 (4), 22847. doi:10.1002/tee.22847

Bu, W., He, F., Li, Z., Zhang, H., and Shi, J. (2018). *Neural Network Inverse System Decoupling Control Strategy of BLIM Considering Stator Current Dynamics*. London: Transactions of the Institute of Measurement and Control.

Bu, W., Li, B., He, F., and Li, J. (2019). Inverse System Decoupling Sliding Mode Control Strategy of BLIM Considering Current Dynamics. *Int. J. Appl. Electromagn. Mech.* doi:10.3233/jae-180094

Bu, W., and Li, Z. (2019). LS-SVM Inverse System Decoupling Control Strategy of a Bearingless Induction Motor Considering Stator Current Dynamics[J]. *IEEE Access* (99), 1. doi:10.1109/ACCESS.2019.2939258

Bu, W., Li, Z., and Wang, X. (2015). "A Control Method of Bearingless Induction Motor Based on Neural Network[C]," in IEEE International Conference on Information & Automation, Lijiang, August 8–10, 2015 (IEEE).

Chen, Y. (2021). College English Teaching Quality Evaluation System Based on Information Fusion and Optimized RBF Neural Network Decision Algorithm. *J. Sensors*. doi:10.1155/2021/6178569

Huang, B., Li, Y., Zhan, F., Sun, Q., and Zhang, H. (2022). A Distributed Robust Economic Dispatch Strategy for Integrated Energy System Considering Cyber-Attacks. *IEEE Trans. Ind. Inf.* 18, 880–890. doi:10.1109/TII.2021.3077509

Jie, H., Xu, H., and Zheng, G. (2020). Adaptive Decoupling Control Using Radial Basis Function Neural Network for PMSM Considering Uncertain and Time-Varying Parameters[J]. *IEEE Access* (99), 1. doi:10.1109/ACCESS.2020.2993648

Li, B., Quan, Z., Bei, S., Zhang, L., and Mao, H. (2021). An Estimation Algorithm for Tire Wear Using Intelligent Tire Concept. *Proc. Institution Mech. Eng. Part D J. Automob. Eng.* doi:10.1177/0954407021999483

Li, S., Won, H., and Fu, X. (2019). Neural-Network Vector Controller for Permanent-Magnet Synchronous Motor Drives: Simulated and Hardware-Validated Results[J]. *IEEE Trans. Cybern.* (99), 1. doi:10.1109/TCYB.2019.2897653

Li, Y., Gao, D. W., Gao, W., Zhang, H., and Zhou, J. (2021). A Distributed Double-Newton Descent Algorithm for Cooperative Energy Management of Multiple Energy Bodies in Energy Internet. *IEEE Trans. Ind. Inf.* 17 (9), 5993–6003. doi:10.1109/tii.2020.3029974

Li, Y., Gao, D. W., Gao, W., Zhang, H., and Zhou, J. (2020). Double-Mode Energy Management for Multi-Energy System via Distributed Dynamic Event-Triggered Newton-Raphson Algorithm. *IEEE Trans. Smart Grid.* 11 (6), 5339–5356. doi:10.1109/tsg.2020.3005179

Li, Y., Zhang, H., and Liang, X. (2019). Event-triggered Based Distributed Cooperative Energy Management for Multienergy Systems. *IEEE Trans. Ind. Inf.* 15 (14), 2008–2022. doi:10.1109/tii.2018.2862436

Pang, Z., Wang, T., Liu, S., Wang, Z., and Gong, L. (2020). Kinematics Analysis of 7-DOF Upper Limb Rehabilitation Robot Based on BP Neural Network," in IEEE 9th Data Driven Control and Learning Systems Conference (DDCLS), Liuzhou, November 20–22, 2020 (IEEE). doi:10.1109/ddcls49620.2020.9275138

Sun, X., Long, C., and Jiang, H. (2016). High-Performance Control for a Bearingless Permanent-Magnet Synchronous Motor Using Neural Network Inverse Scheme Plus Internal Model Controllers[J]. *IEEE Trans. Industrial Electron.* 63 (6), 1. doi:10.1109/tie.2016.2530040

Ting, L. (2017). "An Empirical Study on China's Early Warning of Financial Risks under the New Normal," in 2017 4th International Conference on Industrial Economics System and Industrial Security Engineering, Kyoto, July 24–27, 2017 (IEIS).

Wang, H. F., and Xu, X. A. (2012). Applying RBF Neural Networks and Genetic Algorithms to Nonlinear System Optimization. *Adv. Mater. Res* 16 (6), 115–118. doi:10.4028/www.scientific.net/amr.605-607.2457

Wang, X., Gao, D. W., Yan, J. W., Gao, W., Muljadi, E., and Gevorgian, V. (2018). Implementations and Evaluations of Wind Turbine Inertial Controls with FAST and Digital Real-Time Simulations. *IEEE Trans. Energy Convers.* 33 (4), 1805–1814. doi:10.1109/tec.2018.2849022

Wang, X., Zhao, T., and Parisio, A. (2022). Frequency Regulation and Congestion Management by Virtual Storage Plants. *Sustain. Energy, Grids Netw.* 29 (1), 100586. doi:10.1016/j.segan.2021.100586

Xie, M., and Xie, L. (2020). Decoupling Control of Permanent Magnet Synchronous Motor with Support Vector Regression Inverse System Method. *IEEE Access* 8, 212687–212698. doi:10.1109/access.2020.3039053

Yang, T., George, J., Qin, J., Yi, X., and Wu, J. (2020). Distributed Least Squares Solver for Network Linear Equations. *Automatica* 113.

Yin, F. L., Wang, J., andand Guo, H. (2004). *Advances in Neural Networks - ISNN 2004*. Berlin: Springer Science and Business Media LLC

Yang, T., Yi, X., Wu, J., Yuan, Y., Wu, D., Meng, Z., et al. (2019). A Survey of Distributed Optimization. *Annu. Rev. Control* 47, 278–305. doi:10.1016/j.arcontrol.2019.05.006

Zhang, D. (2010). Energy-Saving Control Based on Neural Network Inverse Decoupling for Asynchronous Motors," in Asia-Pacific Power and Energy Engineering Conference.03.

Zhao, W., and Wang, C. (2022). *Decoupling Control of Nonlinear Inverse System for Chassis-By-Wire System*. Berlin: Springer Science and Business Media LLC.

Zhao, W., and Wang, C. (2022). *Nonlinear Control Technology of Vehicle Chassis-By-Wire System*. Berlin: Springer Science and Business Media LLC.

Zuo, G. L., Niu, F. L., Cheng, Y., and Zhang, Y. X. (2014). Study on the Fault Diagnosis of Gear Pump Based on RBF Neural Network. *Applied Mechanics and Materials*. doi:10.4028/www.scientific.net/amm.556-562.2957

Conflict of Interest: The authors declare that the research was conducted in the absence of any commercial or financial relationships that could be construed as a potential conflict of interest.

Publisher's Note: All claims expressed in this article are solely those of the authors and do not necessarily represent those of their affiliated organizations, or those of the publisher, the editors, and the reviewers. Any product that may be evaluated in this article, or claim that may be made by its manufacturer, is not guaranteed or endorsed by the publisher.

frontiers | Frontiers in Energy Research

ORIGINAL RESEARCH
published: 05 July 2022
doi: 10.3389/fenrg.2022.928681

Measurement Error Estimation for Distributed Smart Meters Through a Modified BP Neural Network

Tian Xia, Cencen Liu, Ming Lei, Shuibin Xia, Ding Li and Dongyue Ming*

Marketing Service Center of State Grid Hubei Electric Power Co., Ltd., Wuhan, China

Smart meters generally suffer degradation of metering accuracy and performance due to aging, faults, and other factors, which, however, are difficult to detect. This study proposes a measurement error estimation method for distributed smart meters based on a modified BP neural network. First, the relationship model between the metering correction coefficient, network loss, and energy consumption measurement value for the distributed system is established. Then, a modified BP neural network for the parameter estimation method is proposed, in which the internal activation function, iterative step size, and other parameters are comprehensively designed. Finally, the parameters of the distributed smart meter measurement error are solved through training and learning. The case study verifies the effectiveness of the proposed method, and this study lays a theoretical foundation for accurate prediction of the measurement error for distributed smart meters.

Keywords: modified BP neural network, smart meters, measurement error, activation function*, linear model

OPEN ACCESS

Edited by:
Yushuai Li,
University of Oslo, Norway

Reviewed by:
Chaoqiang Jiang,
City University of Hong Kong, Hong Kong SAR, China
Hongyu Chu,
Southwest University of Science and Technology, China
Xiaogang Lin,
Chongqing University, China

****Correspondence:***
Tian Xia
cross20210907@163.com

Specialty section:
This article was submitted to Smart Grids, a section of the journal Frontiers in Energy Research

Received: *26 April 2022*
Accepted: *09 May 2022*
Published: *05 July 2022*

Citation:
Xia T, Liu C, Lei M, Xia S, Li D and Ming D (2022) Measurement Error Estimation for Distributed Smart Meters Through a Modified BP Neural Network. Front. Energy Res. 10:928681. doi: 10.3389/fenrg.2022.928681

1 INTRODUCTION

With the popularization of power networks and the full coverage of smart meters, energy metering engineering has become the focus of increasing attention of the operation department of power companies. Among them, the measurement error of the metering device is directly related to the accuracy of the electric energy measurement and is also the basis for the economic accounting of the power company (Wang et al., 2019a). Monitoring and evaluating the measurement error of electric energy metering by metering devices has become an imperative method for the economic interest and fairness of transactions for both power supply companies and users, and it is also an effective means to manage and predict the use of electric energy (Steiner et al., 2018).

Generally, the measurement errors of electric energy metering devices are mainly caused by electric energy meters, transformers, and secondary wiring. Many related works have been presented, including error source detection, error modeling, and error evaluation. Among them, the measurement error model, which describes the differences between the actual value and the estimated value, can be obtained in the calibration study for smart meters (Dong et al., 2018); the corresponding measurement error is commonly detected by the test system based on a pseudorandom distortion test signal and indirect likelihood function (Wang et al., 2019b), which could also be confirmed by testing devices or platforms (Donahue et al., 2014). In addition, the current remote error estimation has also become a state-of-the-art field, in which remote calibration and monitoring systems including some monitoring equipment, communication networks, and the master station should be installed (Gao et al., 2019;Zhang et al., 2018). However, solving the measurement error requires the installation of a large number of standard terminal devices, increasing investment, and operation and maintenance costs (Luan et al., 2015).

Recently, the application of deep learning and mathematical model construction methods to realize the remote analysis of smart meter measurement error has become a state-of-the-art field. A mathematical model of smart electrical meter errors in the smart grid was proposed by Kong et al. (2020, 2021), which was built by using the dimension reduction estimation model and damped recursive least squares, and then the clustering and Kalman prediction methods were presented to estimate smart meter errors. An artificial neural network for power loss estimation was proposed by Kashef et al. (2018a) to estimate line loss; the advantage is that it has real-time estimation and high precision for fast calculation of power loss of each line in the distribution system. A remote estimation method based on the neural network filter and generalized damping recursive least squares was proposed by Kashef et al. (2018b), which can estimate both users' smart meters' errors and the loss accurately. Most of the mentioned methods integrated the analytical formulas of network loss into the estimation models to mitigate the impact of network loss changes (Sun et al., 2016;Liu et al., 2015), which, however, are generally limited by the complexity, calculation accuracy, and applicability of the network loss analytical formulas (Alonso et al., 2020;Xia et al., 2019).

To overcome the above drawbacks, artificial intelligence methods, especially neural networks, have been applied to avoid cumbersome analytical formulas and improve applicability. The back-propagation (BP) neural network algorithm was used to achieve distributed computing of network losses, and finally, obtain a root mean square error that is lower than 5% by Chao et al. (2018). A novel real-time power loss estimation method was proposed by Kashef et al. (2018b) for the distribution system, in which a neural network power loss estimation method was applied. Although neural network-related methods generally need sample training to obtain good performance in estimating network losses (Hao et al., 2020;Ruan et al., 2019), it induces frequent and drastically changing network losses simultaneously (Kashef et al., 2018b), which results in neural networks becoming unstable for remote error estimation (Zhou et al., 2021).

Motivated by the above analysis, this study proposes a novel remote measurement error estimation method for distributed smart meters through a modified BP neural network. The main contributions lie in the following: 1) a measurement error model considering network loss is established, and the k-means clustering method is introduced to simplify the model in estimating the correction parameter; 2) a traditional BP network model is modified to fit the established model, where the intrinsic activation function and iterative rules are optimized to ensure the utilization of new data, estimator change range reduction, and good robustness against the network loss; and 3) a simulated distributed smart electricity meter system is built for analyzing the distributed smart meter data, the feasibility, and effectiveness of which are verified through tests. Finally, the proposed method provides a basis for efficiently detecting smart electricity meters with large measurement errors.

The rest of the article is organized as follows: **Section 2** introduces the distributed smart meter error model, which builds the relationship among the master meters' reading value, network loss, and sub-meters' reading value. Then, an overview of the measurement error estimation method based on a modified BP neural network is described in **Section 3**. In **Section 4**, experiments are carried out, as well as the verification experiment of the measurement error estimation. The conclusions are drawn in **Section 5**.

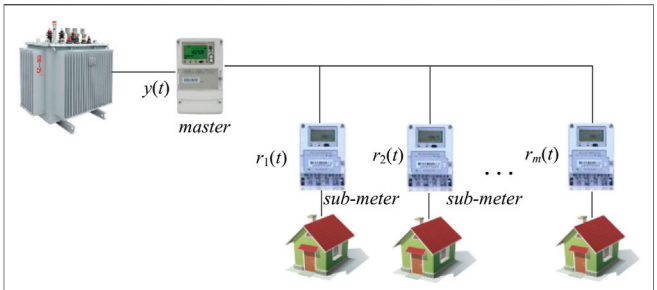

FIGURE 1 | The distribution of smart meters in the electric grid.

2 DISTRIBUTED SMART METER ERROR MODEL

In the distribution energy consumption measurement system, the classic topology for the distribution feeder unit is shown in **Figure 1**. According to the conservation of energy, there is an electric energy relationship between the smart electricity meters of the terminal and the master meter in the distributed topology during the tth measurement period, that is,

$$y(t) = \sum_{i=1}^{m} r_i(t)\xi_i + \Delta w(t) \tag{1}$$

where $y(t)$ is the total electric energy (kW.h) from the master smart meter in the tth measurement period, $r_i(t)$ is the electric energy (kW.h) generated from the ith meter on the user's side, and ξ_i is the correction parameter of the smart meter to evaluate the measurement error. $\Delta w(t)$ is the network loss in the tth measurement period of this distribution system.

Based on the error model analysis in **Eq. 1**, each terminal smart meter (sub-meter) measurement may be biased due to the degradation or lack of proper maintenance, thus leading to the measurement results of the master smart meter being biased from the actual value. For description convenience, the reading value of the smart meters and the master smart meter is applied into **Eq. 1**. Thus, **Eq. 1** can be written as follows:

$$\boldsymbol{Y}(t)_{t\times 1} = \boldsymbol{R}'(t)_{t\times(m+t)}\boldsymbol{X}(t)_{(m+t)\times 1} \tag{2}$$

where $\boldsymbol{Y}(t)_{t\times 1}$ is the matrix represented by $\boldsymbol{Y}(t)_{t\times 1} = [y(1)\ y(2)\ldots y(t)]^T$, $\boldsymbol{R}'(t)_{t\times(m+t)}$ is the matrix written as $\boldsymbol{R}'(t)_{t\times(m+t)} = [\boldsymbol{R}(t)_{t\times m}\ \boldsymbol{I}_{t\times t}]$ with $\boldsymbol{R}(t)_{t\times m} = [\boldsymbol{r}(1)_{1\times m}\ \boldsymbol{r}(2)_{1\times m}\ldots\boldsymbol{r}(t)_{1\times m}]^T$, where $\boldsymbol{r}(i)_{1\times m} = [r_1(i)\ r_2(i)\ldots r_m(i)]$, $i = 1,\ldots, t$, and $\boldsymbol{I}_{t\times t}$ is the identity matrix. Let $X(t)_{(m+t)\times 1} = \begin{bmatrix} \xi_{m\times 1} \\ \Delta w(t)_{t\times 1} \end{bmatrix}$ be the objective matrix where $\Delta \boldsymbol{w}(t)_{t\times 1}$ is the network loss matrix during the tth measurement period.

From the description of linear equations in **Eq. 2**, the final matrix $\boldsymbol{X}(t)$ can be solved by the least-squares method, that is,

$$\boldsymbol{X}(t)_{(m+t)\times 1} = \left(\left[\boldsymbol{R}'(t)_{t\times(m+t)}\right]^T \boldsymbol{R}'(t)_{t\times(m+t)}\right)^{-1} \left[\boldsymbol{R}'(t)_{t\times(m+t)}\right]^T \boldsymbol{Y}(t)_{t\times 1} \tag{3}$$

Generally speaking, the actual model of smart meter errors can be considered as a set of linear equations consisting of t equations. However, $\boldsymbol{X}$ is a matrix of unknowns to be solved since it contains $m + t$ unknown variables. In this situation, if the number of unknown variables is more than those of equations, then the matrix inverse may not be solvable, where $\boldsymbol{R}'(t)$ may contain an indefinite value. To this end, a modified BP neural network is proposed to solve the model parameters for estimating the measurement error of smart electricity meters.

3 PARAMETER ESTIMATION FOR THE MODEL

To estimate the parameters in the distributed energy consumption measurement system, the following strategies are carried out. First, the k-means clustering method is adopted for classifying the data from the master smart meter to simplify the model considering the same network loss in the same class. Then, a traditional BP neural network is modified in terms of an activation function and iterative length to fast fit the model for the distributed measurement system.

3.1 k-Means Clustering Model

The k-means clustering algorithm is a classic clustering method based on Euclidean distance. Since the number of centers k is given, the data will be classified into the center under the criterion that its distance to the center is minimized. Through the cluster centers being updated iteratively, the classes will finally be generated. Generally, the mathematic model is to minimize the within-class variance as follows:

$$SSE = \sum_{i=1}^{k} \sum_{x\in C_i} (x - m_i)^2 \tag{4}$$

where x is the data belonging to the class C_i; k is the number of cluster centers; and m_i is the center of the class C_i containing N_i data, which is obtained by

$$m_i = \frac{1}{N_i} \sum_{x\in C_i} x \tag{5}$$

Based on the rule of the k-means clustering, the number of classes will be obtained once the number of smart meters is set. In each class, network loss can be considered as a constant, that is, $\Delta w(t) \approx \Delta w_c$, so the correction coefficient can be solved by

$$\begin{bmatrix} y(1)^c - \Delta w_c \\ y(2)^c - \Delta w_c \\ \vdots \\ y(t)^c - \Delta w_c \end{bmatrix} = \begin{bmatrix} r_1(1) & r_2(1) & \cdots & r_m(1) \\ r_1(2) & r_2(2) & \cdots & r_m(2) \\ \vdots & \vdots & \vdots & \vdots \\ r_1(t) & r_2(t) & \cdots & r_m(t) \end{bmatrix} \begin{bmatrix} \xi_1 \\ \xi_2 \\ \vdots \\ \xi_m \end{bmatrix} \tag{6}$$

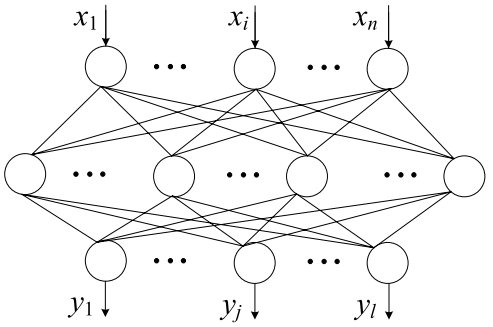

FIGURE 2 | BP neural network structure diagram.

where $y(t)^c$ is the data belonging to cluster C and Δw_c is the constant network loss. If the number of data is larger than the number of smart meters, the correction coefficient ξ_i can be obtained by **Eq. 6**, and $\Delta w(t)$ can be then calculated by **Eq. 1**. Notably, the value of network loss is often positive. So, it is necessary to place the constraint condition to solve the value of $\Delta w(t)$ in cluster C. Here, Δw_c is obtained by the minimum error in **Eq. 7**, that is,

$$\min \left(y(t)^c - \Delta w_c - \hat{y}(t)^c\right)^2 \tag{7}$$

where $\Delta w_c > 0$ and $\hat{y}(t)^c$ is the estimated value calculated by the least-squares method through **Eq. 6**. Nevertheless, the constraint condition $\Delta w_c > 0$ makes it difficult to solve **Eq. 7**directly by the least-squares method. Here, the golden section method (Erik et al., 2018) is used to obtain the value of Δw_c, where the maximum value of Δw_c is set as 10% of the centers.

Notably, the network loss listed in **Eq. 1** is mainly generated by the branch of smart meters. To alleviate the network loss while fitting the model, the number of classes can be set by using the number of meters.

Additionally, Δw_c calculated by **Eq. 6** simplifies the model in **Eq. 1**. However, the network loss still affects the result of the correction coefficient calculated by the least-squares method. Thus, in this article, a modified BP neural network is proposed to achieve the optimal value of the correction coefficient ξ_i.

3.2 BP Neural Network

The BP neural network is regarded as a widely used neural network and has wide applications. The main idea of the BP neural network is to adopt a gradient descent to search for the hypothesis space of possible weight vectors. Thus, the BP neural network is generally taken as a gradient descent method to adjust the weights of each layer of the neural network to minimize the total error. On the one hand, the minimum mean square error of reality and expectation can be achieved through neural network iteration. On the other hand, the BP neural network algorithm takes a forward feedback learning process, which, in essence, is a process where errors propagate backward and the weight coefficients of each layer are connected as well. Since the feedback learning runs through

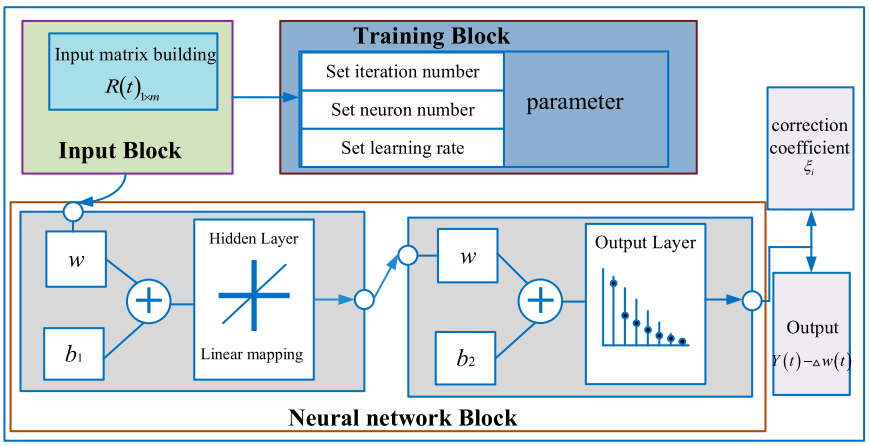

FIGURE 3 | The framework of our model.

the adjustment of the connection mode, weight and threshold of each neuron, and the identification of the whole network, the corresponding neural network structure can be given as in **Figure 2**. Usually, the neural network has three layers, that is, input layer, the hidden layer, and output layer. The data stream often contains two aspects. One aspect is the data forward feedback, that is, the input data x_i is transmitted to the output layer via the hidden layer. In this process, the neuronal state of each layer only affects the neuronal state of the next layer, and the state is determined by the weight and bias terms as well as the activation function. The other aspect is the back-propagation error, that is, network weights and thresholds are adjusted according to the prediction error, such that the BP neural network prediction output can constantly approach the desired output.

To be specific, let $\boldsymbol{x}$ be the input data, $\boldsymbol{\omega}$ and b_1 be the parameters from input layers to the hidden layers, and $\boldsymbol{v}$ and b_2 be the parameters from hidden layers to the output layers. Each neural layer is connected by the activation function, which is designed as follows:

(1) The activation function S_1 from the input layer to the hidden layer

$$net_1 = \boldsymbol{\omega}^T x + b_1, h = S_1(net_1) \tag{8}$$

(2) The activation function S_2 from the hidden layer to the output layer

$$net_2 = \mathbf{v}^T\mathbf{h} + \mathbf{b}_2,\ \hat{y} = S_2(net_2) \tag{9}$$

According to **Eqs 8**, **9**, the predicted value of the neural network can be written as

$$\mathbf{y} = S_2\left(\mathbf{v}^T S_1\left(\boldsymbol{\omega}^T\mathbf{x} + \mathbf{b}_1\right) + \mathbf{b}_2\right) \tag{10}$$

To measure the approximation between the predicted value and the actual value, the expected value of the loss function adopted by the BP neural network is obtained as

$$E(\theta) = \frac{1}{2}\sum_i \left(y_i - \hat{y}_i\right)^2 \tag{11}$$

where θ is the parameter of the inner model. By the derivative of the loss function in **Eq. 11** for $\boldsymbol{v}$ and b_2, respectively, the error terms of the output unit can be calculated as follows:

$$\begin{aligned}\nabla_{(k)}\boldsymbol{v} &= \frac{\partial E}{\partial v} = \frac{\partial E}{\partial \hat{y}}\frac{\partial \hat{y}}{\partial net_2}\frac{\partial net_2}{\partial v}\\ \nabla_{(k)}\boldsymbol{b}_2 &= \frac{\partial E}{\partial b_2} = \frac{\partial E}{\partial \hat{y}}\frac{\partial \hat{y}}{\partial net_2}\frac{\partial net_2}{\partial b_2}\end{aligned} \tag{12}$$

where k is the iteration number and ∇ denotes the gradient operation. The error terms of the hidden neuron can be expressed as

$$\begin{aligned}\nabla_{(k)}\boldsymbol{\omega} &= \frac{\partial E}{\partial \boldsymbol{\omega}} = \frac{\partial E}{\partial \hat{y}}\frac{\partial \hat{y}}{\partial net_2}\frac{\partial net_2}{\partial \boldsymbol{h}}\frac{\partial \boldsymbol{h}}{\partial net_1}\frac{\partial net_1}{\partial \boldsymbol{\omega}}\\ \nabla_{(k)}\boldsymbol{b}_1 &= \frac{\partial E}{\partial \boldsymbol{b}_1} = \frac{\partial E}{\partial \hat{y}}\frac{\partial \hat{y}}{\partial net_2}\frac{\partial net_2}{\partial \boldsymbol{h}}\frac{\partial \boldsymbol{h}}{\partial net_1}\frac{\partial net_1}{\partial \boldsymbol{b}_1}\end{aligned} \tag{13}$$

During back-propagation, the learning rate parameter η is used to update the weights and bias terms of the BP neural network. Then, it can be written as

$$\boldsymbol{v}^{(\mathbf{k})} = \boldsymbol{v}^{(\mathbf{k}-1)} - \eta\frac{\partial E}{\partial \boldsymbol{v}},\ \boldsymbol{b}_2^{(k)} = \boldsymbol{b}_2^{(k-1)} - \eta\frac{\partial E}{\partial \boldsymbol{b}_2} \tag{14}$$

Alternatively, the parameter can then be updated in hidden layers as follows:

$$\boldsymbol{\omega}^{(k)} = \omega^{(k-1)} - \eta\frac{\partial E}{\partial \boldsymbol{\omega}},\ \boldsymbol{b}_1^{(k)} = \boldsymbol{b}_1^{(k-1)} - \eta\frac{\partial E}{\partial \boldsymbol{b}_1} \tag{15}$$

With the neural network iterations described above, the parameters of the weights and biases in the neural network are optimal since the loss function is satisfied with the condition that the error is less than the given threshold or the number of iterations exceeds the setting value. Then, the neural network can work well in terms of classification, prediction, and so on.

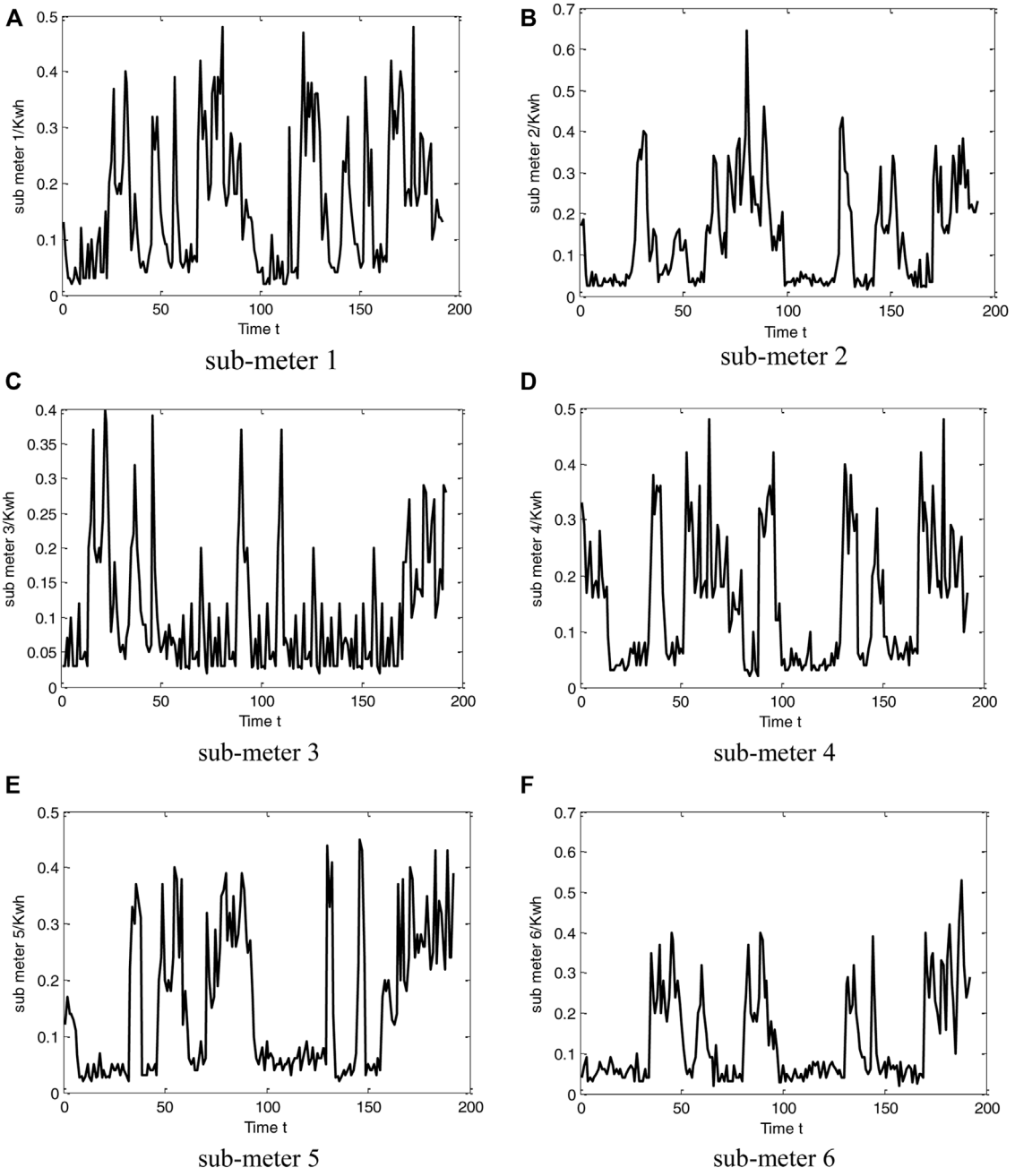

FIGURE 4 | The data from six smart electricity meters: **(A)** sub-meter 1, **(B)** sub-meter 2, **(C)** sub-meter 3, **(D)** sub-meter 4, **(E)** sub-meter 5, and **(F)** sub-meter 6.

3.3 A Modified BP Neural Network for Parameter Estimation

In the BP neural network, the activation function is the core part that enables the neural network to achieve good performance. Traditional activation functions, such as the sigmoid function, generally aim at nonlinear data mapping. The established mathematical model contains linear equations as previously discussed, as seen in **Eq. 3**. The traditional activation functions of the BP neural network may not be suitable to solve the parameters of the model. Thus, the BP neural network is optimized and improved here, the framework of which is shown in **Figure 3**. The details are given as follows.

(1) Parameter for the BP neural network

To facilitate the corresponding modified BP neural network, the input $\boldsymbol{x}$ in the neural network model and neuron weight $\boldsymbol{\omega}$ can be expressed as

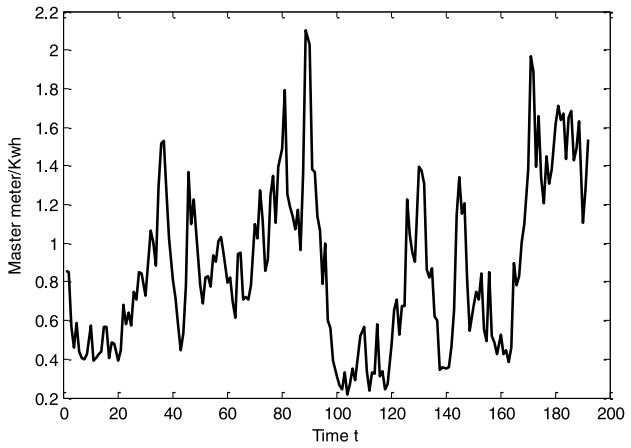

FIGURE 5 | The data from the master meter.

TABLE 1 | The parameter setting of the BP neural network.

Hidden neurons	Maximum iteration number	Learning rate η	Training error
10	1000	0.0002	1e-3

TABLE 2 | The class center and network loss.

	Class center	Network loss
Class 1	0.3713	0.0070
Class 2	0.6146	0.0060
Class 3	0.8436	0.0080
Class 4	1.0962	0.0040
Class 5	1.3752	0.0010
Class 6	1.7671	0.0050

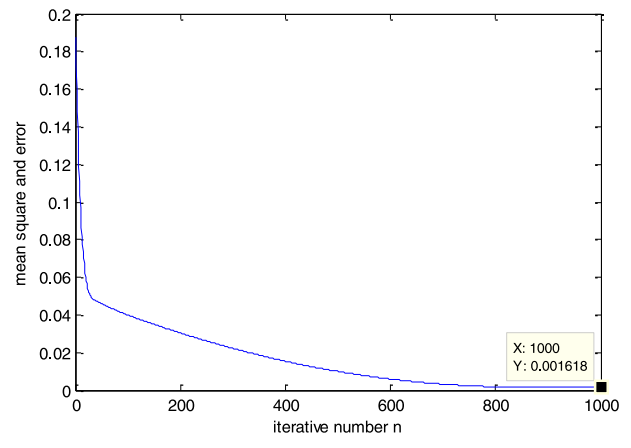

FIGURE 6 | | The modified BP neural network training error during iteration.

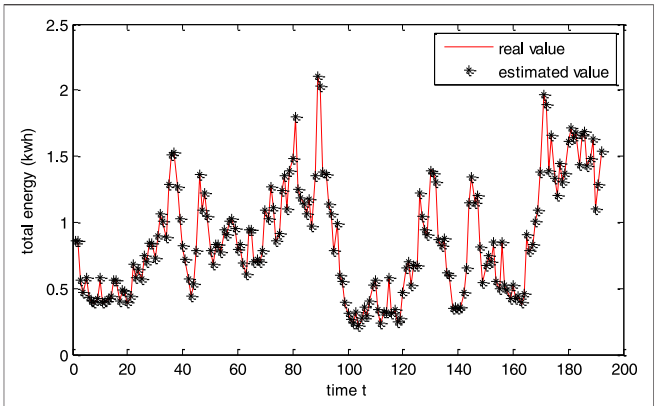

FIGURE 7 | The data from the master meter and the predicted value by the proposed method.

$$\boldsymbol{x} = \begin{pmatrix} r_1 & r_2 & \cdots & r_m \end{pmatrix}^T \tag{16}$$

$$\omega = \begin{pmatrix} \omega_{1,1} & \omega_{1,2} & \cdots & \omega_{1,k} \\ \omega_{2,1} & \omega_{2,2} & \cdots & \omega_{2,k} \\ \vdots & \vdots & \vdots & \vdots \\ \omega_{m,1} & \omega_{m,2} & \cdots & \omega_{m,k} \end{pmatrix} \tag{17}$$

where k is the number of hidden-layer neurons and m is the number of input.

(2) Structure for BP neural network

The BP neural network with one hidden layer in an engineering application usually has better approximation performance, and the number of neurons in the hidden layer plays a role in fitting the output value. Here, the empirical formula is adopted (Erik et al., 2018), which is expressed as

$$l = ceil\left(\sqrt{n+k} + a\right) \tag{18}$$

where n is the number of neurons in the input layer, k is the number of neurons in the output layer, a is a constant selected from the range [1, 10], and ceil (.) is the top integral function.

(3) Activation function for BP neural network

In this article, **Eq. 1** belongs to the multivariate linear model. Thus, the activation functions S_1 and S_2 are set as the linear model:

$$S(z) = z \tag{19}$$

The output can be then written as

$$\boldsymbol{y} = \boldsymbol{v}^T\left(\boldsymbol{\omega}^T\boldsymbol{x} + \boldsymbol{b}_1\right) + \boldsymbol{b}_2 \tag{20}$$

Thus, the correction coefficient ξ_i can be finally determined by $\boldsymbol{\omega}$ and $\boldsymbol{v}$.

(4) Iterative step length for the BP neural network

TABLE 3 | The parameter results from the proposed modified BP neural network.

Layer	Parameter	Value
Input layer to hidden layer	$\boldsymbol{\omega} = [\omega_1, \omega_2, \omega_3, \omega_4, \omega_5, \omega_6]$	(1.0100, 1.1763,1.0071, 1.0075, 1.0053, 1.0019)
	b_1	−0.0128
Hidden layer to output layer	$v = [v_1]$	1.0035
	b_2	0.0095

TABLE 4 | Measurement error estimation.

$1/\xi_1$	$1/\xi_2$	$1/\xi_3$	$1/\xi_4$	$1/\xi_5$	$1/\xi_6$
0.9936	0.8532	0.9964	0.9960	0.9982	1.0016

TABLE 5 | Comparison results.

	Least-squares method	Proposed BP without k-means method
$1/\xi_1$	0.9907	0.9972
$1/\xi_2$	0.8606	0.8550
$1/\xi_3$	0.9915	1.0008
$1/\xi_4$	0.9903	1.0000
$1/\xi_5$	0.9979	0.9984
$1/\xi_6$	0.9959	0.9984

TABLE 6 | Running time.

Method	Time/s
Least-squares method	0.0352
Proposed BP without k-means method	0.1768
Proposed BP with original parameter updated	0.2268
Proposed method	0.1834

Consider the fact that ξ_i is related to the weights that do not change frequently with time in the mathematical model. Thus, let the correction coefficients ξ_i of smart meters be unchanged over time. The updating procedure of parameters can be simplified as

$$\begin{aligned} \boldsymbol{\omega}^{(k)} &= \boldsymbol{\omega}^{(k-1)} - \eta sign\left(\frac{\partial E}{\partial \boldsymbol{\omega}}\right) \\ \boldsymbol{b}_1^{(k)} &= \boldsymbol{b}_1^{(k-1)} - \eta sign\left(\frac{\partial E}{\partial \boldsymbol{b}_1}\right) \end{aligned} \tag{21}$$

where *sign* is a symbolic function and expressed as

$$sign(z) = \begin{cases} -1 & z < 0 \\ 1 & z \geq 0 \end{cases} \tag{22}$$

4 TEST RESULTS AND DISCUSSION

To verify the effectiveness of the proposed method, experiments were carried out in a laboratory. In this case, seven smart meters were installed. One of them was taken as a master meter and the others as sub-meters. In the sub-meters, sub-meter 2 was set with a 15% measurement error for the test, and the remaining measurement accuracy was 0.5 s level. The whole experimental test period was 2 days, and energy consumption data were recorded every 15 min. A total of 192 measuring points were recorded, as shown in **Figure 4** and **Figure 5**. In the test, k was set as 6 in the k-means clustering; the weight $\boldsymbol{\omega}$ of the modified BP neural network was initialized as the full $\mathbf{1}_{m \times k}$ matrix, and other parameters are shown in **Table 1**. Experiments were performed by using MATLAB 2021A on a computer with Intel(R) Core(TM) 2 Duo 2.1 GHz i7 CPU 16G RAM, and Windows 64bit operation system.

Table 2 illustrates the class centers computed by k-means clustering. It can be seen that the network loss in each class is very small. This phenomenon occurred because it only had small loads such as lighting among the master meter and the sub-meters, and the master meter was not far away from the sub-meters in the test environment.

Figure 6 illustrates the error during the proposed modified BP neural network training. It can be seen that the error decreases as the number of iterations increases. After 50 iterations, the error tends to be 0.05, and the final predicted value of the proposed BP model is basically close to the actual value, as shown in **Figure 7**. Thus, it will fit the mathematical model in **Eq. 1**. The parameter of the proposed BP neural network is listed in **Table 3**.

Since the BP neural network is modified as linear mapping as in **Eq. 20**, the proportional coefficient ξ_i can be obtained from $\boldsymbol{\omega}$ and $\boldsymbol{v}$, where $\xi_i = \boldsymbol{v}^T \boldsymbol{\omega_i}^T$. Thus, the measurement accuracy of each sub-meter can be then solved by $1/\xi_i$, $i = 1, 2, \ldots, 6$, as shown in **Table 4**. It can be seen that the value of $1/\xi_2$ is 0.8532. Thus, the measurement error is 0.1468, which is close to the 15% measurement error in sub-meter 2. This demonstrates that our model can effectively detect the measurement error.

Alternatively, to demonstrate the performance of the proposed method in estimating the measurement error, a comparison with the least-squares method was carried out. The results are shown in **Table 5**. It can be seen that the result value $1/\xi_2$ from the least-squares method is 0.8606. Thus, the measurement error is 0.1394, which is a larger offset than the 15% measurement error. Generally, the least-squares method only pursues the minimum error of least-squares equations, regardless of the network loss. Nevertheless, our method uses the k-means clustering method to classify the data, which can eliminate the influence of the unknown network loss during the calculation of the correction coefficient ξ_i. To demonstrate this point, the result of the modified BP neural network without the k-means clustering method is listed, as seen in **Table 5**. It can further

demonstrate the desired performance of the proposed method in detecting the measurement error.

Table 6 illustrates the running time of the above methods. It can be seen that the proposed method costs more CPU time than that of the least-squares method. Nevertheless, to obtain a better parameter, the proposed model utilizes k-means clustering and a modified BP neural network. Generally, it has the same level of running time. However, the original strategy for parameter updating takes a bit more time than the proposed method. This demonstrates the usefulness of the modified strategy.

5 CONCLUSION

In this article, a remote error estimation method is proposed which is based on a modified BP neural network. The method takes the distributed smart electricity meter as the research object and builds the mathematical model inherent in the correction coefficient that is hidden by the energy from the smart meter and the master meter in the system. A classic k-means clustering is applied to classify the data, allowing the model to be simplified during the calculation of parameters. The BP neural network is then optimized to solve the parameter by modifying the activation function and the update rule of the neural network parameter. The experiments show that the desired performance can be obtained by our model. In the near future, the proposed method will be applied to the actual application, and the remote experiment platform will be set up as well.

DATA AVAILABILITY STATEMENT

The raw data supporting the conclusion of this article will be made available by the authors, without undue reservation.

AUTHOR CONTRIBUTIONS

TX provided the idea of work, SX implemented the idea by MATLAB, DL organized the framework of this manuscript, DM set up the experiment platform, ML collected the experiment data, and CL conducted the calculation and proof.

FUNDING

This work is supported by Science and technology project of State Grid Hubei Electric Power Co., Ltd (52154320000P).

REFERENCES

Alonso, A. M., Nogales, F. J., and Ruiz, C. (2020). "Hierarchical Clustering for Smart Meter Electricity Loads Based on Quantile Autocovariances," *IEEE Trans. Smart Grid*, 11(5). 4522–4530. doi:10.1109/tsg.2020.2991316

Chao, S., Zhensheng, L., Jinlei, H., Zhenxing, K., and Zheng, W. (2018). "Line Loss Calculation in Power Distribution Network Based on Power Measurement Data and BP Neural Network," in International Conference on Power System Technology, Guangzhou, China, 6-8 Nov. 2018, 4107–4112. doi:10.1109/powercon.2018.8601813

Donahue, S. T., Storm, C. L., Wetz, D. A., and Lee, W.-J. (2014). Study of the Effects of Smart Meter RF Transmissions on GFCI Outlets. *IEEE Trans. Electromagn. Compat.* 56 (6), 1361–1369. doi:10.1109/temc.2014.2354016

Dong, X., Li, Z., Dai, Y., Wang, Q., Zhang, Z., Wang, P., et al. (2018). "Research on Error Verification of Harmonic Smart Electricity Meter", in 3rd International Conference on Mechanical, Control and Computer Engineering(ICMCCE), Huhhot,China, 2018 sep14-16. 286–290. doi:10.1109/icmcce.2018.00065

Erik, C., Luis, E., and Deniel, Z. (2018). A Selection Method for Evolutionary Algorithms Based on the Golden Section. *Expert Syst. Appl.* 106, 183–196. doi:10.1016/j.eswa.2018.03.064

Gao, Y., Foggo, B., and Yu, N. (2019). A Physically Inspired Data-Driven Model for Electricity Theft Detection with Smart Meter Data. *IEEE Trans. Ind. Inf.* 15 (9), 5076–5088. doi:10.1109/tii.2019.2898171

Hao, X., Song, J., Pei, T., Zhang, C., Li, Y., and Zhou, Z. (2020). Application of FCM and Neural Network in Power Load Data Correction. *Transducer Microsyst. Technol.* 39 (4), 152–155. doi:10.13873/J.1000-9787(2020)04-0152-04

Kashef, H., Mahmoud, K., and Abdel-Nasser, M. (2018). "Power Loss Estimation in Smart Grids Using a Neural Network Model," in International Conference on Innovative Trends in Computer Engineering, Aswan, Egypt, 19-21 Feb. 2018, 258–263. doi:10.1109/itce.2018.8316635

Kashef, H., Mahmoud, K., and Abdel-Nasser, M. (2018). Power Loss Estimation in Smart Grids Using a Neural Network Model. *Proc. Int. Conf. Innov.Trends Comput.Eng.* 1. 258–263. doi:10.1109/itce.2018.8316635

Kong, X., Zhang, X., Li, G., Dong, D., and Li, Y. (2020). An Estimation Method of Smart Meter Errors Based on DREM and DRLS. *Energy* 204, 117774. doi:10.1016/j.energy.2020.117774

Kong, X., Zhang, X., Lu, N., Ma, Y., and Li, Y. (2021). Online Smart Meter Measurement Error Estimation Based on EKF and LMRLS Method. *IEEE Trans. Smart Grid* 12 (5), 4269–4279. doi:10.1109/tsg.2021.3077693

Liu, X., Zhu, P., Zhang, Y., and Chen, K. (2015). A Collaborative Intrusion Detection Mechanism against False Data Injection Attack in Advanced Metering Infrastructure. *IEEE Trans. Smart Grid* 6 (5), 2435–2443. doi:10.1109/tsg.2015.2418280

Luan, W., Peng, J., Maras, M., Lo, J., and Harapnuk, B. (2015). Smart Meter Data Analytics for Distribution Network Connectivity Verification. *IEEE Trans. Smart Grid* 6 (4), 1964–1971. doi:10.1109/tsg.2015.2421304

Ruan, J., Jiang, H., Li, X., Shi, Y., Chan, F. T. S., and Rao, W. (2019). A Granular GA-SVM Predictor for Big Data in Agricultural Cyber-Physical Systems. *IEEE Trans. Ind. Inf.* 15 (12), 6510–6521. doi:10.1109/tii.2019.2914158

Steiner, R., Farrell, M., Edwards, S., Ford, J., and Nelson, T. (2018). "ANIST Testbed for Examining the Accuracy of Smart Meters Under High Harmonic Waveform Loads," in Conference on Precision Electromagnetic Measurements, Prance,France, 8-13 July2018, 1–2. doi:10.1109/cpem.2018.8501026

Sun, Q., Li, H., Ma, Z., Wang, C., Campillo, J., Zhang, Q., et al. (2016). A Comprehensive Review of Smart Energy Meters in Intelligent Energy Networks. *IEEE Internet Things J.* 3 (4), 464–479. doi:10.1109/jiot.2015.2512325

Wang, Y., Chen, Q., Hong, T., and Kang, C. (2019). Review of Smart Meter Data Analytics: Applications, Methodologies, and Challenges. *IEEE Trans. Smart Grid* 10 (3), 3125–3148. doi:10.1109/tsg.2018.2818167

Wang, X., Wang, J., Yuan, R., and Jiang, Z. (2019). Dynamic Error Testing Method of Electricity Meters by a Pseudo Random Distorted Test Signal. *Appl. Energy* 249, 67–78. doi:10.1016/j.apenergy.2019.04.054

Xia, X., Xiao, Y., and Liang, W. (2019). ABSI: An Adaptive Binary Splitting Algorithm for Malicious Meter Inspection in Smart Grid. *IEEE Trans.Inform.Forensic Secur.* 14 (2), 445–458. doi:10.1109/tifs.2018.2854703

Zhang, Z., Gong, H., Li, C., Wang, Z., and Xiang, X. (2018). Research on Estimating Method for the Smart Electric Energy Meter's Error Based on Parameter Degradation Model. *IOP Conf. Ser. Mat. Sci. Eng.* 366, 012065. doi:10.1088/1757-899x/366/1/012065

Zhou, X., Hu, Y., Liang, W., Ma, J., and Jin, Q. (2021). Variational LSTM Enhanced Anomaly Detection for Industrial Big Data. *IEEE Trans. Ind. Inf.* 17 (5), 3469–3477. doi:10.1109/tii.2020.3022432

Conflict of Interest: Authors TX, SX, DL, DM, ML, and CL are employed by the Marketing Service Center of State Grid Hubei Electric Power Co., Ltd.

frontiers | Frontiers in Energy Research

ORIGINAL RESEARCH
published: 12 July 2022
doi: 10.3389/fenrg.2022.930093

A Deep Learning Approach to the Transformer Life Prediction Considering Diverse Aging Factors

Lanfei He[1], Lie Li[2], Ma Li[1], Zhiwei Li[1] and Xiao Wang[2]*

[1]State Grid Hubei Electric Power Co.,Ltd., Economic and Technological Research Institute, Wuhan, China, [2]School of Electrical Engineering and Automation, Wuhan University, Wuhan, China

The reliability of a high-capacity power transformer is fundamental to the stable operation of power systems. However, characterization of the transformer aging process is a difficult task, considering the diverse aging factors in its life cycle. This prevents effective management of such equipment. In the work, we study the aging phenomenon of power system transformers, whose representative degeneration variables are extracted from real transformer operational data. Combining with the average life of the equipment, the extracted features are used as indicators for the transformer reliability evaluations. We developed a deep learning–based approach using a convolutional neural network for effective equipment life prediction. The performance of the transformer life prediction model is verified using field-test data, which demonstrates the superior accuracy of the presented approach.

Keywords: Transformer, life differentiation phenomenon, life prediction, convolutional neural network, aging factors

OPEN ACCESS

Edited by:
Yushuai Li,
University of Oslo, Norway

Reviewed by:
Yin Yao,
Shanghai University of Electric Power, China
Yuan Chen,
Anhui University, China
Hengrui Ma,
Qinghai University, China
Tongmao Zhang,
The University of Manchester, United Kingdom, in collaboration with reviewer HM

****Correspondence:***
Lie Li
lilie@whu.edu.cn

Specialty section:
This article was submitted to Smart Grids, a section of the journal Frontiers in Energy Research

Received: *27 April 2022*
Accepted: *31 May 2022*
Published: *12 July 2022*

Citation:
He L, Li L, Li M, Li Z and Wang X (2022) A Deep Learning Approach to the Transformer Life Prediction Considering Diverse Aging Factors. Front. Energy Res. 10:930093. doi: 10.3389/fenrg.2022.930093

INTRODUCTION

The model power system quickly evolved with the accelerated marketization incentives. In this process, the safety and reliability of the power system became important concerns to be addressed. With the narrower profit margin, the system operators face multiple challenges: ensuring safety, reducing electricity prices, and increasing efficiency. In recent years, the system operator of China, State Grid, has found a relatively low age among scrapped samples and a relatively high proportion of over-aged samples among the transformer equipment. The problems are as follows: First, the scrapping age of substation equipment is usually 6–10 years, and the average service life of main equipment is lower than the transformer depreciation period and the pricing depreciation period. To a certain extent, this will result in a waste of depreciation costs. It is difficult to fully incorporate into the cost of transmission and distribution prices. Second, the over-aged transformers have accounted for 10% of the original value of the physical assets of the power grid. Some of the over-aged transformers can still operate normally. Under strict supervision and examination requirements, the over-aged transformers cannot be depreciated, which reduces the electricity price level and the company's investment capacity.

Reliability is an important indicator for verifying the safe operation of equipment (Song and Cheng, 2015). It refers to the ability or possibility of equipment to perform specified functions without failure within a certain period and under certain conditions (Song, 2001). Overall, the operating life of primary equipment in the power grid is significantly different, and this difference increases the difficulty of primary equipment reliability assessment and reasonable life estimation. Particularly in the field of reasonable life prediction of transformers, this difference in phenomena is rarely studied in current research.

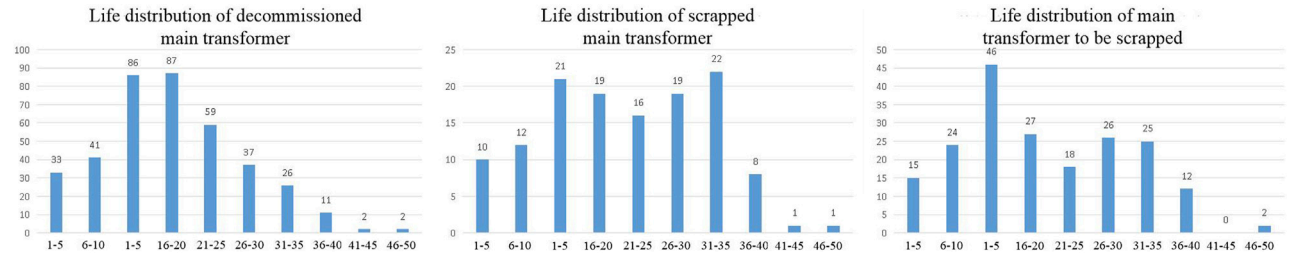

FIGURE 1 | Life distribution.

Transformers are the current representative of large-power equipment, which include multiple failure forms such as discharge, overheating, or both (Castro and Miranda, 2005; Jongen et al., 2007; Zheng et al., 2012; Fox et al., 2019). The reasonable life estimation of the transformer also belongs to the category of fault prediction. The main method is to predict the possible future failures through the historical data obtained by monitoring and to ascertain the remaining life. At present, transformer life prediction models can be divided into physical failure mechanism models and data-driven models (Abu-Elanien and Salama, 2012; Zhou, 2013; Ignacio et al., 2018; Zhang et al., 2018). The physical failure mechanism model is based on the transformer failure mechanism and mathematically characterizes the material failure process. Chen and Liu (2020) proposed a transformer life prediction model based on the hidden Markov model. Shi et al. (2020) established the Arrhenius equation based on the degradation mechanism of variable activation energy and then predicted the remaining life of the transformer. Based on the data-driven life model, the operating parameters that can characterize the degree of transformer degradation are obtained mainly based on the monitoring technology, and the operating trend of the parameters is directly predicted (Hu et al., 2022). Common operating parameters include vibration signal, noise signal, and insulating oil content (Bacha et al., 2012; Ma et al., 2013; Tian et al., 2013; Guo et al., 2017; Yan et al., 2020). This method does not involve a specific failure mechanism, so it has a wider scope including the long-short-term memory network–based life prediction model (Dai et al., 2021), the life prediction model based on the SVM algorithm with RBF as the kernel function, etc. (Wang, 2021).

However, both the physical failure mechanism model and the data-driven model are based on the specific operating conditions of the transformer, that is, monitoring the parameter distribution of the equipment in the time series and space series and predicting the life through the model (Ishak, 2010; Husnayain et al., 2016; Qian et al., 2018). However, the model established based on the aforementioned method has some limitations because the parameters are derived from a single device, so the application object is also limited to a specific type of device. State Grid's transformers have the characteristics of a large number of equipments, wide distribution, and complex sources. It is difficult to use traditional methods to evaluate the life of all equipment.

TABLE 1 | Corresponding parameters of equipment with rated capacity.

Rated capacity	α	β	E	x_h	x_l
1	36.15	4.324	32.91	40%	40%
1.6	18.73	1.995	16.60	0	17%
1.8	29.64	4.504	27.05	0	0
2	22.56	2.218	19.98	0	0
2.5	25.94	2.516	23.02	15%	0

Based on a convolutional neural network, this article proposes a transformer life prediction method considering the difference in transformer life. First, according to the factory information and scrap age information of scrapped transformers provided by a company, four types of data of rated capacity, voltage level, manufacturer, and workplace are screened out. The characteristics of its life distribution are analyzed, respectively, and data of average life, life concentration, and the proportion of high-life equipment and low-life equipment were obtained. The aforementioned total of 16 data were taken as input, and the transformer age was taken as output. The convolutional neural network was trained to obtain the life prediction model. Compared with the traditional life prediction model, the advantages of the model proposed in this article are 1) considering the influence of the life difference phenomenon on the reliability of the transformer, the prediction accuracy is improved; 2) since the input is the equipment delivery and operation information and does not involve the specific operation conditions, the life prediction can be carried out before operation, and the operation and maintenance strategy can be formulated as soon as possible according to the prediction results.

LIFE DIFFERENCE PHENOMENON

Statistical statistics are carried out on the decommissioned, scrapped, and to-be-scrapped transformers of a power supply company, and a statistical graph is drawn, as shown in **Figure 1**. It can be found that the life distribution of the transformer is close to the normal distribution. Most of the equipment life is in the middle interval, and there are few high-life equipment and low-life equipment. However, this phenomenon increases the difficulty of equipment operation and maintenance. For possible low-life equipment, it should be the focus of attention

TABLE 2 | Corresponding parameters of equipment at each voltage level.

Voltage level	α	β	E	x_h	x_l
6kV	31.68	2.516	28.11	29%	12%
10kV	20.75	2.116	18.38	3%	24%
35kV	23.46	2.598	20.84	6%	19%
110kV	26.15	3.428	23.50	4%	14%
220kV	35.18	3.245	31.53	33%	0

TABLE 3 | Corresponding parameters of equipment of each manufacturer.

	α	β	E	x_h	x_l
A company	13.94	5.457	12.86	0	33%
B company	25.45	1.807	22.63	25%	0
C company	28.73	4.241	26.13	7%	7%
D company	27.83	4.59	25.43	0	0
E company	27.13	2.668	24.12	17%	0

TABLE 4 | Corresponding parameters of equipment of all affiliated companies.

	α	β	E	x_h	x_l
A power supply company	18.84	1.817	16.75	3%	31%
B power supply company	19.02	1.799	16.91	5%	21%
C power supply company	25.38	2.099	22.48	0	17%
D power supply company	19.84	1.921	17.60	6%	29%
E power supply company	15.71	1.518	14.16	0	31%

and is necessary to increase the frequency of maintenance, timely maintenance, and improve equipment reliability. For possible long-life equipment, appropriate attention can be reduced to save costs, analyzing the life distribution chart; dividing the equipment into older equipment, normal equipment, and younger equipment according to the distribution law of equipment life; and counting their proportions in the total equipment respectively; and summarizing the distribution law of equipment life. The equipment is divided into 5-year intervals. With the increase in service life, the service life in this interval increases first and then decreases; The pieces of equipment with a service life of 11–15 years are more than twice that of 6–10 years, and the increase is significantly greater than that in other ranges. The pieces of equipment with a service life of 36–40 years are less than 1/2 of that of 31–35 years, and the decrease is significantly greater than that in other intervals. Therefore, equipment with a service life of 10 years or less (main transformer and disconnector) is defined as low-life equipment, equipment with a service life of 36 years or more is defined as high-life equipment, and other equipment is defined as normal equipment.

When the equipment is put into operation, it is necessary to evaluate the reliability of the equipment to facilitate the formulation of the operation and maintenance strategy. Due to the lack of operational data as the basis for evaluation, the equipment can only be roughly evaluated through historical data, such as manufacturer and operation city before the equipment is put into operation. Due to different production processes, equipment produced by different manufacturers will also have different characteristics in reliability. Similarly, different operating cities will have different working environments, which will further affect the reliability of the equipment. The extraction of reliable data from this kind of text information is key to the reliable evaluation of equipment before operation.

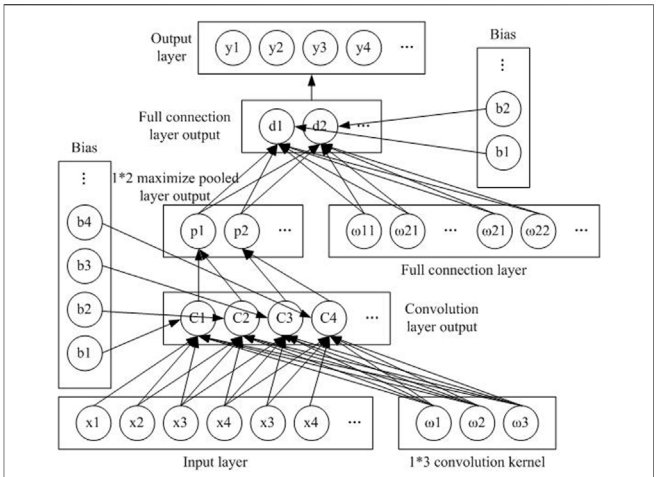

FIGURE 2 | Convolutional neural network.

EXTRACTION OF TRANSFORMER AGING FACTORS

In the transformer operation and maintenance data, the average life is the most intuitive embodiment of equipment reliability, and it is also important data that can be used for life prediction. However, the data on average life cannot reflect the impact of life differentiation. Therefore, it is necessary to extract the aging factors that can reflect the phenomenon of life differentiation from the transformer life distribution data to improve the accuracy of reasonable life prediction.

The life differentiation characteristics of equipment can be described by three parameters: life concentration, the proportion of high-life equipment, and low-life equipment. Life concentration indicates the concentration degree of transformer life distribution. The more the proportion of main transformers is close to the average life, the higher the life concentration. The proportion of high life and low life is the proportion of transformers with a life of more than 35 years and less than 10 years in the total number, which can be obtained directly through statistics.

Because the Weibull distribution can be used to describe the characteristics of equipment life distribution, life concentration and average life can be expressed by the relevant characteristics of the Weibull distribution (Zhou et al., 2013). The Weibull distribution was proposed by Swedish physicist W. Weibull in 1939. It is mainly used to describe the probability distribution of material fatigue strength. The Weibull distribution is widely used in reliability engineering, especially in the distribution form of cumulative wear failure of electromechanical products. Due to the

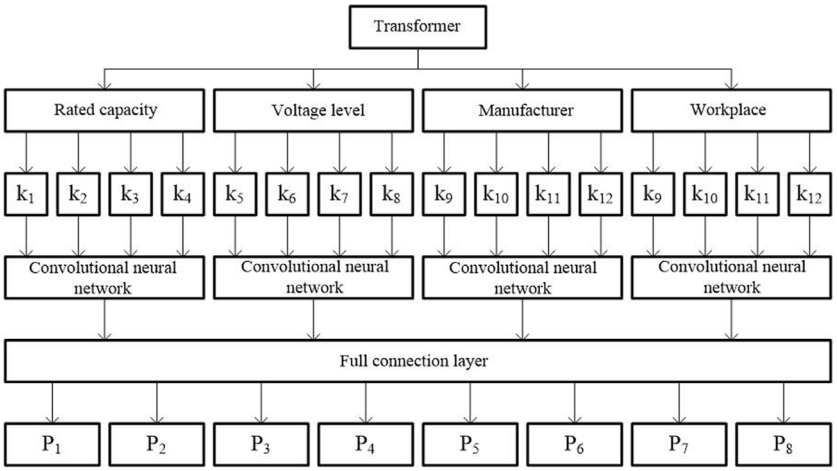

FIGURE 3 | Life prediction model.

TABLE 5 | Life prediction model parameters.

Network layer	Parameters	Parameters	Parameters	Parameters
Input layer	1*4	1∗4	1∗4	1∗4
Convolution layer (Relu)	64-[1∗2]	64-[1∗2]	64-[1∗2]	64-[1∗2]
Convolution layer (Relu)	64-[1∗2]	64-[1∗2]	64-[1∗2]	64-[1∗2]
Convolution layer (Relu)	128-[1∗2]	128-[1∗2]	128-[1∗2]	128-[1∗2]
Flatten layer				
Full connection layer (Tanh)		128		
Full connection layer (Tanh)		128		
Classification layer (Softmax)		8		

ease of inferring the distribution parameters using the probability value, it is widely used in the data processing of various life tests. The probability density of the Weibull distribution is shown in Eq. **(1)**.

$$f(t) = \frac{\beta}{\alpha}\left(\frac{t}{\alpha}\right)^{\beta-1} e^{-\left(\frac{t}{\alpha}\right)^{\beta}}, \tag{1}$$

where α is the scale parameter and β is the shape parameter. According to the properties of the Weibull distribution, the shape parameter β is related to the concentration of life distribution. The larger the β, the more concentrated the life distribution. The smaller the β, the more dispersed the life distribution. The average life of the equipment can be expressed by mathematical expectations. Therefore, the average life of the equipment can be calculated according to the parameters of the Weibull distribution and the service life expectation, as shown in **Eq. (2)**.

$$E = \alpha \cdot \Gamma\left(1 + \frac{1}{\beta}\right). \tag{2}$$

The fitting method of the Weibull distribution characteristic parameters is as follows:

1) The service lives of n different equipment with the same feature were arranged from short to long, which are $N_1, N_2, \ldots, N_n$, respectively;
2) **Eq. (3)** was used to calculate the unbiased estimation of fatigue cumulative distribution F;

$$F = \frac{i-0.3}{n+0.4}. \tag{3}$$

3) **Eq. (4)** was fitted to obtain an unbiased estimation of α, β.

$$\ln(1-F) = -\left(\frac{N}{\alpha}\right)^{\beta}. \tag{4}$$

Now, the reliability information such as the rated capacitance, voltage grade, manufacturer and affiliated company of the main transformer, and the corresponding proportional parameters are counted, respectively; scale parameter, α; shape parameter, β; the average life (mathematical expectation), E; proportion of high-life equipment, x_h; and proportion of low-life equipment, x_i are shown in **Tables 1–4**:

Next, according to the aforementioned data and combined with the life distribution of equipment, a reasonable life prediction model of transformers based on a convolutional neural network is established.

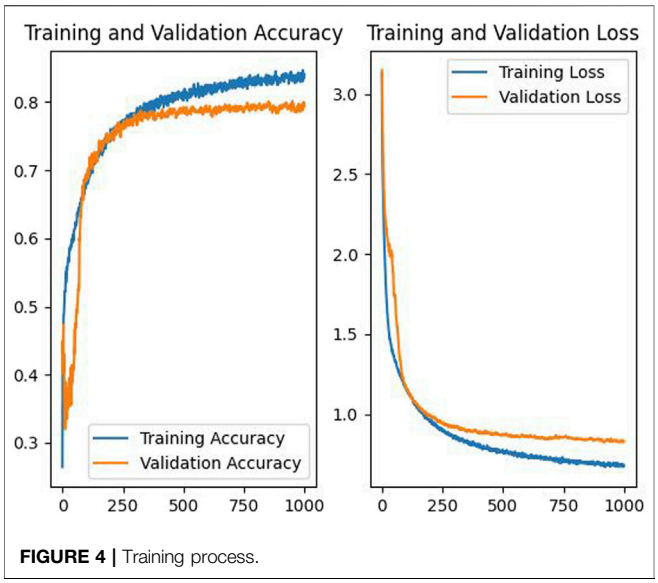

FIGURE 4 | Training process.

AI-BASED APPROACH TO THE LIFE PREDICTION MODEL

Convolutional Neural Network

In recent years, with the rapid development of the computer field, deep learning has been applied to all aspects. The convolutional neural network possesses a considerable ability for face recognition and image recognition and has great application prospects in the field of transformer fault diagnosis. In this article, a reasonable life prediction model of a transformer is constructed based on a convolutional neural network. A convolutional neural network generally includes an input layer, convolution layer, pooling layer, full connection layer, and output layer (Zhou et al., 2017). Taking one-dimensional data as an example, its general structure is shown in **Figure 2**.

The input layer is the input data of some characteristic quantities, including rated capacity, voltage level, manufacturer, and workplace. These are transformed into digital features using the Weibull distribution as input, such as x_1, x_2, x_3, as shown in **Figure 2**.

The convolution layer is equivalent to a feature-extraction process. The important features are extracted through the convolution kernel during the movement of the input layer, as shown in **Figure 2**. Taking the 1*3 convolution kernel as an example, the calculation process is as follows:

$$c_n = x_n \times \omega_1 + x_{n+1} \times \omega_2 + x_{n+2} \times \omega_3 + b_n, \tag{5}$$

where x is input, ω is the weight, and b is the offset. The calculated results can use Relu, Tanh, and other activation functions as the output of each neuron in the convolution layer, that is, $C_n = f(cn)$. The expression of the activation function is as follows:

$$\text{Relu } f(x) = \max(0, x), \tag{6}$$

$$\text{Tanh } f(x) = \frac{e^x - e^{-x}}{e^x + e^{-x}}. \tag{7}$$

The pooling layer mainly reduces the amount of calculation in the neural network, as shown in **Figure 2**. Taking the 1*2 maximum pooling layer as an example, the calculation process is as follows:

$$p_n = \max(C_n, C_{n+1}). \tag{8}$$

The full connection layer is the neural network, as shown in **Figure 2**. Its calculation steps are as follows:

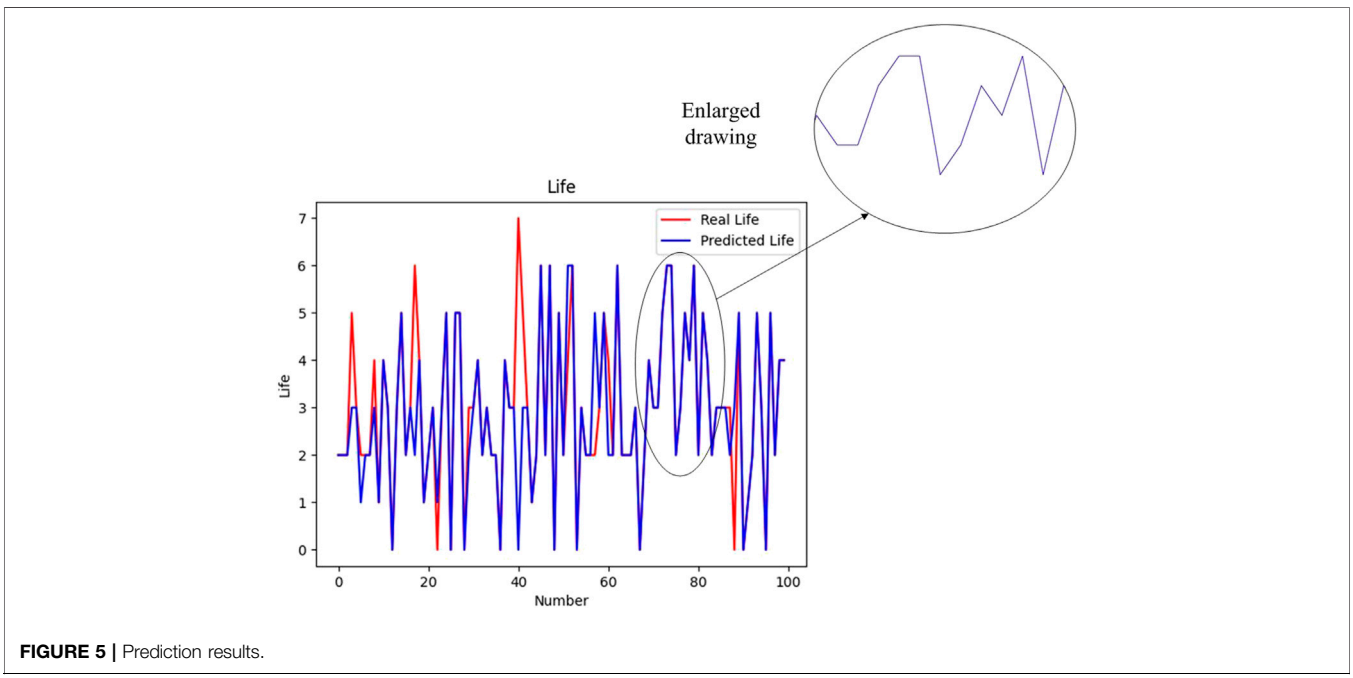

FIGURE 5 | Prediction results.

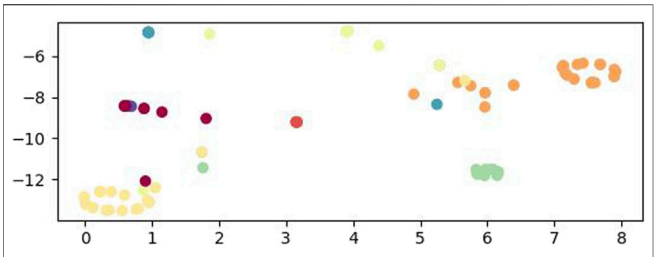

FIGURE 6 | TSNE visualization results.

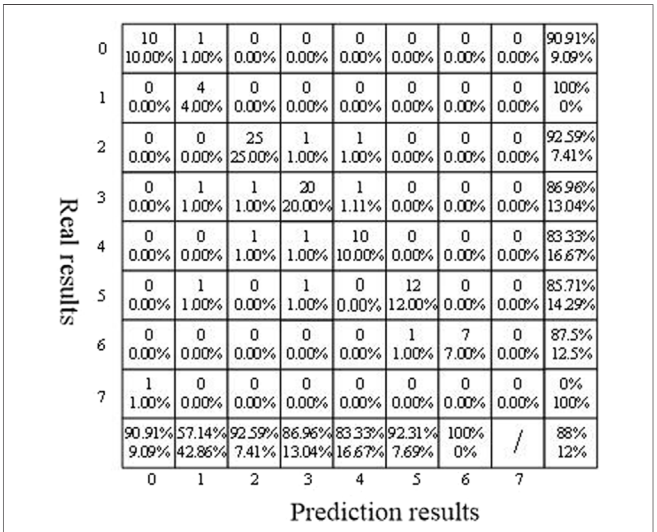

FIGURE 7 | Confusion matrix.

$$d_n = \sum_{m}^{1} p_m \times \omega_{\mathrm{mn}} + b_n. \tag{9}$$

Similarly, the calculated results can use Relu, Tanh, and other activation functions as the output of each neuron in the whole connection layer, that is, $D_n = f(d_n)$.

The calculation process of the output layer is the same as that of the full connection layer. As shown in **Eq. 9**, the Softmax function is used in the activation function, and the expression is as follows:

$$\mathrm{Softmax}\, f(x) = \frac{e_{xi}}{\sum_{i=0}^{n} e_{xi}}. \tag{10}$$

Life Prediction Model

The life prediction model is shown in **Figure 3**. First, the four characteristic quantities of voltage grade, rated capacity, manufacturer, and workplace are obtained using the Weibull distribution, and a total of 16 characteristics are used as the input layer of the model. The data output from the convolution layer is fused through the data, integrated into one-dimensional data, and sent to the fully connected neural network. The life prediction is divided into eight intervals. 1–5 years is the first interval, and the probability of the result falling into this interval is P1. 6–10 years is the second interval, and the probability of the result falling into this interval is P2, and so on. The last interval is 35–40 years, and the probability of the result falling into this interval is P8. The activation layer of the convolutional neural network adopts the Relu function, the fully connected neural network adopts the Tanh function, and the output layer adopts the Softmax function (see **Table 5** for specific parameters).

TABLE 6 | Comparison of different life prediction models.

Life prediction model	Accuracy (%)
Decision tree	65.4
Random forest	71.2
Support vector machine	62.6
Neural network	75.00
Convolutional neural network	84.83

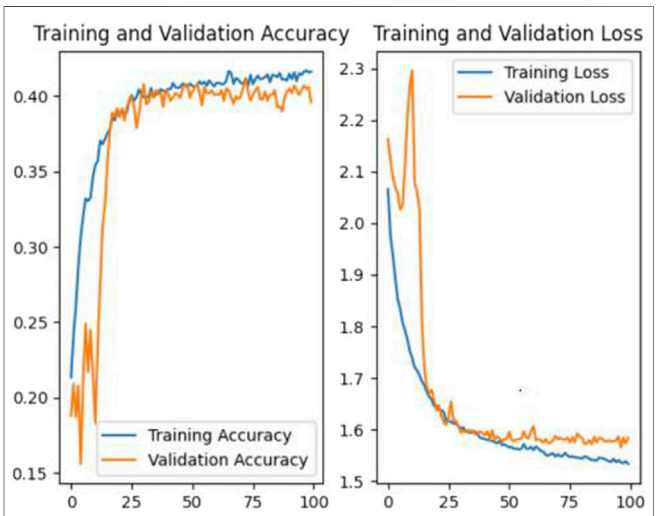

FIGURE 8 | Model training process without considering life difference.

ACCURACY VERIFICATION OF LIFE PREDICTION MODEL

Verification of AI-Based Approach to the Life Prediction Model

K-fold cross-validation is adopted for the data set. That is, the data set is divided into k copies, of which k-1 is used as training data and the remaining one is used as test data. There are 501 groups of transformer data in total. A total of 100 groups were considered test data and the rest as training data. The training process is shown in **Figure 4**.

The prediction results of the last 100 test data are shown in **Figure 5**. Through TSNE visualization, the classification results of 100 data types are displayed, as shown in **Figure 6**.

It can be seen from **Figure 5** that most of the prediction results are consistent. Each color in **Figure 6** represents a prediction interval. It can be seen that the graphs of each interval are well distinguished. It shows that the life prediction model has high accuracy, and the life prediction confusion matrix of each classification is shown in **Figure 7**.

The accuracy is low due to the small number of training and tests in the eighth division. The prediction accuracy of other life intervals is high, which is more than 80%.

Comparison With Other Models

To verify the superiority of the model in transformer life prediction, the model is compared with the following other models.

1) Prediction results of different models

To verify the ability of the convolutional neural network in life prediction, decision tree, random forests, support vector machine, neural network, and deep confidence network were used to simulate the same data. The simulation results are shown in **Table 6**.

It can be seen from **Table 6** that a convolutional neural network has higher prediction accuracy in transformer life prediction. Compared with the current common prediction algorithms, the accuracy is improved by more than 10%.

2) Influence of life differentiation on life prediction results

To verify the impact of life differentiation on life prediction results, only the average life in the data of rated capacity, voltage level, manufacturer, and the working city was considered. Four data of k_1, k_5, k_9, and k_{11} were used as the input of the convolutional neural network. The training results are shown in **Figure 8**.

According to the results, the prediction accuracy of the transformer life prediction model without considering the phenomenon of life differentiation can only reach 40.37%. Compared with the model proposed in this article, the accuracy was reduced by 52.41%. This is because more characteristic information was extracted from the transformer life distribution data, which improved the identification of the training data and thus improved the final accuracy.

CONCLUSION

Based on the statistics of the scrapped data of transformers provided by power supply companies, this article analyzes the impact of life differentiation on the reliability evaluation of transformers. According to this phenomenon, the information containing life-differentiation information is extracted from the data and used as the input of the life prediction model based on a convolutional neural network. Compared with other prediction algorithms, the superiority of the convolutional neural network in life prediction is verified. In comparison with the life prediction model without considering the phenomenon of life differentiation, it is verified that the life prediction model considering the phenomenon of life differentiation has higher prediction accuracy.

In the future, the transformer life prediction method based on an AI approach will become the mainstream in the industry. However, it still needs to overcome the dependence on the data sample size. The data source of this article was limited, and more aging factors were not considered, which need to be further improved.

DATA AVAILABILITY STATEMENT

The raw data supporting the conclusions of this article will be made available by the authors, without undue reservation.

AUTHOR CONTRIBUTIONS

LL—paper writing and submission; LH—data acquisition; ML—model building; ZL—data validation; and XW—proofreading.

REFERENCES

Abu-Elanien, A. E. B., and Salama, M. M. A. (2012). A Monte Carlo Approach for Calculating the Thermal Lifetime of Transformer Insulation. *Int. J. Electr. Power and Energy Syst.* 43 (1), 481–487. doi:10.1016/j.ijepes.2012.06.054

Bacha, K., Souahlia, S., and Gossa, M. (2012). Power Transformer Fault Diagnosis Based on Dissolved Gas Analysis by Support Vector Machine. *Electr. Power Syst. Res.* 83 (1), 73–79. doi:10.1016/j.epsr.2011.09.012

Castro, A. R. G., and Miranda, V. (2005). Knowledge Discovery in Neural Networks with Application to Transformer Failure Diagnosis. *IEEE Trans. Power Syst.* 20 (2), 717–724. doi:10.1109/tpwrs.2005.846074

Chen, C., and Liu, Y. (2020). Remaining Useful Life Analysis of Transformer Based on Hidden Markov Model. *J. Shenyang Univ. Technol.* 42 (4), 5. doi:10.7688/j.issn.1000-1646.2020.04.10

Dai, M., Tang, H., and Xu, K. (2021). A Prediction Method of Residual Life of Railway Transformer Based on Long-Term and Short-Term Memory Network. *Sci. Technol. Innovation* (28), 17–19. doi:10.3969/j.issn.1673-1328.2021.28.007

Fox, J. C., Hadidi, R., Laflair, N., Leonard, J., and Hodges, J. (2019). Heat Generation and Failure in Padmount Transformers Due to Zero Sequence Saturation. *IEEE Trans. Ind. Appl.* 55 (5), 4500–4506. doi:10.1109/tia.2019.2928252

Guo, Y., Wang, Z. K., and Liu, L. (2017). Failure Mechanism Analysis and Preventive Measures of High Voltage Sleeve Head Seal of 500kV Main Transformer. *J. Anhui Electr. Eng. \ Tech. Coll* 22 (1), 38–41. doi:10.3969/j.issn.1672-9706.2017.01.007

Hu, B., Deng, X., and Jia, S. (2022). Transformer Life Estimation and State Assessment Based on ANFIS. *Electr. Meas. Instrum.* 59 (01), 61–68. doi:10.19753/j.issn1001-1390.2022.01.008

Husnayain, F., Latif, M., and Garniwa, I. (2016). Transformer Oil Lifetime Prediction Using the Arrhenius Law Based on Physical and Electrical Characteristics. International Conference on Quality in Research. IEEE. Lombok, Indonesia, 10-13 Aug. 2016.

Ignacio, A., Stephen, M. A., Brian, S., Brandon, L., Games, G. C., and Victoriya, M. C. (2018). Adaptive Power Transformer Lifetime Predictions through Machine Learning & Uncertainty Modelling in Nuclear Power Plants. *IEEE*

Trans. Industrial Electron. 66 (6), 4726–4737. doi:10.1109/TIE.2018.2860532

Ishak, T. M . (2010). Simulation Study on Influencing Parameters of Thermal Ageing for Transformer Lifetime Prediction. *Cheminform* 22 (18), 115–115. doi:10.1002/chin.199118115

Jongen, R., Morshuis, P., Smit, J., and Janssen, A. (2007). A Statistical Approach to Processing Power Transformer Failure Data. Cired 19th International Conference on Electricity DistributionCired 19th International Conference on Electricity Distribution.

Ma, H., Di, Z., Chen, K., Wang, C., Li, K., and Li, Y. (2013). A New Method of Winding Deformation Fault Diagnosis of Power Transformer Based on Vibration . *Automation Electr. Power Syst.* 37 (08), 89–95. doi:10.7500/AEPS201209202

Qian, Y. H., Xiao, H. Z., Nie, M. H., Zhao, Y.-H., Luo, Y.-B., and Gong, S.-L. (2018). Lifetime Prediction and Aging Behaviors of Nitrile Butadiene Rubber under Operating Environment of Transformer. *J. Electr. Eng. Technol.* 13 (2), 918–927. doi:10.19487/j.cnki.1001-8425.2017.11.006

Shi, J., Zhao, D., Hao, W., and Wang, X. (2020). Life Evaluation Model for Transformer Insulating Paper Based on Variable Activation Energy. *Insul. Mater.* 53 (09), 52–57. doi:10.16790/j.cnki.1009-9239.im.2020.09.009

Song, Z., and Cheng, L. (2015). Operation Reliability Analysis of Primary Equipment in UHV DC. *Electr. Eng.* (06), 110–112+118. doi:10.3969/j.issn.1673-3800.2015.06.025

Song, Z. (2001). Discussion on Failure and Fault Interpretation. *China Termin.* 3 (3), 20–23. doi:10.3969/j.issn.1673-8578.2001.03.008

Tian, K., You, D. H., Li, Y. L., Pan, K., and Wang, K. (2013). Analysis of a Transformer Time-Varying Outage Model for Operational Risk Assessment. *Amr* 732-733, 993–998. doi:10.4028/www.scientific.net/amr.732-733.993

Wang, H. (2021). Research on Life Loss of Transformer Based on Machine Learning Algorithms. *Electrotech. Appl.* 40 (01), 72–78. doi:10.3969/j/issn.1672-9560.2021.01.014

Yan, H., Zhang, Y., Zhao, J., and Yu, Z. (2020). An Oil-Paper Insulation Life Prediction Model Based on Dissolved Products Analysis in Oil. *Guangxi Electr. Power* 43 (04), 1–6+23. doi:10.16427/j.cnki.issn1671-8380.2020.04.001

Zhang, M., Liu, J., Chen, X., and Liao, L. (2018). Residual Life Assessment Method of Transformer Oil-Paper Insulation Aging Based on Wiener Modle. *Trans. China Electrotech. Soc.* 33 (21), 11. doi:10.19595/j.cnki.1000-6753.tces.171587

Zheng, Y., Sun, C., and Jian, Li. (2012). Association Rule Analysis on Confidence of Features for Transformer Faults. *High. Volt. Eng.* 38 (1), 7. doi:10.3969/j/issn.1003-6520.2012.01.012

Zhou, D., Chengrong, L. I., and Wang, Z. (2013). Comparison of Parameter Estimation Methods for Transformer Weibull Lifetime Modelling. *High. Volt. Eng.* 39 (5), 1170–1177. doi:10.3969/j.issn.1003-6520.2013.05.022

Zhou, D. (2013). Comparison of Two Popular Methods for Transformer Weibull Lifetime Modelling. *Int. J. Adv. Res. Electr. Electron. Instrum. Eng.* 2 (4).

Zhou, F., Jin, L., and Dong, J. (2017). Review of Convolutional Neural Network. *Chin. J. Comput.* 40 (06), 1229–1251. doi:10.11897/SP.J.1016.2017.01229

Conflict of Interest: Authors LH, ML, and ZL were employed by the State Grid Hubei Electric Power Co., Ltd.

The remaining authors declare that the research was conducted in the absence of any commercial or financial relationships that could be construed as a potential conflict of interest.

Publisher's Note: All claims expressed in this article are solely those of the authors and do not necessarily represent those of their affiliated organizations, or those of the publisher, the editors, and the reviewers. Any product that may be evaluated in this article, or claim that may be made by its manufacturer, is not guaranteed or endorsed by the publisher.

frontiers | Frontiers in Energy Research

ORIGINAL RESEARCH
published: 14 July 2022
doi: 10.3389/fenrg.2022.951192

Polymorphic Distributed Energy Management for Low-Carbon Port Microgrid With Carbon Capture and Carbon Storage Devices

Qihe Shan[1], *Jing Song*[1], *Qi Xu*[2]*, *Geyang Xiao*[2] *and Feifei Yu*[1]

[1]Navigation College, Dalian Maritime University, Dalian, China, [2]Research Institute of Intelligent Networks, Zhejiang Lab, Hangzhou, China

In order to reduce the carbon emission of the port and build a green port, a polymorphic distributed energy management method for the low carbon port microgrid with carbon capture and carbon storage device is proposed. Firstly, this paper presents a low carbon port microgrid in a polymorphic network environment to realize the information interaction among energy subjects in different modes and improve network communication performance among port power generation device, main grid, carbon capture and carbon storage device. Secondly, the energy management model of low-carbon port microgrid is constructed considering the additional carbon capture device and carbon storage device in the port. Then, based on the multi-agent consensus algorithm, a distributed energy management method is proposed, which is respectively oriented to the grid-connected operation mode, island operation mode and switching operation mode of the port microgrid, so as to achieve the economic, low carbon and reliable operation of the port microgrid. Finally, the simulation results of Matlab verify the effectiveness of the proposed method.

Keywords: energy management, polymorphic, carbon tax, distributed, port microgrid

OPEN ACCESS

Edited by:
Yushuai Li,
University of Oslo, Norway

Reviewed by:
Feng Tao,
Southwest Jiaotong University, China
Lingxiao Yang,
Anhui University, China
Weihang Yan,
National Renewable Energy Laboratory (DOE), United States

***Correspondence:**
Qi Xu
xuqi@zhejianglab.com

Specialty section:
This article was submitted to Smart Grids, a section of the journal Frontiers in Energy Research

Received: *23 May 2022*
Accepted: *21 June 2022*
Published: *14 July 2022*

Citation:
Shan Q, Song J, Xu Q, Xiao G and Yu F (2022) Polymorphic Distributed Energy Management for Low-Carbon Port Microgrid With Carbon Capture and Carbon Storage Devices. Front. Energy Res. 10:951192. doi: 10.3389/fenrg.2022.951192

1 INTRODUCTION

Under the accelerated development of the global economy, the demand for cargo transportation in international trade is growing. As the node of global maritime transport, ports are embracing new development opportunities. However, the large amount of carbon dioxide emitted by the port aggravates environmental pollution (Kinnon et al., 2021) and leads to global warming, which hinders the sustainable development of the port. At the same time, under the influence of IMO regulations and the urgent demand for carbon neutrality in the world (Wang et al., 2018), it is critical to reduce CO_2 emissions from ports and build a low carbon port microgrid.

With the transformation of port energy, utilizing new energy sources to supply power for ports has become an effective way to reduce port carbon emissions (Zhang et al., 2021). However, considering the instability and uncertainty of new energy sources (Li et al., 2021; Wang et al., 2022), it is still necessary to include conventional power plants in the port microgrid to ensure the reliability of the port power supply. Energy management of port microgrid is the key to ensure its reliable operation and has been studied by many experts and scholars. The energy management problem is a complex system optimization problem with the objective of maximizing the operating economy and satisfying multiple constraints for safe and stable operation (Deng et al., 2021; Zhang et al., 2022a).

To address the additional cost of specific types of load demand in ports, Kermani (Kermani et al., 2022) proposed an energy storage system that includes multiple energy storage devices to decline power peaks, reduce energy waste and ensure port economics. Kanellos (Gennitsaris and Kanellos, 2019) proposed a multi-agent based real-time load demand response system to limit port carbon emissions and minimize port operating costs to solve the problem of flexible loads and significant carbon emissions in ports. Most current energy management methods are classified as centralized or distributed algorithms (Yang et al., 2019; Yang et al., 1109; Huang et al., 2022), but for low carbon port microgrid that contains large scale clean energy, due to the distributed nature of its generation devices and loads, distributed algorithms have attracted widespread attention. To tackle the existence of multiple generation modes and load types in ports, Zhang (Zhang et al., 2020) proposed a novel distributed energy management approach for ports based on a multi-agent consensus algorithm to optimize port energy allocation and improve energy efficiency. Aiming at the damage caused by false data injection attacks on port power systems, Shan (Shan et al., 2022) proposed a distributed energy management strategy with a topology reconstruction mechanism to mitigate the impact of the attacks and improve the security of port power systems. Port microgrids are divided into two modes of operation: grid-connected mode and island mode. Meanwhile, the network contains a variety of power generation devices such as conventional power plants, photovoltaic power generation, wind turbine power generation, as well as carbon capture and carbon sequestration device, with the diversified mode. Due to the problems of single IP and low suppression of unknown threats in the existing communication networks (Guan et al., 2018; Hu et al., 2019), it is difficult to adapt to the distributed energy management of the low-carbon port microgrid. Therefore, polymorphic networks, that match the actual low carbon port microgrid, must be developed so that the communication network can obtain polymorphic convergence dynamic. And relevant scholars have already conducted wide exploration on polymorphic networks. Wu (Hu et al., 2020) introduced "structure definability" to all aspects of networks to improve the efficiency, performance, functionality and security of the Internet from the perspective of network architecture and to achieve the requirements of nowadays intelligent, diverse, highly robust and efficient networks. Hu (Hu et al., 2022) proposed a scheme of the polymorphic network element based on codesign of domain-specific software and a heterogeneous resource allocation and replacement method to realize efficient resource utilization. The results show that the proposed scheme can provide a basic platform to support the polymorphic network. In (Salamatian, 2011), Kave proposed two propositions: the Internet of the future should be polymorphic and it should be built on a strong foundation of network science. Zhang (Zhang et al., 2022b) constructed a multilateralised distributed cooperative control framework and proposed a communication topology reconfiguration method applicable to multiple multi-agent systems with different functions after networking in order to address the limitations of cooperative control of a single multi-agent system in a unilateral network environment. Thus it can be seen that the polymorphic network promotes the implementation of distributed control and optimization technology. As existing networks cannot meet the communication needs of modern smart ports, how to build a low-carbon port microgrid in a polymorphic network environment and realize its distributed energy management is the issue that needs attention.

Large-scale clean energy is connected to the port microgrid instead of traditional energy, which has achieved the reduction of pollution and carbon emission in the port to a certain extent. To further reduce carbon emissions, carbon capture devices need to be installed in ports to capture carbon dioxide, capturing the carbon dioxide emitted from conventional power plants in ports and then storing it through carbon sequestration devices, which can minimize the emission of carbon dioxide from port microgrid to the air (Damm and Fedorov, 2008) and promote the implementation of a green port. There have been a lot of researches on carbon capture and storage devices. Mostafa (Mostafa et al., 2018) demonstrated that carbon capture devices are more efficient in reducing CO_2 and less expensive to operate by comparing the CO_2 emission quality and operating costs of CO_2 emissions from power systems that include carbon capture devices with those that use chemical absorption. Alireza (Akbari-Dibavar et al., 2021) integrated carbon capture and storage devices into a conventional power plant and proposed the economic-emission dispatch problem using a Pareto frontier in a multi-objective optimization framework to achieve an economical and low-carbon power system. Fang (Fang et al., 2019) proposed a joint generation and demand-side management method under the Energy Efficiency Operating Index (EEOI) constraint to address the power shortage caused by carbon capture devices on board ships and illustrated the feasibility of carbon capture devices to reduce CO_2 emissions from the shipping industry. In addition to the use of clean energy and the installation of carbon capture and storage devices, market mechanisms represented by carbon taxes and carbon trading have become important initiatives to reduce carbon emissions from ports and ships. Arijit (De et al., 2021) proposed a ship fuel management strategy that took into account carbon taxes and explored the impact of fuel prices and carbon taxes on shipping operations in terms of operating costs. Zhen (Lin et al., 2022), on the basis of considering carbon tax, proposed a mathematical model that minimizes the sum of the total carbon emission cost and the total penalty cost of the port and effectively solved the model by using the heuristic algorithm based on the sequential method, to minimize the carbon emission of the port and optimize the spatial allocation of the port. For the problem of vessel scheduling and cargo flow allocation under the carbon emission trading mechanism, Wang (Yu and Wang, 2015) proposed a ship scheduling and cargo flow allocation model considering the cost of container cargo detention time under the mechanism to achieve the maximum emission reduction and profit for liner companies. But, for now, the use of carbon trading to reduce carbon emissions requires multi-sectoral supervision, and the implementation steps are cumbersome,

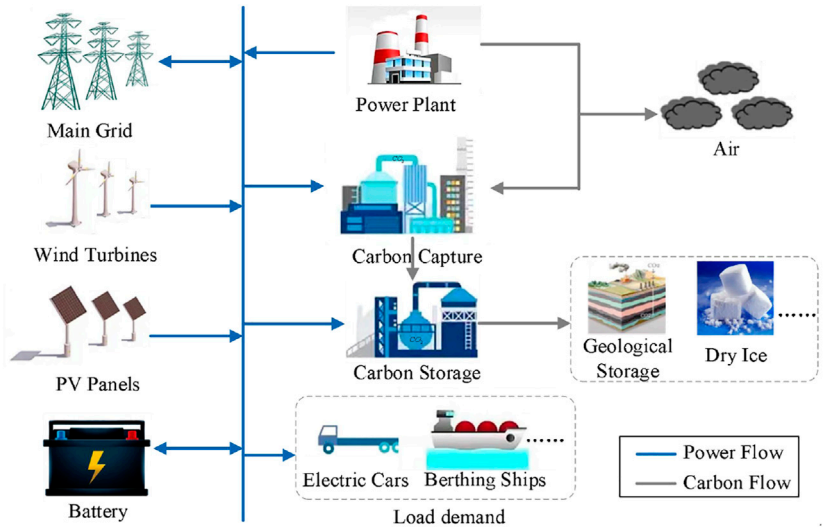

FIGURE 1 | Components of the low-carbon port microgrid.

with the application effect not ideal. Therefore, in the process of distributed energy management for low-carbon port microgrid, how to use the carbon tax to treat the carbon dioxide emitted into the air by the port under the target of reducing the carbon emission of the port and achieving a green port is a critical issue that needs to be solved.

As shown above, this paper is dedicated to constructing a low-carbon port microgrid under the polymorphic network environment and proposes a distributed energy management method under various operating conditions to ensure reliable and economic operation of the port microgrid and to achieve pollution and carbon reduction in the port. The specific contributions are as follows.

1) Construct a low-carbon port microgrid based on the polymorphic network, in order to realize the information interaction among various energy subjects under different modes and improve the performance of network communication among the port power generation device, main grid and carbon capture and storage device.

2) Considering carbon capture and storage devices, the energy management model of the low-carbon port microgrid is constructed. With the objective of minimizing the operating cost of the port microgrid, the power purchase or selling cost of the main power grid and the cost of carbon, as well as considering the supply and demand balance of the port microgrid and other constraints, the energy management model is constructed to achieve economic, low-carbon and reliable operation of the port microgrid.

3) A distributed energy management method for various working conditions of the port microgrid is proposed in this paper. For both grid-connected and island operation modes of the port microgrid, the distributed energy management of the low-carbon port microgrid is implemented based on multi-agent leader-following consensus and average consensus respectively to ensure the reliability and economy of the port.

2 ANALYSIS OF LOW-CARBON PORT MICROGRID ARCHITECTURE UNDER POLYMORPHIC NETWORK

There is a carbon capture device, a carbon sequestration device, and various power generation devices such as the conventional power plant, photovoltaic power generation, and wind turbine power generation in the low-carbon port microgrid, as shown in **Figure 1**.

The port microgrid can be operated in grid-connected mode or island mode. In grid-connected mode, the loads in the port microgrid are powered by the main grid, conventional power plant, photovoltaic power generation, wind turbines, and storage devices. In island mode, the port microgrid is powered by the conventional power plant, photovoltaic power generation, wind turbines and storage devices.

To achieve low-carbon operation, the port microgrid uses the carbon capture device and storage device to treat the carbon dioxide emissions from the conventional power plant. Most of the carbon dioxide emitted is captured by the carbon capture device and a small amount is released into the air. The carbon dioxide captured by the carbon capture device is then encapsulated and stored in a carbon storage device, and this part of carbon dioxide can be used for various purposes, including as a raw material for P2G, making dry ice, etc.

Due to the diverse working conditions and device types of low-carbon port microgrids, it is difficult for the existing traditional communication network architecture to adapt to modern smart low-carbon ports. Therefore, this paper proposes a diversified, specialized and intelligent low-carbon port microgrid based on the polymorphic network, and its network architecture is shown in **Figure 2**. The low carbon port microgrid based on the polymorphic network is mainly divided into three layers: the data layer, the control layer, and the service layer, with different functions. The data

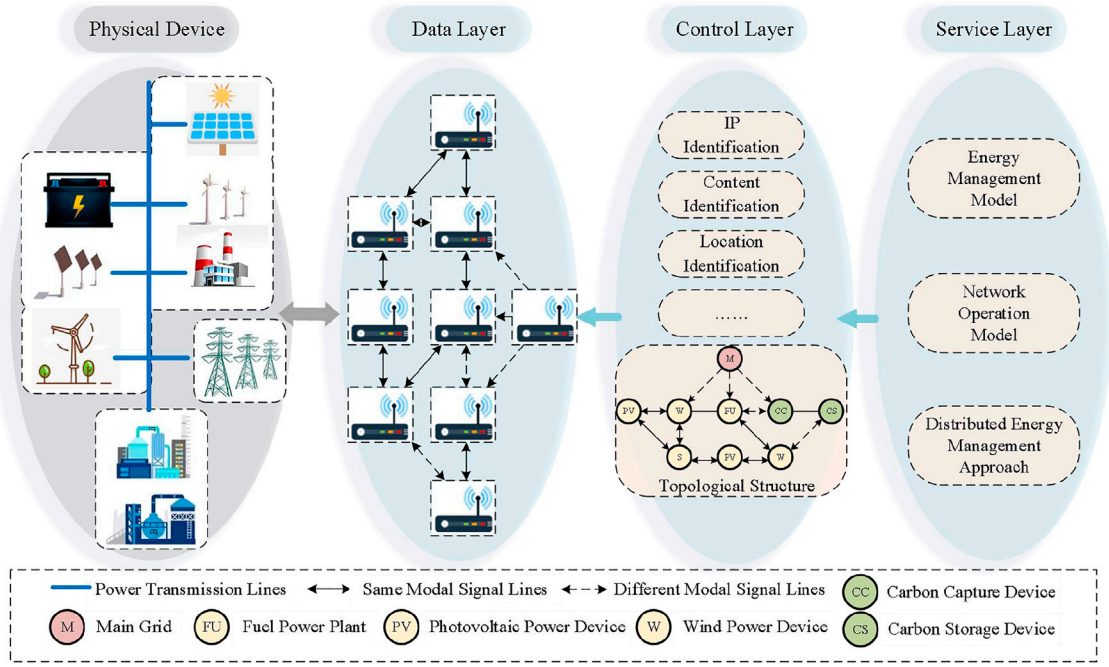

FIGURE 2 | The polymorphic network architecture of low-carbon port microgrid.

layer is mainly responsible for the full-dimensional definition of the topology, protocols, software and hardware, and interfaces of the port microgrid, providing refined services for diversified applications and essential support for the realization of future network intelligence, flexibility, and diversity. The control layer undertakes the service layer upward to address and route between single modality and different modalities, and controls the data layer downward to calculate and convert the different requirements of the upper-layer business into the control information of the data layer. Through the polymorphic controller, the diversified routes are defined according to the service requirements, and the communication topology is constructed according to the constraint conditions to realize polymorphic addressing interconnection and on-demand switching, so as to lay the foundation for the subsequent distributed energy management. The service layer mainly realizes the distributed energy management of the low-carbon port microgrid. The essence of polymorphic network is the process of top-down functional fitting from business requirements to fine-grained resource partitioning on the basis of a fully-dimensional definable network structure. The three layers implement business and service fitting, service and route fitting, route and resource fitting which are driven by business requirements, respectively. First, various device operation models are established, then the low-carbon port microgrid energy management model is constructed, and finally the distributed energy management method is designed according to the port microgrid operation mode.

3 LOW-CARBON PORT MICROGRID ENERGY MANAGEMENT MODEL

3.1 Objective Function

This paper aims to minimize the operating cost of polymorphic low-carbon port microgrid. The objective function includes three parts: one is the operating cost of the power generation and energy storage device; one is the cost of trading with the main grid; the other is the carbon cost. The function is as follows:

$$F = \min\{F_1 + F_2 + F_3\} \tag{1}$$

where, F is the total operating cost of the polymorphic low carbon port microgrid, F is the operating cost of the power generation and energy storage device, F_2 is the cost of trading with the main grid and F_3 is the carbon cost.

3.1.1 The Operating Cost of the Power Generation and Energy Storage Device

The operating costs of power generation and energy storage devices include the conventional power plant generation costs, wind turbine generation costs, photovoltaic generation costs, and energy storage device operating costs. The details are as follows.

$$F_1 = \sum_{n_1} f_{fu} + \sum_{n_2} f_w + \sum_{n_3} f_{pv} + \sum_{n_4} f_s \tag{2}$$

where, f_{fu} is the cost of conventional power plant generation, f_w is the cost of wind turbine generation, f_{pv} is the cost of photovoltaic generation and f_s is the cost of energy storage device operation, n is the total number of powered devices in the port microgrid, $n_1 + n_2 + n_3 + n_4 = n$.

Since the operating cost functions of the considered generation and storage devices are generally in the quadratic form (Teng et al., 2020), they can be uniformly expressed as:

$$f_i = \frac{(P_i - \alpha_i)^2}{2\beta_i} + \varphi_i, i \in 1, 2, 3...n \tag{3}$$

where, f_i is the operating cost of the i th device, P_i is the amount of power supplied by the i th device, $\alpha_i \leq 0$, $\beta_i \geq 0$ and φ_i are the cost coefficients of the i th device.

3.1.2 The Cost of Trading With the Main Grid

When the port microgrid is connected to the main grid, the port and the grid company agree on a trading price for electricity. When the port microgrid generates more electricity than it needs and still has a large surplus, it can sell the excess electricity into the market at the price agreed by the grid company to earn the difference; when the microgrid generates less electricity than it needs, it can buy the required electricity at the price agreed by the grid company to ensure the safe and reliable operation of the port. The cost of trading with the main grid is as follows

$$F_2 = \lambda_0 P_M \tag{4}$$

where, λ_0 is the trading electricity price agreed with the main grid and P_M is the power purchased from (sold to) the main grid.

3.1.3 The Carbon Cost

In the carbon cost, since the carbon storage device needs to store carbon dioxide through a series of methods, and the stored carbon dioxide requires a harsh storage environment, the cost of carbon sequestration should be additionally considered here. For this reason, the carbon cost includes the carbon storage costs and carbon tax costs. And the formula is as follows:

$$F_3 = f_{cs} + f_{tax} \tag{5}$$

where, f_{cs} is the cost of carbon storage, f_{tax} is the cost of the carbon tax.

In the cost of carbon, as the operation of the carbon capture device consumes electricity, it can be seen as an electrical load and is not additionally accounted for in the cost of carbon. However, carbon storage device requires various methods to sequester carbon dioxide. The sequestered carbon dioxide requires a harsh preservation environment, so the cost of carbon sequestration is also considered here. The energy consumption of a carbon capture device includes both operational and fixed energy consumption. Operational energy consumption is proportional to the mass of carbon dioxide captured. With the more carbon dioxide captured, the more operational energy is used. The amount of carbon dioxide that a carbon capture plant can capture is related to the quality of carbon dioxide emitted by conventional power plants. In contrast, the quality of carbon dioxide emitted by the port is related to the amount of electricity produced by the port plant. At the same time, the carbon capture plant consumes a certain amount of power to keep running, even when it is not in operation, and this is used as fixed energy consumption. The relevant equation for the carbon capture device is expressed as follows.

$$\begin{aligned} P_{cc} &= P_{fec} + P_{oec} = P_{fec} + \psi E_{cc} \\ E_{cc} &= \tau E_{fu} = \tau \omega P_{fu} \end{aligned} \tag{6}$$

where, P_{cc} is the total energy consumption of carbon capture device, P_{fec} is the fixed energy consumption of carbon capture device, P_{oec} is the operating energy consumption of carbon capture device, ψ is the energy consumption coefficient of the carbon capture device to capture unit CO_2, E_{cc} is the mass of CO_2 captured by the carbon capture device, τ is the efficiency of the carbon capture device to capture CO_2, E_{fu} is the mass of CO_2 emitted by the port conventional power plant, ω is the mass of CO_2 produced by the unit power output of the conventional power plant in the port, P_{fu} is the electricity produced by the port conventional power plant.

The cost of carbon storage is relative to the quantity of carbon dioxide trapped by the carbon capture device, while its energy consumption is relative to the amount of carbon dioxide stored. The details are as follows

$$\begin{aligned} f_{cs} &= \sigma E_{cc} \\ P_{cs} &= \gamma E_{cc} \end{aligned} \tag{7}$$

where, σ is the cost coefficient of storing unit carbon dioxide, P_{cs} is the energy consumption of carbon storage, and γ is the energy consumption factor of storing a unit of carbon dioxide.

Among the carbon cost, the formula for the carbon tax is as follows.

$$f_{tax} = C_{tax} E_e \tag{8}$$

where, C_{tax} is the unit price of the tax per unit of CO_2 emitted and E_e is the mass of CO_2 emitted into the air by the port microgrid.

3.2 Constraint

To ensure the reliable operation of the port microgrid, the following constraints should be followed.

1) Power balance constraint

$$\sum_{i=1}^{n} P_i + P_M = \sum_{i=1}^{n} P_{load} + P_{cc} + P_{cs} \tag{9}$$

where, P_M is the main grid input and output power, and P_{load} is the load of the port microgrid.

2) Output power constraints for power generation devices

$$P_i^{\min} \leq P_i \leq P_i^{\max} \tag{10}$$

where, $P_i^{\min}$ and $P_i^{\max}$ are the minimum output power and maximum output power of the i th generation device, respectively.

3) Energy consumption constraints for carbon capture devices

$$P_{cc}^{\min} \leq P_{cc} \leq P_{cc}^{\max} \tag{11}$$

where, $P_{cc}^{\min}$ and $P_{cc}^{\max}$ are the minimum and maximum energy consumption of the carbon capture device, respectively.

4) Energy storage constraints

$$SoC^{\min} \leq \left| 1 - \frac{P_s}{P_e} \right| \leq SoC^{\max} \tag{12}$$

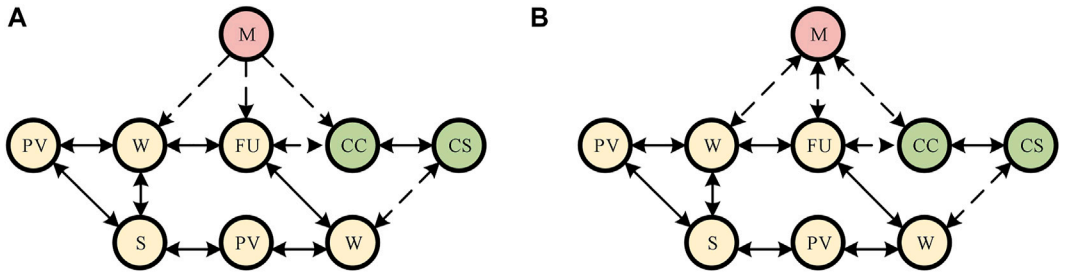

FIGURE 3 | The topology of low carbon port microgrid based on polymorphic network. **(A)** is the topology of the information flow, **(B)** is the topology of the energy flow.

where, P_e is the rated power of the energy storage device, $SoC^{\min}$ and $SoC^{\max}$ are the upper and lower limits of the capacity of the energy storage device, respectively.

4 DISTRIBUTED ENERGY MANAGEMENT METHOD FOR LOW CARBON PORT MICROGRID

The polymorphic port microgrid has two modes of operation: grid-connected mode and island mode. Since there are differences in the energy management methods of the two modes, the distributed energy management methods are designed in this section for the two operation modes and the operation mode switching states, respectively. The topology of the information flow of the low-carbon port microgrid based on the polymorphic network is shown in **Figure 3A**, and the topology of the energy flow is shown in **Figure 3B**, where information can be exchanged between different modes by routing. Information can be exchanged directly within the modes.

4.1 Graph Theory

A directed graph can be represented as $G = \{V, E\}$, N is the number of nodes. Where $V = \{v_1, v_2, v_3, ...v_N\}$ is the set of nodes and $E = \{e_1, e_2, e_3, ...e_M\}$ is the set of lines connecting two points, that is, the set of relations between two points. a_{ij} denotes the edges (v_i, v_j), when $(v_i, v_i) \in E$, $a_{ij} = 1$; when $(v_i, v_i) \notin E$, $a_{ij} = 0$. The adjacency matrix represents the relations between vertices, and $A = (a_{ij})_{N\times N}$, is an N-order square matrix (Li et al., 2020).

4.2 Grid Connection Mode

In the grid-connected mode, since the electricity price of the main grid is not affected by other factors, the main grid does not receive information, but only transmits information. However, in the energy flow, the main grid is able to exchange energy with the generation plant, carbon capture and storage plant. In the event that the port microgrid generates too much power, or does not generate enough power to meet the required load, it can sell power or buy power from the main grid.

Since port microgrids exhibit distributed characteristics, this section proposes a distributed energy management approach for port microgrids in grid-connected mode, where the model for the energy management problem can be written as the following equation.

$$\begin{aligned} \min \quad & \left\{ \sum_{i=1}^{N} F_1 + F_2 + F_3 \right\} \\ \text{s.t.} \quad & \sum_{i=1}^{n} P_i + P_M = \sum_{i=1}^{n} P_{load} + P_{cc} + P_{cs} \\ & P_i^{\min} \le P_i \le P_i^{\max} \end{aligned} \tag{13}$$

Taking (1)–(8) into (13), the objective function is further expressed as:

$$\min \left\{ \sum_{i=1}^{N} \left(\frac{(P_i - \alpha_i)^2}{2\beta_i} + \varphi_i \right) + \lambda_0 P_M + C_{tax} E_e + \sigma E_{cc} \right\} \tag{14}$$

Since in the objective function, E_e and E_e in the carbon cost function are both linearly related to P_i, which can be combined with the power generation cost, the objective function (14) can be organized as the following formula.

$$\min \left\{ \sum_{i=1}^{N} \left(\frac{\left(P_i - \alpha_i^{'}\right)^2}{2\beta_i^{'}} + \varphi_i^{'} \right) + \lambda_0 P_M \right\} \tag{15}$$

where, $\alpha_i^{'}$, $\beta_i^{'}$ and $\varphi_i^{'}$ are the cost coefficients of the collapsed function.

The Lagrangian function of the model for this problem takes the form of:

$$\begin{aligned} & L(P_1, P_2..., P_N, P_M, \lambda, \bar{\nu}, \underline{\nu}) \\ & = \sum_{i=1}^{N} \left(\frac{\left(P_i - \alpha_i^{'}\right)^2}{2\beta_i^{'}} + \varphi_i^{'} \right) + \lambda_0 P_M + \lambda \left(\sum_{i=1}^{n} P_i + P_M - \sum_{i=1}^{n} P_{load} - P_{cc} - P_{cs} \right) \\ & \quad + \sum_{i=1}^{n} \overline{\nu_i} \left(P_i - P_i^{\max}\right) + \sum_{i=1}^{n} \underline{\nu_i} \left(P_i^{\min} - P_i\right) \end{aligned} \tag{16}$$

where, λ, $\bar{\nu}$ and $\underline{\nu}$ are all Lagrangian multipliers, and the carbon capture and carbon storage loads can be expressed as $P_{cc} + P_{cs} = D_i P_i$, D_i is a coefficient matrix.

As the low carbon port microgrid distributed energy management model contains inequality constraints, in order to find its optimal solution, its KKT (Karush Kuhn Tucker) condition is analyzed.

$$\begin{cases} \dfrac{\partial L\left(P_1^*, P_2^*..., P_N^*, P_M^*, \lambda^*, \overline{\nu^*}, \underline{\nu^*}\right)}{\partial\{P_1, P_2..., P_N, P_M\}} = 0 \\ \sum_{i=1}^{n} P_i + P_M - \sum_{i=1}^{n} P_{load} - P_{cc} - P_{cs} = 0 \\ \overline{\nu_i^*}\left(P_i - P_i^{\max}\right) = 0 \\ \underline{\nu_i^*}\left(P_i^{\min} - P_i\right) = 0 \end{cases} \tag{17}$$

According to (17), we get:

$$\begin{cases} \lambda^* = \dfrac{P_i - \alpha_i{}'}{\beta_i^{'}(1 - D_i)} \\ \lambda^* = \lambda_0 \end{cases} \tag{18}$$

Bringing (18) into (17) gives the global optimum result as:

$$P_i^* = \begin{cases} \lambda^*\beta_i^{'}(1 - D_i) + \alpha_i{}' & \underline{P_i} \le \lambda^*\beta_i^{'}(1 - D_i) + \alpha_i{}' \le \overline{P_i} \\ \overline{P_i} & \lambda^*\beta_i^{'}(1 - D_i) + \alpha_i{}' > \overline{P_i} \\ \underline{P_i} & \lambda^*\beta_i^{'}(1 - D_i) + \alpha_i{}' < \underline{P_i} \end{cases} \tag{19}$$

$$P_M^* = \sum_{i=1}^{n} P_{load} + \sum_{i=n}^{N} D_i P_i - \sum_{i=1}^{n} P_i \tag{20}$$

When in grid-connected mode, the iterative approach of electricity prices follows the leader-following consistency (Chen and Li, 2021), with the following iterative process. According to (21), the amount of power generated by each generating unit can be obtained as:

$$\lambda_i(k+1) = \lambda_i(k) + \mu_i\left[\sum_{j\in N_i} a_{ij}\left(\lambda_j(k) - \lambda_i(k)\right) + a_{i0}\left(\lambda_0 - \lambda_i(k)\right)\right] \tag{21}$$

The above equation represents that the λ of each node follows the leader-following consensus to the main grid price λ_0 and the node $a_{i0} = 1$, which is capable of receiving direct main grid communication information from the main grid.

According to (21), the power generation capacity of each generation unit can be obtained as follows.

It can be obtained that the power generation capacity of each generation unit is as follows.

$$P_i(k) = \begin{cases} \lambda(k)\beta_i^{'} \quad (1 - D_i) + \alpha_i^{'} & \underline{P_i} \le \lambda(k)\beta_i^{'}(1 - D_i) + \alpha_i{}' \le \overline{P_i} \\ \overline{P_i} & \lambda(k)\beta_i^{'}(1 - D_i) + \alpha_i{}' > \overline{P_i} \\ \underline{P_i} & \lambda(k)\beta_i^{'}(1 - D_i) + \alpha_i{}' < \underline{P_i} \end{cases} \tag{22}$$

where, $P_i(k)$ is the amount of electricity generated by the i th node at the k th iteration.

Then, based on the known estimated local mismatch values $P_i(k)$, the formula is as follows.

$$\begin{cases} \rho_i(k+1) = \Delta\widehat{P}_i(k) + \varepsilon\left[\sum_{j\in N_i} a_{ij}\left(\Delta\widehat{P}_j(k) - \Delta\widehat{P}_i(k)\right)\right] + \Delta P_i(k+1) - \Delta P_i(k) \\ \Delta\widehat{P}_i(k+1) = (1 - a_{0i})\rho_i(k+1) \end{cases} \tag{23}$$

where, $\Delta P_i(k)$ is the actual local mismatch at the k th iteration and $\Delta\widehat{P}_i(k)$ is the estimated local mismatch at the k th iteration. $\Delta\widehat{P}_i(k+1) = (1 - a_{0i})\rho_i(k+1)$ means that for the neighbor unit of the main grid, the power complement of the main grid is obtained directly in each iteration. At the $k+1$ th iteration, the estimation of the local power mismatch becomes zero.

$$P_M(k+1) = P_M(k) + \sum_{i=n}^{N} a_{0i}\rho_i(k+1) \tag{24}$$

where, $P_M(k+1)$ is the supplementary power value of the main grid to neighbor nodes at the $k+1$ th iteration, which equals the sum of the supplementary power value of the k th iteration and the mismatch value of all neighbor nodes.

For the above algorithm, for a connected undirected graph G, when the step size of the algorithm satisfies $\mu_i \in (0, \frac{1}{\sum_{j=0}^{N} a_{ij}})$ and $\varepsilon \in (0, \frac{1}{\max_{i=1,2,3...N}\sum_{j=0}^{N} a_{ij}})$, it can be obtained that:

$$\begin{aligned} &\lim_{k\to\infty}\lambda_i(k) = \lambda(0), \ \ i = 1, 2, 3...N \\ &\lim_{k\to\infty}P_i(k) = P_i^*, \ \ i = 1, 2, 3...N \\ &\lim_{k\to\infty}\Delta\widehat{P}_i(k) = 0, \ \ i = 1, 2, 3...N \\ &\lim_{k\to\infty}P_M(k) = \sum_{i=1}^{n} P_{load} + \sum_{i=n}^{N} D_i P_i^* - \sum_{i=1}^{n} P_i^* = P_M^* \end{aligned} \tag{25}$$

where, the value of $P_M(k)$ can be positive or negative.

The low carbon port microgrid under the grid-connected mode considered in this paper can both buy electricity from and sell electricity to the port's main grid, ensuring a balance between energy supply and demand and enabling the economic operation of the port microgrid.

4.3 Island Mode

In island mode, the port microgrid cannot buy power from the main grid and has to be powered by a generation device to supply the load. In this case, not only the economy of the port must be considered, but also its security. The economic optimization of the port microgrid is achieved on the basis that the port load demand can be met. In this section, the incremental cost of the islanding model is corrected by adding a penalty factor to meet the supply-demand balance of the port microgrid. The iterative formula used is as follows.

$$\lambda_i(k+1) = \lambda_i(k) + \mu_i{}'\left[\sum_{j=1}^{N} a_{ij}\left(\lambda_j(k) - \lambda_i(k)\right)\right] + \zeta(k)\Delta\widehat{P}_i(k) \tag{26}$$

where, $\mu_i{}'$ is the step size of the algorithm and $\zeta(k)$ is the feedback gain.

According to (26), the power generation capacity of each generation unit can be obtained by

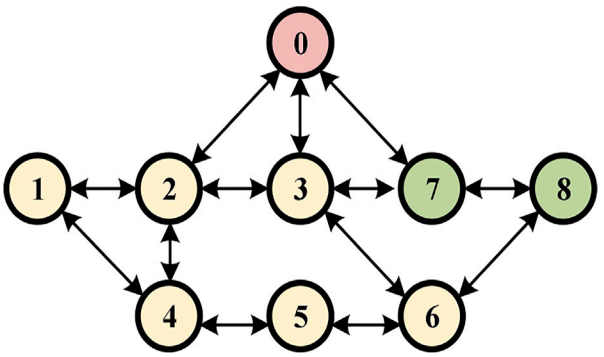

FIGURE 4 | The energy flow topology of the low-carbon port microgrid.

TABLE 1 | The port microgrid energy supply device parameters.

	FU	PV1	PV2	W1	W2	S
α_i	2.1	3.1	2.3	2.9	2.5	2.7
β_i	25	20	26	19	30	10
φ_i	0.44	0.1	0.05	0.2 0	05 0	44

$$P_i(k) = \begin{cases} \lambda(k)\beta_i^{'} \quad (1-D_i) + \alpha_i^{'} & \underline{P_i} \le \lambda(k)\beta_i^{'}(1-D_i) + \alpha_i{}' \le \overline{P_i} \\ \overline{P_i} & \lambda(k)\beta_i^{'}(1-D_i) + \alpha_i{}' > \overline{P_i} \\ \underline{P_i} & \lambda(k)\beta_i^{'}(1-D_i) + \alpha_i{}' < \underline{P_i} \end{cases} \tag{27}$$

where, $P_i(k)$ is the amount of electricity generated by the i th node at the k th iteration.

Then, according to the known $P_i(k)$, the local mismatch value is estimated, and the formula is as follows.

$$\begin{cases} \rho_i(k+1) = \Delta\hat{P}_i(k) + \varepsilon'\left[\sum_{j\in N_i} a_{ij}\left(\Delta\hat{P}_j(k) - \Delta\hat{P}_i(k)\right)\right] + \Delta P_i(k+1) - \Delta P_i(k) \\ \Delta\hat{P}_i(k+1) = \rho_i(k+1) \end{cases} \tag{28}$$

where, $\Delta P_i(k)$ is the actual local mismatch value at the k th iteration and $\Delta\hat{P}_i(k)$ is the estimated (local) mismatch value at the k th iteration.

For a connected undirected graph G, when the step size of the above algorithm satisfies $\mu_i^{'} \in (0, \frac{1}{\sum_{j=0}^{N} a_{ij}})$ and $\varepsilon' \in (0, \frac{1}{\max_{i=1,2,3\ldots N}\sum_{j=0}^{N} a_{ij}})$, for feedback gains $\zeta(k)$, it satisfies $\lim_{k\to\infty}\zeta(k) = 0$ and $\sum_{k=0}^{\infty}\zeta(k) = \infty$. $\lambda_i(0)$ is any given initial value, then we can obtain that, in the island mode, when the local estimate of the initial value of the mismatch value satisfies $\Delta\hat{P}_i(0) = \sum_{i=1}^{n} P_{load} + \sum_{i=n}^{N} D_i P_i(0) - \sum_{i=1}^{n} P_i(0)$, it can be obtained that:

$$\begin{aligned} &\lim_{k\to\infty}\lambda_i(k) = \lambda_i^*, \ \ i = 1,2,3\ldots N \\ &\lim_{k\to\infty}P_i(k) = P_i^*, \ \ i = 1,2,3\ldots N \\ &\lim_{k\to\infty}\Delta\hat{P}_i(k) = 0, \ \ i = 1,2,3\ldots N \end{aligned} \tag{29}$$

In the island model considered in this paper, security and the guarantee of supply and demand balance are more important as the port microgrid is not connected to the main grid. The essence of the algorithm is to follow the average consensus and add a penalty factor for feedback gain to correct the incremental cost in order to achieve safety and economy of port operation.

4.4 Switching Mode

Low carbon port microgrid switching mode operation refers to the process of switching from grid-connected mode to island mode or from island mode to grid-connected mode. In the switching process, it is necessary to realize the economical operation of the port microgrid as much as possible on the basis of ensuring the supply and demand balance. At this time, the iterative process of the electricity price λ is as follows.

$$\begin{aligned} \lambda_i(k+1) = \ &\lambda_i(k) + \mu_i{}'\left[\sum_{j\in N_i} a_{ij}\left(\lambda_j(k) - \lambda_i(k)\right) + m a_{i0}\left(\lambda_0 - \lambda_i(k)\right)\right] \\ &+ \zeta'(k)\Delta\hat{P}_i(k) \end{aligned} \tag{30}$$

where, m denotes the mode of operation of the port microgrid, when in grid-connected mode, $m = 1$, otherwise, $m = 0$; when $m = 1$, λ of each node follows the leader-following consensus to the main grid electricity price λ_0, where $a_{i0} = 1$ represents the node can directly receive the communication information from the main grid; when $m = 0$, λ of each node follows the average consensus, and adopts the penalty factor correction method to tend to λ^*.

According to the above equation, the power generation capacity of each generation unit can be obtained by:

$$P_i(k) = \begin{cases} \lambda(k)\beta_i^{'} \quad (1-D_i) + \alpha_i^{'} & \underline{P_i} \le \lambda(k)\beta_i^{'}(1-D_i) + \alpha_i{}' \le \overline{P_i} \\ \overline{P_i} & \lambda(k)\beta_i^{'}(1-D_i) + \alpha_i{}' > \overline{P_i} \\ \underline{P_i} & \lambda(k)\beta_i^{'}(1-D_i) + \alpha_i{}' < \underline{P_i} \end{cases} \tag{31}$$

where, $P_i(k)$ is the amount of power generated by the generation unit at the i th node at the k th iteration.

Then, based on the known estimated local mismatch values $P_i(k)$, the formula is as follows.

$$\begin{cases} \rho_i(k+1) = \Delta\hat{P}_i(k) + \varepsilon'\left[\sum_{j\in N_i} a_{ij}\left(\Delta\hat{P}_j(k) - \Delta\hat{P}_i(k)\right)\right] + \Delta P_i(k+1) - \Delta P_i(k) \\ \Delta P_{Mi}(k+1) = m a_{0i}\rho_i(k+1) \\ P_{Mi}(k+1) = m[P_{Mi}(k) + a_{0i}\Delta P_{Mi}(k+1)] \\ \Delta\hat{P}_i(k+1) = \rho_i(k+1) + a_{0i}[P_{Mi}(k) - P_{Mi}(k+1)] \end{cases} \tag{32}$$

Among them, $\sum_{i=1}^{N}\Delta\hat{P}_i(0) = \sum_{i=1}^{n} P_{load} + \sum_{i=n}^{N} D_i P_i(0) - \sum_{i=1}^{n} P_i(0)$ and $P_{Mi}(0) = 0$.

Then, the power exchanged with the main grid can be expressed as:

$$P_M(k) = \sum_{i=1}^{N} P_{Mi}(k) \tag{33}$$

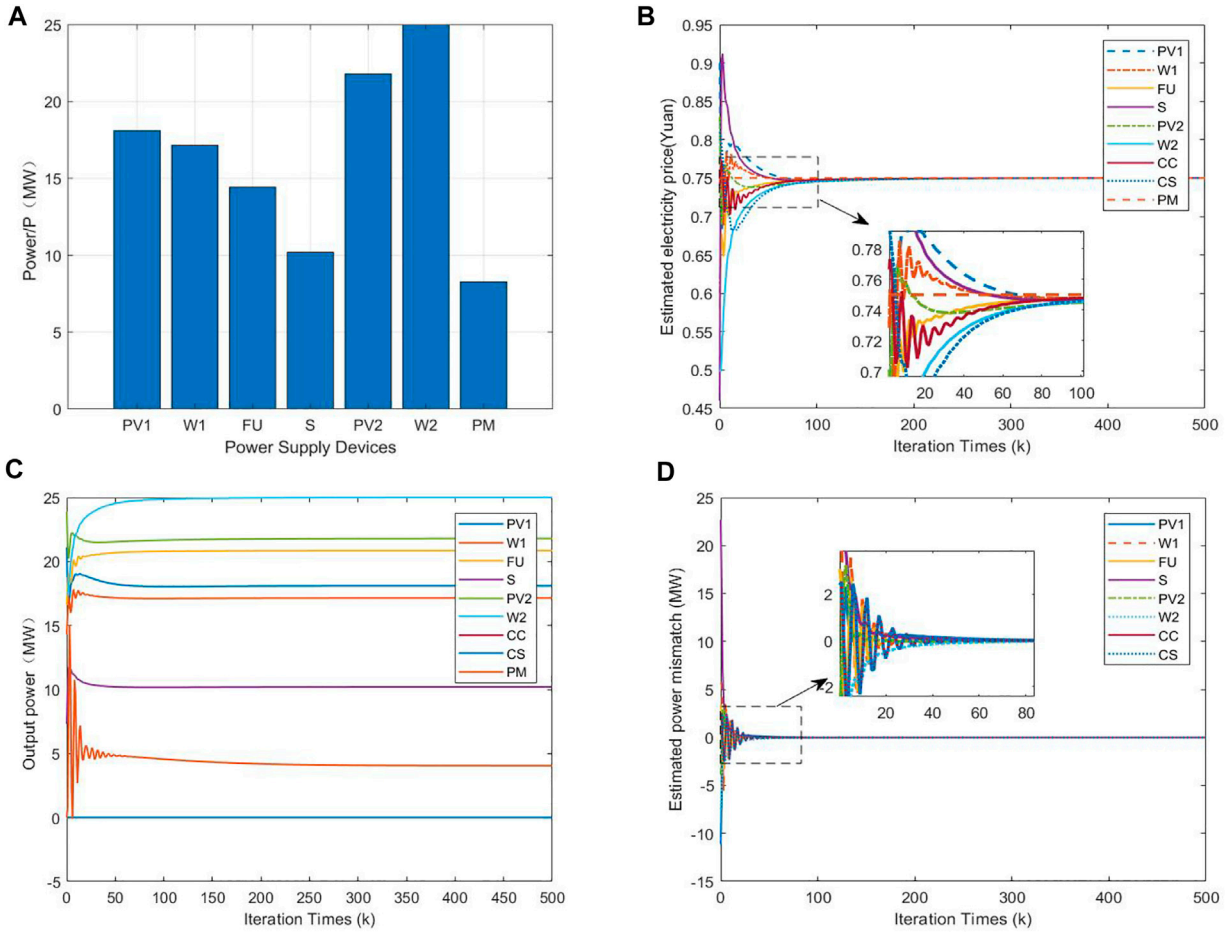

FIGURE 5 | Simulation results of power purchase from the main grid in grid-connected mode. **(A)** is the results of centralized algorithm, **(B)** is the dynamic curve of the electricity price λ, **(C)** is the dynamic curve of the power output, **(D)** is the dynamic curve of the estimated power.

The switching mode considered in this paper is the switching of the port microgrid between grid-connected mode and island mode. With the algorithm used in this paper, the safe and economic operation of the port microgrid can be achieved on the basis of ensuring a balance between supply and demand in the port microgrid.

5 SIMULATION RESULTS

In this paper, Matlab is used to simulate and verify the proposed method. The considered low carbon port microgrid consists of a conventional power plant, two photovoltaic power generation devices, two wind power generation devices, a storage device, a carbon capture device, a carbon sequestration device and the main grid. The energy flow topology of the low-carbon port microgrid based on the polymorphic network is shown in **Figure 4** and the parameters of the power generation device are shown in **Table 1**. The following simulation cases are conducted in grid-connected mode, island mode and switching mode respectively.

5.1 Grid-Connection Mode

For this case, the operation of a polymorphic port microgrid in grid-connected mode is considered and divided into two scenarios: buying electricity from and selling electricity to the main grid.

5.1.1 Purchase Power From the Main Grid

When the low-carbon port microgrid generation cannot meet the required load of the port, the port will purchase power from the main grid to meet the port load demand. In this section, in order to verify the accuracy and convergence of the algorithm, the proposed model is solved using the centralized algorithm and the distributed algorithm, respectively. The simulation results of the centralized algorithm are shown in **Figure 5A**, and the results obtained by the distributed algorithm are shown in **Figures 5B–D**. The total load demand of the port microgrid is 110 MW.

The minimum cost result obtained in the centralized algorithm with grid-connected power purchase is 4,005.39 ¥ of each supply device as shown in **Figures 5B–D**. Since electricity price from the main grid is relatively high, the amount of electricity supplied

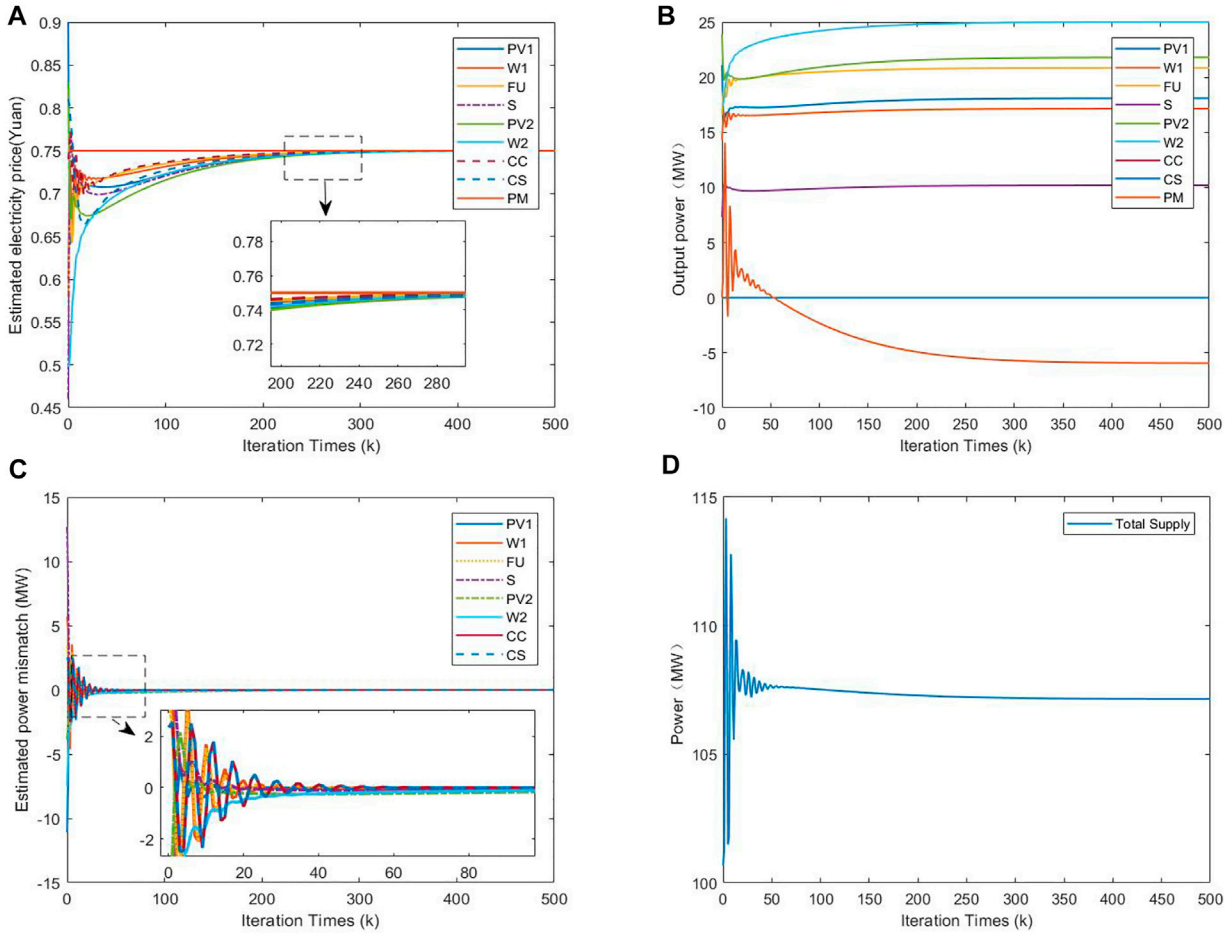

FIGURE 6 | Simulation results of power selling to the main grid in grid-connected mode. **(A)** is the dynamic curve of the electricity price λ, **(B)** is the dynamic curve of the power output, **(C)** is the dynamic curve of the estimated power, **(D)** is the dynamic curve of the total supply.

from the main grid is lower. At the same time, the figure shows that the traditional power plant supplies less power and emits less CO_2, which further illustrates that the model built in this paper can effectively reduce the carbon emission of the port. By using distributed algorithms, the operating cost of the low-carbon port microgrid is 4088.13 ¥, with 4.44 t of CO_2 emitted into the air and 10.36 t of CO_2 treated by carbon capture and storage device which are very little different from the results obtained by the centralized algorithm, further proving the accuracy of the proposed algorithm in this paper. The electricity price λ follows multi-agent leader-following consensus, and $\lambda = 0.75$. The main grid acts as the leader and its final electricity price converges to the electricity price of the main grid when $k = 100$. The power supply of each power generation unit is [4.05, 18.09, 17.15, 20.85, 10.20, 21.80, 24.98], of which 4.05 MW is bought from the main grid to maintain a balance between supply and demand in the port microgrid. The total electricity consumption of the port microgrid is 117.13 MW, which is larger than the initially set load demand of 110 MW. This is because the energy consumption of carbon capture and carbon storage device varies according to the amount of electricity produced by conventional power plants during operation.

5.1.2 Sell Power to the Main Grid

When the generation capacity of the low carbon port microgrid is larger than the load required by the port itself, the port will sell electricity to the main grid to earn a profit. In this simulation case, the total load demand of the port is 100 MW, and the simulation results are shown in **Figures 6A–D**.

In grid-connected mode, when the port load is 100 MW, the operating cost of the low carbon port microgrid is 3,338.28 ¥, the carbon dioxide emitted into the air is 4.44 t, and the carbon dioxide treated by the carbon capture and storage device is 10.36 t. The incremental cost (electricity price) converges to the electricity price of the main power grid when $k = 260$, and $\lambda = 0.75$. The electricity production of each unit is [-5.94, 18.09, 17.15, 20.85, 10.20, 21.80, 24.98]. The total electricity consumption of the port microgrid is 107.13 MW. The main grid supply is negative because the main grid does not supply electricity to the port. There exists excess electricity generation in the port, which is sold to the main grid to make a profit; and the electricity sold to the main grid is 5.94 MW.

As shown in **Figure 5** and **Figure 6**, most of the carbon dioxide emitted from conventional power plants will be treated

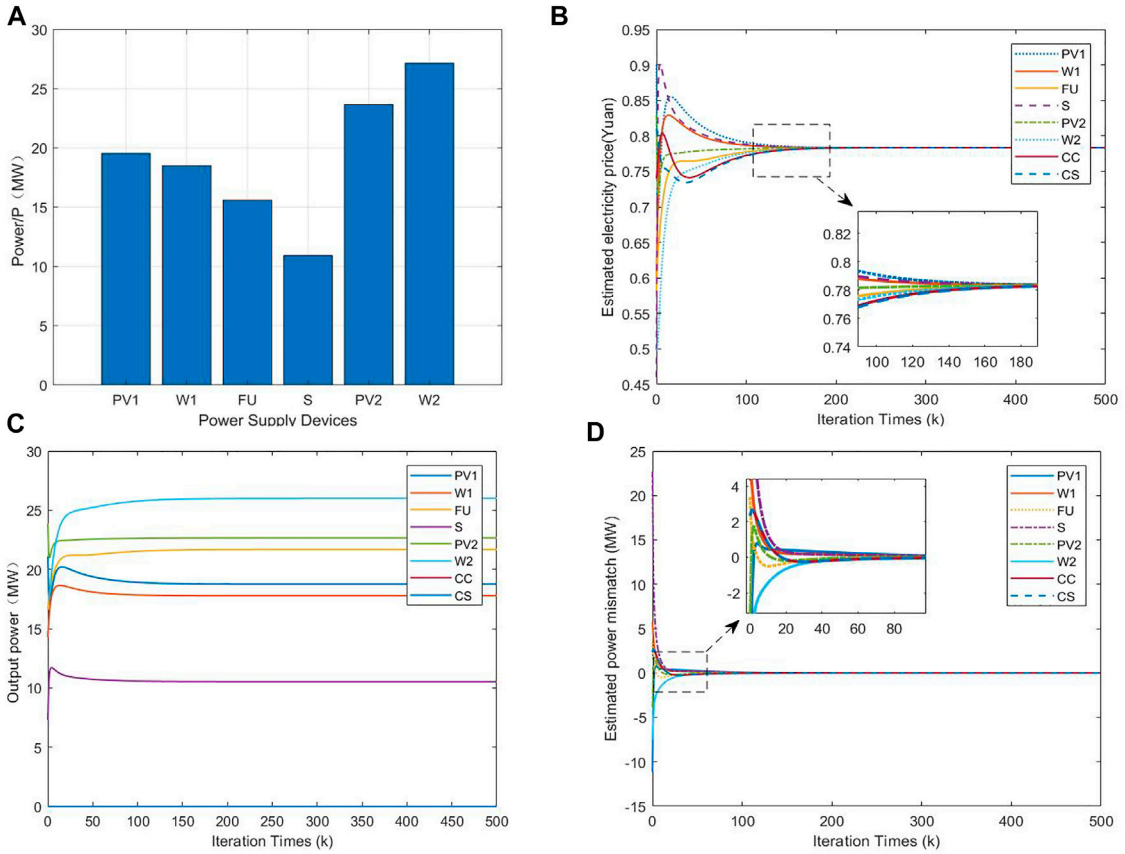

FIGURE 7 | Simulation results in island mode. **(A)** is the results of centralized algorithm, **(B)** is the dynamic curve of the electricity price λ, **(C)** is the dynamic curve of the power output, **(D)** is the dynamic curve of estimated power.

by carbon capture and storage devices, incurring carbon treatment costs. Although carbon dioxide is still being emitted into the air, but most of it is treated by carbon capture and storage devices, which can greatly reduce the pollution to the environment. A small proportion of the carbon dioxide emitted into the atmosphere will be subject to a carbon tax, resulting in higher power generation cost, so the port microgrid produces more electricity from photovoltaic and wind power than conventional power plants. Regardless of whether the port generates less or more than the required port load, the total generation can satisfy the supply-demand balance constraint, and its mismatch value eventually stabilizes at 0, as shown in **Figure 5D** and **Figure 6C**. If the port generates less than the required load for the port, it needs to buy electricity from the main grid, in this case $P_M > 0$, as shown in **Figure 5C**, and conversely, sell electricity to the main grid for profit, as shown in **Figure 6B**. The convergence of the simulation results proves the effectiveness of the proposed algorithm.

5.2 Island Mode

For this case, the operation of a polymorphic port microgrid in island mode is considered. Unlike the grid-connected mode, in the island mode, it is not possible to purchase power from the main grid, so it is essential to ensure the economics and the security of the polymorphic port microgrid. In this section, the centralized algorithms and the distributed algorithms are used to solve the proposed model, and the obtained simulation results are shown in **Figures 7A–D**.

The results obtained using the centralized algorithm are shown in **Figure 7A**, which shows the power supply of each power supply device, and the lowest cost result is 4,035.78 ¥. By using distributed algorithms, the low-carbon port microgrid costs 4,116.80 ¥, and emits 4.61 t of CO_2 into the air, with 10.77 t of CO_2 treated by the carbon capture and storage device. The difference between the results obtained by the centralized algorithm and the distributed algorithm proposed in this paper is small, which can prove the accuracy of the proposed algorithm. In this mode, there is no leader and the values for each unit follow an average consensus under the penalty factor correction method. It can be seen in the graph that the values converge to consistency at k = 25, with a faster convergence rate, $\lambda = 0.78$ at this time. The power supply for each device is [18.76, 17.78, 21.68, 10.53, 22.66, 26.01], and the total power used by the port microgrid is 117.42 MW, which is able to meet the required load of the port.

The cost is reduced compared to the grid-connected mode because the port's power generation device powers all loads. At the same time, as the island mode cannot purchase power from the main grid, to ensure the safety of the port during island mode operation and to meet

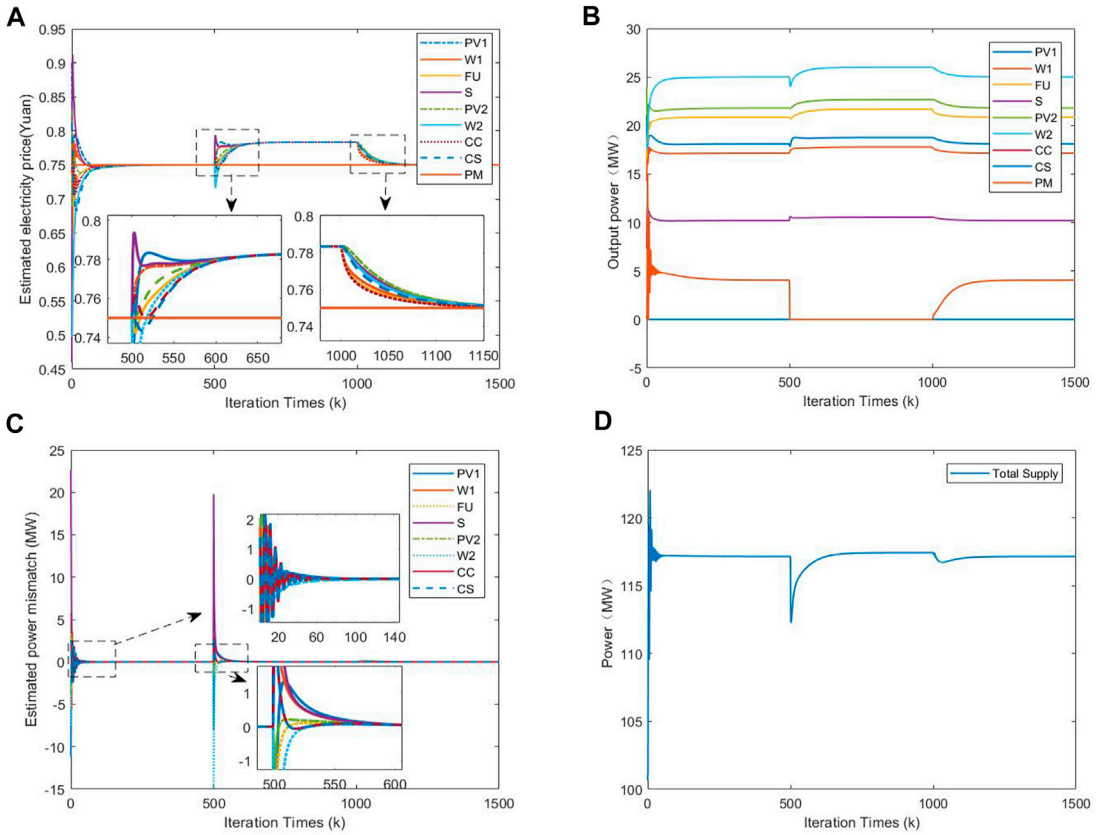

FIGURE 8 | Simulation results of "grid-island-grid" switching mode. **(A)** is the dynamic curve of the electricity price λ, **(B)** is the dynamic curve of the power output, **(C)** is the dynamic curve of estimated power, **(D)** is the dynamic curve of the total supply.

the balance of supply and demand of the port microgrid, the conventional power plant generates more power and emits more carbon dioxide into the air, illustrating that the grid-connected mode can effectively reduce carbon emissions from the port and is more friendly to the environment. In terms of convergence speed, the island model uses average consensus, which is significantly faster than the grid-connected model. The simulation results for both the grid-connected and island modes, which eventually reach convergence, prove the effectiveness of the proposed algorithm.

5.3 Switching Mode

During the operation of the port microgrid, the possible emergencies will lead to its failure to connect with the main grid, changing it from grid-connected mode to island mode, which will make the supply-demand balance and security unable to be guaranteed. While the port, as an essential transport hub node, is obliged to operate continuously and reliably. Therefore, it is necessary to ensure the safety and reliability of the port microgrid during operation. In this section, a distributed energy management algorithm is used to study the switching mode of the port microgrid, which is divided into two switching modes: "grid-connected–island–grid-connected" and "island–grid-connected–island" for energy management. The simulation results are shown in **Figures 8A–D** and **Figures 9A–D**.

5.3.1 Switching "Grid-Island-Grid"

From **Figure 8**, it can be seen that at k = 501, the port microgrid switches from grid-connected mode to island mode; at k = 1001, the port microgrid switches from island mode to grid-connected mode. In grid-connected mode, the devices are supplied with [18.76, 17.78, 21.68, 10.53, 22.66, 26.01]; in island mode, the supply of each device is supplied with [4.05, 18.09, 17.15, 20.85, 10.20, 21.80, 24.98]. After each switchover, the values go out of line with short fluctuations and after about 100 iterations, the port microgrid can reach convergence again after adjustment quickly. From **Figure 8C**, we can see that the mismatch values converge to 0 after switching mode, indicating that the port microgrid can satisfy the supply-demand balance constraint after switching modes.

5.3.2 Switching "Island-Grid-Island"

At k = 501, the port microgrid switches from island mode to grid-connected mode; at k = 1001, the port microgrid switches from grid-connected mode to island mode. **Figure 9** shows that when the port microgrid is switched from grid-connected mode to grid-connected mode, the system values fluctuate more, and the system needs to go through more iterations to reach stability. With the port load all being 110 MW, the total power supply is higher when in island mode, as its conventional power plant generates more power and produces more CO_2, which also represents higher energy consumption of the carbon

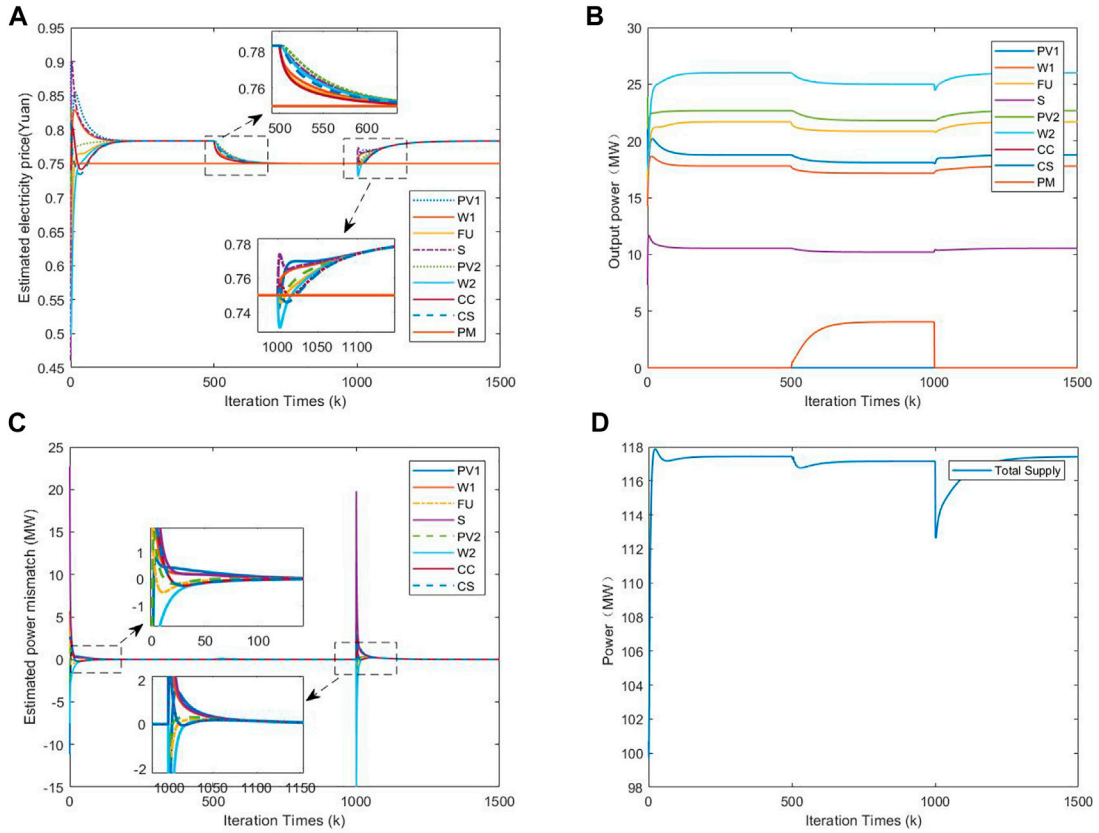

FIGURE 9 | Simulation results of "island-grid-island" switching mode. **(A)** is the dynamic curve of the electricity price λ, **(B)** is the dynamic curve of the power output, **(C)** is the dynamic curve of the estimated power, **(D)** is the dynamic curve of the total supply.

capture device and carbon storage device. At the same time, more CO_2 is emitted into the air in island mode.

In switching mode, the low-carbon port microgrid is still able to reduce the carbon emissions of the port. The simulation results show that the carbon emission is less in grid-connected mode than in island mode, the reason is that in island mode, the conventional power plant needs to generate more electricity to maintain the safe and stable operation of the port microgrid, so the carbon emission is more in island mode.

However, the low-carbon port microgrid is able to operate safely, economically, and at a low carbon level, whether switching from grid-connected mode to island mode or from island mode to grid-connected mode. The simulation results further validate the effectiveness of the algorithm.

6 CONCLUSION

The large amount of carbon emissions from the port leads to serious environmental pollution problems, so building low carbon ports is of great practical importance. In this paper, a low-carbon port microgrid with carbon capture and storage devices has been constructed in a polymorphic network environment, and its energy management problems have been investigated, and distributed solutions have been proposed for various operation modes. Firstly, a low carbon port microgrid in a polymorphic network environment has been proposed, which consists of a data layer, a control layer and a service layer, enabling the information interaction among various energy bodies in different modes and improving the performance of network communication among the power generation device, the main grid and the carbon capture and storage device. Secondly, the energy management model of a low carbon port microgrid has been constructed to minimize the operating cost of the low carbon port microgrid. Then, applicable distributed energy management methods have been proposed for various operating conditions of the port microgrid. For both grid-connected and island operation modes, the distributed energy management of the low carbon port microgrid has been implemented based on the multi-agent leader-following consensus and average consensus, respectively. In addition, the port microgrid grid-connected and island operation switching model has been discussed. Finally, the simulation results have verified

the effectiveness of the proposed low-carbon port microgrid energy management method. The distributed energy management method proposed in this paper has reduced the operating cost and carbon emissions of the port microgrid, as well as realized the economical, safe and stable operation of the port.

In this paper, only the low carbon operation in the port microgrid is achieved, but not the zero carbon emission of the port. In the future, we can consider abandoning the use of traditional power plants of the port to supply electricity. The port microgrid has been kept in grid-connected mode, and when its own generation device cannot meet its own load, it purchases insufficient electricity from the main grid to realize the zero carbon operation of the port.

DATA AVAILABILITY STATEMENT

The original contributions presented in the study are included in the article/Supplementary Material, further inquiries can be directed to the corresponding author.

AUTHOR CONTRIBUTIONS

QS and JS provide research ideas for energy management and microgrid; QX and GX provide formal analysis of the polymorphic network. JS and FY write the original manuscript and are responsible for revisions of the paper. All authors have read and agreed to the published version of the manuscript.

FUNDING

This research is supported by the National Key R&D Program of China (2019YFB1802501) and Key Research Project of Zhejiang Lab (2021LE0AC02); High Level Talents Innovation Support Plan of Dalian (Young Science and Technology Star Project) (under Grant No. 2021RQ058); National Natural Science Foundation of China (under Grant Nos. 51939001, 61976033, 61751202, 61903092, U1813203); the Science and Technology Innovation Funds of Dalian (under Grant No. 2018J11CY022); the Liaoning Revitalization Talents Program (under Grant Nos. XLYC1908018, XLYC1807046).

REFERENCES

Akbari-Dibavar, A., Mohammadi-Ivatloo, B., Zare, K., Khalili, T., and Bidram, A. (2021). Economic-Emission Dispatch Problem in Power Systems with Carbon Capture Power Plants. *IEEE Trans. Ind. Appl.* 57 (4), 3341–3351. doi:10.1109/tia.2021.3079329

Chen, W., and Li, T. (2021). Distributed Economic Dispatch for Energy Internet Based on Multiagent Consensus Control. *IEEE Trans. Automatic Control* 66 (1), 137–152. doi:10.1109/TAC.2020.2979749

Damm, D. L., and Fedorov, A. G. (2008). Conceptual Study of Distributed CO_2 Capture and the Sustainable Carbon Economy. *Energy Convers. Manag.* 49 (6), 1674–1683. doi:10.1016/j.enconman.2007.11.011

De, A., Wang, J., and Tiwari, M. K. (2021). Fuel Bunker Management Strategies within Sustainable Container Shipping Operation Considering Disruption and Recovery Policies. *IEEE Trans. Eng. Manage.* 68 (4), 1089–1111. doi:10.1109/tem.2019.2923342

Deng, X., Guan, P., Hei, C., Li, F., Liu, J., and Xiong, N. (2021). An Intelligent Resource Allocation Scheme in Energy Harvesting Cognitive Wireless Sensor Networks. *IEEE Trans. Netw. Sci. Eng.* 8 (2), 1900–1912. doi:10.1109/tnse.2021.3076485

Fang, S., Xu, Y., Li, Z., Ding, Z., Liu, L., and Wang, H. (2019). Optimal Sizing of Shipboard Carbon Capture System for Maritime Greenhouse Emission Control. *IEEE Trans. Ind. Appl.* 55 (6), 5543–5553. doi:10.1109/tia.2019.2934088

Gennitsaris, S. G., and Kanellos, F. D. (2019). Emission-Aware and Cost-Effective Distributed Demand Response System for Extensively Electrified Large Ports. *IEEE Trans. Power Syst.* 34 (6), 4341–4351. doi:10.1109/tpwrs.2019.2919949

Guan, P., Deng, X., Liu, Y., and Zhang, H. (2018). Analysis of Multiple Clients' Behaviors in Edge Computing Environment. *IEEE Trans. Veh. Technol.* 67 (9), 9052–9055. doi:10.1109/tvt.2018.2850917

Hu, Y., Cui, Z., Li, Z., Dong, Y., Cui, P., and Wu, J. (2022). Construction Technologies of Polymorphic Network Environment Based on Codesign of Domain-Specific Software/Hardware[J]. *J. Commun.* 43 (04), 3–13. doi:10.11959/j.issn.1000–436x.2022086

Hu, Y., Li, D., Sun, P., Yi, P., and Wu, J. (2020). Polymorphic Smart Network: An Open, Flexible and Universal Architecture for Future Heterogeneous Networks. *IEEE Trans. Netw. Sci. Eng.* 7 (4), 2515–2525. doi:10.1109/tnse.2020.3006249

Hu, Y., Ying, P., Sun, P., and Wu, J. (2019). Research on the Full-Dimensional Defined Polymorphic Smart Network[J]. *J. Commun.* 40 (08), 1–12. doi:10.11959/j.issn.1000–436x.2019192

Huang, B., Li, Y., Zhan, F., Sun, Q., and Zhang, H. (2022). A Distributed Robust Economic Dispatch Strategy for Integrated Energy System Considering Cyber-Attacks. *IEEE Trans. Ind. Inf.* 18 (2), 880–890. doi:10.1109/tii.2021.3077509

Kermani, M., Shirdare, E., Parise, G., Bongiorno, M., and Martirano, L. (2022). A Comprehensive Technoeconomic Solution for Demand Control in Ports: Energy Storage Systems Integration. *IEEE Trans. Ind. Appl.* 58 (2), 1592–1601. doi:10.1109/tia.2022.3145769

Kinnon, M. M., Razeghi, G., and Samuelsen, S. (2021). The Role of Fuel Cells in Port Microgrids to Support Sustainable Goods Movement. *Renew. Sustain. Energy Rev.* 147 (3), 1–17. doi:10.1016/j.rser.2021.111226

Li, Y., Gao, D. W., Gao, W., Zhang, H., and Zhou, J. (2021). A Distributed Double-Newton Descent Algorithm for Cooperative Energy Management of Multiple Energy Bodies in Energy Internet. *IEEE Trans. Ind. Inf.* 17 (9), 5993–6003. doi:10.1109/tii.2020.3029974

Li, Y., Gao, D. W., Gao, W., Zhang, H., and Zhou, J. (2020). Double-Mode Energy Management for Multi-Energy System via Distributed Dynamic Event-Triggered Newton-Raphson Algorithm. *IEEE Trans. Smart Grid* 11 (6), 5339–5356. doi:10.1109/tsg.2020.3005179

Lin, S., Zhen, L., Wang, W., and Tan, Z. (2022). Green Berth and Yard Space Allocation Under Carbon Tax Policy in Tidal Ports. *Marit. Policy & Manag.*, 1–22. doi:10.1080/03088839.2022.2047816

Mostafa, S. S., Hedengren, J. D., and Powell, K. M. (2018). Performance Comparison of Low Temperature and Chemical Absorption Carbon Capture Processes in Response to Dynamic Electricity Demand and Price Profiles. *Appl. Energy* 228, 577–592. doi:10.1016/j.apenergy.2018.06.098

Salamatian, K. (2011). Toward a Polymorphic Future Internet: A Networking Science Approach. *IEEE Commun. Mag.* 49 (10), 174–178. doi:10.1109/mcom.2011.6035832

Shan, Q., Zhang, X., Zhang, Q., and Sun, Q. (2022). Distributed Energy Management for Port Power System Under False Data Injection Attacks. *Complexity* 2022, 1. doi:10.1155/2022/5995281

Teng, F., Shan, Q., and Li, T. (2020). Intelligent Ship Integrated Energy System and its Distributed 488 Optimal Scheduling Algorithm. *ACTA Autom. Sin.* 46 (9), 1809–1817. doi:10.1038/s41598-022-10958-7

Wang, X., Gao, D. W., Wang, J., Yan, W., Gao, W., Muljadi, E., et al. (2018). Implementations and Evaluations of Wind Turbine Inertial Controls with

FAST and Digital Real-Time Simulations. *IEEE Trans. Energy Convers.* 33 (4), 1805–1814. doi:10.1109/tec.2018.2849022

Wang, X., Zhao, T., and Parisio, A. (2022). Frequency Regulation and Congestion Management by Virtual Storage Plants. *Sustain. Energy, Grids Netw.* 29 (1), 100586. doi:10.1016/j.segan.2021.100586

Yang, L., Sun, Q., Zhang, N., and Li, Y. (2022). Indirect Multi-Energy Transactions of Energy Internet with Deep Reinforcement Learning Approach. *IEEE Trans. Power Syst.*, 1. doi:10.1109/TPWRS.2022.3142969

Yang, T., Yi, X., Wu, J., Yuan, Y., Wu, D., Meng, Z., et al. (2019). A Survey of Distributed Optimization. *Annu. Rev. Control* 47, 278–305. doi:10.1016/j.arcontrol.2019.05.006

Yu, S., and Wang, C. (2015). Schedule Coordination and Cargo Allocation Optimization for Liner Container Shipping Network Under Carbon Emission Trading Mechanism. *J. Wuhan Univ. Technol. Transp. Sci. Eng.* 39 (5), 1073–1078. doi:10.3963/j.issn.2095-3844.2015.05.038

Zhang, N., Sun, Q., Yang, L., and Li, Y. (2022). Event-Triggered Distributed Hybrid Control Scheme for the Integrated Energy System. *IEEE Trans. Ind. Inf.* 18 (2), 835–846. doi:10.1109/tii.2021.3075718

Zhang, Q., Shan, Q., and Li, T. (2020). "Large Port Energy Management Based on Distributed Optimization," in 2020 7th International Conference on Information, Cybernetics, and Computational Social Systems (ICCSS), Guangzhou, China, 13-15 November 2020, 108–113. doi:10.1109/ICCSS52145.2020.9336919

Zhang, R., Xiao, G., Shan, Q., Zou, T., Li, D., and Teng, F. (2022). Communication Topology Reconstruction Method for Multi-Agent Cooperative Control in Polymorphic Networks[J]. *J. Commun.* 43 (04), 50–59. doi:10.11959/j.issn.1000–436x.2022077

Zhang, Y., Shan, Q., Teng, F., and Li, T. (2021). Distributed Economic Optimal Scheduling Scheme for Ship-Integrated Energy System Based on Load Prediction Algorithm. *Front. Energy Res.* 9, 720–374. doi:10.3389/fenrg.2021.720374

Conflict of Interest: The authors declare that the research was conducted in the absence of any commercial or financial relationships that could be construed as a potential conflict of interest.

Publisher's Note: All claims expressed in this article are solely those of the authors and do not necessarily represent those of their affiliated organizations, or those of the publisher, the editors and the reviewers. Any product that may be evaluated in this article, or claim that may be made by its manufacturer, is not guaranteed or endorsed by the publisher.

frontiers | Frontiers in Energy Research

TYPE Original Research
PUBLISHED 22 July 2022
DOI 10.3389/fenrg.2022.952396

OPEN ACCESS

EDITED BY
Bonan Huang,
Northeastern University, China

REVIEWED BY
Yanfang Hou,
Chongqing University of Technology, China
Peiyuan Guan,
University of Oslo, Norway
Bingyu Wang,
North China Electric Power University Beijing, China

*CORRESPONDENCE
Hanguang Luo,
luohg@zhejianglab.com

SPECIALTY SECTION
This article was submitted to Smart Grids,
a section of the journal
Frontiers in Energy Research

RECEIVED 25 May 2022
ACCEPTED 29 June 2022
PUBLISHED 22 July 2022

CITATION
Teng F, Wang J, Luo H, Zhang Q and Shen C (2022), Distributed low-carbon energy management method for port microgrid based on we-energies under polymorphic network.
Front. Energy Res. 10:952396.
doi: 10.3389/fenrg.2022.952396

Distributed low-carbon energy management method for port microgrid based on we-energies under polymorphic network

Fei Teng[1], Jianyuan Wang[1], Hanguang Luo[2]*, Qing Zhang[1] and Congqi Shen[2]

[1]Marine Electrical Engineering College, Dalian Maritime University, Dalian, China, [2]Research Institute of Intelligent Networks, Zhejiang Lab, Hangzhou, China

In order to reduce port pollution and carbon emissions and improve the utilization rate of clean energy, a port microgrid based on we-energies (WEs) and its polymorphic distributed low-carbon energy management method is proposed. First, this study considers a variety of heterogeneous Wes, such as ship we-energies (SWEs), to establish a polymorphic energy management system for port microgrids and to achieve reliable information exchange between WEs under different communication networks. Second, considering the bidirectional energy transmission characteristic of the port WEs, the operating cost function of heterogeneous WEs is established. In addition, with the objective of economic and low-carbon operation of port microgrids, the energy management model of a port microgrid is constructed, and the optimal solution is obtained based on distributed optimization theory. Finally, simulation cases are performed to verify the effectiveness of the proposed method.

KEYWORDS

port microgrid, clean energy, low carbon, distributed energy management, we-energy, polymorphic network

1 Introduction

With the development of the shipping industry, maritime transport is responsible for nearly 90% of global trade in goods. As important transportation hubs for sea and land transport, ports consume huge amounts of energy (Coppola et al., 2016; Huang et al., 2022). In addition, ships and large port equipment emit a lot of air pollutants, causing poor air quality in the port and the surrounding environment (Tang et al., 2018; Alamoush et al., 2020). Therefore, in order to solve the problem of port energy consumption and environmental pollution, it is urgent to build a green and low-carbon port microgrid with clean energy as the main energy (Nikolaos and Theocharis, 2021). In order to ensure the reliability of operation of the port microgrid, it is crucial to study its energy management issues (Çağatay and Jasmine, 2019).

The essence of port microgrid energy management is an optimization problem with constraints, which requires meeting the conditions of reliable operation for port microgrid and minimizing port operating costs by using suitable optimization strategies (Hein et al., 2021). Research results on port microgrids have mainly considered the uncertainty of renewable energy supply on the energy supply side (Çağatay and Jasmine, 2021) and the reliability of supplying flexible loads such as ships on the demand side (Parise et al., 2016; Fang et al., 2020). Considering the presence of a large number of flexible loads in the port power system, an energy management model with multiple decision variables and constraints has been proposed to vary the flexible loads' power demand at high loads or high electricity prices in order to optimize the operating costs of the port power system (Kanellos et al., 2019). Studies on energy management in port microgrids are often solved by using centralized optimization methods (Olivares et al., 2014; Kermani et al., 2020). The centralized methods rely on the design of the centralized controller, which will need to be redesigned if the structure of the port microgrid changes. At the same time, although the centralized controller is capable of handling huge amounts of data in the microgrid, its failure would cause huge losses to the port. To sum up, the centralized methods have problems such as difficult network expansion and single point of failure. Moreover, port microgrids with large-scale clean energy present a distributed structure, so the distributed methods are attracting extensive attention of researchers (Li et al., 2020; Li et al., 2021). In the distributed methods, each agent needs to obtain information about its neighbors with the help of a communication network and performs local calculations based on the exchange of information between itself and its neighbors to achieve distributed energy management (Yang et al., 2019). For port power systems with flexible loads, such as ships, a distributed hierarchical control method has been proposed to solve the problem of reducing the operating costs of the port power system (Gennitsaris and Kanellos, 2019). A multiobjective operation scheduling method based on an innovative virtual fuzzy electricity price has been proposed to address the problem of carbon emissions for large ports in a short period of time (Kanellos, 2019). A distributed alternating direction method of multipliers algorithm has been proposed for the existence of energy entities with different energy forms in the port energy system, in which the energy bodies only share local information with their neighbors to complete the information update, solving the problem of optimal operating costs of the port energy system (Zhang et al., 2020). A distributed hierarchical topology reconfiguration approach has been proposed for port power systems with false data attacks, solving the problem of energy management in port power systems with an unknown and arbitrarily large number of attacked nodes (Shan et al., 2022).

The high level of clean energy connected to the port microgrid increases the flexibility of the energy supply and gives rise to a manufacturing and marketing integration of energy main body – WEs, which contains at least one type of energy production equipment or energy consumption equipment (Sun et al., 2017; Sun et al., 2019). According to the type of energy consumption of the power generating equipment, the port microgrid includes traditional energy generating equipment WEs (TWEs) and clean energy generating equipment WEs (CWEs). However, as more and more all-electric ships fueled by clean energy come into service (Wen et al., 2021; Zhang et al., 2021), they can either be connected directly to the shore power plant with generators switched off and powered by the port microgrid for the purpose of reducing pollution (Fang et al., 2020) or they can be used as power generators to supply electricity to the shore loads, giving them manufacturing and marketing integration of behavior. Therefore, all-electric ships fueled by clean energy can also be considered a dynamic type of WE in port, namely ship WEs (SWEs). The bidirectional energy transmission characteristic of WEs makes them both energy suppliers and energy consumers (Sun et al., 2019), to the extent that the operating costs of WEs are no longer just the cost of the power generating equipment. This not only increases the complexity of the WE operating cost function but also creates difficulties in modelling the energy management of the port microgrid. In addition, the distributed energy management methods for the considered port microgrid rely on the information interaction between WEs, which is based on the premise that all WEs need to be in the same communication network. However, the SWEs and various heterogeneous WEs ashore are always in different traditional communication networks. Due to the problems of closed network element structure and single communication mode in the traditional communication network, the network convergence has a low support capability, with the result that the information interaction between the WEs based on the traditional communication network cannot be realized, thus, the distributed energy management of the port microgrid cannot be realized. In recent years, the polymorphic network is a newly emerging type of smart network in different communication networks, which uses a dynamic combination of resources and network reconfiguration to enhance the functions, performance, and other needs of the network and fundamentally meet the service needs of network intelligence, diversity, personality, high tenacity, and high performance (Hu et al., 2019). Polymorphic network breaks the traditional network structure to achieve flexible interconnection of heterogeneous networks, and new networks with hybrid addressing based on polymorphic identification can achieve efficient interaction of different data in space (Hu et al., 2020). The implementation of distributed energy management for port microgrids based on WEs can be guaranteed under a polymorphic network.

In summary, this study is dedicated to solving the energy management problem of port microgrids containing WEs and proposes a distributed method under a polymorphic network, with the following main contributions:

1) A polymorphic energy management system was established for a port microgrid based on WEs. Considering various WEs in different communication networks, such as SWEs and CWEs in the port microgrid, in order to guarantee the information interaction between neighbor WEs, the port microgrid energy management system was established based on a polymorphic network to realize distributed energy management.
2) Considering the bidirectional energy transmission characteristic of WEs, the operating cost function for WEs was constructed. The manufacturing and marketing integration of the behavior of WEs meant that the operating cost for WEs not only included the cost of WE's power generation but also the cost or benefit of trading with neighbor WEs or the main grid. We constructed operating cost functions for WEs with incremental cost as a variable, simplified the cost functions based on rotation symmetry, and analyzed the convexity of the operating cost functions.
3) Considering the cost of carbon emissions, a port microgrid energy management model was constructed, and a distributed solution method was proposed. With the objective of minimizing the operating cost of all WEs and the carbon emissions of the port, taking into account the constraints on the reliable operation of the port microgrid, the energy management model of port microgrid was constructed, and a distributed energy management strategy was proposed based on a multi-agents consensus algorithm.

The structure of the rest of the article is as follows. In Section 2, a polymorphic energy management system for WE-based port microgrid is established. In Section 3, the port microgrid energy management model is established, and a distributed solution method is proposed. In Section 4, the proposed method is validated by simulation using MATLAB. Finally, the results of the study are summarized.

2 Polymorphic energy management system for port microgrid based on WEs

The port microgrid considered in this study is composed of a large number of WEs, which can be classified according to the type of power generating equipment: TWEs and CWEs. In particular, CWEs include wind turbine WEs (WWEs) and photovoltaic generating equipment WEs (PWEs). Unlike traditional ships that use shore power after berthing, all-electric ships fueled by clean energy are also dynamic WEs for port microgrids – SWEs. The widespread presence of WEs gives the port microgrid a distributed characteristic and requires a distributed method based on a multi-agents system to solve the port microgrid energy management problem. Distributed energy management relies on the interaction of information between agents corresponding to each WEs, provided that all the agents are in the same communication network and that their communication topology meets certain constraints. However, the shore-based WEs and berthing SWEs are in different communication networks, making information interaction between neighbor agents impossible. Polymorphic network supports polymorphic identification, such as content identification and identity identification. Identification based on polymorphic addressing can realize flexible networking and provide a channel for information interaction between WEs in different communication networks. Therefore, a polymorphic energy management system for a port microgrid was constructed, and its structure is shown in Figure 1.

As can be seen in Figure 1, the port microgrid polymorphic energy management system consists of a data layer, a control layer, and a service layer from the bottom up. The function of the data layer is fitting the routing and resources of a variety of heterogeneous infrastructure platforms, providing basic data support and security for the construction of port microgrid network elements, receiving operational data, and broadcasting the scheduling instructions. The control layer is used for polymorphic addressing for heterogeneous WEs based on different identities and forming a dynamic communication topology network following certain constraints so as to enable peer-to-peer information interaction between neighbor WEs. The function of the service layer is to enable the energy management of the port microgrid. First, the generating cost functions of different WEs are obtained, and various WEs' operating cost functions are established, considering the bidirectional energy transmission characteristic. Second, the energy management model of the port microgrid with the economic and low-carbon objective is constructed. Finally, based on the communication topology of the WEs given by the control layer, a distributed solution method is designed to realize the distributed energy management of the port microgrid.

In summary, the polymorphic energy management system of the port microgrid is based on a polymorphic network to achieve the compatibility of heterogeneous traditional communication networks, which enables the interaction of information between WEs in different modes and lays the foundation for the subsequent implementation of distributed energy management in the port microgrid.

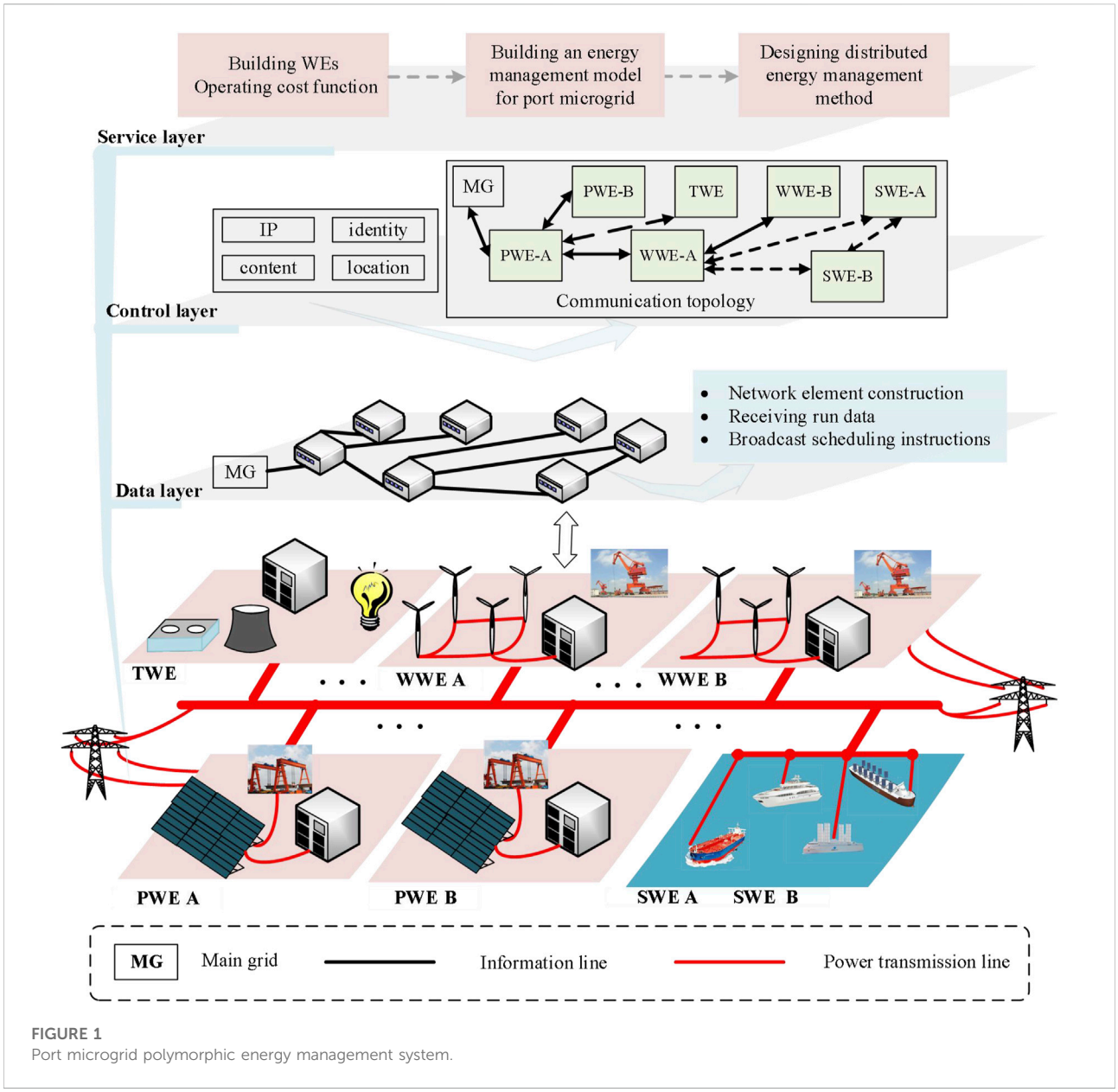

FIGURE 1
Port microgrid polymorphic energy management system.

3 Distributed energy management for port microgrid

3.1 Communication network

Port microgrid energy management relies on the exchange of information between neighbor WEs, and its communication topology is represented as $G(V, E, A)$, which is an undirected and strongly connected graph (Liu et al., 2017), where the set of nodes $V = \{v_1, v_2, v_3, \ldots, v_n\}$ denotes the finite non-empty set of all WE nodes in G. The set of edges $E = \{e_1, e_2, e_3, \ldots, e_n\}$ denotes the existence of communication paths between WEs and neighbors in G. A is the matrix of connection weights for information interactions between WEs. $a_{ij} > 0$ if there is a path of information exchange between any heterogeneous WEs v_i and v_j; otherwise, $a_{ij} = 0$. It is worth noting that there are no self-looping connected paths in G, that is, there is no $a_{ii} = 0$ in graph G.

3.2 Operating cost function of WEs

The bidirectional energy transmission of WEs in port microgrids complicates their operating cost, which includes not only the cost of generating equipment but also the cost

associated with energy interaction between WEs. As the energy consumed by the load in the WE can be supplied by the WE itself, neighbor WEs *via* the microgrid, or even the main grid. Therefore, the operating cost of individual WE in the port microgrid in this study includes the following: the generating electricity cost of the WEs, the cost of purchasing electricity from neighbors and the main grid, and the cost of selling electricity to neighbors and the main grid. Based on the above-stated analysis, the operating cost of individual WE in the port microgrid is expressed as follows:

$$\begin{aligned}\tilde{f}(P_{rk}) = {} & C_{ok}(P_{rk}) - \sum_{j=1}^{N} a_{kj} P_{rk} P_{k\to j} + \sum_{j=1}^{N} a_{jk} P_{rj} P_{j\to k} \\ & + P_{rg}\left[P_{load}^{k} + P_{loss}^{k} + \sum_{j=1}^{N} a_{kj} P_{k\to j} - P_{k} - \sum_{j=1}^{N} a_{jk} P_{j\to k}\right],\end{aligned} \tag{1}$$

where $C_{ok}(P_{rk})$ represents the generating cost function expressed with incremental cost as a variable, $P_{k\to j}$ represents the port WE k supplying energy to WE j, P_{load}^{k} represents the load of the WE k, P_{loss}^{k} represents the energy loss from the WE k, P_{rg} represents the main grid electricity price, P_{rk} represents the incremental cost of WE k, depending on the output power of generating equipment for the WE, P_k represents the power generation from WE k, and a_{jk} represents that the WE k can transmit electricity to the WE j.

Remark 1. The unit price of electricity trading between WEs is the incremental cost of each WE's generation equipment.

Assuming a port microgrid containing N WEs, and considering the bidirectional energy transmission between WEs, based on the constructed operating cost function of the individual WE, the operating cost of the port microgrid can be expressed as follows:

$$\begin{aligned}\sum_{k=1}^{N}\tilde{f}(P_{rk}) = {} & \sum_{k=1}^{N} C_{ok}(P_{rk}) - \sum_{k=1}^{N}\sum_{j=1}^{N} a_{kj} P_{rk} P_{k\to j} + \sum_{k=1}^{N}\sum_{j=1}^{N} a_{jk} P_{rj} P_{j\to k} \\ & + \sum_{k=1}^{N} P_{rg}\left[P_{load}^{k} + P_{loss}^{k} + \sum_{j=1}^{N} a_{kj} P_{k\to j} - P_{k} - \sum_{j=1}^{N} a_{jk} P_{j\to k}\right],\end{aligned} \tag{2}$$

where N represents the number of WEs in the port microgrid.

Noting that $a_{jk}P_{rj}P_{j\to k}$, $a_{kj}P_{rk}P_{k\to j}$, and $a_{kj}P_{k\to j}$, $a_{kj}P_{j\to k}$ have a special symmetry structure in the port microgrid, a rotational symmetry-based analysis yields

$$\begin{aligned}&\sum_{k=1}^{N}\sum_{j=1}^{N} a_{jk} P_{rj} P_{j\to k} - \sum_{k=1}^{N}\sum_{j=1}^{N} a_{kj} P_{rk} P_{k\to j} = 0 \\ &\sum_{k=1}^{N} a_{kj} P_{k\to j} - \sum_{k=1}^{N} a_{jk} P_{j\to k} = \mathbf{0}.\end{aligned} \tag{3}$$

According to Eq. 3, it can be seen that the cost of energy interaction between WEs in the port microgrid offsets each other. Therefore, the operating cost function of port microgrid based on WEs can be expressed as

$$\begin{aligned}\tilde{f}(P_r) &= \sum_{k=1}^{N} C_{ok}(P_{rk}) + P_{rg}\left[P_{load} + P_{loss} - \sum_{k=1}^{N} P_k\right] \\ &= \sum_{k=1}^{N} C_{ok}(P_{rk}) + P_{rg}\left[P_{load} + P_{loss} - \sum_{k=1}^{N}\frac{(P_{rk} - b_k)}{2a_k}\right] \\ &= \sum_{k=1}^{N}\left[C_{ok}(P_{rk}) - \frac{P_{rg}P_{rk}}{2a_k} + \frac{P_{rg}b_k}{2a_k} + P_{rg}\left(P_{load}^{k} + P_{loss}^{k}\right)\right] \\ &= \sum_{k=1}^{N} f^{k}(P_{rk}).\end{aligned} \tag{4}$$

Remark 2. Due to the manufacturing and marketing integration of WEs, the energy supply–demand balance of the WE is ensured by considering the electricity trading between WEs and the electricity trading between the WE and the main grid. Furthermore, the relationship between the incremental cost P_{rk} and the power generation P_k of the kth WE has the following relationship:

$$P_{rk}(P_k) = \frac{dC_k(P_k)}{dP_k}. \tag{5}$$

For CWEs and TWEs, the cost function $C_k(P_k)$ with the power generation P_k of the kth WE is generally a convex quadratic function (Huang et al., 2016; Kanellos, 2019); therefore, $P_{rk} = 2a_kP_k + b_k$, where a_k and b_k denote the generating cost coefficients, respectively, $a_k > 0$, $b_k > 0$. In turn, it can be obtained that $P_k = \frac{(P_{rk} - b_k)}{2a_k}$. The second row in model **(4)** makes variable substitution according to the relationship between P_k and P_{rk}.

3.3 Convexity analysis

As the process of analyzing the operating cost function of WEs requires modeling with the incremental cost P_{rk}, the generating cost function of WEs also needs to be converted to a function with P_{rk}. Thus, the equivalence of the generating cost function for the WEs with P_{rk} and P_k as variables is defined as

$$C_{ok}(P_{rk}) \cong C_k(P_k) = C_k\left(C_k^{'-1}\left(C_k^{'}(P_k)\right)\right) = C_k\left(C_k^{'-1}(P_{rk})\right). \tag{6}$$

The character of the port microgrid operating cost function is closely related to the design of subsequent distributed energy management methods for the port microgrid, so it is necessary to prove whether the constructed port microgrid operating cost function is convex. As P_{rk} in the port microgrid operating cost function Eq. 4 is transformed so that the two added terms $\frac{P_{rg}b_k}{2a_k}$ and $-\frac{P_{rg}P_{rk}}{2a_k}$ are linearly related to P_{rk}. Whether the constructed operating cost function of the port microgrid is convex depends critically on whether the WE generating cost function with the incremental cost P_{rk} is convex. To prove that the equivalently transformed cost function $C_{ok}(P_{rk})$ of the WEs is convex, we present **Lemma 1**.

Lemma 1. It is assumed that the cost function of electricity generation $C_k(P_k)$ of the WE is a smooth convex function and satisfies the inequality condition:

$$\left(C''_k(P_k)\right)^2 - C'_k(P_k)C'''_k(P_k) \geq 0. \tag{7}$$

Then, the cost function $C_{ok}(P_{rk})$ of electricity generation with the incremental cost P_{rk} as the variable for the WE is a smooth convex function.

Proof. The cost function $C_{ok}(P_{rk})$ of electricity generation from WEs is a smooth convex function that yields the second order derivative of the function $C_{ok}(P_{rk})$ with P_{rk} as the variable.

$$\begin{aligned}\frac{\partial^2 C_{ok}(P_{rk})}{\partial P_{rk}^2} &= \frac{\partial\left[C'_k\left(C'^{-1}_k(P_{rk})\right)\frac{1}{C''_k\left(C'^{-1}_k(P_{rk})\right)}\right]}{\partial P_{rk}} \\ &= \frac{C''_k(P_k) - C'_k(P_k)\frac{C'''_k(P_k)}{C''_k(P_k)}}{\left(C''_k(P_k)\right)^2} \\ &= \frac{\left(C''_k(P_k)\right)^2 - C'_k(P_k)C'''_k(P_k)}{\left(C''_k(P_k)\right)^3}.\end{aligned} \tag{8}$$

From **Lemma 1**, we know that $\left(C''_k(P_k)\right)^2 - C'_k(P_k)C'''_k(P_k) \geq 0$ and $C_k(P_k)$ is a smooth convex function, and we know that $\left(C''_k(P_k)\right)^3 > 0$. Therefore, the conclusion $\frac{\partial^2 C_{ok}(P_{rk})}{\partial P_{rk}^2} > 0$ is obtained from Eq. 7, and the cost function described by incremental cost is a smooth convex function, that is, $C_{ok}(P_{rk})$ is a convex function. **The proof is completed**.

Since the cost function of electricity generation $C_k(P_k)$ for WE is a smooth quadratic convex function, based on **Lemma 1**, $C_{ok}(P_{rk})$ is also a smooth convex function and therefore the port microgrid operating cost function is a smooth convex function.

3.4 Energy management model of port microgrid

In order to build a green, low-carbon, and economic port microgrid, the objective of energy management for port microgrid is to minimize the operating cost and carbon emissions. Based on the operating cost function for port microgrid and considering the cost of port carbon emissions, the energy management model for port microgrid is constructed as follows:

$$\begin{aligned} &\min \sum_{k=1}^{N} f^k(P_{rk}) + eco \sum_{k=1}^{m} Em^k(P_{rk}), \\ &s.t. \quad P_{k,min} \leq P_k \leq P_{k,max} \end{aligned} \tag{9}$$

where $N = m + n$, m represents the number of TWEs, n represents the number of CWEs, eco represents the cost per unit of carbon emissions, $Em^k(.)$ represents the carbon emissions generated by traditional energy generating equipment from WEs, and $P_{k,min}$ and $P_{k,max}$ represent the minimum and maximum output of electricity generating equipment from WE k, respectively.

Remark 3. The first term in Eq. 9, namely the operating cost of the port microgrid based on WE, is a convex function. The second item is the cost of carbon emissions for WE. As CWEs do not produce carbon emissions, that is, $\sum_{k=1}^{n} Em(P_k) = 0$, only the cost of carbon emissions for TWEs are considered. The cost functions of carbon emissions for TWEs are quadratic in relation to the output power of the equipment (Pourakbari-Kasmaei et al., 2020). To ensure uniformity of variables in the port microgrid energy management model, the cost functions of carbon emissions for TWEs need to be expressed in the form of the incremental cost P_{rk}. After transformation by Eq. 5, P_{rk} is linearly related to P_k, so that the cost functions of carbon emissions for TWEs with incremental cost P_{rk} are also convex functions after variable replacement through **Lemma 1**. In summary, the objective function of the energy management model for the port microgrid is convex. In addition, as the energy supply–demand balance of every WE is ensured, the energy supply–demand balance of the whole port microgrid is also ensured. Therefore, there is a potential supply–demand balance constraint in the objective function of the port microgrid energy management model and only the output power constraints of generating equipment for the WE need to be considered. Therefore, the port microgrid energy management problem is essentially a convex optimization problem with inequality constraints and can be solved by distributed methods.

3.5 Distributed energy management method

Considering the distributed structure presented by the port microgrid, the convex optimization problem **(9)** with inequality constraints can be solved based on the distributed optimization method **(10)**.

$$\begin{cases} P^* - g\left(P^* - \alpha\left(\nabla f(P^*) + Lz^*\right)\right) = 0 \\ LP^* = 0 \end{cases}, \tag{10}$$

where $P^* = \{P^*_{rk}, k = 1, \ldots, N\}$, α represents the update step (positive number), different steps affect the reliability of the method, L represents the Laplace matrix, $\nabla f(.)$ represents the gradient of the objective functions for port microgrid, $g(.)$ represents the projection operator, Ω' represents a hyper-rectangular set, $\Omega' = \{P_{rk} \in R_r^N : P_{rk}^{min} \leq P_{rk} \leq P_{rk}^{max}\}$, and the projection operator $g(.)$ is equivalently described as

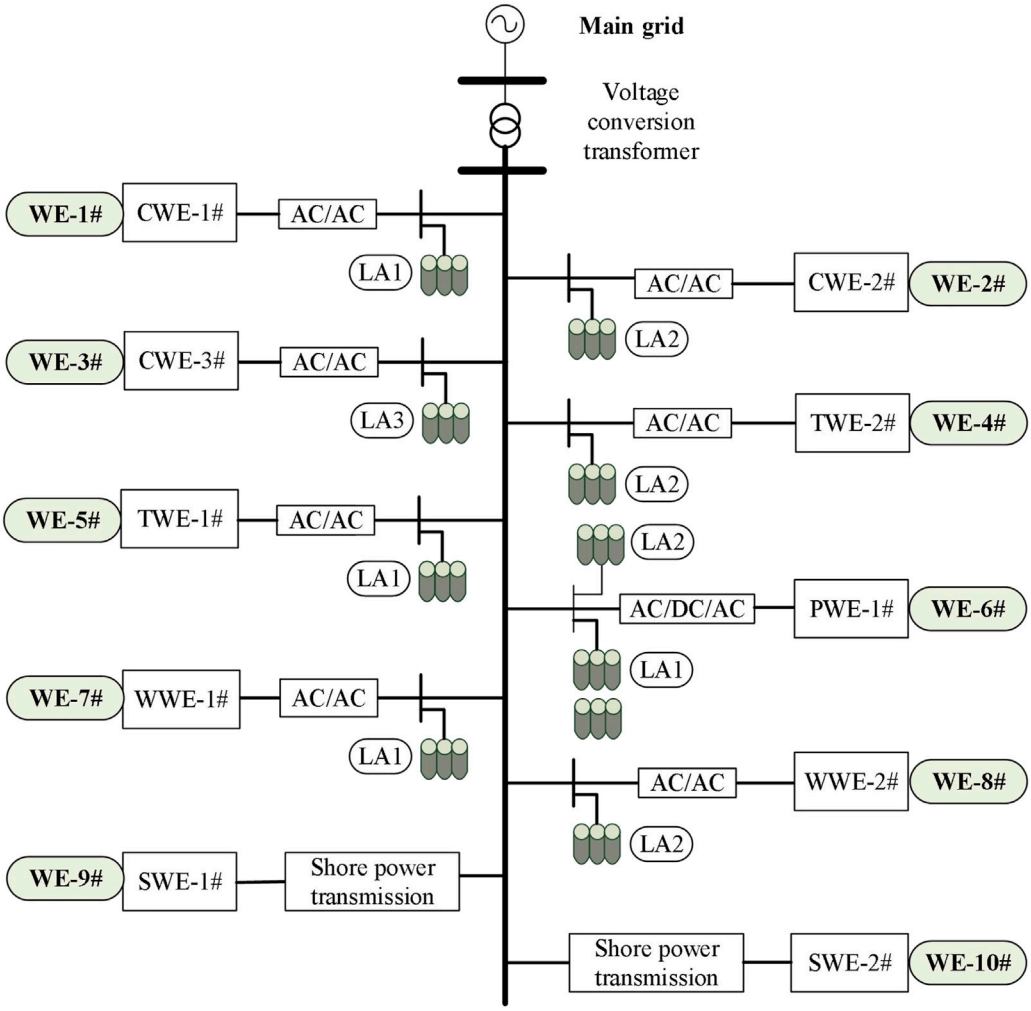

FIGURE 2
Simulation and validation model of a port microgrid based on WEs.

$$P_{rk} = \begin{cases} P_{rk}^{max} & P_{rk} > P_{rk}^{max} \\ P_{rk} & other \\ P_{rk}^{min} & P_{rk} < P_{rk}^{min} \end{cases}.$$

According to Eq. 10, a distributed solution method for the energy management problem for the port microgrid is proposed. The method is expressed in the following iterative way:

$$\begin{cases} P_{rk+1} = g\left(P_{rk} - \alpha\left(\nabla f\left(P_{rk}\right) + L\left(z_k + P_{rk}\right)\right)\right) \\ z_{k+1} = z_k + LP_{rk+1} \end{cases}. \quad (11)$$

Since model **(9)** is differentiable and its gradient is continuous as a convex function, and there exists an auxiliary variable z satisfying condition **(10)** (Liu et al., 2017), the incremental cost of WEs can converge to an optimal solution, and then a distributed optimal solution to the energy management problem for the port microgrid is obtained.

4 Simulation

4.1 Port microgrid simulation model based on WEs

In this subsection, we used MATLAB as an experimental tool to verify the effectiveness of the distributed energy management method for the port microgrid proposed in this article. The considered port microgrid model based on WEs is shown in Figure 2.

The port microgrid model contains 10 WEs, including 6 CWEs (2 WWEs and 1 PWE), 2 TWEs, and 2 SWEs. The port microgrid has a total of 41555W of load and line losses. The electricity required is provided by both the main grid and the WEs, at the cost of 5 Yuan per unit of carbon emissions. It is assumed that there are no energy losses in the generating

TABLE 1 Parameters of power generating equipment.

Energy type	a	b	c	P_i^{min}	P_i^{max}	α_i	β_i	γ_i
TR energy	0.000533	0.869	213.1	50	200	0.0000004	0.3	4.5
Clean energy1	0.008890	0.333	200	37.5	150	0	0	0
	0.000741	0.833	240	45	180	0	0	0
Clean energy2	0.0001	0.50000	10	0	180000	0	0	0
	0.0005	0.20000	15	0	125000	0	0	0

TABLE 2 Operating data of WEs.

	WE-1	WE-2	WE-3	WE-4	WE-5
Distributed method	37.5	37.5	37.5	122.9	122.9
Centralized method	37.5	37.5	37.5	122.6	122.6
	WE-1	WE-2	WE-3	WE-4	WE-5
Distributed method	8000.0	8000.0	25000.0	112.7	112.7
Centralized method	7997.3	7997.3	24987.0	112.5	112.5
Port microgrid	Distributed method	Cost	30821.0	Carbon emissions	82.8
	Centralized method	Cost	30801.0	Carbon emissions	82.6

equipment during the simulations for the heterogeneous WEs. The parameters related to the operation of the generating equipment in the heterogeneous WE during regular operation of the microgrid are shown in Table 1 (Huang et al., 2016).

4.2 Case 1: Traditional port microgrid energy management model with P_k

An energy management model with the objective of minimizing the operating cost and carbon emissions of the port microgrid, without considering the trading of electricity between WEs and the trading of electricity between the WE and the main grid, is as follows:

$$\begin{aligned} &\min \sum_{k=1}^{N} f^k(P_k) + eco \sum_{k=1}^{m} Em^k(P_k) \\ &s.t. \begin{cases} P_{k,min} \le P_k \le P_{k,max} \\ P_{load} + P_{loss} = P_{MG} + \sum_{k=1}^{N} P_k \end{cases} \end{aligned} \quad . \tag{12}$$

It is assumed that the total energy losses remain constant during the regular operation of the port microgrid. It was solved by using the centralized method and the distributed method based on the leader-following consensus algorithm (Huang et al., 2016), respectively. The results of the operation of each generating equipment in the port microgrid are shown in Table 2.

According to Table 2, the centralized method and the leader-following consensus method result in different operating costs for the port microgrid, namely 30,821 Yuan and 30,801 Yuan, respectively.

4.3 Case 2: Traditional port microgrid energy management model with P_{rk}

$$\begin{aligned} &\min \quad F(P_r) = \sum_{k=1}^{N} C_{ok}(P_{rk}) + P_{rg} P_{MG} \\ &s.t. \quad \begin{cases} \sum_{k=1}^{N} P_k + P_{MG} = P_{load} + P_{loss} \\ P_k^{min} \le P_k \le P_k^{max} \end{cases} \end{aligned} \quad . \tag{13}$$

In this study case, the load demand, transmission line energy losses, and main grid electricity price are kept constant in the port microgrid, and a distributed method (Liu et al., 2017) is used to solve the port microgrid energy management problem **(13)**. The parameter α is taken as 0.000001, and the incremental cost of the heterogeneous WEs converges around 0.9 when the simulation reaches the 300000th step. The operation of the microgrid is analyzed considering the operating cost of the WEs. Figure 3 shows the simulation curves based on the distributed method. Table 3 shows the output of WEs power generating equipment through different cases.

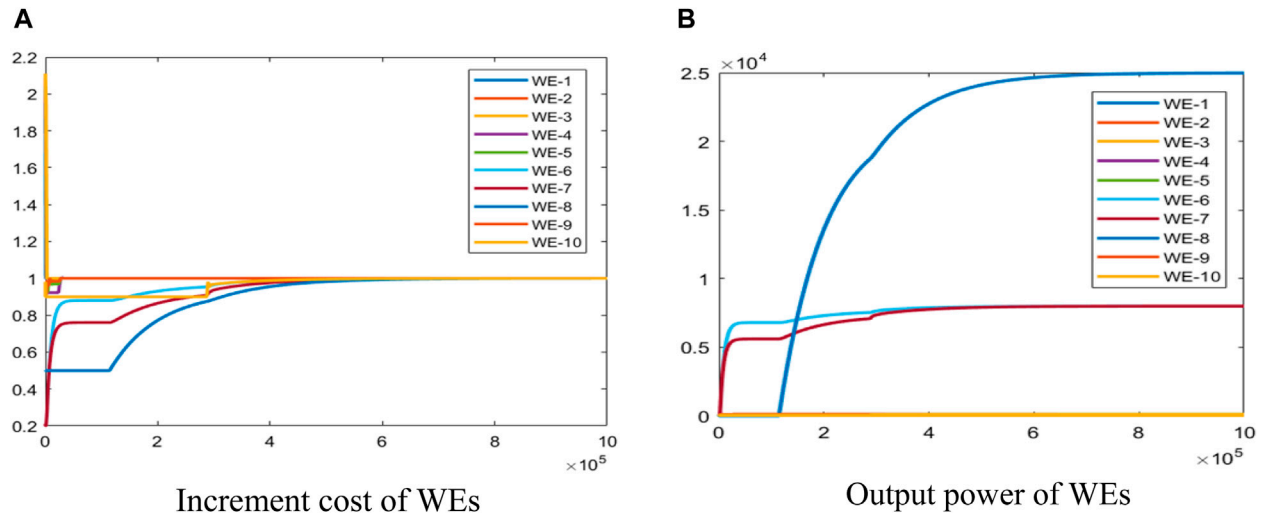

FIGURE 3
Operating curves of WEs. **(A)** Increment cost of WEs. **(B)** Output power of WEs

TABLE 3 Operating data of WEs by using the distributed method.

	WE-1	WE-2	WE-3	WE-4	WE-5
Case 2	37.5	37.5	37.5	122.7	122.7
Case 3	37.5	37.5	37.5	122.6	122.5
	WE-1	WE-2	WE-3	WE-4	WE-5
Case 2	7997.6	7997.6	24979.5	112.5	112.5
Case 3	7997.5	7997.4	24986.9	112.5	112.5
Port microgrid	Case 2	Operating cost	30381.0	Carbon emissions cost	413.2
	Case 3		30792.0		412.7

As can be seen from Figure 3, the incremental cost of WEs is ultimately 1.0 Yuan per kWh. In the port microgrid, TWEs are operating, and there is not only the operating cost of the WE but also carbon emissions cost. According to Table 3, the operating cost of the port microgrid during regular operation of the heterogeneous WEs is 30,381 Yuan. This case has a lower operating cost compared with Case 1 without carbon emissions cost.

4.4 Case 3: The proposed model and method

In this case, the distributed method **(11)** proposed in this article is used to solve the energy management problem **(9)** for the port microgrid. It is assumed that load demand, transmission line energy losses, and main grid electricity price in the port microgrid remain constant. α is taken as 0.000000015, and the incremental cost of the heterogeneous WEs converges around 1.0 when the simulation reaches the 300000th step. Figures 4 and 5 show the simulation curves obtained based on the distributed method.

A comparative analysis between Case 3 and Case 1 shows that the power output of heterogeneous WEs does not differ significantly under the three solution methods. Therefore, the distributed method proposed in this paper can enable port microgrid energy management. As can be seen from Figure 4, the incremental cost of WEs converges to 1.0 Yuan per kWh when the port microgrid is operating steadily. The output power and operating cost of the heterogeneous WEs in the port microgrid during regular operation can be seen in Table 3. The operating cost of the port microgrid is 30,792 Yuan, of which the cost of carbon emissions is 412.7 Yuan. In this study case, there are not only low operating costs but also low carbon emissions.

A comparison between Case 1 and Case 3 shows that the distributed solution method proposed in this article can solve the port microgrid energy management problem, indicating

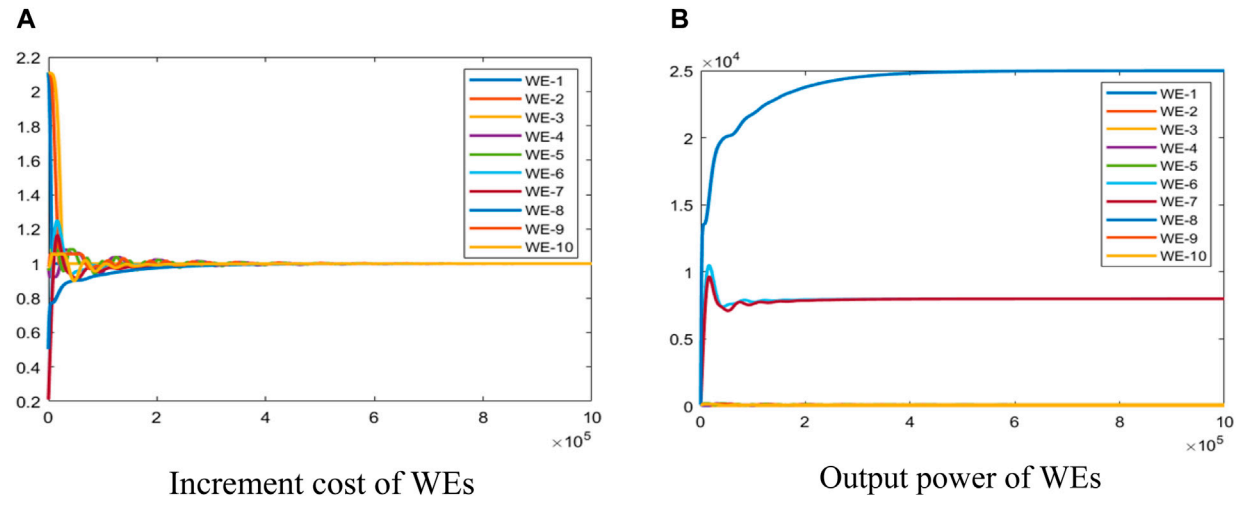

FIGURE 4
Operating curves of WEs. **(A)** Increment cost of WEs. **(B)** Output power of WEs

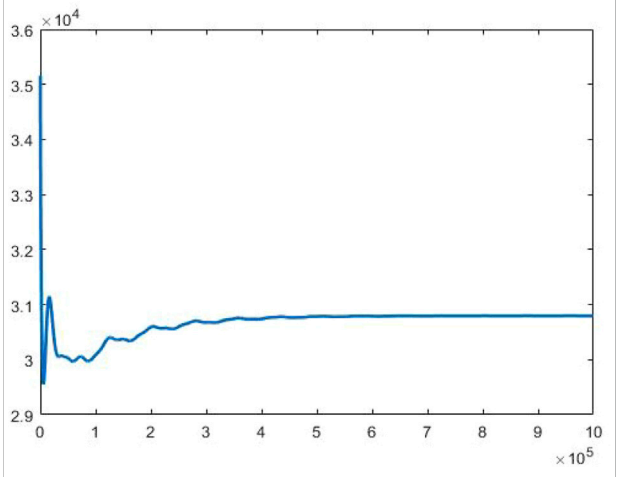

FIGURE 5
Operating cost of the port microgrid.

the effectiveness of the distributed solution method proposed in this article. In addition, Case 3 has lower operating costs compared with Case 1. The comparison between Case 2 and Case 3 shows that Case 3 is able to maximize the use of clean energy, which not only reduces the operating cost of the port microgrid but also reduces carbon emissions, contributing to the development of a green and low-carbon port.

5 Conclusion

The large-scale use of clean energy in port microgrids has given rise to WEs in the port, and the widespread presence of WEs has made the port microgrid a distributed structure. A distributed energy management strategy for WE-based port microgrid under a polymorphic network has been proposed in this article. First, this article has established a polymorphic energy management system for port microgrids based on WEs, ensuring reliable information interaction between heterogeneous WEs, including SWEs, and laying the foundation for the subsequent implementation of distributed energy management. Then, considering the characteristic of bidirectional energy transmission between WEs in the port, the operating cost function of WEs has been analyzed and established. Furthermore, an energy management model for the port microgrid has been constructed considering both the operating cost and the carbon emissions of WEs. Finally, this article has proposed a distributed method to solve the energy management problem of the port microgrid based on the multi-agents consensus method. Through the comparison and analysis of different simulation cases, it has been concluded that the method proposed in this article can not only reduce the operating cost of the port microgrid but also reduce carbon emissions, which can help the development and construction of the green low-carbon port.

Data availability statement

The original contributions presented in the study are included in the article/Supplementary Material; further inquiries can be directed to the corresponding author.

Author contributions

HL constructed the polymorphic energy management system for the port microgrid. FT built the model, designed the method, and adapted the article. The experimental simulations, data processing, and draft writing were carried out by JW. QZ collated and revised the format of the references. CS participated in proofreading and organizational management. All authors have read and agreed to the publication of the manuscript.

Funding

This research was supported by the National Key R&D Program of China (2019YFB1802501), the Key Research Project of Zhejiang Lab (2021LE0AC02), the National Natural Science Foundation of China (under Grant Nos. 51939001, 61976033, 61751202, 61903092, and U1813203), the Science and Technology Innovation Funds of Dalian (under Grant No. 2018J11CY022), and the Liaoning Revitalization Talents Program (under Grant Nos. XLYC1908018 and XLYC1807046).

Conflict of interest

The authors declare that the research was conducted in the absence of any commercial or financial relationships that could be construed as a potential conflict of interest.

Publisher's note

All claims expressed in this article are solely those of the authors and do not necessarily represent those of their affiliated organizations, or those of the publisher, the editors, and the reviewers. Any product that may be evaluated in this article, or claim that may be made by its manufacturer, is not guaranteed or endorsed by the publisher.

References

Alamoush, A. S., Ballini, F., and Ölçer, A. I. (2020). Ports' technical and operational measures to reduce greenhouse gas emission and improve energy efficiency: a review. *Mar. Pollut. Bull.* 160 (2020), 111508. doi:10.1016/j.marpolbul.2020.111508

Çağatay, I., and Jasmine, S. L. L. (2019). A review of energy efficiency in ports: Operational strategies, technologies and energy management systems. *Renew. Sustain. Energy Rev.* 112, 170–182. doi:10.1016/j.rser.2019.04.069

Çağatay, I., and Jasmine, S. L. L. (2021). Optimal energy management and operations planning in seaports with smart grid while harnessing renewable energy under uncertainty. *Omega* 103 (2021), 102445. doi:10.1016/j.omega.2021.102445

Coppola, T., Fantauzzi, M., Lauria, D., Pisani, C., and Quaranta, F. (2016). A sustainable electrical interface to mitigate emissions Due to power supply in ports. *Renew. Sustain. Energy Rev.* 54, 816–823. doi:10.1016/j.rser.2015.10.107

Fang, S., Wang, Y., Gou, B., and Xu, Y. (2020). Toward future green maritime transportation: An overview of seaport microgrids and all-electric ships. *IEEE Trans. Veh. Technol.* 69 (1), 207–219. doi:10.1109/TVT.2019.2950538

Gennitsaris, S. G., and Kanellos, F. D. (2019). Emission-aware and cost-effective distributed demand response system for extensively electrified large ports. *IEEE Trans. Power Syst.* 34 (6), 4341–4351. doi:10.1109/TPWRS.2019.2919949

Hein, K., Xu, Y., Gary, W., and Gupta, A. K. (2021). Robustly coordinated operational scheduling of a grid-connected seaport microgrid under uncertainties. *IET Gener. Transm. Distrib.* 15 (2), 347–358. doi:10.1049/gtd2.12025

Hu, Y., Li, D., Sun, P., Yi, P., and Wu, J. (2020). Polymorphic smart network: An open, flexible and universal architecture for future heterogeneous networks. *IEEE Trans. Netw. Sci. Eng.* 7 (4), 2515–2525. doi:10.1109/TNSE.2020.3006249

Hu, Y., Yi, P., Sun, P., and Wu, J. (2019). Research on the full-dimensional defined polymorphic smart network. *J. Commun.* 40 (08), 1–12. doi:10.11959/j.issn.1000–436x.2019192

Huang, B., Li, Y., Zhang, H., and Sun, Q. (2016). Distributed optimal Co-multi-microgrids energy management for energy internet. *IEEE/CAA J. Automatica Sinica* 3 (4), 357–364. doi:10.1109/JAS.2016.7510073

Huang, Y., Huang, W., Wei, W., Tai, N., and Li, R. (2022). Logistics-energy collaborative optimization scheduling method for large seaport integrated energy system. *Proc. CSEE*, 1–12. doi:10.13334/j.0258-8013.pcsee.211093

Kanellos, F. D. (2019). Multiagent-system-based operation scheduling of large ports' power systems with emissions limitation. *IEEE Syst. J.* 13 (2), 1831–1840. doi:10.1109/JSYST.2018.2850970

Kanellos, F. D., Volanis, E. M., and Hatziargyriou, N. D. (2019). Power management method for large ports with multi-agent systems. *IEEE Trans. Smart Grid* 10 (2), 1259–1268. doi:10.1109/TSG.2017.2762001

Kermani, M., Parise, G., Shirdare, E., and Martirano, L. (2020). "Transactive energy solution in a port's microgrid based on blockchain Technology," in 2020 IEEE international conference on environment and electrical engineering and 2020 IEEE industrial and commercial power systems europe (EEEIC/I&CPS europe), Madrid, Spain, 09-12 June 2020, 1–6. doi:10.1109/EEEIC/ICPSEurope49358.2020.9160833

Li, Y., Gao, D. W., Gao, W., Zhang, H., and Zhou, J. (2021). A distributed double-Newton descent algorithm for cooperative energy management of multiple energy bodies in energy internet. *IEEE Trans. Ind. Inf.* 17 (9), 5993–6003. doi:10.1109/TII.2020.3029974

Li, Y., Gao, D. W., Gao, W., Zhang, H., and Zhou, J. (2020). Double-mode energy management for multi-energy system via distributed dynamic event-triggered Newton-raphson algorithm. *IEEE Trans. Smart Grid* 11 (6), 5339–5356. doi:10.1109/TSG.2020.3005179

Liu, Q., Yang, S., and Hong, Y. (2017). Constrained consensus algorithms with fixed step size for distributed convex optimization over multiagent networks. *IEEE Trans. Autom. Contr.* 62 (8), 4259–4265. doi:10.1109/TAC.2017.2681200

Nikolaos, S., and Theocharis, T. (2021). Planning zero-emissions ports through the nearly zero energy port concept. *J. Clean. Prod.* 286 (2021), 125448. doi:10.1016/j.jclepro.2020.125448

Olivares, D. E., Cañizares, C. A., and Kazerani, M. (2014). A centralized energy management system for isolated microgrids. *IEEE Trans. Smart Grid* 5 (4), 1864–1875. doi:10.1109/TSG.2013.2294187

Parise, G., Parise, L., Martirano, L., Chavdarian, P. B., Su, C., and Ferrante, A. (2016). Wise port and business energy management: port facilities, electrical power distribution. *IEEE Trans. Ind. Appl.* 52 (1), 18–24. doi:10.1109/TIA.2015.2461176

Pourakbari-Kasmaei, M., Lehtonen, M., Contreras, J., and Mantovani, J. R. S. (2020). Carbon footprint management: a pathway toward smart emission

abatement. *IEEE Trans. Ind. Inf.* 16 (2), 935–948. doi:10.1109/TII.2019.2922394

Shan, Q., Zhang, X., Zhang, Q., Sun, Q., and Cai, N. (2022). Distributed energy management for port power system under false data injection attacks. *Autom* 102 (2019), 34–44. doi:10.1155/2022/5995281

Sun, Q., Fan, R., Li, Y., Huang, B., and Ma, D. (2019). A distributed double-consensus algorithm for residential we-energy. *IEEE Trans. Ind. Inf.* 15 (8), 4830–4842. doi:10.1109/TII.2019.2921431

Sun, Q., Wang, R., Ma, D., and Liu, Z. (2017). An islanding control strategy research of we-energy in energy internet. *Proc. CSEE* 37 (11), 3087–3098+3364. doi:10.13334/j.0258-8013.pcsee.161002

Tang, R., Li, X., and Lai, J. (2018). A novel optimal energy-management strategy for A maritime hybrid energy system based on large-scale global optimization. *Appl. Energy* 228 (2018), 254–264. doi:10.1016/j.apenergy.2018.06.092

Wen, S., Zhao, T., TangXu, Y, Y., Zhou, M., Zhu, M., Fang, S., et al. (2021). Coordinated optimal energy management and voyage scheduling for all-electric ships based on predicted shore-side electricity price. *IEEE Trans. Ind. Appl.* 57 (1), 139–148. doi:10.1109/TIA.2020.3034290

Yang, T., Yi, X., Wu, J., Yuan, Y., Wu, D., Meng, Z., et al. (2019). A survey of distributed optimization. *Annu. Rev. Control* 47 (2019), 278–305. doi:10.1016/j.arcontrol.2019.05.006

Zhang, Q., Shan, Q., and Li, T. (2020). "Large port energy management based on distributed optimization," in 2020 7th international conference on information, cybernetics, and computational social systems (ICCSS), Guangzhou, China, November 13–15, 2020, 108–113. doi:10.1109/ICCSS52145.2020.9336919

Zhang, Y., Shan, Q., Teng, F., and Li, T. (2021). Distributed economic optimal scheduling scheme for ship-integrated energy system based on load prediction algorithm. *Front. Energy Res.* 9, 720374. doi:10.3389/fenrg.2021.720374

frontiers | Frontiers in Energy Research

ORIGINAL RESEARCH
published: 25 July 2022
doi: 10.3389/fenrg.2022.953485

Green Polymorphic Cooperative Formation Strategy of Low-Carbon Unmanned Surface Vessels

Yuzhou Lu[1], Qihe Shan[1], Geyang Xiao[2]*, Yuan Liang[2] and Wei Liu[1]*

[1]Navigation College, Dalian Maritime University, Dalian, China, [2]Research Institute of Intelligent Networks, Zhejiang Lab, Hangzhou, China

At the current stage of a global energy shortage, the optimization of marine energy consumption has received attention. In order to save marine energy consumption and reduce pollution, research on low-energy-consumption Unmanned Surface Vessels (USVs) and their green and low-carbon cooperative operation methods needs to be paid attention to. Due to the ever-changing environment of USVs in actual sea conditions and the increasingly complex tasks, the cooperation of a single swarm of USVs is incompetent. First, in order to cope with larger-scale and complex tasks, we construct the multilateral cooperative control system for USVs with topology scalability under a polymorphic network and propose the multilateral distributed control protocol. Second, in order to reduce the energy consumption of the cooperative operation of USVs, the low-energy-consumption and low-carbon USVs are selected with the lowest EEOI index as the optimization goal, and based on ad hoc on-demand distance vector routing (AODV), the optimal path between USVs is obtained. Then, the swarms are grouped by External Equitable Partition (EEP), and the green autonomous cooperative formation strategy is proposed. Finally, the simulation examples are used to verify the effectiveness of the method proposed in this article.

Keywords: low-carbon USV, polymorphic network, low-energy consumption, multilateral distributed control protocol, green autonomous cooperative formation strategy

OPEN ACCESS

Edited by:
Bonan Huang,
Northeastern University, China

Reviewed by:
Yongfeng Gao,
Dalian University of Technology, China
Xiting Peng,
Shenyang University of Technology, China
Peiyuan Guan,
University of Oslo, Norway

****Correspondence:***
Qihe Shan
shanqihe@163.com
Geyang Xiao
xgyalan@outlook.com

Specialty section:
This article was submitted to Smart Grids, a section of the journal Frontiers in Energy Research

Received: *26 May 2022*
Accepted: *20 June 2022*
Published: *25 July 2022*

Citation:
Lu Y, Shan Q, Xiao G, Liang Y and Liu W (2022) Green Polymorphic Cooperative Formation Strategy of Low-Carbon Unmanned Surface Vessels. Front. Energy Res. 10:953485. doi: 10.3389/fenrg.2022.953485

1 INTRODUCTION

Due to the lack of global energy and serious marine pollution, the pressure on energy conservation and emission reduction is unprecedented, and it is necessary to strengthen the work of saving energy, reducing consumption, and reducing the pollution of ships (Źarko et al., 2021; Yushuai et al., 2021). Under such environmental conditions, it has become the general trend to vigorously develop and use green USVs.

USV is an intelligent system that is unmanned (Zhenyu and Ge, 2018), green, and energy-saving (Bertaska et al., 2015) and navigates on the water surface by remote control or autonomous means (Zheng et al., 2021; Sharma et al., 2012). It has the characteristics of low cost, small size, and high controllability (Rui et al., 2017). A single USV has major limitations in its operations—a limited mission area, a lack of system autonomy, and a lack of sufficient fault tolerance. With the development of the marine economy and technology, mission-oriented USVs emerge as the times require, which consist of multiple USVs and operate in a swarm mode (Joseph et al., 2005). In the process of driving or when performing a certain task, maintaining a certain formation can greatly improve the work efficiency of task completion (Lewis and Tan, 1997) and has high fault

tolerance and robustness (Zhengfeng et al., 2021). The USV control technology has continuously made new research progress. In the process of the development, it gradually established a USV autonomous cooperative control theory that meets the clustered marine operation tasks under the complex environment, with the characteristics of high reliability, high precision, strong adaptation, anti-interference, autonomous cooperation, low carbon, low-energy consumption, and the capabilities of fast swarm task response, cluster formation reconstruction, and transformation (Yan et al., 2021; Zhouhua et al., 2021). As a typical agent, the USVs' cooperative control can be researched and designed based on a multi-agent system (MAS). The agents in the system use appropriate communication routing protocols and distributed cooperative control methods to make their states consistent (Garey and David, 1978; Durfee and Corkill, 1989), to solve the resource allocation problem (Qiaoyun et al., 2007; Chou and Abraham, 1982), the task division problem (Lei and Qi, 2002), and the communication problem between agents (Smith, 1980).

Due to the constantly changing environment of USVs under actual sea conditions and the increasingly complex tasks they face, the cooperation of a group of USVs is often incompetent under some special conditions, requiring USVs with different functions under a variety of different morphic networks to jointly perform tasks. For example, when performing a maritime search, rescue, and salvage tasks, the USV formation responsible for communication with the ground, salvage, and transportation needs to work together, though these three kinds of USVs, each with their own mission objectives, use different control algorithms under different communication networks. The key to distributed cooperative control is the information interaction between neighbor USVs. However, multiple groups of USVs are in different unilateral communication networks. After regrouping, they cannot directly exchange information and thus cannot achieve cooperative control under the traditional communication network. Therefore, the polymorphic network architecture has been proposed, of which the basic idea is to design an open network architecture with the characteristics of a "reconfigurable network" based on a fully dimensional definable platform (Julong et al., 2014), to meet the needs of the diversified development of the multilateral network (Jiangxing and Yuxiang, 2021; Li et al., 2019) and have achieved the goals of multilateral co-management, equality and openness, and high performance (Hui et al., 2019). The polymorphic network development paradigm adopts the idea of separating the network from the supporting environment and combines various existing or future networks (including business or service or management functions) in a modal form, dynamically loading and running a definable network support environment on the full dimension. Realize the symbiotic coexistence, independent evolution, and transformation of multiple network modalities in the same technical and physical environment (Jiangxing and Kaizhi, 2022) according to the modal customized software and hardware configuration, message format, routing protocol, exchange mode, forwarding logic, business characteristics, operation and maintenance specifications, security policies, etc. To sum up, the polymorphic network provides a channel for the communication required by the USVs under multiple unilateral communication networks. Therefore, in the face of increasingly complex working conditions and mission requirements, when designing the communication network between the different groups of USVs, we cannot borrow from the design concept of the traditional unilateral communication network because these USVs have the characteristics of independence, autonomy, cooperation, distribution, and heterogeneity. Also, it is necessary to build a multilateral distributed cooperative control system for USVs under a polymorphic network. The meaning of multilateral distributed cooperative control refers to the task-oriented regrouping of multiple groups of USVs under the polymorphic network by constructing a reasonable communication topology and designing a suitable routing protocol and distributed control protocol, in which case all USVs in each group can maintain communication with each other after regrouping, and the state eventually tends to be consistent. In this way, the cooperative control of multiple groups of USVs with different functions is realized. When designing a new communication network, we should consider the characteristics of distributed, multilateral co-management, plug-and-play, equal openness, scalable structure, and at the same time meeting the control requirements of each group of USVs. It is in line with the characteristics of polymorphic networks, so the future cooperative control of USVs will rely on polymorphic networks. Therefore, the polymorphic network is the basis for realizing the cooperative control of green USVs.

To develop green shipping, reduce marine pollution, and reduce carbon emissions, driven by specific tasks, how to build a low-carbon and low-energy-consumption USVs under the polymorphic network to efficiently and greenly achieve multilateral cooperative control is an issue that requires further research. Green and energy-saving USVs should be selected to achieve energy saving and emission reduction. The energy utilization efficiency of USVs can be evaluated by EEOI (the Ship Energy Efficiency Operational Indicator), which is an evaluation obtained by comprehensively considering the ship's cargo capacity, sailing distance, fuel consumption, greenhouse gas emissions, and other factors (Chon et al., 2019). The smaller the EEOI index, the higher the energy efficiency of the ship. The reduction of EEOI can be achieved by optimizing the speed of the ship, the route, rational stowage, recovering the waste heat from the main engine exhaust gas, and using clean energy with low CO_2 emissions (Jingmin, 2016). Based on the EEOI index, the energy efficiency index of the selectable USVs can be quantified, and the low-carbon and low-energy-consumption USVs can be selected. For the selected green USVs under the polymorphic network, although the information exchange between multiple groups of USVs can be realized, the temporary network cannot guarantee the realization of multilateral distributed cooperative control. Therefore, there are two key issues that need to be studied: one is how to analyze and reorganize the USVs originally under a unilateral communication network considering some suitable conditions, and the other one is how to design a reasonable ad hoc network topology and realize multilateral distributed cooperative control based on multi-agent multi-consensus theory (Olfati-Saber et al., 2007; Gambuzza and Mattia, 2019). The ad hoc network of the USVs adopts a distributed structure, and

each node in the network has an equal status and makes independent decisions (Scott, 2013). Also, these nodes form the network in a self-organization manner (Scott et al., 2003), which makes the network have strong stability, openness, and invulnerability (Xueli et al., 2017; Yang et al., 2021). Adopting the AODV protocol is beneficial to save energy when USV exchange information (Bhagyalakshmi and Dogra, 2018; Mohsen and Naif, 2019) and obtain the optimal path for inter-swarm communication (Yuan et al., 2007; Qiang et al., 2011). Therefore, how to use the fewest routes to reorganize the selected low-carbon and low-energy-consumption USVs, build the topology of the ad hoc network of multiple groups of USVs in a green and low-energy-consumption manner, and design a multilateral distributed cooperative control strategy is a concerning issue.

In order to solve the aforementioned problems, under the polymorphic network, a green autonomous cooperative formation strategy for multiple groups of USVs is proposed to achieve low-carbon and low-energy-consumption multilateral cooperative control, which can cope with the current large-scale and complex maritime tasks, helping the shipping industry reduce pollution and carbon emission. Also, the contributions are as follows:

1) Utilize the EEOI index to quantify the energy efficiency operation index of the USVs under the optional unilateral communication network and construct a low-carbon and low-energy-consumption restructured USVs. Based on the AODV protocol of the wireless ad hoc network, the optimal network routing of the USVs is established so as to complete the low-energy-consumption networking of multiple groups of USVs.
2) According to the EEP, the multiple groups of USVs are reasonably grouped, and the communication topology reconstruction method is proposed under the polymorphic network. Also, based on the multi-agent multi-consensus algorithm, a green autonomous cooperative formation strategy of multiple groups of USVs is proposed to realize multilateral distributed cooperative control.

The rest of this article can be written as follows: in **Section 2**, the multilateral distributed cooperative control framework is introduced. In **Section 3**, we introduce some basic theoretical knowledge. In **Section 4**, we propose the communication topology reconstruction method and green autonomous cooperative formation strategy for multiple groups of USVs. In **Section 5**, we conduct an experimental simulation and analyze the data generated by the experiment.

2 LOW-ENERGY-CONSUMPTION MULTILATERAL DISTRIBUTED COOPERATIVE CONTROL FRAMEWORK FOR LOW-CARBON UNMANNED SURFACE VESSELS

The low-energy-consumption multilateral distributed cooperative control framework of multiple groups of USVs is an ad hoc network system based on the polymorphic network, as shown in **Figure 1**. It can independently complete the networking process with the characteristics of distributed, plug-and-play, and scalable structure (Shirani et al., 2012). Multiple groups of USVs respond quickly and efficiently according to mission requirements. Under the polymorphic network, low-energy-consumption and low-carbon USVs are selected based on the EEOI index for re-networking. Meanwhile, based on AODV and EEP, the task-oriented routing protocol and communication topology of the reorganized low-energy-consumption and low-carbon USVs are designed to realize low-energy-consumption multilateral distributed cooperative control. Finally, green autonomous cooperative formation can be realized.

The framework is designed with the following core thinking: In the face of large-scale and complex maritime tasks, it is no longer completed by a single USV under the traditional unilateral communication network. Instead, it is realized by multiple groups of MAS composed of multiple low-carbon USVs under the polymorphic network through low-energy-consumption multilateral distributed cooperative control. When USVs perform tasks, after receiving the task sent by the base station on the shore, all agents should only rely on the information exchange between each other. Also, some agents with sufficient energy and low EEOI index are selected as virtual leaders to form a temporary MAS with their surrounding neighbors and are responsible for communicating with other agents in the MAS and with virtual leaders of other MASs. Through the appropriate routing protocol and communication topology, a low-energy-consumption multilateral distributed cooperative control system with autonomous and dynamic connection functions is established to realize green autonomous cooperative formation. When the task is completed, the MASs are eliminated, and all agents maintain the same level. With the new task generating, a new low-energy-consumption multilateral distributed cooperative control system will be formed.

The multilateral distributed cooperative control framework of multiple groups of USVs consists of two levels, namely, the task sender and the task executor. The task sender is to analyze and evaluate the task risk and difficulty level, divide the task reasonably, and send the task to USVs. The task executor, that is, the MAS corresponding to each group of USVs, can choose to accept or reject the tasks assigned by the nearby task senders through information exchange according to its own situation. When accepting tasks, it can form a cooperative control system with other MASs to achieve low-energy-consumption multilateral distributed cooperative control. The specific operation steps are as follows:

Step 1: Task sending. In the Part 1 of **Figure 1**. Analyze and evaluate the risks and difficulties of maritime tasks and deploy tasks to USVs through base stations on the shore.

Step 2: Task acceptance. The USVs accept the task and evaluate the energy consumption of the USV to perform the task according to the EEOI index of each USV. In the Part 2 of **Figure 1** shows the green USVs selected based on the EEOI index. The green USV with low carbon and low-energy consumption is selected as the virtual leader, accepts the assigned task, and forms a MAS with the green

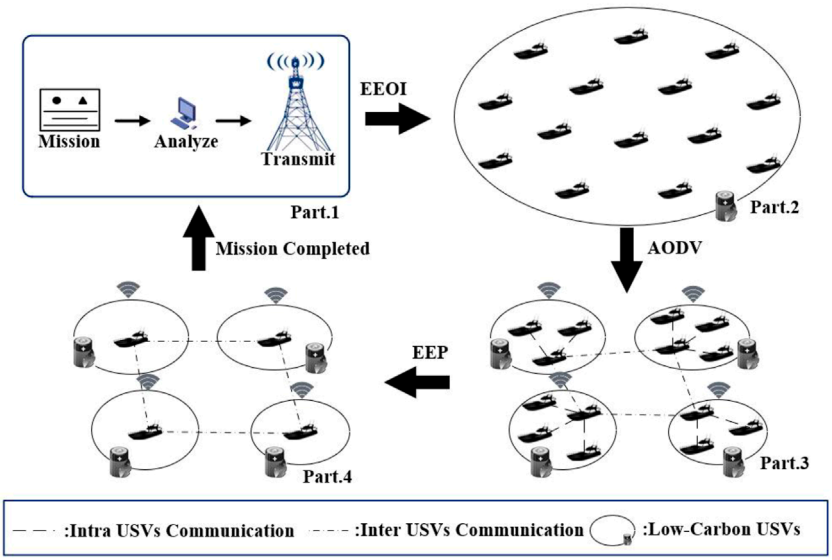

FIGURE 1 | Low-energy-consumption multilateral distributed cooperative control framework for multiple USVs.

USV with low carbon and low-energy consumption within a suitable distance in which the state of the USV can achieve consensus. The virtual leader is also responsible for establishing communication with virtual leaders of other MASs. As shown in the Part 3 of **Figure 1**, all virtual leaders form a temporary ad hoc network, temporarily forming a simple low-energy-consumption multilateral distributed cooperative control system. The selection principles of USVs with low carbon and low-energy consumption are as follows:

$$\min \sum_{i=1}^{n} EEOI_i = \frac{\sum_j FC_j \times C_{Fj}}{m_{cargo} \times D},$$

where $EEOI_i$ is the EEOI index of the i-th USV, j is the fuel type, FC_j is the sailing fuel consumption, C_{Fj} is the carbon dioxide conversion coefficient, m_{cargo} is the cargo capacity, and D is the cargo distance.

Step 3: Task execution. According to the specific requirements of the tasks accepted by the MAS composed of each USV, as shown in the Part 4 of **Figure 1**, the optimal routing design and structural topology design are carried out for the temporary ad hoc network of the virtual leaders of all MASs. The reconstructed ad hoc network realizes communication and achieves a multi-consistency state with the least routing and realizes low-energy-consumption multilateral distributed cooperative control to perform tasks.

Step 4: Mission complete. When a mission is completed, the cooperative control system disbands itself, the MAS of all USVs is disbanded, and the virtual leaders disconnect from communication and restore independence and maintain the same level of status as other USV agents. The entire system waits for the next task assignment, maintains the state in the Part 1 of **Figure 1**, and re-organizes the network according to the tasks and according to the above four steps.

The aforementioned multilateral distributed cooperative control framework of multiple groups of USVs is a kind of ad hoc network designed in the polymorphic network environment according to the actual characteristics of the application scenario. The low-carbon and low-energy-consumption USVs agents in this scene have a certain specificity in moving and performing different tasks; therefore, the constructed low-energy-consumption multilateral distributed cooperative control framework of the USVs not only inherits the characteristics of the polymorphic network and ad hoc network but also has the characteristics of green energy saving, pollution reduction, and carbon reduction. This framework can realize the green autonomous cooperative formation of multiple groups of USVs.

3 PRELIMINARIES

3.1 Graph Theory

MAS is a loosely coupled system composed of multiple agents, which aims to describe the connection between agents in the system, reveal the information and control relationship between agents, and reflect the storage and sharing methods of information in the system and the distribution pattern of problem-solving capabilities. The network structure of the MAS system is represented by matrix $\mathcal{G} = (\mathcal{V}, \mathcal{E}, \mathcal{A})$, where the number of nodes (or vertices) in the network is n, the number of edges (or links) is e, $\mathcal{V} = \{w_1, w_2, \ldots, w_n\}$ is used to represent a set of finite non-empty node sets, and $\mathcal{E} \subseteq \mathcal{V} \times \mathcal{V}$ is the edge formed by the nodes in $\mathcal{G}$. The edge represents the communication relationship

between nodes. Then, for any two nodes $w_i, w_j \in \mathcal{V}$, where $i \neq j$, there is $(w_i, w_j) \in \mathcal{E}$, and it is said that w_i and w_j can communicate with each other. Each edge has a corresponding value, that is, a weight, and the weight of the edge can be positive or negative according to the direction. The adjacency matrix of the system is $\mathcal{A} = [w_{ij}]_{n\times n}$, if $(w_i, w_j) \in \mathcal{E}$, then $w_{ij} = 1$, otherwise $w_{ij} = 0$, where $i \neq j$; the degree matrix of the system is $\mathcal{D} = diag\{d_1, d_2, \ldots, d_n\}$, where $d_i = \Sigma_{j\neq i} w_{ij}$.

The Laplace matrix of the system is $\mathcal{L}(\mathcal{G}) = [l_{ij}]_{n\times n}$:

$$l_{ij} = \begin{cases} \sum_{j\neq i} w_{ij}, & i = j \\ -w_{ij}, & i \neq j \end{cases}$$

It satisfies the relation:$\mathcal{L}(\mathcal{G}) = \mathcal{D} - \mathcal{A}$.

3.2 Unmanned Surface Vessel Model

The dynamic equation of the considered low-carbon and low-energy-consumption USV is as follows (Alslaim et al., 2016):

$$\dot{\eta} = R(\psi)\nu, \tag{1}$$

$$M\dot{\nu} + C(\nu)\nu + D(\nu)\nu + g(\nu, \eta) = w + \tau, \tag{2}$$

where $\eta = [x, y, \psi]^T \in \Re^3$ is used to denote the position and heading of the USV. $R(\psi) \in \Re^{3\times3}$ is a given rotation matrix, $\nu = [u, v, r]^T \in \Re^3$ is the surge, sway, and yaw velocities in the ship reference frame. $M \in \Re^{3\times3}$ is the inertia matrix. $D(\nu) \in \Re^{3\times3}$ is the nonlinear damping matrix. $C(\nu) \in \Re^{3\times3}$ is the Coriolis-centripetal matrix. τ, w, and (ν, η) are controller input, disturbance, and unmodeled fluid dynamics, respectively.

3.3 Multi-Agent System

The USV model studied in this article is essentially an agent, and the USVs can be represented by MAS. The research on USVs is carried out by using a MAS controlled by a linear first-order integral. The state of its MAS satisfies the following dynamic equation:

$$\dot{x}_i(t) = Ax_i(t) + Bu_i(t), \tag{3}$$

where $x_i(t) \in \mathbb{R}^n$ is the state of the agent, $u_i(t) \in \mathbb{R}^p$ is the controller input of the system, and A and B are the Laplace matrix corresponding to the state of the agent and the controller, respectively.

Through the dynamic equation in **Eq. 3**, its discrete consistent control equation is obtained

$$\dot{x}_i = -\sum_{j=1}^{n} a_{ij}\left(x_i - x_j\right), \qquad i = 1, 2, \ldots, n, \tag{4}$$

which is

$$\dot{x} = -\mathcal{L}x, \tag{5}$$

where $\mathcal{L}$ is the Laplace operator of MAS.

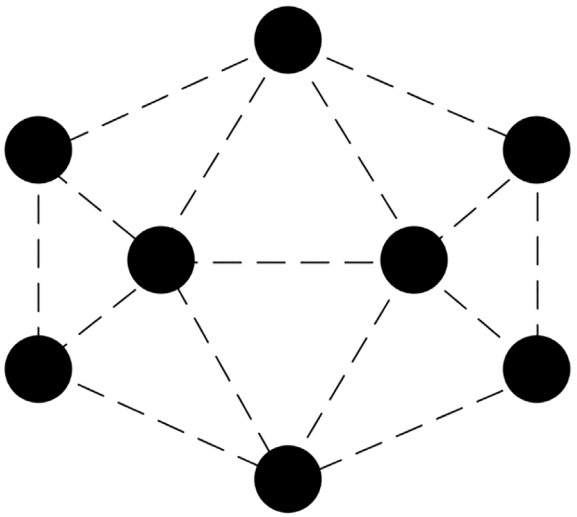

FIGURE 2 | Schematic diagram of ad hoc network structure.

3.4 Mobile Ad Hoc Networks

Mobile ad hoc network (MANET) refers to a network that is temporarily composed of mobile nodes through wireless communication in which these nodes act as routers for each other to forward packets without relying on any fixed infrastructure and services. Due to the transmission coverage of mobile nodes being so limited that long-distance communication generally needs to be carried out by means of multi-hop transmission, mobile networks are also called mobile multi-hop wireless networks. The schematic diagram of the mobile ad hoc network is shown in **Figure 2**. Its operation is completely distributed, and the tasks related to network control and organization are all assigned to each node. Due to the independence of nodes, the networking of ad hoc networks has quite significant characteristics compared with other communication networks (Lei et al., 2011), i.e., distributed ad hoc architecture, wireless transmission technology, multi-hop routing, and mobile network topology.

4 GREEN AUTONOMOUS COOPERATIVE CONTROL METHOD FOR MULTIPLE GROUPS OF LOW-ENERGY-CONSUMPTION UNMANNED SURFACE VESSELS

When multiple groups of USVs perform ad hoc networks based on polymorphic networks and perform large-scale and complex maritime tasks due to the differences in the EEOI index as well as communication distance and control algorithm of each USV in the swarm, and when designing the ad hoc network of USVs, USV with low-carbon and low-energy-consumption is first selected as the virtual leader agent according to the earlier indicators. With the virtual leader agent as the center, the low-carbon and

low-energy-consumption USVs within a certain communication range form a MAS, and then multiple MASs form a low-energy-consumption multilateral distributed cooperative control system. To realize the low-energy-consumption multilateral cooperative control of multiple groups of USVs, first an ad hoc network is established between low-carbon and low-energy-consumption virtual leader agents through a suitable routing protocol, and then an appropriate topology design is carried out for the ad hoc network so that the entire cooperative control system can meet the multi-consensus requirements; eventually, the green autonomous cooperative formation of multiple groups of low-energy-consumption USVs can be realized.

4.1 Ad Hoc On-Demand Distance Vector Routing Protocol of Low-Energy-Consumption Unmanned Surface Vessels

When performing large-scale and complex tasks in the ocean, the high speed and random movement of USVs without infrastructure or supply measures as well as the changeable wind and waves at sea which affect the channel, posing challenges to the reliability of the routing and the energy of the network system. The routing refers to the process of transmitting information from the source to the destination through the network, and the routing protocol is the regulation that needs to be followed in the routing process. It is also an important mechanism to ensure that the relevant information can be effectively shared among routers. In the ad hoc network of USVs, USVs are affected by the wind and waves, and they always correct their tracks to keep sailing. Therefore, the USVs need to rebuild the topology at a relatively fast speed and transport the data to the destination in a reasonable way.

In the self-organizing network of USVs, commonly used routing protocols are divided into active routing protocols and reactive routing.

The DSDV (Destination-Sequenced Distance Vector) routing protocol is a typical active routing protocol. All USVs using this protocol will actively maintain routes where they can communicate with other nodes while moving. When the state of the USV changes, DSDV will update its state in time. Due to DSDV maintaining and updating the routing network of large-scale USV clusters frequently, although the delay is effectively reduced and network reliability is improved, it increases the operating cost of USVs and significantly increases energy consumption (AL-Dhief et al., 2018).

AODV is a typical reactive routing. USVs using this protocol do not have to maintain the routing at all times, and the protocol takes effect only when information is transmitted between USVs, in which case it can better adapt to the dynamic changes of the link as well as reduce the overhead of mutual communication between nodes. AODV has the characteristics of fast adaptation to a dynamic link environment, low overhead, and support for multicast. The routing algorithm used in this protocol is a dynamic algorithm. Even when the USV is moving at a high speed, the construction of the route can be completed quickly, and the information can be accurately delivered to the destination. If there are some errors, they can be repaired in a relatively short period of time based on a specific repair method, minimizing communication interruption time and thereby reducing the energy consumption of the USV routing network.

Through the introduction of DSDV and AODV protocols and under the condition of limited energy reserve of USVs, choosing the ADOV protocol can make the maintenance process of information more concise and effectively reduce the energy consumption of USVs.

The topology of the USV ad hoc network will continue to change according to the task situation and the surrounding environment, and the energy reserve is limited. To sum up, the AODV protocol is applicable to the continuous topology change, multi-hop, high dynamic, and large-scale USV network. Based on the AODV protocol, the low-energy-consumption USVs will only issue an application to build a route when it has to transmit data, and it is not necessary to maintain the state of the topology during the task execution, which can reduce the routing overhead. If the USV in the middle also has a reply mechanism, it only takes a relatively short time to find a route in this case, and the communication link can be reconfigured in a short time.

Three message types are defined in the AODV routing protocol: Route Request (RREQ) message, Route Reply (RREP) message, and Route Error (RERR) message (Deepak and Anandakumar, 2019), and three node types are defined: source node, intermediate node (forward node), and destination node (destination). If a node in an ad hoc network is to successfully transmit a data message, two conditions must be met:

1) Node w_j is within the transmission range of node w_i, which is

$$|w_i - w_j| \leqslant d. \tag{6}$$

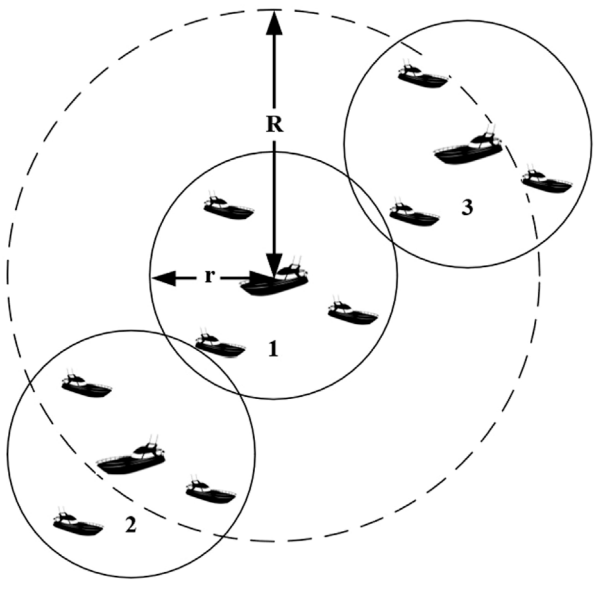

FIGURE 3 | Communication model of USV ad hoc network.

2) At the same time, all other nodes w_j in the network that are sending data packets to the destination node w_k satisfy:

$$|w_k - w_j| \geqslant (1+\Delta)|w_i - w_j \qquad (\Delta > 0), \tag{7}$$

where Δ is a constant greater than zero, representing the protection area.

As shown in **Figure 3**, in USVs 1, the virtual leader communicates with other members in the swarm with a routing distance of radius r, and communicates with the virtual leaders of USVs 2 and USVs 3 with a routing distance of radius R. Suppose to communicate with a swarm with a routing distance greater than R, a communication link needs to be established through the AODV routing protocol.

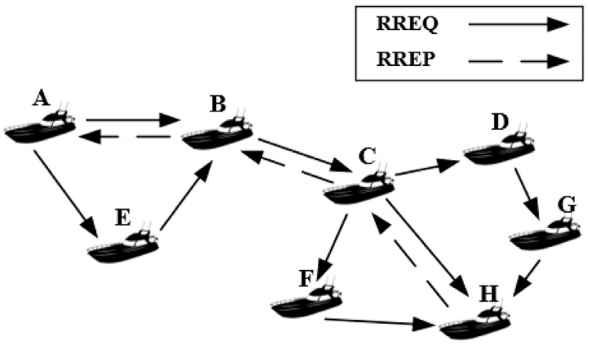

FIGURE 4 | Route establishment process.

4.1.1 Reverse Route Establishment

When the AODV protocol in the ad hoc network of multiple groups of USVs starts to execute, when a USV sends the RREQ message to the destination USV, each node that the RREQ message passes through will be recorded to the reverse path of the source node. After the destination node is found, it is no longer necessary to broadcast the RREQ message. The RREP message will be propagated along this path, and the node that receives the RREQ message records the address of the previous hop node. While establishing a reverse route, sufficient time should be maintained so that the RREQ message traverses the entire network and generates an RREP message to the node sending the RREQ message (Parveen and Chaubey, 2019).

4.1.2 Forward Route Establishment

When the RREQ message reaches the node or destination node that contains the routing information of the destination node, the reverse path will be used to send the RREP message. A forward route is established while forwarding the RREP message. It can be said that the forward route is the opposite of the reverse route. Once the forward route is established, the source node can begin data transfer.

After a certain RREP message is forwarded by a node, it can receive another RREP message. The RREP message is discarded or forwarded, depending on its destination node sequence number. If a new RREP message has a higher destination node sequence number, the route will be updated and the new RREP message will be forwarded. If the destination node sequence number of the old RREP message and the new RREP message is the same and the new RREP message has a smaller hop count, the new RREP message will be preferentially selected and forwarded; otherwise, all RREP messages arriving later will be discarded. Other RREP messages are discarded, which reduces the number of RREP messages transmitted to the source node and ensures the update of routing information. When the source node receives the first RREP message, the source node can start the destination node data transmission (Kitts et al., 2012).

The routing establishment process of the USVs is shown in **Figure 4**. When USV A needs to send a message to the destination USV H, USV A will broadcast an RREQ message to USVs B and E. The USV receiving the RREQ message will judge whether the reverse route needs to be updated according to the number of hops and select the best route according to the principle of the smallest number of hops. When USV B receives the RREQ message from USV A, it will compare whether the IP address of USV B is the same as the destination USV address in the RREQ message. If they are the same, add 1 to the serial number of USV B and generate an RREP message. Otherwise, USV B is not the destination USV. It will update the reverse route to USV A to establish a reverse route and forward the RREQ message to other USVs. By analogy, when the destination USV H receives the RREQ message from USV A, USV H generates an RREP message and returns to USV A along the reverse route. When USV A receives the RREP message from the destination USV H, USV A starts to transmit data. So far, the route selection from USV A to the destination USV H has been completed.

4.2 Topological Design of Unmanned Surface Vessels Based on External Equitable Partition

When studying ad hoc networks of USVs, the network topology is usually represented by the underlying network, which has been extensively studied on the issues of multi-consensus. The topology design of the underlying network of the USVs is carried out by graph division, and the nodes with a constant number of in-degrees are grouped into the same cell. EEP is a typical graph division, and the topology design of the communication network composed of virtual leader agents of each group of USVs in the re-networked multiple groups of low-energy-consumption USVs is performed to achieve green autonomous cooperative formation.

After multiple groups of low-energy-consumption USVs establish an ad hoc network based on the AODV protocol, the network routing composed of virtual leader agents of each group of MAS in the ad hoc network is represented by a directed graph $\mathcal{G}$. Then, we can design the topology of graph $\mathcal{G}$. Thus, the entire low-energy-consumption multilateral cooperative control system can achieve the expected multi-consensus control requirements.

Given a directed graph $\mathcal{G}$ and its vertex set $\mathcal{V}(\mathcal{G})$ and edge set $\mathcal{E}(\mathcal{G})$, if there are two nodes $(w_i, w_j) \in \mathcal{E}$, there is a directed edge between w_i and w_j. w_i is the tail of the edge, and w_j is the head of the edge, then w_i is said to be the neighbor of w_j. For each

partition, π is a map of vertices that divides $\mathcal{V}$ into m different cells, namely, $q_1, q_2, \ldots, q_m$, with $\bigcup_{l=1}^{m} q_l$ and $q_i \cap q_j = \varnothing$, where $i \neq j$.

Definition 1: If any two cells q_l and q_k in $\pi = \{q_1, q_2, \ldots, q_m\}$ are divided, including $l = k$, there is a constant $d_l k$ such that each node in q_l has $d_l k$ neighbors in q_k, then the division $\pi = \{q_1, q_2, \ldots, q_m\}$ is said to be equitable.

Definition 2: Given a division $\pi = \{q_1, q_2, \ldots, q_m\}$ of a graph $\mathcal{G}$ and a vertex set $\mathcal{V}(\mathcal{G})$, if for any pair of units q_l and q_k, where $l \neq k$, each node in cell q_l has $d_l k$ neighbors in q_k, then π is called external equitable partition (EEP).

In EEP, the nodes in a cell do not necessarily have the same number of neighbors because the graph produced by the partition is not regular. While a cell in a fair partition has the same out-degree to every cell, in EEP, this only applies to the number of connections between different cells.

Divide a given graph $\mathcal{G}$ into m cells, each of which can be represented by a feature matrix $P \in R^{n \times m}$.

$$P_{ij} = \begin{cases} 1, & \text{node i is in cell j} \\ 0, & \text{node i is not in cell j} \end{cases}$$

Through the feature matrix P, let $N = P^T P$, where $N \in R^{m \times m}$, and the element on the diagonal of N is the size of each cell $|q_l|$. Because the diagonal terms of $P^T P$ are not zero, $P^T P$ is invertible. Moreover, there is the following relationship between the Laplacian matrix $\mathcal{L}$ of the graph $\mathcal{G}$ and the Laplacian matrix $\mathcal{L}^\pi$ of the quotient graph

$$\mathcal{L}P = P\mathcal{L}^\pi, \tag{8}$$

and obtain

$$\mathcal{L}^\pi = \left(P^T P\right)^{-1} P^T \mathcal{L}P. \tag{9}$$

By **Eqs 8** and **9**, we obtain

$$\mathcal{L}P = P\left(P^T P\right)^{-1} P^T \mathcal{L}P. \tag{10}$$

Multiplying both sides of **Eq. 10** by $(P^T P)^{-1} P^T$, we obtain

$$\mathcal{L}P\left(P^T P\right)^{-1} P^T = P\left(P^T P\right)^{-1} P^T \mathcal{L}P\left(P^T P\right)^{-1} P^T. \tag{11}$$

Define the relevant feature matrix as $P_H = P(P^T P)^{-1} P^T$ and bring it into (**Eq. 11**), we get

$$\mathcal{L}P_H = {P_H}^T \mathcal{L}P_H. \tag{12}$$

Now, through the definition of directed graph, this article further illustrates the graph topology. Given a Laplacian $\mathcal{L}$ associated with a graph $\mathcal{G}$, there is a directed path from node w_j to node w_i. For the node w_j, its reachable set $\mathcal{R}(w_j)$ can be defined as including node w_j and all nodes w_i reached by w_j through directed paths.

Let $\mathcal{R}_1, \mathcal{R}_2, \ldots, \mathcal{R}_t$ represent the reachable set of graph $\mathcal{G}$. Define the exclusive part set $\mathcal{H}_i = \mathcal{R}_i \backslash \cup_{j \neq i} \mathcal{R}_j$ of $\mathcal{R}_i$, where $\mathcal{H}_i \cap \mathcal{H}_j = \varnothing$; define the common part set $\mathcal{C}_i = \mathcal{R}_i \backslash \mathcal{H}_i$ of $\mathcal{R}_i$.

The MAS model corresponding to the low-energy-consumption USVs is given:

$$\dot{x}(t) = -\mathcal{L}x(t) + u. \tag{13}$$

In **Eq. 13**, $[x_1(t), x_2(t), \ldots, x_n(t)]^T \equiv x(t) \in R^n$. $\mathcal{L}$ represents the directed graph Laplacian of MAS, and u is the distributed proportional controller

$$u = -\mathcal{L}^u x(t). \tag{14}$$

By dividing the graph $\pi = \{q_1, q_2, \ldots, q_m\}$, the multi-consensus condition is defined:

$$\lim_{t \to \infty} \left[x_i(t) - x_j(t)\right] = 0 \qquad \forall i, j | x_i \in q_v, x_j \in q_v, i \neq j,\ v = 1, 2, \ldots, m. \tag{15}$$

The asymptotically stable flow of consistent trajectories after system partitioning is defined as follows:

$$\mathcal{M}^\pi = \left\{x \in \mathbb{R}^n | x_i = x_j, \forall i, j | x_i \in q_v, x_j \in q_v, i \neq j,\ v = 1, 2, \ldots, m\right\}. \tag{16}$$

By designing the Laplacian operator of the controller u of the MAS, we get:

$$\dot{x}(t) = -\left(\mathcal{L} + \mathcal{L}^u\right) x(t). \tag{17}$$

Let $\mathcal{L}^\pi = \mathcal{L} + \mathcal{L}^u$ in **Eq. 17** and perform $\overline{x} = Tx$ replacement on the node cooperates of $\mathcal{L}^\pi$, separate the exclusive set from the common set, and express it in the style of the following triangle:

$$\overline{L} = \begin{pmatrix} L_1 & 0 & \cdots & 0 & 0 \\ 0 & L_2 & \cdots & 0 & 0 \\ \vdots & \vdots & \ddots & \vdots & \vdots \\ 0 & 0 & \cdots & L_t & 0 \\ M_1 & M_2 & \cdots & M_t & M \end{pmatrix}. \tag{18}$$

In **Eq. 18**, L_i is the $h_i \times h_i$ Laplace matrix associated with the exclusive set $\mathcal{H}_i$, M_i is the $\delta \times h_i$ matrix, M is an δ-order square matrix associated with the union of all common parts, and the elements on its diagonal represent the number of connections between the common part and the exclusive part ($h_i := |\mathcal{H}_i| \delta := |\cup_{i=1}^{t} \mathcal{C}_i|$).

Through the previous methods, the controllers u of multiple groups of low-energy-consumption USVs ad hoc networks are designed to change the structure diagram of the original system, and the expected topology diagram $\mathcal{L}^\pi$ is obtained. Then, transpose the $\mathcal{L}^\pi$ to obtain the transposed matrix $\overline{L}$, which can more clearly reflect the influence of the grouped information and the change of the topology structure on the multi-consensus of the ad hoc network of multiple groups of USVs.

Based on EEP, the topology design of the ad hoc network structure of USVs is carried out, and the MAS of the low-energy-consumption USVs is grouped according to the task requirements, so that the grouped MAS reaches a multi-consensus state, improves the efficiency of task execution, and achieves the green autonomous cooperative formation strategy.

5 SIMULATION

Under the polymorphic network, when facing complex maritime tasks, multiple groups of USVs form a low-energy-consumption multilateral distributed cooperative control system to achieve green autonomous cooperative formation.

5.1 Routing Design of Low-Energy-Consumption Unmanned Surface Vessels Under Ad Hoc On-Demand Distance Vector Routing Protocol

The simulation scenario is set as follows: by evaluating the EEOI index of each USV in the ad hoc network of the USVs, in the selection of the USVs with the smallest EEOI index, eight USVs are selected to form a network with the surrounding neighbors within the range of the communication radius r, respectively, forming the MAS of eight USVs. Based on the AODV protocol and the Prim algorithm, a node is used as the starting point, and the edge with the minimum weight of each vertex is gradually found to construct the minimum spanning tree so as to find the best route with the minimum number of hops. As shown in **Figure 5**, the eight black circles in the figure represent eight MAS, respectively, and the radius of the route established by each MAS is R (the dotted circle in the figure is the routing radius), where eight USVs are represented by eight nodes, and their coordinates are (3, 31) m, (12, 31) m, (6.5, 23) m, (9, 16) m, (18, 19) m, (23, 26) m, (6, 7) m, (13, 0.2) m. Let the radius of the route established by each USV be R = 10 m, and calculate the distance between the two points by **Eq. 6**. When $d \leqslant R$, a route can be established directly between two nodes. When $d > R$, no route can be established directly between nodes. Then, according to the AODV routing protocol, according to the principle of the smallest number of hops, find a suitable intermediate node.

A) The route is established with node 1 as the starting point and node 4 as the endpoint. According to Eq. 6, the distance between node 1 and node 4 is d = 16.16 m, which is greater than the routing radius R = 10 m of the node. The route between node 1 and node 4 cannot be established directly. The routing radius of node 1 includes node 2 and node 4, while the routing radius of node 3 includes node 1, node 2, and node 4. As shown in **Figure 6**, there are two routes from node 1 to node 4, namely, $1 \rightarrow 2 \rightarrow 3 \rightarrow 4$ and $1 \rightarrow 3 \rightarrow 4$. Considering the principle of green energy saving and the minimum number of hops, the AODV protocol obtains the optimal route as $1 \rightarrow 3 \rightarrow 4$.

B) The route is established with node 6 and node 4 as the endpoints. According to Eq. 6, the distance between node 6 and node 4 is d = 86 m, which is greater than the routing radius of the node R = 10 m. The route between node 6 and node 4 cannot be established directly. The routing radius of node 6 includes node 5, and the routing radius of node 5 includes node 5 and node 4. As shown in **Figure 7**, the route from node 6 to node 4 is derived as $6 \rightarrow 5 \rightarrow 4$ based on the AODV protocol.

C) The route is established with node 8 and node 4 as the endpoints. According to **Eq. 6**, the distance between node 8 and node 4 is d = 655.64 m, which is greater than the routing radius of the node R = 10 m. The route between node 8 and node 4 cannot be established directly. The routing radius of node 8 includes node 7, and the routing radius of node 7 includes node 8 and node 4. As shown in **Figure 8**, the route from node 6 to node 4 is derived as $8 \rightarrow 7 \rightarrow 4$ based on the AODV protocol.

Through the simulation results, it can be seen that in the multilateral distributed cooperative control system of multiple groups of low-carbon and low-energy-consumption USVs, the virtual leader agent of each group of low-energy-consumption USVs achieves the goal of establishing routes with long-distance nodes with the minimum number of hops based on the AODV protocol, which follows the green energy-saving concept of

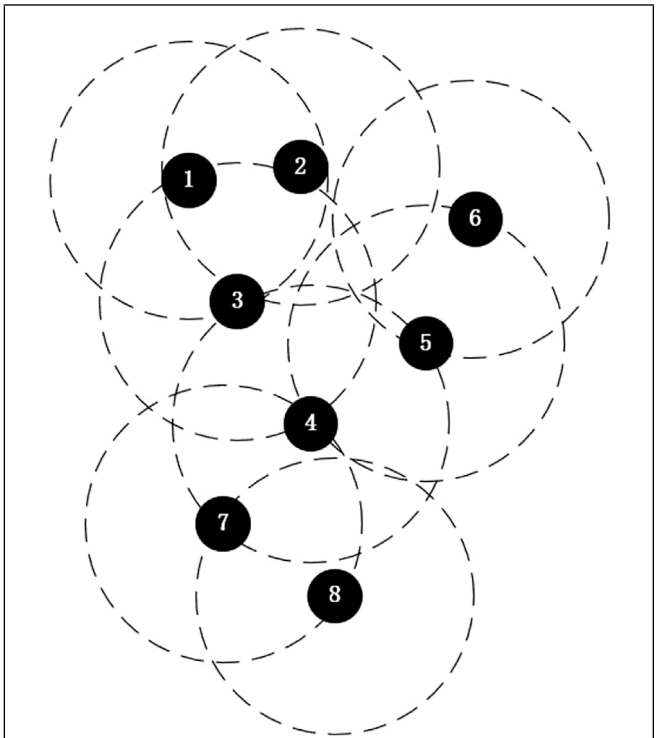

FIGURE 5 | Eight USV ad hoc network structure diagram.

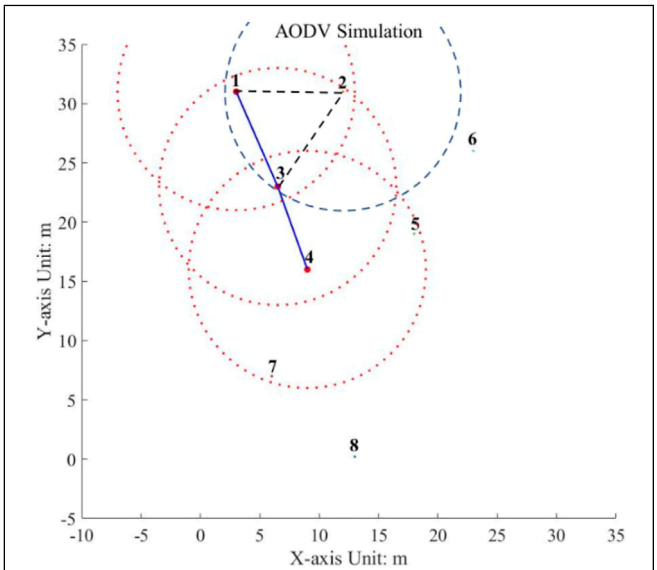

FIGURE 6 | Routing simulation diagram from node 1 to node 4.

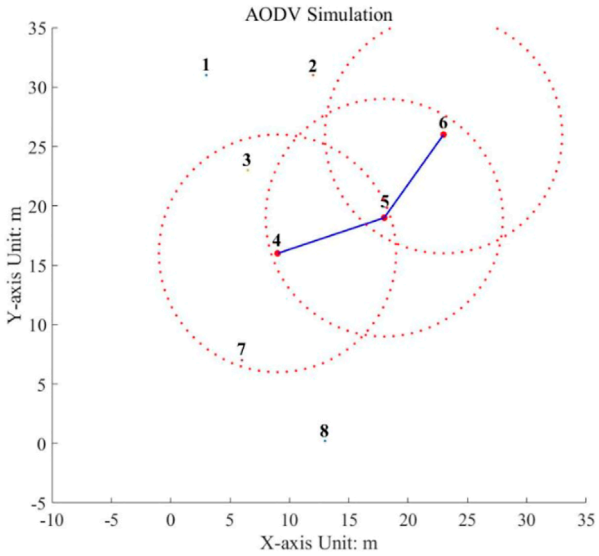

FIGURE 7 | Routing simulation diagram from node 6 to node 4.

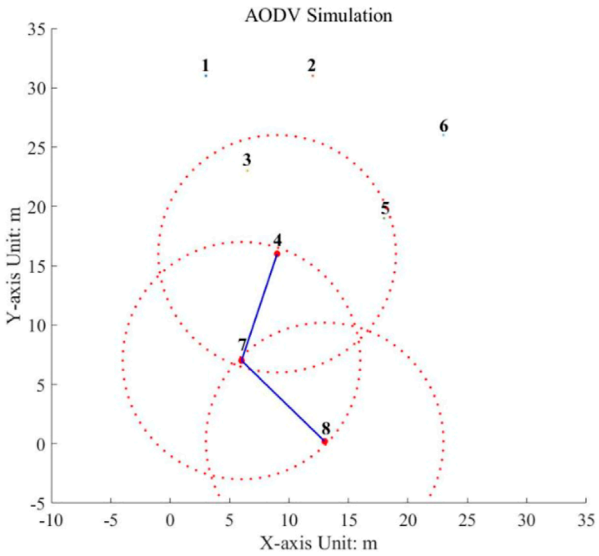

FIGURE 8 | Routing simulation diagram from node 8 to node 4.

realizing communication between swarms with the least routing and effectively reduces the energy consumption caused by the re-networking of multiple groups of low-carbon and low-energy-consumption USVs facing complex tasks under the polymorphic network.

5.2 Topology Design of Low-Energy-Consumption Unmanned Surface Vessel Communication Network Under External Equitable Partition

The simulation scenario is set as follows: after the route formation of the low-energy-consumption USVs is completed, in order to enable the low-energy-consumption USVs to further perform

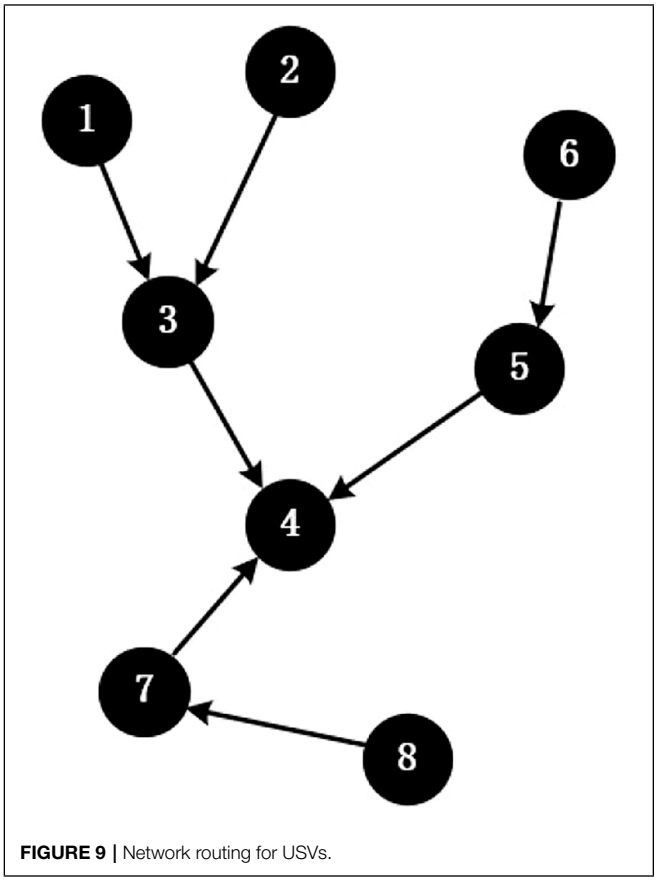

FIGURE 9 | Network routing for USVs.

tasks according to the assignment of tasks, it is necessary to design the topology of the communication network of the low-energy-consumption USVs based on the connectivity of network routing. The established network routing of the low-energy-consumption USVs is shown in **Figure 9**.

Based on graph theory, the Laplacian operator for network routing in **Figure 9** is:

$$\mathcal{L} = \begin{bmatrix} 0 & 0 & 0 & 0 & 0 & 0 & 0 & 0 \\ 0 & 0 & 0 & 0 & 0 & 0 & 0 & 0 \\ -2 & 1 & 1 & 0 & 0 & 0 & 0 & 0 \\ 0 & 0 & -1 & 3 & -1 & 0 & -1 & 0 \\ 0 & 0 & 0 & 0 & 1 & -1 & 0 & 0 \\ 0 & 0 & 0 & 0 & 0 & 0 & 0 & 0 \\ 0 & 0 & 0 & 0 & 0 & 0 & 1 & -1 \\ 0 & 0 & 0 & 0 & 0 & 0 & 0 & 0 \end{bmatrix}.$$

Let the initial state of the eight USVs be $x_0 = [1;3;5;7;2;4;6;8]$ and the time to be $t \in [1,10]$. Through the dynamic equation $\dot{x} = -\mathcal{L}x$ of **Eq. 3**, the time evolution diagram of $\dot{x}$ is obtained as shown in **Figure 10**, in which each USV cannot achieve the expected consensus within the specified time. Therefore, the topology of the system is designed.

According to the task requirements, the following topology design is carried out on the structure of the system through EEP: node 1, node 2, and node 3 are divided into a group for operations, node 5 and node 6 are divided into a group, node 7

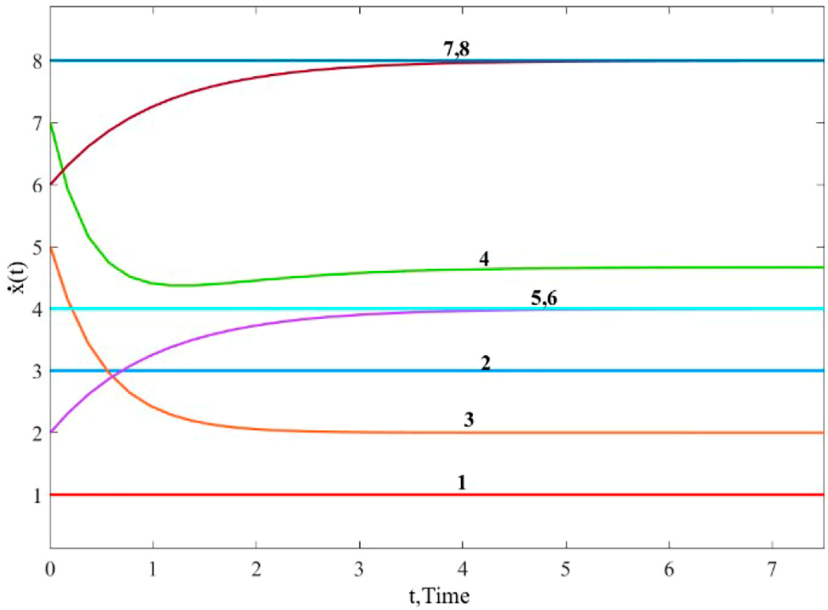

FIGURE 10 | Time evolution plot of $\dot{x}(t)$.

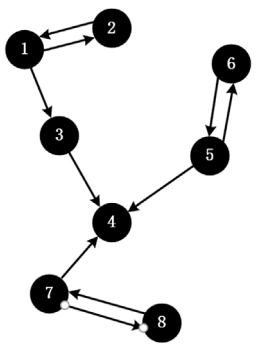

$$\mathcal{L}+\mathcal{L}^u=\begin{bmatrix}1&-1&0&0&0&0&0&0\\-1&1&0&0&0&0&0&0\\-1&0&1&0&0&0&0&0\\0&0&-1&3&-1&0&-1&0\\0&0&0&0&1&-1&0&0\\0&0&0&0&-1&1&0&0\\0&0&0&0&0&0&1&-1\\0&0&0&0&0&0&-1&1\end{bmatrix}$$

FIGURE 11 | Network routing after topology design of USVs and Laplacian operator after division.

and node 8 are divided into a group, and the bidirectional link from node 1 to node 2 is added through controller u, the route from node 5 to node 6 is added, and the route from node 7 to node 8 is added; delete the route from node 2 to node 3. Get the following 4 grouping sets, which are $\mathcal{H}_1=\{1,2,3\}$, $\mathcal{H}_2=\{5,6\}$, $\mathcal{H}_3=\{7,8\}$, and $\mathcal{C}=\{4\}$ and get the partition: $\pi=\{\mathcal{H}_1,\mathcal{H}_2,\mathcal{H}_3,\mathcal{C}\}$. As shown in **Figure 11**, the divided structure diagram and the corresponding Laplace operator are obtained:

$$\mathcal{L}+\mathcal{L}^u=\begin{bmatrix}1&-1&0&0&0&0&0&0\\-1&1&0&0&0&0&0&0\\-1&0&1&0&0&0&0&0\\0&0&-1&3&-1&0&-1&0\\0&0&0&0&1&-1&0&0\\0&0&0&0&-1&1&0&0\\0&0&0&0&0&0&1&-1\\0&0&0&0&0&0&-1&1\end{bmatrix}.$$

Transpose $\mathcal{L}+\mathcal{L}^u$, get the transposed Laplacian:

$$\mathcal{L}+\mathcal{L}^u=\begin{bmatrix}1&-1&0&0&0&0&0&0\\-1&1&0&0&0&0&0&0\\-1&0&1&0&0&0&0&0\\0&0&0&1&-1&0&0&0\\0&0&0&-1&1&0&0&0\\0&0&0&0&0&1&-1&0\\0&0&0&0&0&-1&1&0\\0&0&-1&-1&0&-1&0&3\end{bmatrix}.$$

The characteristic matrix P of **Figure 11** and the Laplace matrix $\mathcal{L}^\pi$ of its quotient graph:

$$P=\begin{bmatrix}1&0&0&0\\1&0&0&0\\1&0&0&0\\0&1&0&0\\0&1&0&0\\0&0&1&0\\0&0&1&0\\0&0&0&1\end{bmatrix}\mathcal{L}^\pi=\begin{bmatrix}0&0&0&0\\0&0&0&0\\0&0&0&0\\-1&-1&-1&3\end{bmatrix}. \tag{19}$$

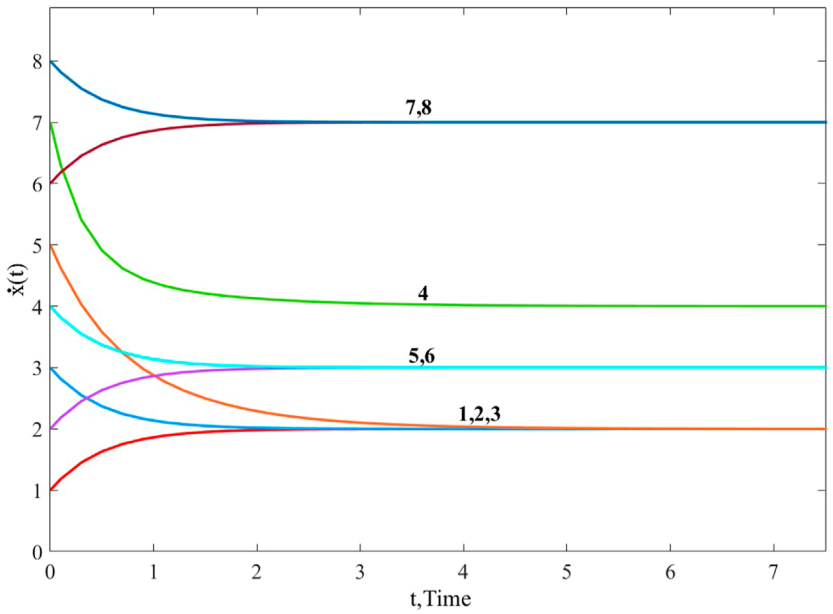

FIGURE 12 | Time evolution diagram of $\dot{x}(t)$ after EEP design.

The relation of $\mathcal{L}+\mathcal{L}^u$, P and $\mathcal{L}^\pi$ satisfies (**Eq. 8**). Through **Eqs 9–11**, the matrix P_H of **Figure 11** is obtained:

$$P_H = \begin{bmatrix} 0.3 & 0.3 & 0.3 & 0 & 0 & 0 & 0 & 0 \\ 0.3 & 0.3 & 0.3 & 0 & 0 & 0 & 0 & 0 \\ 0.3 & 0.3 & 0.3 & 0 & 0 & 0 & 0 & 0 \\ 0 & 0 & 0 & 0.5 & 0.5 & 0 & 0 & 0 \\ 0 & 0 & 0 & 0.5 & 0.5 & 0 & 0 & 0 \\ 0 & 0 & 0 & 0 & 0 & 0.5 & 0.5 & 0 \\ 0 & 0 & 0 & 0 & 0 & 0.5 & 0.5 & 0 \\ 0 & 0 & 0 & 0 & 0 & 0 & 0 & 1 \end{bmatrix}. \quad (20)$$

$\mathcal{L}+\mathcal{L}^u$ and P_H are verified by **Eq. 12**, and the result of **Eq. 12** is satisfied.

The exclusive set after the graph is divided as $\mathcal{H} = \{\mathcal{H}_1, \mathcal{H}_2, \mathcal{H}_3\} = \{\{1,2,3\},\{5,6\},\{7,8\}\}$, the common set is $\mathcal{C} = \{4\}$, the initial state of the eight USVs is $x_0 = [1;3;5;7;2;4;6;8]$, and the time is $t \in [1,10]$, and the time evolution diagram is obtained by the dynamic equation $\dot{x} = -\mathcal{L}x$ of **Eq. 3** which is shown in **Figure 12**:

The experimental results show that on the basis of ensuring the connectivity of the entire network routing of multiple groups of low-energy-consumption USVs, the topology design of network routing is carried out based on EEP, improving the work efficiency of multiple groups of low-energy-consumption USVs, achieving the expected multi-consensus state, realizing low-energy-consumption multilateral cooperative control, and finally realizing the green autonomous cooperative formation of multiple groups of low-energy-consumption USVs.

6 CONCLUSION

In the polymorphic network environment, both artificial intelligence and ad hoc networks have been rapidly developed and widely used. In this article, a low-energy-consumption networking method for USVs that perform large-scale and complex tasks has been presented. Combined with the characteristics of the polymorphic network, such as multilateral co-management, green energy saving, and scalable structure, a low-energy-consumption multilateral distributed cooperative control system framework for multiple groups of USVs has been proposed. First, through the evaluation of the EEOI index, low-carbon and low-energy-consumption USVs have been selected to form a system for the task. Second, a green networking method for low-energy-consumption USVs with minimum routings has been proposed. In addition, a distributed cooperative control protocol based on the MAS multi-consensus algorithm has been designed to realize the multilateral cooperative control of multiple groups of low-energy-consumption USVs. Furthermore, the green autonomous cooperative formation can be realized, and USVs can perform tasks efficiently and quickly in groups. Finally, the effectiveness of the proposed method has been verified by a simulation example, which provides technical support and a theoretical basis for realizing green energy-saving autonomous cooperative control of USVs in a polymorphic network environment.

DATA AVAILABILITY STATEMENT

The original contributions presented in the study are included in the article/Supplementary Material; further inquiries can be directed to the corresponding authors.

AUTHOR CONTRIBUTIONS

YL and GX constructed low-energy-consumption multilateral distributed cooperative control framework for ad hoc of low-carbon USVs. QS built the USV model, designed the method, adapted the article, and processed the experimental simulations data. YL collated and proofread the whole article. WL corrected the format of the references. All authors have read and agreed to the publication of the manuscript.

FUNDING

This research is supported by the National Key R&D Program of China (2019YFB1802501) and Key Research Project of Zhejiang Lab (2021LE0AC02); High Level Talents Innovation Support Plan of Dalian (Young Science and Technology Star Project) (under Grant No. 2021RQ058); the National Natural Science Foundation of China (under Grant Nos. 51939001, 61976033, 61751202, 61903092, and U1813203); the Science and Technology Innovation Funds of Dalian (under Grant No. 2018J11CY022); and the Liaoning Revitalization Talents Program (under Grant Nos. XLYC1908018 and XLYC1807046).

REFERENCES

AL-Dhief, F. T., Sabri, N., Salim, M. S., Fouad, S., and Aljunid, S. A. (2018). Manet Routing Protocols Evaluation: Aodv, Dsr and Dsdv Perspective. *Matec Web Conf.* 150, 06024. doi:10.1051/matecconf/201815006024

Alslaim, M. N., Devi, P. M., and Sharmila, B. (2016). Comparative Study of Manet Routing Protocols. *Asia. Jour. Rese. Soci. Scie. Hum.* 6, 1924. doi:10.5958/2249-7315.2016.00337.3

Bertaska, I. R., Shah, B., and von Ellenrieder, K. (2015). Experimental Evaluation of Automatically-Generated Behaviors for Usv Operations. *Ocean. Eng.* 106, 496–514. doi:10.1016/j.oceaneng.2015.07.002

Bhagyalakshmi, and Dogra, A. K. (2018). Q-Aodv: A Flood Control Ad-Hoc on Demand Distance Vector Routing Protocol. In 2018 First International Conference on Secure Cyber Computing and Communication (ICSCCC). 294–299. doi:10.1109/icsccc.2018.8703220

Chon, S., Haiyan, W., Chao, L., and Ye, Z. (2019). Dynamic Prediction and Optimization of Energy Efficiency Operational Index (Eeoi) for an Operating Ship in Varying Environments. *J. Mar. Sci. Eng.* 7, 402. doi:10.3390/jmse7110402

Chou, T. C. K., and Abraham, J. A. (1982). Load Balancing in Distributed Systems. *IIEEE Trans. Softw. Eng.* SE-8, 401–412. doi:10.1109/TSE.1982.235574

Deepak, S., and Anandakumar, H. (2019). "Aodv Route Discovery and Route Maintenance in Manets," in 2019 5th International Conference on Advanced Computing & Communication Systems (ICACCS), 1187–1191. doi:10.1109/ICACCS.2019.8728456

Durfee, E. H., and Corkill, D. D. (1989). Trends in Cooperative Distributed Problem Solving. *IEEE Trans. Knowl. Data Eng.* 1, 63–83. doi:10.1109/69.43404

Gambuzza, L. V., and Frasca, M. (2019). A Criterion for Stability of Cluster Synchronization in Networks with External Equitable Partitions. *Automatica* 100, 212–218. doi:10.1016/j.automatica.2018.11.026

Garey, M. R., Graham, R. L., and Johnson, D. S. (1978). Performance Guarantees for Scheduling Algorithms. *Operations Res.* 26, 3–21. doi:10.2307/169888

Hui, L., Xiangui, W., and Zhili, L. (2019). *Systems and Methods for Managing Top-Level Domain Names Using Consortium Blockchain*.

Jiangxing, W., and Kaizhi, H. (2022). Innovating the Paradigm of Network Development and Constructing a Polymorphic Network Environment ‖ Introduction to the Special Topic of "Key Technologies of Polymorphic Network Environment". *J. Commun.* 43, 1.

Jiangxing, W., and Yuxiang, H. (2021). The Development Paradigm of Separation between Network Technica System and Supporting Environment. *Inf. Commun. Technol. Policy* 47, 1–11. doi:10.12267/j.issn.2096-5931.2021.08.001

Jingmin, H. (2016). Analysis of Ship Energy Efficiency Operation Index and Energy Efficiency Management Practice. *World Shipp.* 39, 5. doi:10.16176/j.cnki.21-1284.2016.07.007

Joseph, C., John, L., and Andrew, P. (2005). "Scout - a Low-Cost Autonomous Surface Platform for Research in Cooperative Autonomy," in Proceedings of OCEANS 2005 MTS/IEEE. doi:10.1109/OCEANS.2005.1639838

Julong, L., Dongnian, C., and Yuxian, H. (2014). Research on Reconfigurable Information Communication Basal Network Architecture. *J. Commun.* 35, 12. doi:10.3969/j.issn.1000-436x.2014.01.015

Kitts, C., Mahacek, P., Adamek, T., Rasal, K., Howard, V., Li, S., et al. (2012). Field Operation of a Robotic Small Waterplane Area Twin Hull Boat for Shallow-Water Bathymetric Characterization. *J. Field Robot.* 29, 924–938. doi:10.1002/rob.21427

Lei, H., Huang, B., and Chunxia, Z. (2011). Geographic Routing Algorithm Based on Link Quality in Mobile Ad-Hoc Networks. *Comput. Sci.* 38, 51–54. doi:10.3969/j.issn.1002-137X.2011.10.010

Lei, T., and Qi, F. (2002). Cooperative Distributed Planning in Artificial Intelligence. *Comput. Eng. Appl.* 38, 4. doi:10.1007/s11769-002-0038-4

Lewis, M. A., and Tan, K.-H. (1997). High Precision Formation Control of Mobile Robots Using Virtual Structures. *Aut. Robots* 4, 387–403. doi:10.1023/A:1008814708459

Li, H., Han, Y., Li, G., Wang, H., Lv, S., Ma, J., et al. (2019). Prototype and Testing Report of a Multi-Identifier System for Reconfigurable Network Architecture under Co-governing. *Sci. Sin.-Inf.* 49, 1186–1204. doi:10.1360/N112019-00070

Mohsen, S. A., and Naif, D. A. (2019). Routing Protocols Design and Performance Evaluation in Wireless Mesh Networks. *Int. J. Technol. Diffusion* 10, 60–74. doi:10.4018/IJTD.2019010105

Olfati-Saber, R., Fax, J. A., and Murray, R. M. (2007). Consensus and Cooperation in Networked Multi-Agent Systems. *Proc. IEEE* 95, 215–233. doi:10.1109/JPROC.2006.887293

Parveen, S., and Chaubey, V. K. (2019). An Enhanced Ad Hoc on Demand Distance Vector Routing Protocol for Vehicular Ad Hoc Networks (Vanet's). *SSRN Electron. J.*, 799–805. doi:10.2139/ssrn.3355137

Qiang, M., Danlin, Y., and Zongfu, Y. (2011). Energy Effective Routing Algorithm Based on Aodv. *Comput. Eng. Des.* 32, 4. doi:10.1080/01932691003662381

Qiaoyun, M., Liu, H., and Xueguang, C. (2007). Analysis and Modeling of Task Allocation Problem in MAS[J]. *J. Huazhong Univ. Sci. Technol. (Nat. Sci. Ed.)* 2007 (01), 54–57. doi:10.13245/j.hust.2007.01.017

Rui, S., Yuanchang, L., and Richard, B. (2017). A Multi-Layered Fast Marching Method for Unmanned Surface Vehicle Path Planning in a Time-Variant Maritime Environment. *Ocean. Eng.* 129, 301–317. doi:10.1016/j.oceaneng.2016.11.009

Scott, R., Dowdell, J., and Perkins, C. (2003). Ad Hoc on-demand Distance Vector (Aodvv2) Routing. *Internet Draft Draft Ietf Manet Aodv Txt* 6, 90. doi:10.1109/MCSA.1999.749281

Scott, R. (2013). Mobile Ad-Hoc Networks (Manet). *IETF Work. Group Chart.* doi:10.1109/GreenCom-CPSCom.2010

Sharma, D. K., Kumar, C., Jain, S., and Tyagi, N. (2012). "An Enhancement of Aodv Routing Protocol for Wireless Ad Hoc Networks," in 2012 1st International Conference on Recent Advances in Information Technology (RAIT), 290. doi:10.1109/RAIT.2012.6194522

Shirani, R., Marc, H., and Yifeng, Z. (2012). "Combined Reactive-Geographic Routing for Unmanned Aeronautical Ad-Hoc Networks," in Wireless Communications & Mobile Computing Conference, 820–826. doi:10.1109/iwcmc.2012.6314310

Smith, S. (1980). The Contract Net Protocol: High-Level Communication and Control in a Distributed Problem Solver. *Comput. IEEE Trans. C* 29, 1104–1113. doi:10.1109/TC.1980.1675516

Xueli, Z., Qian, Q., Qingwen, W., and Yongqiang, L. (2017). "An Adaptive Density-Based Routing Protocol for Flying Ad Hocnetworks," in 2nd International Conference on Materials Science, Resource and Environmental Engineering. doi:10.1063/1.5005315

Yan, S., Songlin, Y., Yuxiao, H., Weisun, K., and Chengjin, Z. (2021). Comprehensive Optimization Analysis of Green Energy Catamaran Unmanned Craft. *Ship Sci. Technol.* 43, 5. doi:10.3404/j.issn.1672-7649.2021.03.020

Yang, D., Sun, Y., Wei, Q., Zhang, H., and Li, T. (2021). Topology Prediction and Structural Controllability Analysis of Complex Networks without Connection Information. *IEEE Trans. Syst. Man. Cybern. Syst.* 1, 1–13. doi:10.1109/TSMC.2021.3131490

Yuan, G., Zhengzhong, W., and Jiande, L. (2007). Optimization to Ad Hoc On-Demand Distance-Vector Routing Protoco through Path Collection. *Comput. Eng.* 33, 4. doi:10.1016/j.cageo.2006.02.011

Yushuai, L., Wenzhong, G., Wei, G., and Huaguang, Z. (2021). A Distributed Double-Newton Descent Algorithm for Cooperative Energy Management of Multiple Energy Bodies in Energy Internet. *IEEE Trans. Industrial Inf.* 17, 5993–6003. doi:10.1109/TII.2020.3029974

Źarko, K., Darijo, M., and Romana Capor, H. (2021). Analysis of Sea Pollution by Sewage from Vessels. *Sustainability* 14, 1–21. doi:10.3390/su14010263

Zheng, W., Guangfu, L., and Jia, R. (2021). Dynamic Path Planning for Unmanned Surface Vehicle in Complex Offshore Areas Based on Hybrid Algorithm. *Comput. Commun.* 166, 49–56. doi:10.1016/j.comcom.2020.11.012

Zhengfeng, L., Longhui, Z., Naxin, W., and Xiaofeng, K. (2021). Study on Path Planning and Following Control of Unmanned Surface Vehicles in Restricted Areas. *J. Ship Mech.* 25, 10. doi:10.3969/j.issn.1007-7294.2021.09.001

Zhenyu, G., and Ge, G. (2018). Research Status and Progress in Cooperative Formation of Multiple Autonomous Surface Vehicles. *Inf. Control* 47, 13. doi:10.13976/j.cnki.xk.2018.7381

Zhouhua, P., Wentao, W., Dan, W., and Lu, L. (2021). Cooperative Control of Multiple Unmanned Surface Vehicles: Recent Advances and Future Trends. *Chin. J. Ship Res.* 16, 15. doi:10.19693/j.issn.1673-3185.01923

Conflict of Interest: The authors declare that the research was conducted in the absence of any commercial or financial relationships that could be construed as a potential conflict of interest.

Publisher's Note: All claims expressed in this article are solely those of the authors and do not necessarily represent those of their affiliated organizations, or those of the publisher, the editors, and the reviewers. Any product that may be evaluated in this article, or claim that may be made by its manufacturer, is not guaranteed or endorsed by the publisher.

frontiers | Frontiers in Energy Research

TYPE Original Research
PUBLISHED 24 August 2022
DOI 10.3389/fenrg.2022.960278

OPEN ACCESS

EDITED BY
Yushuai Li,
University of Oslo, Norway

REVIEWED BY
Tsung-Chow Su,
Florida Atlantic University, United States
Ming Li,
Ocean University of China, China
Jinhai Liu,
Northeastern University, China

*CORRESPONDENCE
Kai Sun,
sunk@sia.cn

SPECIALTY SECTION
This article was submitted to Smart Grids,
a section of the journal
Frontiers in Energy Research

RECEIVED 02 June 2022
ACCEPTED 18 July 2022
PUBLISHED 24 August 2022

CITATION
Sun K and Han Z (2022), Autonomous underwater vehicle docking system for energy and data transmission in cabled ocean observatory networks.
Front. Energy Res. 10:960278.
doi: 10.3389/fenrg.2022.960278

Autonomous underwater vehicle docking system for energy and data transmission in cabled ocean observatory networks

Kai Sun[1,2]* and Zekai Han[1,2,3]

[1]State Key Laboratory of Robotics, Shenyang Institute of Automation, Chinese Academy of Sciences, Shenyang, China, [2]Institutes for Robotics and Intelligent Manufacturing, Chinese Academy of Sciences, Shenyang, China, [3]University of Chinese Academy of Sciences, Beijing, China

Cabled ocean observatory networks (COON) are used for long-term all-weather observation of submarine scientific data, which contribute to low-carbon ocean energy research. Autonomous underwater vehicles (AUV) with clean energy can provide active search capabilities by connecting with the docking station (DS) on the COON to complete energy and data transmission in long-term detection tasks. The AUV is guided by optical active landmarks and a vision system for short-range docking. In this study, we propose an active landmarks tracking framework to solve the problem of detecting failure caused by incomplete observation of landmarks. First, a two-stage docking algorithm based on CNN is used to estimate the 3D relative position and orientation between DS and AUV during docking, including detect phase and PnP pose estimator. Then extended Kalman filter and Hungarian matching algorithm are introduced to improve the robustness of the algorithm. The reliability of the vision-based short-range docking algorithm is verified in the pool, and the robustness of the algorithm to the field environment is shown in the lake field experiment combined with long-range guidance. The experimental results indicate that the algorithm framework can effectively leverage the landmarks information and enhance the scope of the visual guidance algorithm.

KEYWORDS

autonomous underwater vehicle, underwater docking, visual navigation, underwater active landmarks, marine robotics, low carbon

Introduction

Cabled ocean observatory networks (COON) can realize all-weather, *in situ*, long-term, continuous, real-time, high-resolution, and high-precision observations of the ocean from the seabed to the sea surface, and the observations can be used to study scientific problems such as sea-air exchange, climate change, ocean circulation, low-carbon ocean bioenergy, and ecosystems (De Leo et al., 2018; Seyfried et al., 2022).

While the observation range of the COON is limited by cable, scholars have proposed that the use of autonomous underwater vehicles (AUV) in the COON to combine the advantages of AUV and COON (Manalang and Delaney, 2016; Liu et al., 2021; Deeb et al.,

2019). AUV are not limited by cables and can provide more powerful and flexible solutions for long-term missions of exploring underwater renewable energy, deep-sea minerals, and acquiring natural data. When applying AUV in the COON, the main factors restricting AUV are the limited energy carrying capacity and information transmission capacity, which can be solved by underwater docking (Palomeras et al., 2018; Yazdani et al., 2020; Lin et al., 2022). It is of great significance for the application of AUV in COON to provide a reliable docking and recovery system in the actual use scenario.

The main sensors of the AUV docking are acoustic, electromagnetic, and optical sensors. For the short-range guidance in the recovery task, Deltheil et al. (2000) compared various sensing methods and proposed that the optical sensor has excellent robustness and flexibility and is the best scheme for AUV recovery. Numerous research have successfully completed the short-range docking and recovery task through visual detection algorithm and active landmarks, which has verified the feasibility of this technology. Optical landmarks are mainly divided into active landmarks and passive landmarks. Passive landmarks do not emit light actively, identified by their own texture features. They have a close range of visibility and have high requirements for water quality (Maire et al., 2009; Wang et al., 2021). The active landmarks have higher visibility than the passive ones, and an effective terminal guidance scheme can be provided by arranging appropriate light landmarks (Li D. J. et al., 2015; Li Y. et al., 2015; Ghosh et al., 2016; Sans-Muntadas et al., 2019).

Park et al. (2009) used five light landmarks for guidance and successfully completed docking within 15 m in the pool environment. However, the detection failed as part of DS entered the blind area of vision at close range, resulting in docking failure. Zhou et al. (2014) Proposed a video tracking algorithm to solve the problem of landmarks loss. However, the landmarks layout and docking method limit the applicable scene and guiding distance of the algorithm.

The aforementioned experiments are carried out in the pool environment, and different water quality and optical interference in the natural environment have a great impact on the detection and segmentation algorithm. Liu et al. (2019) proposed a two-stage docking framework of detection and pose estimation, which successfully completed the guidance in the lake environment. The experimental results show that the two-stage framework can detect docking stations and estimate their relative pose more efficiently and successfully, compared with the state-of-the-art baseline systems. However, limited by the framework, the detection fails in the absence of enough landmarks. Considering a DS with n landmarks, a minimum of n-1 landmarks is required, which leads to a narrow entrance angle required in the early stage of docking.

Most visual methods are tested in the pool; however, the interference of the field environment reduces the control performance of the AUV, which puts forward higher requirements for the robustness of the guidance algorithm. Our method improves on real-world usage, expanding the workspace of the system. Using the information more effectively of the landmarks to improve the guidance performance in the field environment is the main research goal of this study. There are the following main problems in the guidance of underwater recovery docking using active landmarks:

1) Image variance is caused by different water quality and environment, and landmarks intensity changes caused by different distances and angle, which makes detection more difficult.
2) In the docking process, only part of the landmarks of the docking DS can be observed due to short distance or large pose deviation, failing the target detection algorithm.
3) The identification of the landmarks cannot be correctly matched when the coordinates of the landmarks are not completely observed.

In order to solve the aforementioned problems, we propose active landmarks tracking algorithm for docking tasks. The main contributions of this study are as follows:

1) A tracking framework combined with a two-stage docking algorithm of detection and pose estimation is proposed to make full use of landmarks information in docking tasks. Compared with the original one, the tracking algorithm can work effectively despite the failure of target detection and incomplete observation.
2) Field experiments were carried out in the water pool and lake, providing the first angle of view data for the successful docking of underwater landmarks.

In this study, we introduce the system overview in the second section. In the third section, the framework of the tracking algorithm for active landmarks will be introduced. In the fourth section, we show the docking experimental results of the pool and lake environment, which verifies the reliability and robustness of the algorithm.

Docking system overviews

In this section, an overview of our recycling system will be introduced. Our recycling system includes DS and AUV, as shown in Figures 1A, B. DS includes acoustic guidance module, light landmarks, and electromagnetic tightening devices. The length and width of the funnel-shaped entrance of the DS is 1.2 m, the acoustic guidance system is arranged above the funnel, and the landmarks are arranged around the opening of the funnel for the visual guidance system, as shown in

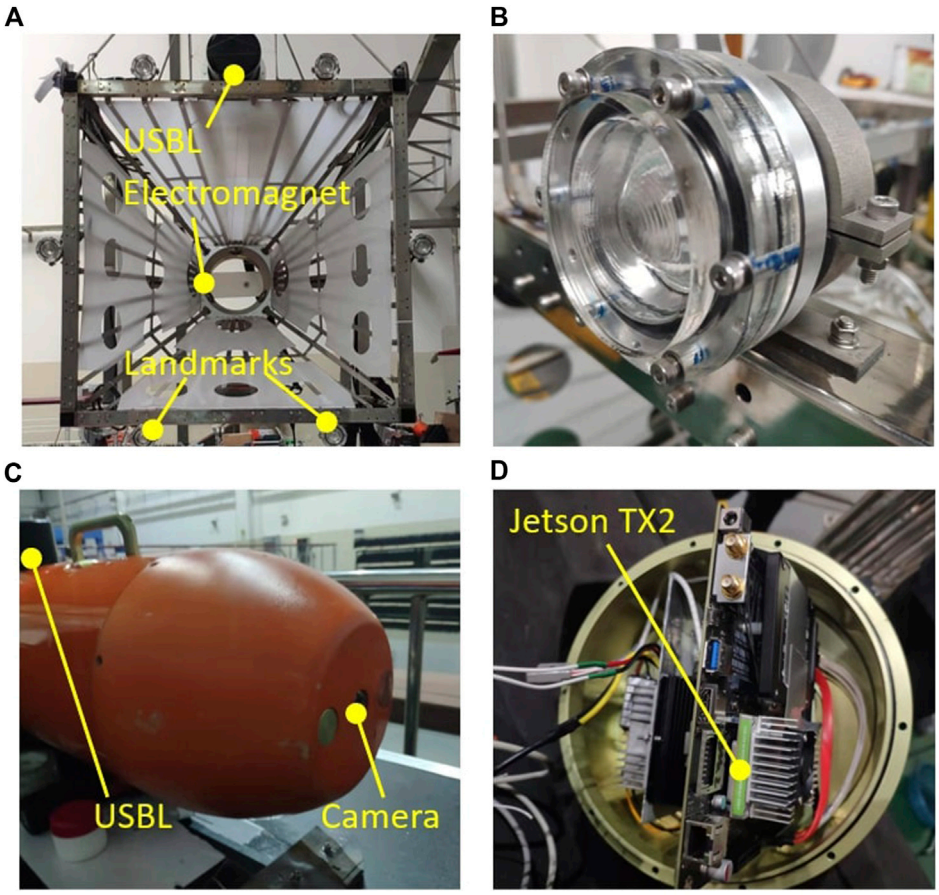

FIGURE 1
Docking systems. **(A)**Docking station **(B)** Active landmark **(C)** Portable AUV **(D)** JetsonTX2.

Figure 1C. Considering the underwater absorption of light, a 460 nm blue LED light source is used to make the landmarks better spread in the underwater environment. In addition, the landmarks lamp is added with a 60° angle convex lens to enhance the effective guiding distance. The intensity of the light is adjusted to a suitable range for the capture of the camera, in order to avoid the fusion of the boundary of the two lights on the image.

Our AUV is a small torpedo-shaped vehicle called Portable AUV(PAUV). The PAUV has an air weight of 80 kg, a length of 2 m, a diameter of 240 mm, and a maximum speed of 5 knots. Equipped with two tail thrusters, two culvert thrusters, and two tail rudders. PAUV mainly includes a control computer, Doppler velocity log(DVL), inertial measurement unit (IMU), GPS, acoustic sensor, optical sensor, battery units, and motors. Ultra-short baseline system (USBL) is used as acoustic guidance for long-distance navigation tasks, which can work effectively within 2 km and provide ranging and direction-finding functions. It is switched to the optical guidance method at a short range to complete the final precise docking. A NanoSeaCam monocular color camera and embedded computer NVIDIA Jetson TX2 are used for optical guidance. The camera with 20fps is installed at the bow of the PAUV, and an embedded computer is installed in the middle of the PAUV, as shown in Figures 1C,D. Jetson TX2 is an excellent embedded edge computing platform with 256 CUDA cores. The computing performance reaches 1.33 TFLOPS and only 15 W power consumption is required when running. The first view color image of the PAUV is captured by the camera and sent to Jetson TX2 for calculation. Then, the obtained guidance information is sent to the main control computer for control. Data exchange between each module is realized through LAN.

Underwater docking algorithm

In this section, we introduce the two-stage docking algorithm and landmarks tracking method. The main task of the underwater docking algorithm is to accurately identify the DS within the visual range of active landmarks and give the 3D relative position and orientation information for docking navigation. Then the AUV uses

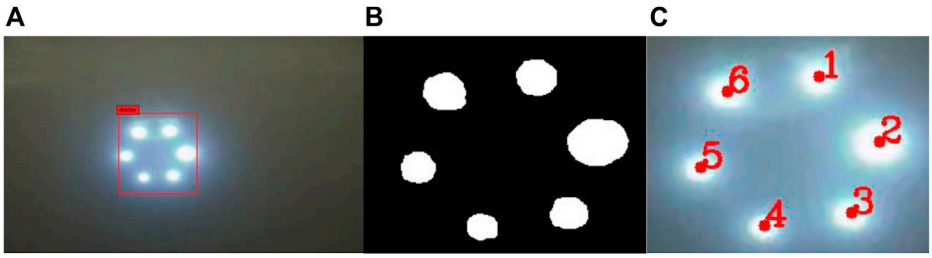

FIGURE 2
(A) Output of DoNN **(B)** Binary image **(C)** Landmarks with identification.

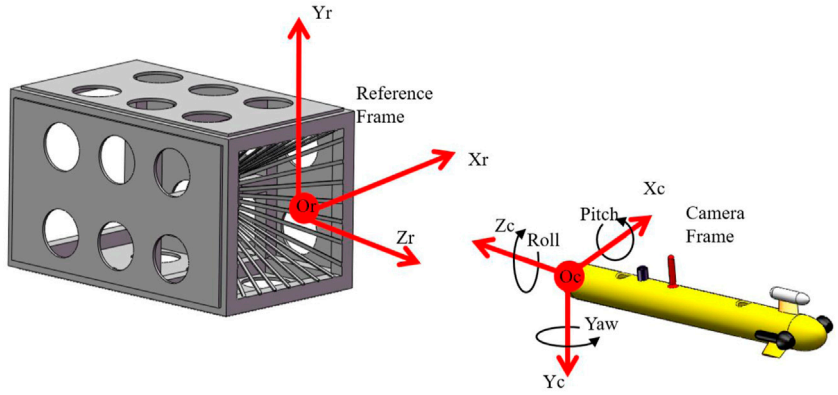

FIGURE 3
Coordinate frames used in underwater docking.

the relative attitude information to update the endpoint of the line tracking task, so as to achieve the docking mission.

Two-stage docking algorithm

The two-stage docking algorithm divides the underwater docking task into two parts: target detection and poses estimation. Target detection computes the size and position of the underwater DS obtained from the color image during the docking process, then the 2D image coordinates of each landmark are obtained through image segmentation and clustering algorithm. Pose estimation gives the relative position and orientation from the landmarks 2D coordinates by using different PnP algorithm considering the different light numbers.

Target detection

The difficulty of target detection is that the image of the underwater environment will appear blurred, noise, color shift, contrast reduction, and interference light source and occlusion in the actual environment. The above problems can be effectively solved by introducing a convolutional neural network (CNN), which has surpassed the traditional method in many target recognition tasks. A CNN called Docking Neural Network (DoNN) (Liu et al., 2019) inspired by the YOLO (Redmon et al., 2016) is used to detect DS. We first briefly introduce YOLO so that the improvement of the DoNN algorithm on docking datasets can be explained intuitively.

YOLO divides the input image into S × S grid cells, each cell predicts B bounding boxes. The bounding box is denoted by $B = (x, y, w, h, \text{confidence})$, where (x, y) denotes the center coordinate of the box and (w, h) is the width and height of the box. Confidence refers to the IOU between the predicted box and ground truth. Moreover, $\Pr(\text{Class}_i|\text{Object}) \cdot \Pr(\text{Object})$ is used as the class score for the category distribution. The loss of YOLO is as follows:

$$l_{\text{coord}}(\theta) = \sum_{i=0}^{S^2}\sum_{j=0}^{B} 1_{ij}^{\text{obj}} \left[(x_i - \hat{x}_i)^2 + (y_i - \hat{y}_i)^2 \right] + \sum_{i=0}^{S^2}\sum_{j=0}^{B} 1_{ij}^{\text{obj}} \left[\left(\sqrt{w_i} - \sqrt{\hat{w}_i} \right)^2 + \left(\sqrt{h_i} - \sqrt{\hat{h}_i} \right)^2 \right] \quad (1)$$

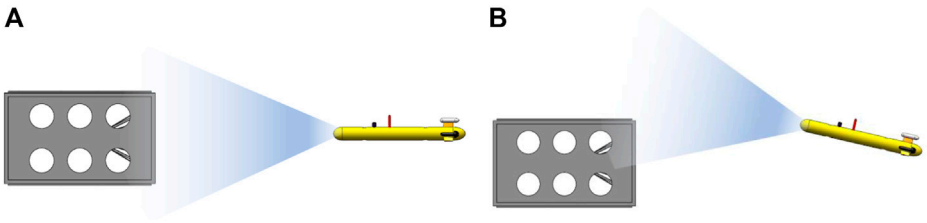

FIGURE 4
(A) Complete observation; **(B)** Incomplete observation.

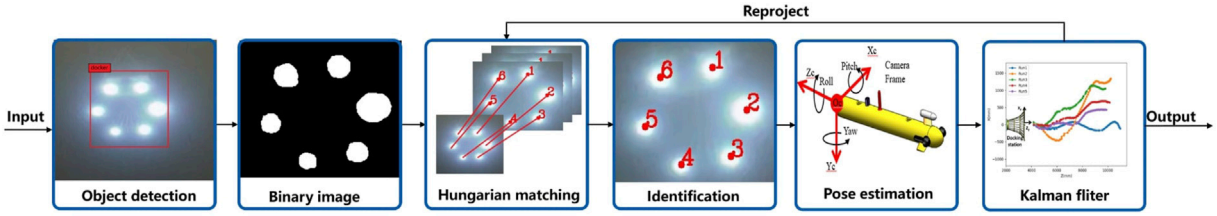

FIGURE 5
Tracking framework combing two-stage docking and SORT algorithm.

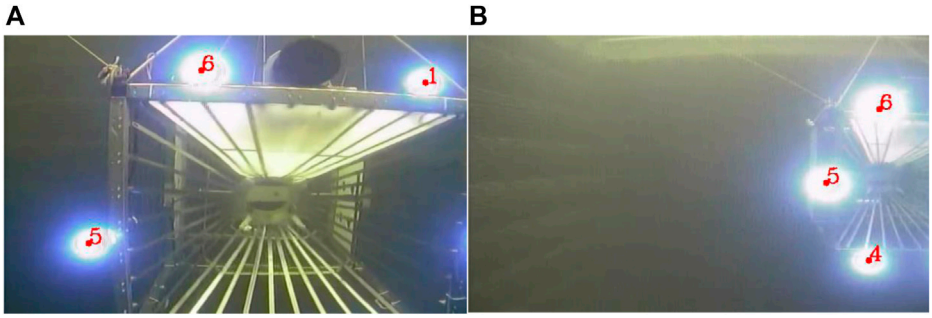

FIGURE 6
(A) Tracking results in close incomplete observation **(B)** Tracking result in big deviation incomplete observation.

$$l_{\text{obj}}(\theta) = \sum_{i=0}^{S^2} \sum_{j=0}^{B} 1_{ij}^{\text{obj}} \left(C_i - \hat{C}_i\right)^2 \tag{2}$$

$$l_{\text{noobj}}(\theta) = \sum_{i=0}^{S^2} \sum_{j=0}^{B} 1_{ij}^{\text{noobj}} \left(C_i - \hat{C}_i\right)^2 \tag{3}$$

$$l_{\text{classes}}(\theta) = \sum_{i=0}^{S^2} 1_{i}^{\text{obj}} \sum_{c \in \text{classes}} \left(p_i(c) - \hat{p}_i(c)\right)^2 \tag{4}$$

$$l_{\text{YOLO}}(\theta) = \lambda_{\text{coord}}\, l_{\text{coord}}(\theta) + l_{\text{obj}}(\theta) + \lambda_{\text{noobj}}\, l_{\text{noobj}}(\theta) + l_{\text{classes}}(\theta) \tag{5}$$

where θ denotes the network parameters (weights), 1_i^{obj} denotes if an object appears in the cell i and 1_{ij}^{obj} denotes that the j th bounding box predictor in the cell i is used for that prediction. Parameters λ_{coord} , λ_{noobj} are used to control the contribution of different parts of the loss function.

The major difference between DoNN and YOLO is the loss function. DoNN redesigned the loss function used in YOLO and remove both the class loss and the confidence partial of class is compatible with docking datasets which contain only one object class. Relatively, the class score using $\Pr(\text{Dock})$ to reduce the

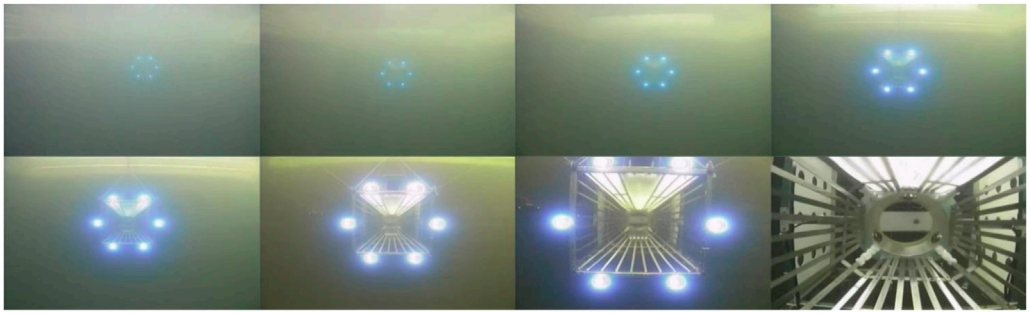

FIGURE 7
Docking process image in water pool.

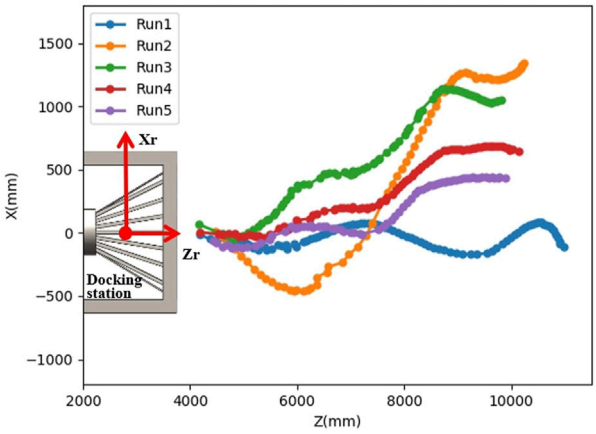

FIGURE 8
Trajectories of the five recovery processes in water-pool.

instability introduced by $\Pr(\text{Class}_i|\text{Object})$ in one sure target class. The loss of DoNN is shown in the formula.

$$l_{\text{DoNN}}(\theta) = \lambda_{\text{coord}}\, l_{\text{coord}}(\theta) + \lambda_{\text{obj}}\, l_{\text{noobj}}(\theta) + \lambda_{\text{noobj}}\, l_{\text{noobj}}(\theta) \quad (6)$$

The experiment shows that DoNN can effectively obtain the 2D position of the DS from the pictures of the complex environment for the underwater DS image. The neural network runs on the Jetson TX2, and each image takes 0.17s. With the bounding box given by DoNN, a threshold-based segmentation is used to obtain the 2D coordinates of the landmarks. The output box of the DoNN is considered the segmented target region, which effectively shields the impact of ambient light on the landmarks division of the DS. The coordinates and numbers of lights are given by a clustering algorithm. Under the condition of observation with at least 5 landmarks, the prior knowledge is used to obtain the identification number corresponding to each landmark coordinate required by the PNP algorithm. The detection process is shown in Figure 2.

Pose estimation

Pose estimation in underwater docking refers to recovering 3D relative position and orientation between docking stations and AUVs from 2D images. The basic principle of the pose estimation algorithm considers that the 2D coordinates of the landmarks are the projection of the real landmarks on the visual plane, so the real 3D pose can be restored from the 2D image. In this case, the PNP algorithm estimates through several pairs of control points, one of which is in the 2D plane and the other in 3D space.

The pose referred to in this study is the position and orientation of the AUV relative to the DS, we employ Euler angles to represent rotation between the camera and the landmarks as shown in Figure 3. We denote pose vector as $p = (t_1, t_2, t_3, r_1, r_2, r_3)$, where t_i is the position X_c, Y_c, Z_c, and r_i refer to the orientation Yaw, Pitch, and Roll.

Non-iterative 3D pose estimation methods based on control points mainly include DLT (Abdel-Aziz and Karara, 1971), EPnP (Lepetit et al., 2009), R-PnP (Li, S et al., 2012). For a small number of control points, the EPnP method remains the best choice. However, as the AUV approaches or deviates greatly from the DS, it may cause incomplete observation of landmarks. Considering that the landmarks are arranged in a uniform circle, there may be only three pairs of effective control points when half or less of DS are observed, which is also common in the practical scenario, the problem will degenerate to P3P.

Although the P3P problem has four solutions, considering the continuity of video, we can still get an effective solution sequence. Intuitively, we propose to find the best solution by finding a pose vector p_m^n that minimizes the pose error with the last pose.

$$argmin_{P_m^n}\left(\lambda_x \sum_1^3 \left|t_i^{P_m^n} - t_i^{p^{n-1}}\right| + \sum_1^3 \left|r_i^{P_m^n} - r_i^{p^{n-1}}\right|\right) \quad (7)$$

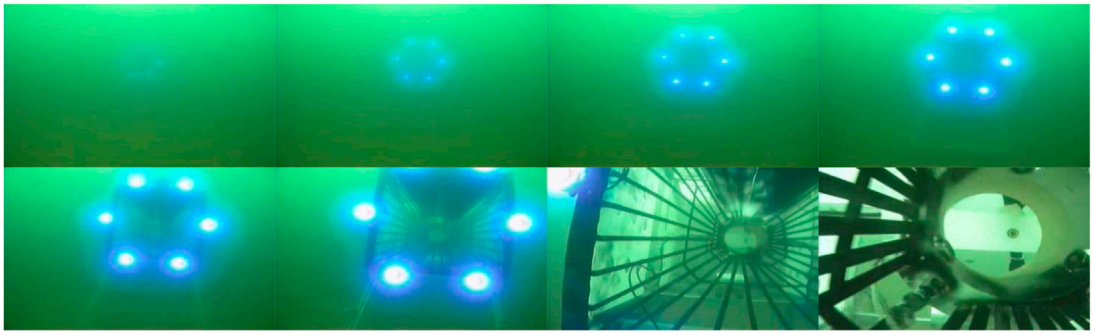

FIGURE 9
Docking process image in the lake (success).

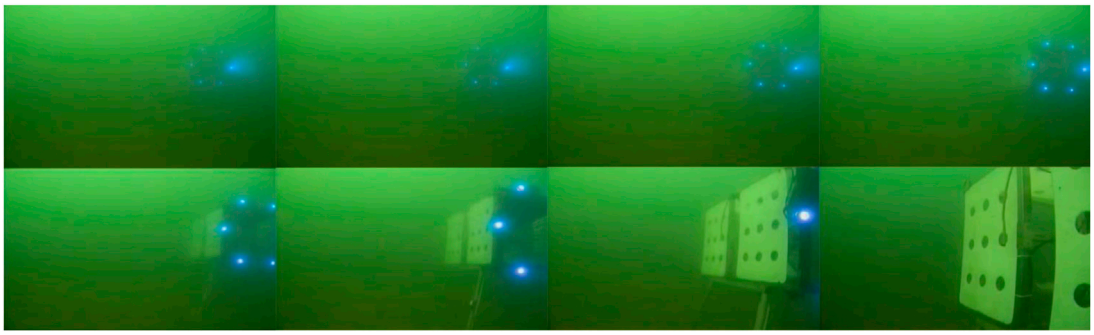

FIGURE 10
Docking process image in the lake (failed).

where p^{n-1} is the last pose and denotes the m th possible pose in frame n. λ_x is used to balance the weight between position and orientation error.

Landmark tracking algorithm

The two phases tracking algorithm remain some problem. For example, once the first stage of target detection fails, the image cannot be used for segmentation even if the image meets the estimation conditions. As shown in Figure 4, during the docking process of AUV, with the gradual reduction of the distance from the DS, it is easy to enter the blind area of the camera. Similarly, under the large initial error condition, AUV will enter the camera blind area and lose guidance too early. The larger the error in the early stage of docking, the more eager guidance information is needed (Xie et al., 2021). If we can effectively use the observation information of the landmarks in a short distance to give the estimated relative position and orientation can effectively improve the reliability of terminal guidance.

The aforementioned problems can be effectively solved by introducing the landmarks tracking method. SORT was proposed as a classic multi-target tracking framework (Bewley et al., 2016). Referring to this algorithm, a landmarks-based tracking framwork is proposed. The proposed tracking framework combining two-stage docking and SORT is shown in Figure 5.

Based on the two-stage algorithm, Hungarian matching and Kalman filter in the SORT algorithm are introduced for tracking. For the tracking part, we retain the IOU loss function in SORT and delete the targets with large IOU loss. In addition, considering that the DS is a whole, instead of predicting multi landmarks, the Kalman filter is applied directly to the final detection results to estimate the pose of the next frame. The predicted result is then projected on the 2D coordinate plane so that it can be matched with the current incomplete observation to obtain the match of control points, which is required in the PnP algorithm. Considering the continuity of the docking process, we believe that there will not be much change in a continuous sequence of images, so the neural network method can be

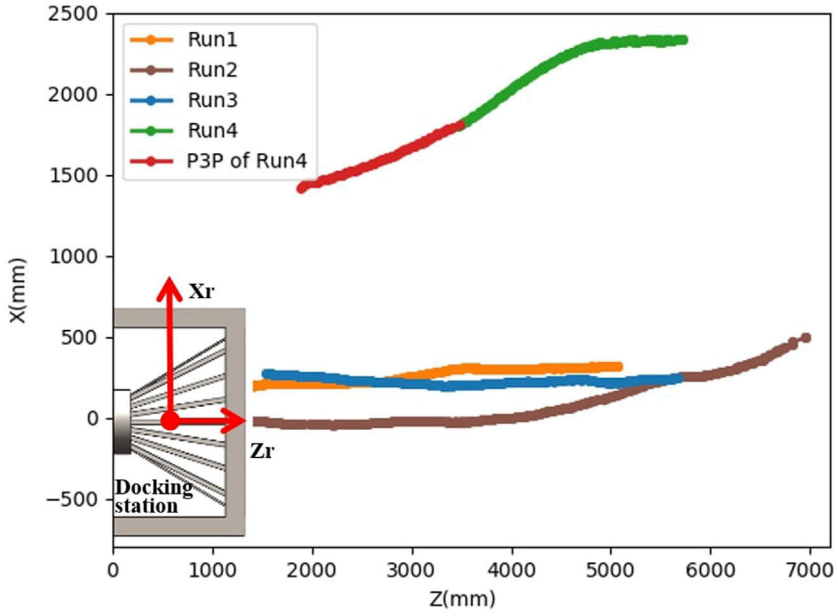

FIGURE 11
Trajectories of the four recovery processes in the lake.

independent of the segmentation method after the DS is detected. Through this structure, the segmentation algorithm can continue to work, using the information of the previous frame in the case of detection failure. Figure 6 shows that the algorithm can still effectively match control point pairs when only three landmarks are observed.

Experimental analysis and results

In this part, we compared and verified the algorithm by only executing optical guidance in the pool environment. In the lake experiment, the acoustic guidance system was used for long-distance guidance, and the robustness of the algorithm was verified in combination with short-range optical guidance.

Water pool experiment

Our goal in the pool experiment is to verify the feasibility of close-range guidance and evaluate the performance by using only the visual guidance algorithm. The pool experiment provides the basis for the real environment experiment on the lake. We experimented with a 10 m wide, 25 m long, and 7 m deep pool, and the water quality was clear. The center of the DS is hoisted to a position 2 m underwater from the water surface. When the AUV is 20 m away from the DS radially, it performs the underwater docking task from the water surface. The forward speed is 0.5 m/s. The whole docking process is only completed by the visual method. A successful docking is shown in Figure 7. In the pool environment, five docking operations were carried out with different initial positions and angles, all the docking was successful. The trajectories of the five recovery processes are shown in Figure 8.

Field experiment

The purpose of the outfield test is to verify the robustness of the algorithm in the field environment based on the pool experiment and to verify the system stability of the acoustic system for correct optical terminal guidance. The field test was carried out in Fuxian Lake, China. The elevation of Fuxian Lake is 1722.5 m, the average water depth is 95.2 m, and the water quality is relatively clear. We selected a relatively flat terrain and placed the DS at the bottom of the lake in advance to ensure its stability. The center of the DS is about 15 m underwater away from the water surface. The AUV dives from the water surface at a distance of 1000 m from the DS and starts the homing and docking mission. First, rough guidance is carried out through acoustic guidance, and then switched to optical guidance when it is 15 m away from the DS.

When performing short-range optical docking, the forward speed is 0.5 m/s. We conducted 4 docking tests on the lake, including 3 successes and 1 failed docking. Figures 9, 10 show a

successful and a failed docking process. Data show that the docking distance on the lake has been reduced, accompanied by more disturbances.

As shown in Figure 10, when the DS is seen, the optical module gives a correct estimation. It can be seen from the image that AUV is deflecting towards DS. However, AUV cannot enormously adjust pose within a short distance owing to inherent mobility, and it missed the DS.

It is noteworthy that in the failed run4 as shown in Figure 11, the prediction of P3P accounted for 33% of the effective output and lasted for 1.6 m in the final stage. If the position and attitude information provided by P3P is missing, AUV will lose guidance information earlier with a large deviation. It can be seen that the P3P algorithm can still provide final help at the boundary of the visual blind area, to expand the workspace of the docking algorithm.

Conclusion

In this study, an underwater active landmark tracking algorithm is proposed to complete the terminal optical guidance. The beneficial characteristics of the neural network are used to effectively identify the DS in the field environment. By introducing the tracking framework, observation failure caused by short-range and large observation angles is improved, and good docking accuracy and robustness are shown in the water pool and field experiments.

Acoustic guidance is the pre-step of optical landmarks guidance in the outfield experiment. It is found that if the USBL system cannot effectively bring the vehicle into the visual range of landmarks for optical guidance, the whole docking process will fail no matter how accurate the optical guidance algorithm is. Therefore, if the effective working scopes of optical guidance can be effectively improved, it will be of great significance to the whole guidance system. In the future, further research will be carried out on how to improve the directivity and working range of optical guidance.

Data availability statement

The raw data supporting the conclusion of this article will be made available by the authors, without undue reservation.

Author contributions

KS made substantial contributions to the supervision and environmental support of the work. ZH completed the writing of the manuscript. All authors participated in the design and act of the experiment, data analysis, report development, revision, and approved the final version.

Funding

This study is supported by the State Key Laboratory of Robotics Foundation (No. 2017-Z05).

Conflict of interest

The authors declare that the research was conducted in the absence of any commercial or financial relationships that could be construed as a potential conflict of interest.

Publisher's note

All claims expressed in this article are solely those of the authors and do not necessarily represent those of their affiliated organizations, or those of the publisher, the editors, and the reviewers. Any product that may be evaluated in this article, or claim that may be made by its manufacturer, is not guaranteed or endorsed by the publisher.

References

Adbel-Aziz, Y. I., and Karara, H. M. (1971). "Direct linear transformation from comparator coordinates into object space in close-range photogrammetry," in ASP Symp. Proc. on Close-Range Photogrammetry, Falls Church, 1971 (American Society of Photogrammetry), 1–18.

Bewley, A., Ge, Z., Ott, L., Ramos, F., and Upcroft, B. (2016). "Simple online and realtime tracking," in 2016 IEEE international conference on image processing (ICIP), Phoenix, AZ, USA, 25-28 September 2016 (IEEE), 3464–3468. doi:10.1109/ICIP.2016.7533003

De Leo, F. C., Ogata, B., Sastri, A. R., Heesemann, M., Mihály, S., Galbraith, M., et al. (2018). High-frequency observations from a deep-sea cabled observatory reveal seasonal overwintering of Neocalanus spp. in Barkley Canyon, NE Pacific: Insights into particulate organic carbon flux. *Prog. Oceanogr.* 169, 120–137. doi:10.1016/j.pocean.2018.06.001

Deeb, A., Svendsen, K., Gregson, E., Seto, M., Burchill, N., and Covill, J. (2019). "Intelligent subsea lander network to support resident AUVs for long duration under-ice ocean observations," in OCEANS 2019 MTS/IEEE SEATTLE, Seattle, WA, USA, 27-31 October 2019 (IEEE), 1–9. doi:10.23919/OCEANS40490.2019.8962766

Deltheil, C., Didier, L., Hospital, E., and Brutzman, D. P. (2000). Simulating an optical guidance system for the recovery of an unmanned underwater vehicle. *IEEE J. Ocean. Eng.* 25 (4), 568–574. doi:10.1109/48.895364

Ghosh, S., Ray, R., Vadali, S. R. K., Shome, S. N., and Nandy, S. (2016). Reliable pose estimation of underwater dock using single camera: A scene invariant approach. *Mach. Vis. Appl.* 27 (2), 221–236. doi:10.1007/s00138-015-0736-4

Lepetit, V., Moreno-Noguer, F., and Fua, P. (2009). Epnp: An accurate o (n) solution to the pnp problem. *Int. J. Comput. Vis.* 81 (2), 155–166. doi:10.1007/s11263-008-0152-6

Li D. J., D. J., Chen, Y. H., Shi, J. G., and Yang, C. J. (2015). Autonomous underwater vehicle docking system for cabled ocean observatory network. *Ocean. Eng.* 109, 127–134. doi:10.1016/j.oceaneng.2015.08.029

Li, S., Xu, C., and Xie, M. (2012). A robust O (n) solution to the perspective-n-point problem. *IEEE Trans. Pattern Anal. Mach. Intell.* 34 (7), 1444–1450. doi:10.1109/tpami.2012.41

Li, Y., Jiang, Y., Cao, J., Wang, B., and Li, Y. (2015). AUV docking experiments based on vision positioning using two cameras. *Ocean. Eng.* 110, 163–173. doi:10.1016/j.oceaneng.2015.10.015

Lin, M., Lin, R., Yang, C., Li, D., Zhang, Z., Zhao, Y., et al. (2022). Docking to an underwater suspended charging station: Systematic design and experimental tests. *Ocean. Eng.* 249, 110766. doi:10.1016/j.oceaneng.2022.110766

Liu, S., Ozay, M., Okatani, T., Xu, H., Sun, K., and Lin, Y. (2018). Detection and pose estimation for short-range vision-based underwater docking. *IEEE Access* 7, 2720–2749. doi:10.1109/access.2018.2885537

Liu, S., Xu, H., Lin, Y., and Gao, L. (2019). Visual navigation for recovering an AUV by another AUV in shallow water. *Sensors* 19 (8), 1889. doi:10.3390/s19081889

Liu, S., Yu, J., Deng, S., and Wan, S. (2021). "An efficient-communication federated learning approach for vehicular edge computing in 6G communication networks. *IEEE Transact. Intell. Transportat. Syst.* 23 (2), 1616–1629.

Maire, F., Prasser, D., Dunbabin, M., and Dawson, M. (2009). "A vision based target detection system for docking of an autonomous underwater vehicle," in Proceedings of the 2009 Australasian Conference on Robotics and Automation, May12-17, 2009, Kobe, Japan (Australian Robotics & Automation Association), 1–7.

Manalang, D., and Delaney, J. R. (2016). "Axial seamount-restless, wired and occupied: A conceptual overview of resident AUV operations and technologies," in OCEANS 2016 MTS/IEEE Monterey, Monterey, CA, USA, 19-23 September 2016 (IEEE), 1–7. doi:10.1109/OCEANS.2016.7761305

Palomeras, N., Vallicrosa, G., Mallios, A., Bosch, J., Vidal, E., Hurtos, N., et al. (2018). AUV homing and docking for remote operations. *Ocean. Eng.* 154, 106–120. doi:10.1016/j.oceaneng.2018.01.114

Park, J. Y., Jun, B. H., Lee, P. M., and Oh, J. (2009). Experiments on vision guided docking of an autonomous underwater vehicle using one camera. *Ocean. Eng.* 36 (1), 48–61. doi:10.1016/j.oceaneng.2008.10.001

Redmon, J., Divvala, S., Girshick, R., and Farhadi, A. (2016). "You only look once: Unified, real-time object detection," Proceedings of the IEEE conference on computer vision and pattern recognition. Las Vegas, NV, USA, 27-30 June 2016, 779–788. doi:10.1109/CVPR.2016.91

Sans-Muntadas, A., Kelasidi, E., Pettersen, K. Y., and Brekke, E. (2019). Learning an AUV docking maneuver with a convolutional neural network. *IFAC J. Syst. Control* 8, 100049. doi:10.1016/j.ifacsc.2019.100049

Seyfried, W. E., Jr, Tan, C., Wang, X., Wu, S., Evans, G. N., Coogan, L. A., et al. (2022). Time series of hydrothermal vent fluid chemistry at Main Endeavour Field, juan de Fuca Ridge: Remote sampling using the NEPTUNE cabled observatory. *Deep Sea Res. Part I Oceanogr. Res. Pap.* 186, 103809. doi:10.1016/j.dsr.2022.103809

Wang, T., Zhao, Q., and Yang, C. (2021). Visual navigation and docking for a planar type AUV docking and charging system. *Ocean. Eng.* 224, 108744. doi:10.1016/j.oceaneng.2021.108744

Xie, T., Li, Y., Jiang, Y., Pang, S., and Wu, H. (2021). Turning circle based trajectory planning method of an underactuated AUV for the mobile docking mission. *Ocean. Eng.* 236, 109546. doi:10.1016/j.oceaneng.2021.109546

Yazdani, A. M., Sammut, K., Yakimenko, O., and Lammas, A. (2020). A survey of underwater docking guidance systems. *Robotics Aut. Syst.* 124, 103382. doi:10.1016/j.robot.2019.103382

Zhou, J., Zhang, W., Wu, D., and Hao, Y. (2014). "Underwater recovery realization for an AUV using positioning-to-line strategy," in 2014 IEEE Conference and Expo Transportation Electrification Asia-Pacific (ITEC Asia-Pacific), Beijing, 31 August 2014 - 03 (IEEE), 1–5. doi:10.1109/ITEC-AP.2014.6940744

frontiers | Frontiers in Energy Research

TYPE Original Research
PUBLISHED 20 September 2022
DOI 10.3389/fenrg.2022.953883

OPEN ACCESS

EDITED BY
Jianhua Zhang,
Clarkson University, United States

REVIEWED BY
Xian Zhang,
Ministry of Science and Technology, China
Weihang Yan,
National Renewable Energy Laboratory (DOE), United States
Lei Gan,
Hohai University, China

*CORRESPONDENCE
Yiyuan Zhou,
zhouyiyuan@ctgu.edu.cn

SPECIALTY SECTION
This article was submitted to Smart Grids,
a section of the journal
Frontiers in Energy Research

RECEIVED 26 May 2022
ACCEPTED 08 August 2022
PUBLISHED 20 September 2022

CITATION
Ding C, Zhou Y, Pu G and Zhang H (2022), Low carbon economic dispatch of power system at multiple time scales considering GRU wind power forecasting and integrated carbon capture.
Front. Energy Res. 10:953883.
doi: 10.3389/fenrg.2022.953883

Low carbon economic dispatch of power system at multiple time scales considering GRU wind power forecasting and integrated carbon capture

Can Ding, Yiyuan Zhou*, Guang Pu and Hongrong Zhang

College of Electrical Engineering and New Energy, China Three Gorges University, Yichang, China

To achieve carbon neutrality in electricity, measures such as increasing the share of renewable energy sources such as wind power and achieving more accurate and faster wind power forecasting, and low carbon retrofitting of thermal power units are all important to achieve the goal. Firstly, the GRU prediction algorithm was used to forecast wind power, which performed well in terms of prediction accuracy and model training speed. Then, we continue to fully utilize the source-side low-carbon characteristics by installing flue gas bypass systems and liquid storage in carbon capture plants to form an integrated carbon capture plant operation, thereby reducing carbon emissions and the proportion of abandoned wind. Secondly, a three-stage low carbon economic dispatch model is established to reduce wind abandonment by combining wind power forecasts on different time scales. Finally, a case study was carried out using a modified IEEE-39 node system. The results show that the proposed three-stage integrated dispatching method can make full use of wind energy and achieve the goal of economic dispatching of the power system.

KEYWORDS

low carbon, multiple time scales, GRU, carbon capture, dispatch of power system

1 Introduction

Currently, renewable energy sources such as wind power are gradually replacing traditional fossil energy sources (Duan et al., 2021). Unlike other renewable energy sources, wind power generation is random and volatile, and has certain anti-peak characteristics. The large-scale grid connection of wind power increases the pressure on the system for peaking, and if necessary, some wind power needs to be abandoned to ensure system safety. The problem of wasted wind power is no longer negligible. The main causes of wind power wastage are shifted between generation and load peaks, the low accuracy of wind power forecasts, and the insufficient adjustment rate of thermal power units (Huang et al., 2021; Han et al., 2022; Zhu et al., 2022). Highly accurate wind power forecasting can be achieved through artificial intelligence algorithms. The problem of the adjusting rate of thermal power units can be solved by introducing integrated carbon

capture plants. In conclusion, wind power can be absorbed through a reasonable dispatch control strategy, combined with multi-timescale wind power forecasting (Cheng et al., 2022; Tian et al., 2022; Wei et al., 2022).

At present, wind power forecasting focuses on the study of forecast errors and multi-time scale forecasting, and is used to improve the utilization-ratio of wind power by matching it with dispatch schedules on different timescales (Aslam and Albassam, 2022; Chen W et al., 2021). The accuracy of wind power forecasting improves as the time scale is shortened, and it is relevant that multi-timescale forecasting can correct deviations in long time scales. The wind power forecasts currently used in power system dispatching are mainly long-timescale for day-ahead dispatching. At the same time, there has been a lot of research on traditional and artificial intelligence algorithms to effectively deal with the volatility and randomness of wind power and improve its accuracy (Li et al., 2021; Sun et al., 2021). Traditional algorithms include statistical models such as autoregressive integrated moving average (ARIMA), which uses statistical methods to establish the relationship between historical and forecast values. However, traditional algorithms are poor at predicting volatility. Artificial intelligence algorithms include machine learning algorithms and neural network algorithms (Sun et al., 2021; Sahra et al., 2022). Machine learning algorithms such as least squares support vector machines (LSSVM) and support vector regression (SVR). Neural network algorithms such as convolutional neural network (CNN), recurrent neural network (RNN), long short-term memory (LSTM), and gated recurrent unit (GRU), of which RNN, LSTM, and GRU are recurrent neural networks, can store sequence history information and combine it with current input values, which are calculated and then continued into subsequent units (Tanveer and Zhang 2022). Recurrent neural networks are specifically used for time series, which can effectively improve prediction accuracy and reduce model training time.

Due to its time-series nature, LSTM and GRU have great advantages in processing wind power data. For power prediction of multiple wind turbines, CNN can be used to extract the spatial features of the data first, and then the temporal characteristics of the power series can be established by LSTM to achieve the power prediction of wind turbines (Chen et al., 2021a). When the historical data is few, the pre-trained model can be fine-tuned in the target domain with small data by transfer learning (TL) to make full use of the source domain data and improve the performance of the model on the target domain data. GRU is then used to extract temporal feature information from wind power and meteorological data (Chen et al., 2021b). For ultra-short-term wind power prediction, the key features of the input data can be extracted by CNN and the dynamic changes of the features proposed by CNN can be learned by bi-directional modeling using bidirectional gated recurrent unit (Bi-GRU) network (Meng et al., 2022). In this paper, the GRU is used to predict wind power as preparatory data for input into a dispatch model containing carbon capture technology to achieve integrated economic dispatch of the power system.

After the multi-timescale wind power forecasts have been made, they are fed into the dispatching model. Wind abandonment can be improved by considering regulation devices in the dispatch plan. Typical regulation devices are storage devices, high energy-carrying devices, pumped storage plants, etc. Conditioning devices are effective in improving wind power utilization-ratio, but energy storage devices have significant energy losses. High energy-carrying devices are often difficult to create links with wind farms due to the constraints of where the resource is located (Xiang et al., 2021; Zhang Z et al., 2022). Carbon capture devices, on the other hand, are converted from traditional thermal power plants and do not have geographical restrictions (Gao et al., 2021; Huang et al., 2022; Xie et al., 2022).

Today, coal is still the dominant fuel, and carbon capture and storage (CCS) is an important technology to combat global climate change by allowing the continued use of fossil fuels and significantly reducing CO2 emissions. However, there are potential risks associated with carbon storage and CCS is currently a high investment. CO2 transport and storage should therefore be given more consideration where coal-fired power plants have a large installed capacity and are densely distributed. The investment risk can be solved by using better capture solvents, better boiler systems, and more efficient turbines, which can effectively reduce costs and energy losses (Fan et al., 2018; Fan et al., 2021).

The dispatch mathematical model in this paper is divided into optimization objectives and constraints. The optimization objective includes the start-up and shut-down and coal consumption costs of thermal power units, the cost of wind abandonment penalties, the cost of carbon trading, the depreciation cost of carbon capture plants, and the cost of solvent losses in the carbon capture process. The CCS technology includes carbon capture, transport, and storage. However, in general, the cost of the carbon capture process is the largest and changes with the capture method, so this paper focuses on the cost of carbon capture (Fan et al., 2019). Constraints include power balance constraints, wind power output constraints, thermal unit output constraints, thermal unit climbing constraints, thermal unit start/stop constraints, and integrated carbon capture plant operation constraints.

The dispatch model in this paper includes an integrated carbon capture plant. Carbon capture and storage is an important technology for decarbonization (Qian et al., 2020; Liu et al., 2022; Nie et al., 2022). While thermal power is still the dominant energy source, the addition of carbon capture equipment to conventional thermal power plants can increase system operational flexibility while achieving low-carbon and effectively improving wind power utilization (Chen et al., 2021; Zhang G et al., 2022). Carbon capture plants have the advantage of regulating peak load curves, making them an ideal source of power to complement wind power. However, current research has mainly used split-flow carbon capture plants, where the

CO2 absorption process is coupled with the CO2 resolution process, which does not allow for energy time-shifting, resulting in an increase in carbon capture energy consumption with increasing thermal power plant output, which is not conducive to achieving economics. The integrated carbon capture plant, however, introduces a liquid storage type on top of the split-flow type, which enables the decoupling of the CO2 absorption process from the CO2 resolution process and makes the system more flexible and economical to operate (Jin et al., 2021; Xing et al., 2021).

This paper first uses LSTM and GRU to forecast wind power in three dimensions (1h, 15min, and 5min), with GRU performing better in terms of both prediction accuracy and model training speed. A three-stage (day-ahead, intra-day, and dynamic) economic dispatch model for power systems with integrated carbon capture plants is then constructed, with wind power forecasts as inputs to the dispatch model, and each time scale corresponding to the other. The dispatching results show that the proposed three-stage integrated dispatching model can make full use of wind energy and achieve the goal of low-carbon economic dispatch. Section 2 presents the low-carbon mechanism analysis, Section 3 introduces the principles of the forecasting algorithm and the construction of the three-stage dispatch model, and Section 4 presents the case study validation and analysis.

The main contributions of this paper are as follows:

1) Combining wind power forecasting with power system dispatch, more accurate wind power forecasting accuracy will facilitate optimal system dispatch. This is reflected in the reduction of wind power waste and the economy of dispatching costs.
2) A combination of split-flow and liquid storage carbon capture technology has been constructed, which is based on the transformation of the original thermal power plant and does not have geographical restrictions. At the same time, the addition of liquid storage carbon capture enables the decoupling of CO2 absorption and extraction processes, making system operation more flexible.
3) Existing research mostly focuses on day-ahead dispatching. This paper combines day-ahead, intra-day, and dynamic stages, to form a three-stage dispatching model, which can improve the system energy structure and reduce wind abandonment and load loss.

2 operational mechanisms that take into account multi-timescale wind power projections and the low carbon characteristics of carbon capture plants

A carbon capture plant is a traditional thermal power plant with a flue gas bypass system or solution storage to achieve either split-flow carbon capture or liquid storage carbon capture, while a combination of the two forms of carbon capture results in an integrated carbon capture plant.

Carbon capture and storage (CCS) is an important way to achieve low carbon development in the power industry. It consists of three components: carbon capture, transport, and storage, of which the capture process is closely linked to the power plant. By converting a traditional thermal power plant into a carbon capture plant, a large amount of CO2 is separated from the flue gas emitted by the plant and processed through a series of processes to form a high concentration of CO2, which is eventually isolated from the atmosphere through geological storage and deep-sea storage.

CCS, as one of the key measures for CO2 reduction, is considered to be the most promising technology for development. Numerous studies have reported that CCS technology has an important contribution to make to the global goal of controlling temperature rise. In addition to this, CCS technology can not only improve the recovery of conventional energy but also facilitate the development and utilization ratio of unconventional energy and mineral resources. Considering the irreversible trend of the global low-carbon energy transition, accelerating the research and implementation of CCS technology is an inevitable choice to support global energy security, which is conducive to the rational allocation of energy, promoting the efficient use of resources, and effectively solving the bottleneck problem of regional development. At the same time, CCS technology can turn waste into treasure, promote the formation of new economic points, and inject vitality into the development of the market economy. Although CCS is an important way to reduce carbon dioxide emissions in the future, CCS projects still have problems such as large investment, high energy consumption and uncertain risks, and some of the key technologies are still being worked out and solved, making it difficult to play a large role in a short period. Overall, it is still at the stage of research and development and implementation, and there is still a gap between it and large-scale promotion, which requires continued in-depth research.

Carbon capture is divided into post-combustion, pre-combustion and oxygen-enriched combustion carbon capture. Post-combustion capture is the most mature technology and is widely used. This paper uses post-combustion carbon capture technology.

An integrated carbon capture plant can respond to system demand for active CO2 emissions, but can also transfer carbon capture consumption from peak load times to valley times, and absorb carbon capture energy during valley times. This improves dispatch decision flexibility while relieving operational pressure at peak load times. An integrated carbon capture plant can improve wind power utilization-ratio, but can also achieve a time-shift of carbon capture

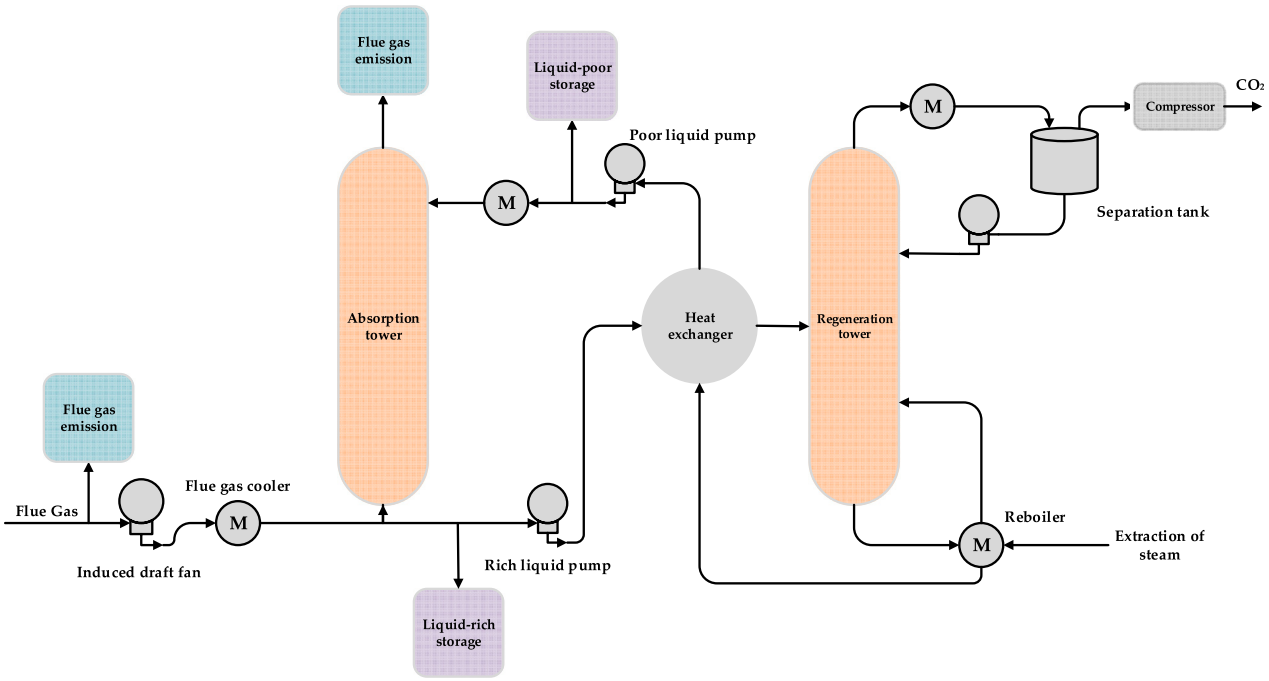

FIGURE 1
Internal schematic of an integrated carbon capture plant.

energy consumption, enabling low carbon economic operation of the system.

The transfer of energy consumption for carbon capture is achieved by the amount of fluid-rich and fluid-poor storage. The process is that when the system energy consumption increases at a certain time, the carbon capture will also be intensified and the carbon capture energy consumption will increase. At this point, the carbon capture rich-tank will start to store CO2 and not resolve it until the load is low. In summary, a liquid storage carbon capture plant can divert carbon capture energy from peak loads and increase net system output.

Figure 1 shows the internal schematic of an integrated carbon capture plant. Post-combustion carbon capture in thermal power plants consists of CO2 separation and CO2 compression. Firstly, the processed flue gas is fed into an absorption tower containing monoethanolamine (MEA) solvent. Under certain operating conditions the MEA absorbs the CO2 in the flue gas to form a rich liquid containing CO2, while the rest of the flue gas (mainly O2 and N2) is discharged directly into the atmosphere through the top of the tower. The rich liquid is then pumped into the regeneration tower, where the operating conditions are changed to achieve CO2 resolution and MEA solvent regeneration, with the resolved CO2 being compressed and stored, and the lean liquid from the regeneration tower being returned to the absorption tower to complete the recycling of the solution.

The MEA solution has a strong alkaline and is therefore often used as an absorbent for acidic gases such as CO2 and is widely used in the absorption of CO2 in coal-fired power plants. The MEA solution reacts rapidly with CO2 at 20–50°C to produce a more stable carbamate, which removes CO2 from the flue gas. The MEA solution hardly reacts with other gases in the flue gas. When the temperature of the MEA solution is raised to 105°C or higher, the carbamate can thermally decompose, thus regenerating the MEA solvent and releasing the CO2.

The reaction equation of MEA with CO2 is:

$$\begin{gathered} H_2O + MEAH^+ \rightleftharpoons MEA + H_3O^+ \\ 2H_2O \rightleftharpoons H_3O^+ + OH^- \\ HCO_3^- + H_2O \rightleftharpoons H_3O^+ + CO_3^{2-} \\ CO_2 + OH^- \rightarrow HCO_3^- \\ HCO_3^- \rightarrow CO_2 + OH^- \\ MEA + CO_2 + H_2O \rightarrow MEACOO^- + H_3O^+ \\ MEACOO^- + H_3O^+ \rightarrow MEA + H_2O + CO_2 \end{gathered} \tag{1}$$

The net output of a carbon capture plant needs to reduce the carbon capture energy consumption, which is divided into operational energy and fixed energy consumption. The energy used to resolve CO2 in the carbon capture process is much greater than the energy used to absorb it. Thus, the mathematical

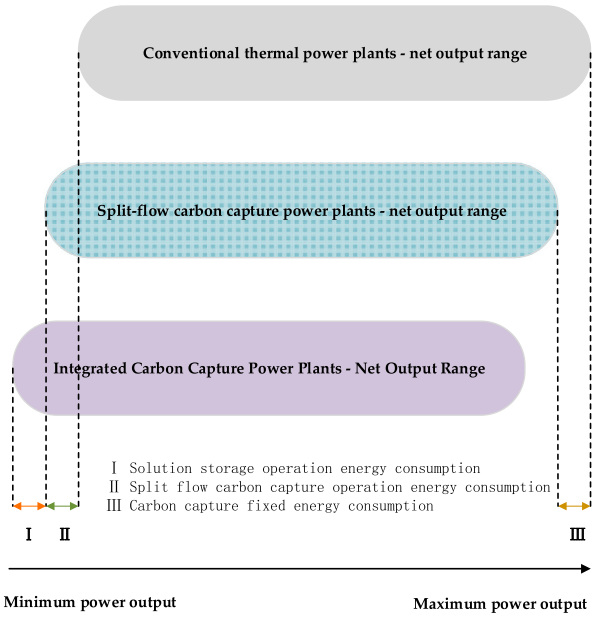

FIGURE 2
Net output range for conventional thermal power plants, split-flow carbon capture plants and integrated carbon capture plants.

model of a carbon capture plant, considering only the energy consumption for resolution and compression, is as follows.

$$\begin{cases} E_{Gi,t} = e_{gi} P_{Gi,t} \\ 0 \le \delta_i \le 1 \\ E_{totalCO2i,t} = E_{CGi,t} + \beta \delta_i E_{Gi,t} \\ 0 \le E_{totalCO2i,t} \le \eta \beta e_{gi} P_{Gi,\max} \\ P_{Bi,t} = \lambda E_{totalCO2i,t} \\ P_{Gi,t} = P_{Ji,t} + P_{Di} + P_{Bi,t} \end{cases} \tag{2}$$

where $P_{Gi,t}$ is the total output of unit i at time t. e_{gi} is the carbon intensity of unit i. $E_{Gi,t}$ is the total CO2 emissions of unit i at time t. δ is the flue gas split ratio of unit i. β is the carbon capture efficiency. $E_{CGi,t}$ is the amount of CO2 to be captured supplied by the solution storage of unit i in period t. $E_{totalCO2i,t}$ is the total CO2 captured by unit i at time t. η is the maximum operating factor of the solution regeneration and the compression tower. $P_{Gi,\max}$ is the maximum output of unit i at time t. λ is the energy consumption required to capture each unit of CO2. $P_{Bi,t}$ is the operational energy consumption of carbon capture plant i at time t. P_{Di} is the fixed energy consumption of carbon capture plant i. $P_{Ji,t}$ is the net output of carbon capture plant i at time t.

From eq. (2), it can be deduced that the net output range for integrated carbon capture plants and the split-flow carbon capture plants are:

$$\begin{aligned} P_{Gi,\min} - \lambda\eta\beta\delta_{i\max} e_{gi} P_{Gi,\max} - P_{Di} \le P_{Ji,t} \le P_{Gi,\max} - P_{Di} \\ P_{Gi,\min} - \lambda\beta\delta_{i\max} e_{gi} P_{Gi,\min} - P_{Di} \le P_{Ji,t} \le P_{Gi,\max} - P_{Di} \end{aligned} \tag{3}$$

It can be seen from the equations that the integrated carbon capture plants have a greater net output range than the split flow plants, using Figure 2 depicts the net output range of the three plants.

Compared to conventional thermal power plants, split-flow carbon capture plants have a lower net bottom output limit. The time-shifting nature of the carbon capture energy consumption of a carbon capture plant, based on the addition of a storage tank to the plant, results in a lower net bottom output limit for an integrated carbon capture plant. With the same rotating reserve requirements, the lower net output limit facilitates the absorption of wind power, resulting in energy savings and emission reductions. In addition, carbon capture plants can change the plant operation by changing the flue gas split ratio, whereas traditional thermal plants require boiler adjustments. Changing the flue gas split ratio is more time-sensitive and can effectively address wind abandonment and load loss.

Wind power is a key source for decarbonizing power system because it is low-cost and zero-carbon. However, unlike other forms of energy, wind power generation is random and highly volatile, and exhibits certain anti-peak characteristics. Nowadays, the large-scale grid connection of wind power puts greater pressure on system peaking, and sometimes some of the wind energy has to be abandoned to ensure system safety. Shortening the forecast scale can effectively improve the accuracy of wind power forecast, while the lack of efficiency of thermal regulation can be solved by fast regulation devices (carbon capture plants). If the two are combined, more wind energy can be absorbed. At the same time, low wind power forecasting accuracy requires flexibility in the dispatch. Therefore, improving the accuracy of wind power forecasting, promoting the absorption of wind power and reducing the level of system carbon emissions remain topical issues.

There are two ways to improve the accuracy of wind power forecasting, one is to shorten the time scale and the other is to use forecasting algorithms that conform to the pattern of wind power generation.

The accuracy of wind power forecasting improves with the shortening of the time scale. The results of wind power forecasting on different time scales are sent to the dispatching model, which helps to correct the deviation between the long-time scale pre-dispatching plan and the short time scale working conditions. At present, the economic dispatch of power systems containing wind power is mostly concentrated in the long-time scale dispatch phase, so it is of practical significance to study the combination of wind power prediction and dispatch on multiple time scales.

Because of the stochastic and highly volatile nature of wind power, the use of forecasting algorithms that match its characteristics has a crucial impact on the results. Traditional statistical model-based forecasting algorithms establish a mapping relationship between input and output quantities

and do not focus on the influence of the stochastic component, nor do they take into account the decaying nature of the stochastic component over time. In the paper, GRU is used to forecast wind power. As a variant of the RNN, GRU is suitable for processing time series data and can effectively extract the correlation information between each time sub-series. Compared with the LSTM, GRU has fewer parameters and is more computationally efficient.

Due to the large-scale wind power grid connection, the traditional day-ahead dispatching strategy is no longer sufficient to meet the requirements of system safety and economy. Combining multi-time-scale wind power forecasting with multi-time-scale dispatching enables the system to have a deeper regulation range and a faster regulation rate, based on the energy transfer characteristics of carbon capture plants. The deeper regulation range allows for the absorption of wind abandonment during the day-ahead and intra-day dispatch stages. The faster regulation rate allows the system to participate in the dynamic dispatch stage.

The three-stage dispatching strategy is: the day-ahead stage sets the next day's 24 h unit start-up and shutdown and output plan, the intra-day stage can correct the unit output according to the 15min short-term wind power forecast, and the dynamic stage can adjust the net output of the carbon capture plant according to the 5-min ultra-short-term wind power forecast.

The carbon capture plant can increase or decrease the energy consumption of the carbon capture equipment at any time in response to system requirements, changing the net output and increasing the speed of output regulation of the thermal plant. At the same time, due to the presence of carbon capture consumption, the net output of the carbon capture plant is lower and the regulation range is deeper. The specific mechanisms for eliminating wind abandonment are as follows.

For the same standby requirements, carbon capture plants have a lower net output threshold, thus enabling less wind to be abandoned. On the one hand, carbon capture plants can provide more up-rotating reserves. When more up-rotation reserve is required, conventional thermal plants can only turn on additional units, resulting in wind abandonment. Carbon capture plants, do not need to restart units with the required up-rotation reserve, which effectively reduces wind abandonment.

On the other hand, carbon capture equipment can change the net output of a carbon capture plant by adjusting the shunt ratio, essentially regulating the rate of steam extraction, which is faster. Compared to conventional thermal power plants, which require 5–10 min for standby response, carbon capture plants can respond to standby requirements in less than 5 min. As a result, conventional thermal plants are unable to respond quickly to a 5-min wind forecast during the dynamic stage, whereas carbon capture plants have limited regulation but can effectively reduce wind abandonment.

3 Multi-timescale low carbon economic dispatch model

3.1 Predictive model

3.1.1 Pre-processing

Exponential weighted moving average (EWMA) is often used to describe trends of time series. It considers the high weight of recent data, at the same time, gradually reduces the weight of recent data to compensate overall trend. This feature can describe future trends in wind power and further enrich the dataset.

The process of constructing the EWMA feature is as follows. For wind power, n is the total number of time points.

$$\begin{cases} e_i = l_0, i = 0, 1 \\ e_i = (1-\alpha)e_{i-1} + \alpha l_{i-1}, i = 2, 3 \ldots n \\ e_i = (1-\alpha)e_n + \alpha l_n, i > n \end{cases} \tag{4}$$

Where, α is the smoothing parameter. The value range of α is $(0, 1]$, and differential evolution method is used to minimize the objective function to obtain the optimal α value. The calculated objective is as follows.

$$\alpha = \text{argmin}\left(\sum_{i=1}^{N}\sqrt{(l_i - e_i)^2}\right) \tag{5}$$

Simple moving average (SMA) is an unweighted arithmetic average of the n values preceding a given variable. For example, a 96-point simple moving average of a 15-min wind power forecast refers to the average of the previous day's wind power. If the power at each point is p_1 to p_n, and when calculating successive values, a new point is added while an old point is dropped out, the SMA is calculated as.

$$SMA_{t1,n} = SMA_{t0,n} - \frac{p_1}{n} + \frac{p_{n+1}}{n} \tag{6}$$

Figure 3 shows the wind power (15 min) and its EWMA and SMA features for Belgium in July 2021. The red line in the figure is the EWMA, which reflects the trend of wind power in the short term and provides reference information for wind power forecasting. The blue line in the figure is the SMA. SMA is the wind power average over the first N points and is a simple extraction of the wind power trend. EWMA can extract the trend while eliminating the effect of complex noise and enriching the dataset.

Curve features include average, minimum, maximum, and average difference values, respectively used to describe average trend and extreme value of time series data and changes of time series data on different days. For time-series data of impact quantity V, V_w^i means impact quantity within time-window w, point i changes from 1 to 4. Equations show calculation of V_{mean} and $V_{\text{mean\_diff}}$. The time-window w is set as four for insight into hourly changes in wind power.

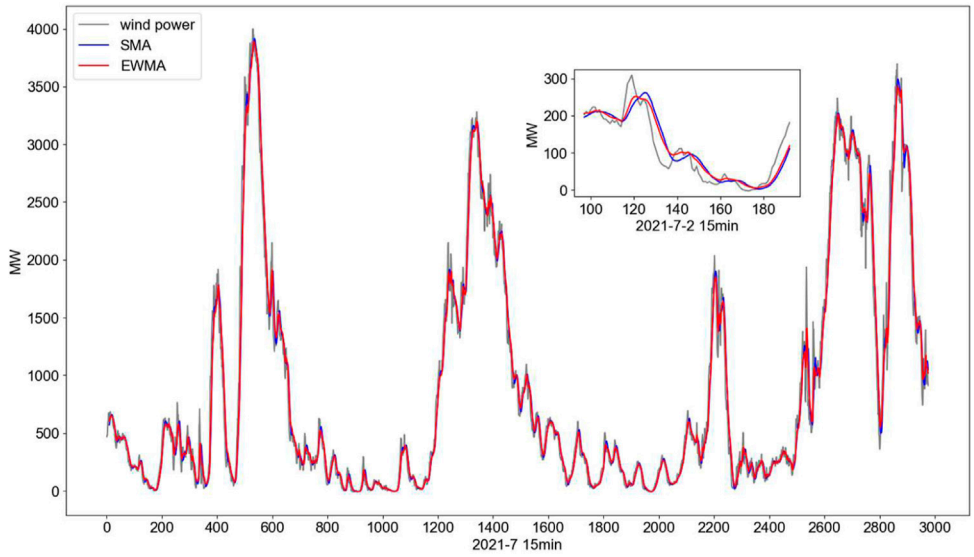

FIGURE 3
EWMA and SMA features of wind power from Belgium July 2021.

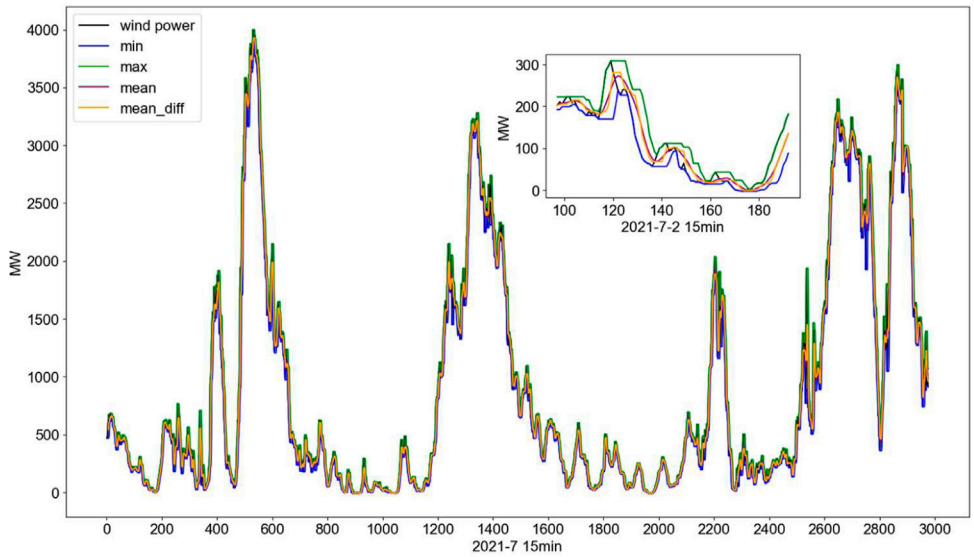

FIGURE 4
Curve features for wind power from Belgium in July 2021.

$$V_{\text{mean}} = \sum_{i=1}^{w} v_w^i \Big/ w \tag{7}$$

$$V_{\text{mean\_diff}} = \sum_{i=2}^{w} \left(v_w^i - v_w^{i-1}\right) \Big/ (w-1) \tag{8}$$

Figure 4 shows the curve characteristics of wind power. Constructing curve features for wind power can maximize the use of data trends and help the model learn. Using average, extreme and average difference values, wind power prediction models will be more sensitive. Data that is only one-dimensional

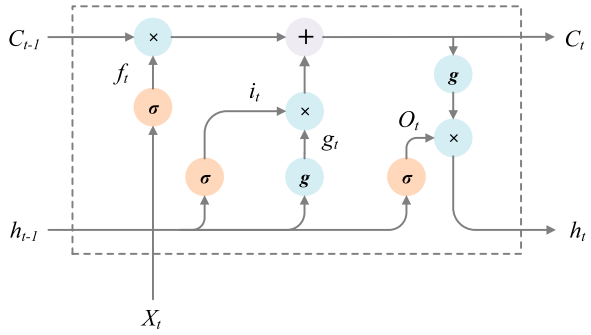

FIGURE 5
Schematic diagram of the basic unit structure of LSTM.

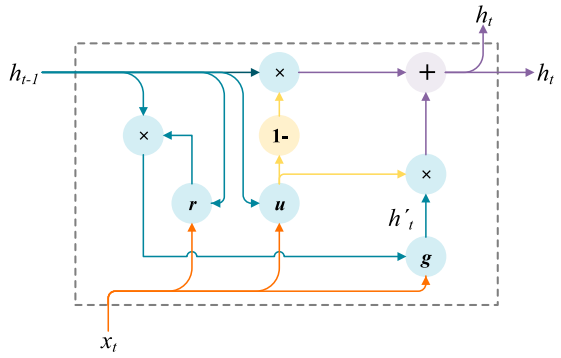

FIGURE 6
Schematic diagram of the basic unit structure of GRU.

is extended to four dimensions. As the amount of data increases, the model can also get better prediction results.

3.1.2 LSTM

Long short-term memory network (LSTM) solves the gradient disappearance of recurrent neural network (RNN) during remote transmission. LSTM currently has an excellent performance in natural language processing and time series prediction. The basic unit structure diagram is shown in Figure 5 (Farah, Aneela and Muhammad., 2021).

In Figure 5, X_t and h_t are the input and output of the basic unit at time t, i_t and f_t are the output of the input gate and forget gate at time t respectively, and O_t is the output of the outputting-gate at time t, and g_t is the unit state at time t. The specific calculation equations are as follows:

1) Input status

$$g_t = \tanh\left(W_{ig}x_t + b_{ig} + W_{hc}h_{t-1} + b_{hg}\right) \tag{9}$$

2) Gating status

$$i_t = sigmoid\left(W_{ij}x_t + b_{ii} + W_{hi}h_{t-1} + b_{hi}\right) \tag{10}$$

$$f_t = sigmoid\left(W_{if}x_t + b_{if} + W_{hf}h_{t-1} + b_{hf}\right) \tag{11}$$

$$O_t = sigmoid\left(W_{io}x_t + b_{io} + W_{ho}h_{t-1} + b_{ho}\right) \tag{12}$$

3) Memory status

$$C_t = f_t \times C_{t-1} + i_t \times g_t \tag{13}$$

4) Output status

$$h_t = o_t \times \tanh\left(C_t\right) \tag{14}$$

where: *tanh* is the hyperbolic tangent function; W is the weight vector; b is the bias.

It can be seen from Eqs (10)–(12) that LSTM fully considers the correlation between various data while making predictions, and gives sufficient space for important information. Therefore, it can usually obtain more desirable results when performing time-series data prediction.

3.1.3 GRU

Traditional convolutional networks do not have the computational ability to take into account time propagation, and the current moment output value of a recurrent neural network (RNN) is influenced by the input values of previous moments. For the wind power prediction problem, there is a time-dependent characteristic, that is, there is some correlation in the time dimension of wind power. RNN has an advantage over linear prediction models in dealing with non-linear relationships between variables. At the same time, although RNN solves the problem of long-term dependence of the prediction target, there is the problem of gradient disappearance or explosion when the network is back-propagated for calculation. The long short-term memory (LSTM) network only updates the internal states of the cells through linear transformations, allowing the information to be smoothly propagated backward across the entire time axis, thus increasing the information propagation distance, but the complex network structure of the LSTM often takes more time to train. The gated recurrent unit (GRU) simplifies the LSTM cell, which not only retains the strong time-series dependent capture capability but also effectively reduces the model training time (Niu et al., 2020).

To fully exploit the temporal characteristics of wind power to improve prediction accuracy, this section introduces a deep learning algorithm, Gated Recurrent Unit (GRU), with temporal memory capability. The deep learning framework used is TensorFlow and Keras, based on which the prediction model and structural parameters of GRU are designed to forecast

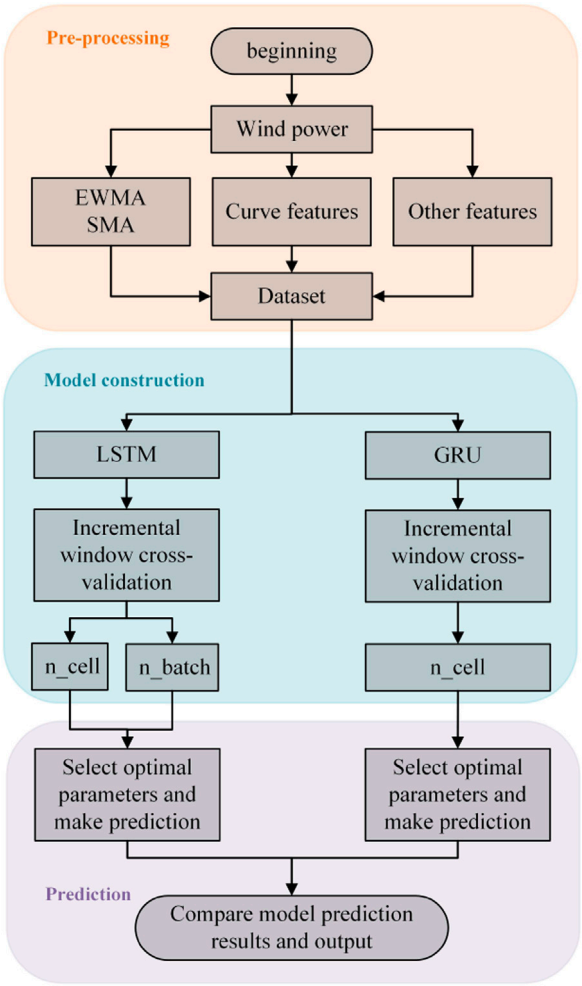

FIGURE 7
Flow chart of the prediction algorithm.

on three time-scales to match the economic dispatch on each time scale for wind power.

3.1.3.1 Principle of prediction algorithm

GRU is a variant of the LSTM that simplifies the gating structure of the LSTM, thus effectively reducing the training time of the network. While the LSTM consists of three gating mechanisms, GRU unifies the forgetting and updating gates of the LSTM into a new updating gate, and thus contains only two gating mechanisms. The update gate allows adaptive control of the information flowing through the hidden unit, combining it with new inflow content for information update. The reset gate allows the contents of the memory cell to be reset. The GRU schematic is shown in Figure 6.

Where x_t and h_t are unit input and output variables. h_{t-1} and h_t are internal state variables at two moments before and after the hidden layer. g is a non-linear operator. In the schematic diagram +, -, 1- are linear operators. The GRU concrete state update equation is as follows.

Resetting gate

$$r_t = \sigma(W_r x_t + R_r h_{t-1} + b_r) \tag{15}$$

Candidate Status:

$$h_t^{'} = g(W_z x_t + R_z(r_t \odot h_{t-1}) + b_z) \tag{16}$$

Update Gate:

$$u_t = \sigma(W_u x_t + R_u h_{t-1} + b_u) \tag{17}$$

New Status:

$$h_t = u_t \odot h_t^{'} + (1 - u_t) \odot h_{t-1} \tag{18}$$

where x_t is the input vector at moment t. W_r, W_z and W_u are the weight matrices associated with the input status. R_r, R_z and R_u are the weight matrices associated with the recurrent state. b_r, b_z and b_u are the bias vectors. σ is the activation function: Sigmoid. g is the activation function tanh. $\odot$ is the dot product. r_t, u_t take values in the range [0,1], if both take 1, the GRU is equivalent to an RNN. the smaller the value of u_t, the smaller the update of the state information of the GRU, more for the previously saved information.

The incremental cross-validation model is shown in Figure 7. Cross-validation is commonly used in the process of building predictive models and selecting model parameters. Specifically, the dataset is sliced in different ways and then various combinations of training and validation sets are fed into the model, where the training set is used for model training and the validation set is used to verify the model. With different slicing methods, data that was last used as the training set may become samples in the test set in the next iteration, thus enabling cross-validation. For time series data, incremental window cross-validation or fixed window cross-validation can be used to ensure time integrity and also to prevent future data leakage. Grid search is an automated method of adjusting parameters by continuously searching through a given range of parameter to find the best parameters. This method is even more advantageous when applied to small dataset and the sklearn provides a function GridSearchCV specifically. Applying cross validation to small dataset maximizes sample information. Also, by using models with different parameters, overfitting can be reduced to a certain extent, thus improving the robustness of the model. After grid adjustment of the parameters, the prediction accuracy and time lapse of the model are optimized.

A comparison of the predictions before and after cross-validation using incremental cross-validation is shown in Figure 8, which includes the wind power prediction targets (measured and upscaled) and the GRU predictions before and after cross-validation. As can be seen from the graph, the GRU forecasts are superior in terms of prediction accuracy and time delay when using incremental cross-validation.

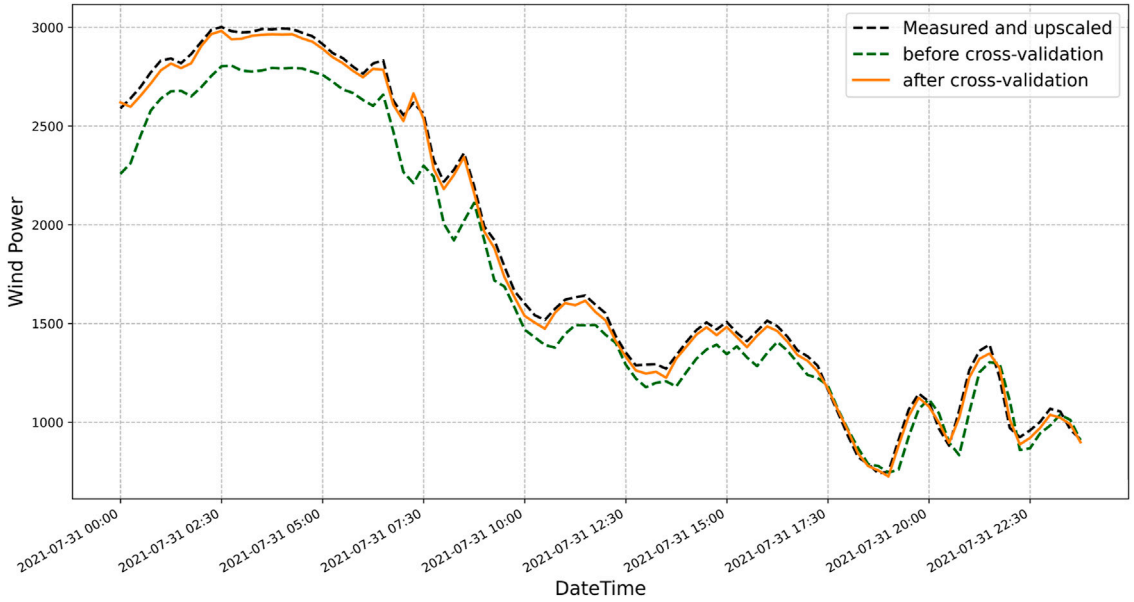

FIGURE 8
GRU predicted wind power before and after incremental cross-validation.

3.2 Low-carbon dispatch modeling considering multi-time-scale wind power forecasting and integrated carbon capture power plants

3.2.1 Multi-timescale low carbon dispatch framework

Multi-timescale wind power forecasting combined with integrated carbon capture plants can exploit the low carbon potential of the system. Firstly, the time-shifted nature of integrated carbon capture energy can both reduce the system's lower net output limit and respond positively to the system's need to emit CO2. Secondly, multi-timescale wind power predictions reduce wind power prediction errors and enable more accurate system dispatch plans to be made. This enables the full utilization of wind power, reduces the output of high carbon units and optimizes the low carbon and economic performance of the system. Thirdly, liquid storage carbon capture plants have a certain effect in the dynamic dispatch stage. Errors are reduced through highly accurate wind power predictions. The flue gas diversion ratio is then set in both the day-ahead and within-day phases, thus improving system dispatch flexibility, maximizing carbon capture and exploring low-carbon potential. In summary, multi-timescale wind power load predictions together with integrated carbon capture plants work together in the three stages of dispatch to optimize the system energy structure, resource allocation, reduce wind abandonment and load loss situations, and thus achieve low carbon economic dispatch.

Figure 9 shows the multi-timescale low carbon economic dispatch framework. The dispatch plan is developed 24 h in advance and the time unit is 1 h. The dispatch quantities to be determined are the unit start/stop plan and the unit output plan, which are brought into the within-day dispatch model as the determined quantities. The within-day scheduling plan is a 4 h plan with a 15min interval. Within-day scheduling is a good way of correcting the deviations between the day-ahead scheduling plan and the actual working conditions during the day. What needs to be determined in the intra-day stage is the unit output plan for the next 4 h and the results are brought into the dynamic dispatch model. The dynamic dispatch plan is advanced every 5 min to develop a post 15 min plan, to combine a highly accurate wind power forecast with the dispatch plan to adjust the carbon capture energy consumption. The amount of carbon capture energy needs to be determined during the dynamic stage.

Wind power forecasting on multiple time scales can improve the accuracy and combine it with the dispatching of carbon capture plants to develop more accurate dispatching plans to effectively deal with load loss and wind abandonment while maximizing the low carbon performance of the system and reducing system costs.

3.2.2 Day-ahead dispatching model

3.2.2.1 Optimization objective

The objective function for the day-ahead dispatch stage is:

$$C_1 = \min\left(C_K + C_H + C_Q + C_T + C_Z + C_R\right) \tag{19}$$

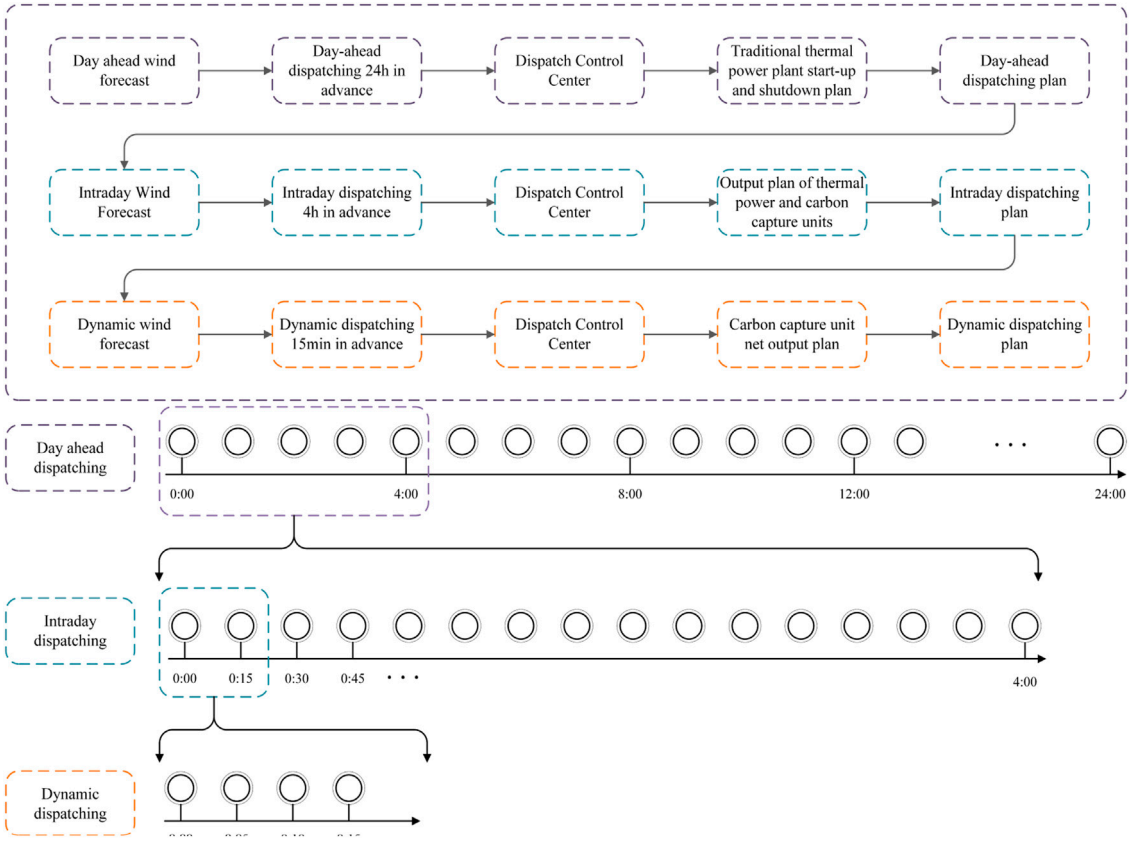

FIGURE 9
Low carbon economic dispatch framework for systems considering multi-time scale wind power predictions.

1) C_K is the start-up and shutdown cost of the thermal unit, C_H is the coal consumption cost of the thermal unit, C_Q is the penalty cost of wind abandonment, C_T is the cost of carbon trading, C_Z is the depreciation cost of the carbon capture plant, and C_R is the cost of solvent loss in the carbon capture process.

$$C_K = \sum_{t=1}^{24}\sum_{i=1}^{N}\left(U_{i,t}\left(1-U_{i,t-1}\right)+U_{i,t-1}\left(1-U_{i,t}\right)\right)C_i \tag{20}$$

where N is the number of thermal power units. $U_{i,t}$ is the start-stop state of unit i at time t. C_i is the start-stop cost of unit i.

2) Coal consumption costs for thermal power units.

$$C_H = \sum_{t=1}^{24}\sum_{i=1}^{N}U_{i,t}\left(a_i P_{\mathrm{G}i,t}^2 + b_i P_{\mathrm{G}i,t} + c_i\right) \tag{21}$$

Where a_i, b_i and c_i is the coal consumption cost factors for unit i. $P_{\mathrm{G}i,t}$ is the total unit output of unit i at time t.

3) Cost of wind abandonment.

$$C_Q = \sum_{t=1}^{24} K_q\left(P_{w,t}^{pre,1} - P_{w,t}\right) \tag{22}$$

K_q is the wind abandonment cost factor. $P_{w,t}$ is the wind power online in period t. $P_{w,t}^{pre,1}$ is the predicted day-ahead wind power in period t.

4) Cost of carbon capture.

$$C_T = K_T\left(E_c - \sum_{i=1}^{N}\sum_{t=1}^{24}\left(\delta_h P_{\mathrm{G}i,t}\right)\right) \tag{23}$$

K_T is the carbon trading price. E_c is the total amount of CO2 produced by thermal power units. δ_h is the carbon emission allowance factor.

5) Depreciation costs of carbon capture equipment.

$$C_z = \frac{C_{FL}(1+r)^{N_{ZJ}} r}{365\left((1+r)^{N_{ZJ}}-1\right)} + \frac{P_{RY} V_{RY}(1+r)^{N_{RY}} r}{365\left((1+r)^{N_{RY}}-1\right)} \quad (24)$$

C_{FL} is the total cost of the carbon capture equipment. N_{ZJ} is the depreciable year of the carbon capture equipment. r is the discount rate for the carbon capture plant project. P_{RY} is the cost per unit volume of solution storage. V_{RY} is the volume of solution storage. N_{RJ} is the depreciable year of the solution storage.

6) The cost of solvent loss during carbon capture.

$$C_R = \sum_{t=1}^{24}\sum_{i=1}^{N} K_R \varphi E_{totalCO2i,t} \quad (25)$$

K_R is the ethanolamine solution cost factor. φ is the solvent loss factor. $E_{totalCO2i,t}$ is the mass of CO2 captured by unit i at time t.

3.2.2.2 Constraints

1) Power balance constraint.

$$P_{1.t} = P_{w,t} + \sum_{i=1}^{N} P_{Ji,t} \quad (26)$$

Where $P_{1.t}$ is the load. $P_{Ji,t}$ is the net output of unit i in period t. $P_{w,t}$ is the online wind power at period t.

2) Wind power output constraints.

$$0 \le P_{w,t} \le P_{w,t}^{pre,1} \quad (27)$$

3) Thermal power unit output constraints.

$$\begin{cases} P_{Gi,\min} \le P_{Gi,t} \le P_{Gi,\max} & U_{i,t} = 1 \\ P_{Gi,t} = 0 & U_{i,t} = 0 \end{cases} \quad (28)$$

$P_{Gi,\min}$ is the minimum technical output of unit i. $P_{Gi,\max}$ is the maximum output of unit i.

4) Thermal power unit climbing constraints.

$$\begin{cases} P_{Gi,t} - P_{Gi,t-1} \le U_{i,t} R_i^u \\ P_{Gi,t-1} - P_{Gi,t} \le U_{i,t-1} R_i^d \end{cases} \quad (29)$$

R_i^u is the uphill climb rate of unit i and R_i^d is the downhill climb rate of thermal unit i.

5) Start/stop constraints for thermal power units.

$$\begin{cases} \left(T_{i,t-1}^{on} - T_{i,\min}^{on}\right)\left(U_{i,t-1} - U_{i,t}\right) \ge 0 \\ \left(T_{i,t-1}^{off} - T_{i,\min}^{off}\right)\left(U_{i,t} - U_{i,t-1}\right) \ge 0 \end{cases} \quad (30)$$

where, $T_{i,\min}^{on}$ is the minimum start-up time of unit i. $T_{i,\min}^{off}$ is the minimum shutdown time of unit i. $T_{i,t-1}^{on}$ is the time that unit i has been on continuously up to period t. $T_{i,t-1}^{off}$ is the time that unit i has been continuously shut down to period t. The start/stop constraint for thermal power units is intended to govern. The start/stop time must not be less than a fixed value to avoid affecting the safety of the unit.

6) Operational constraints on integrated carbon capture plants.

Carbon capture power plants add a flue gas bypass and storage tank based on a conventional thermal power plant, so their unit output constraints, creep constraints and start-stop constraints are the same as those of a conventional thermal power plant. A split-flow carbon capture plant will limit the flue gas split ratio, thus limiting the carbon capture energy consumption. Integrated carbon capture plants directly limit the amount of total CO2 resolved.

$$(1-\delta_{xz}) \le \delta_i \le \delta_{xz} \quad (31)$$

$$\begin{cases} (1-\delta_{xz})\lambda\beta e_{gi} P_{Gi,t} \le P_{Bi,t} \\ P_{Bi,t} \le \eta\lambda\beta e_{gi} P_{Gi,\max} - (1-\delta_{xz})\lambda\beta e_{gi} P_{Gi,t} \end{cases} \quad (32)$$

where, δ_{xz} is the flue gas split ratio limit. λ is the energy required to capture a unit of CO2. β is the carbon capture efficiency. e_{gi} is the carbon emission intensity. $P_{Bi,t}$ is the energy consumption to operate the carbon capture unit i at time t. η is the maximum operating factor of the solution regeneration tower and the compression tower.

Reservoir carbon capture is an important component of integrated carbon capture. A storage solution is CO2 in the form of a compound in an alcoholic amine solution. The mass of CO2 captured using a solution volume equivalent transformation is as follows.

$$V_{CAi,t} = \frac{E_{CGi,t} M_{MEA}}{M_{CO2}\theta C_R \rho_R} \quad (33)$$

Where $V_{CAi,t}$ is the volume of solution required to release CO2 from the solution reservoir installed in the carbon capture plant i at time t. M_{MEA} is the molar mass of MEA. M_{CO2} is the molar mass of CO2. θ is the amount of CO2 resolved in regeneration towers. C_R is the concentration of alcoholic amine solution. ρ_R is the density of the alcohol-amine solution.

The solution storage constraints mainly include the reservoir volume constraint and the reservoir volume variation constraint, as in the following equation.

$$\begin{cases} V_{FYi,t} = V_{FYi,t-1} - V_{CAi,t} \\ V_{PYi,t} = V_{PYi,t-1} + V_{CAi,t} \\ 0 \le V_{FYi,t} \le V_{CRi} \\ 0 \le V_{PYi,t} \le V_{CRi} \\ V_{FYi,0} = V_{FYi,24} \\ V_{PYi,0} = V_{PYi,24} \end{cases} \quad (34)$$

$V_{FYi,t}$ is the volume of solution in the liquid-rich storage of unit i at time t. $V_{CAi,t}$ is the volume of solution required to release CO2 from the solution storage installed at carbon capture plant i at time t. $V_{PYi,t}$ is the volume of solution in the depleted solution storage of unit i at time t. V_{CRi} is the solution storage capacity of unit i. $V_{FYi,0}$ is the volume of solution in unit i's liquid-rich tank

at time 0. $V_{FYi,24}$ is the volume of solution in the rich tank of unit i at time 24. $V_{PYi,0}$ is the volume of solution in the liquid-poor tank of unit i at time 0. $V_{PYi,24}$ is the volume of solution in the poor tank of unit i at time 24.

7) Rotating standby constraints.

$$\begin{cases} \sum_{i=1}^{N} \min\left[R_i^{u}, \left(U_{i,t}P_{GJi,\max} - P_{GJi,t}\right)\right] \geq r_{sys}^{up,t} \\ \sum_{i=1}^{N} \min\left[R_i^{d}, \left(P_{GJi,t} - U_{i,t}P_{GJi,\min}\right)\right] \geq r_{sys}^{down,t} \end{cases} \tag{35}$$

Where $r_{sys}^{up,t}$ is the required upper rotating reserve for the system at time t. $r_{sys}^{down,t}$ is the required lower rotation reserve of the system at time t. $P_{GJi,\max}$ is the upper net output limit of unit i. $P_{GJi,\min}$ is the lower net output limit of unit i.

8) flow constraints.

3.2.2.3 Power balance constraint

$$\sum_{i\in C_{G,j}} P_{i,t} - \sum_{(h,j)\in C_{F,j}} f_{hj,t} + \sum_{(h,j)\in C_{E,j}} f_{hj,t} - D_{j,t} = 0 \tag{36}$$

Where, $C_{G,j}$ is the set of units (thermal units, wind turbines) connected to node j. $f_{hj,t}$ is the power flow of line (h, j). $C_{F,j}$ is the set of lines starting at node j. $C_{E,j}$ is the set of lines ending at node j. $D_{j,t}$ is the load demand of node j.

Line transmission capacity and node voltage constraints. Flow analysis using DC flow.

$$\begin{gathered} f_{hj,t} = \frac{\theta_{h,t} - \theta_{j,t}}{x_{hj}} \\ -f_{hj}^{\max} \leqslant f_{hj,t} \leqslant f_{hj}^{\max} \\ -\theta_j^{\max} \leqslant \theta_{j,t} \leqslant \theta_j^{\max} \\ \theta_{ref,t} = 0 \end{gathered} \tag{37}$$

Where, $\theta_{h,t}$ is the phase angle of the voltage at node h. $\theta_{j,t}$ is the voltage phase angle at node j. x_{hj} is the reactance of line (h, j). $f_{hj}^{\max}$ is the maximum value of the transmission capacity of line (h, j). $\theta_j^{\max}$ is the maximum voltage phase angle. $\theta_{ref,t}$ is the voltage phase angle of the balance node.

3.2.3 Intraday dispatching model

3.2.3.1 Optimization objective

The intra-day dispatch stage, compared to the day-ahead dispatch, is the stage where the change in the predicted wind power causes a change in the cost of wind abandonment. In addition, the cost of loss of load needs to be taken into account during this stage.

$$C_2 = \min\left(C_H + C_Q + C_T + C_Z + C_R + C_S\right) \tag{38}$$

$$C_Q = \sum_{t=1}^{\Delta T} K_q\left(P_{w,t}^{pre,2} - P_{w,t}\right) \tag{39}$$

$$C_S = \sum_{t=1}^{\Delta T} K_S P_{S,t} \tag{40}$$

Where $P_{w,t}^{pre,2}$ is the intra-day wind power forecast in 15min C_S is the cost of the lost load. K_S is the penalty cost per unit of lost load. $P_{S,t}$ is the lost load power of the system at time t.

3.2.3.2 Constraints

The parts of the intraday dispatch model that change are the thermal unit climbing constraint and the rotating reserve constraint. Unit start-up and shutdown are not considered in the intraday dispatch stage, and therefore unit start-up and shutdown constraints are not considered. The unit output constraints and carbon capture operation constraints are similar to those of the day-ahead dispatch model.

1) Load balance constraint.

$$P_{2.t} = P_{w,t} + \sum_{i=1}^{N} P_{Ji,t} + P_{S,t} \tag{41}$$

Where: $P_{2.t}$ is the predicted load within the day. $P_{w,t}$ is the grid power of wind power at time t. $P_{Ji,t}$ is the net output of unit i in period t. $P_{S,t}$ is the lost load of the system in period t.

2) Thermal power unit climbing constraints.

$$\begin{cases} P_{Gi,t} - P_{Gi,t-1} \leq U_{i,t}R_i^{u}/4 + P_{Gi,\max}\left(1 - U_{i,t-1}\right) \\ P_{Gi,t-1} - P_{Gi,t} \leq U_{i,t}R_i^{d}/4 + P_{Gi,\max}\left(1 - U_{i,t}\right) \end{cases} \tag{42}$$

3) Rotating alternate restraint.

$$\begin{cases} \sum_{i=1}^{N} \min\left[R_i^{u}/4, \left(U_{i,t}P_{GJi,\max} - P_{GJi,t}\right)\right] \geq r_{sys}^{up,t} \\ \sum_{i=1}^{N} \min\left[R_i^{d}/4, \left(P_{GJi,t} - U_{i,t}P_{GJj,\min}\right)\right] \geq r_{sys}^{down,t} \end{cases} \tag{43}$$

3.2.4 Dynamic dispatching model

The dynamic dispatch stage focuses on adjusting wind power output and correcting carbon capture energy consumption. The wind power data is forecasted over a very short period of 5 min. The accurate forecasts help the system to adjust the net output of the carbon capture plant, thus increasing the wind power utilization and reducing the loss of load.

3.2.4.1 Optimization objective

The adjustment target for the Dynamic dispatch stage is the carbon capture energy consumption within the carbon capture plant. The dynamic dispatch stage has a short cycle time and the start-up and shutdown of the units and the total output are already determined in the day-ahead and intra-day dispatch

stages. The dynamic phase adjusts the system's CO2 emissions, wind abandonment, and load loss by adjusting the variables within the carbon capture plant.

$$C_3 = \min\left(C_Q + C_T + C_Z + C_R + C_S\right) \tag{44}$$

$$C_Q = \sum_{t=1}^{\Delta T} K_q\left(P_{w,t}^{pre,3} - P_{w,t}\right) \tag{45}$$

where: $P_{w,t}^{pre,3}$ is the dynamic predicted wind power.

3.2.4.2 Constraints

The dynamic dispatch phase does not take into account the thermal unit output plan as it is already established in the intraday dispatch phase. The remaining constraints such as individual unit output and carbon capture plant constraints are similar to the previous two stages.

1) Load balance constraint.

$$P_{3,t} = P_{w,t} + \sum_{i=1}^{N} P_{J,t} + P_{S,t} \tag{46}$$

Where: $P_{3,t}$ is the dynamic forecast power of the load. $P_{w,t}$ is the grid power of wind power at time t. $P_{Ji,t}$ is the net output of unit i in period t. $P_{S,t}$ is the lost load power of the system in period t.

2) Carbon capture power regulation constraint.

The dynamic stage focuses on the adjustment of the carbon capture energy consumption, which is mainly borne by the solution storage.

$$\begin{cases} \Delta P_{BSi,t} = P_{Bi,t} \\ \Delta P_{BXi,t} = P_{Bi\,max} - P_{Bi,t} \\ P_{Bi\,max} = \lambda\eta\beta e_{gi} P_{Gi,\,max} \end{cases} \tag{47}$$

where: $\Delta P_{BSi,t}$ is the maximum net output adjustment for carbon capture unit i at time t. $\Delta P_{BXi,t}$ is the minimum net output adjustment value for carbon capture unit i at time t. $P_{Bi\,max}$ is the maximum operating energy consumption of the regeneration and compression towers, in other words, the carbon capture energy consumption. λ is the energy required to capture a unit of CO2. η is the maximum operating factor of the regenerative and compression towers of the solution. β is the carbon capture efficiency. e_{gi} is the carbon emission intensity. $P_{Gi,\,max}$ is the maximum output of unit i.

Liquid storage carbon capture enables energy time-shifting, but at the same time, the net output regulation of the carbon capture unit should be kept within the regulation range.

$$-\sum_{i=1}^{n} \Delta P_{BXi,t} \le \sum_{i=1}^{n} \Delta P_{Ji,t} \le \sum_{i=1}^{n} \Delta P_{BSi,t} \tag{48}$$

where $\Delta P_{Ji,t}$ is the net output adjustment of carbon capture unit i at time t.

4 Case study and analysis

4.1 Case settings

The wind power in this paper uses data from the Belgian grid in July 2021. Various forecasting algorithms were first used to forecast wind power on three time-scales, with the GRU algorithm performing well in terms of training speed and accuracy. Figure 10 shows the 15min wind power forecast results, Measured and upscaled is the raw Belgian wind power data, most recent forecast is the forecast for wind power from the Belgian grid, the SVR forecast is the result of the SVR model forecast, the LSTM forecast uses the model LSTM, and the model used in this paper is GRU, which is the GRU forecast with cross-validation labeled in the figure. The wind power is scaled to match the system of 488.3 MW(Li et al., 2021).

This paper is validated with a modified IEEE-39 nodal system containing 10 thermal power units. Wind farms of 198.5, 191.5, and 98.3 MW are introduced at nodes 9, 19, and 22 respectively. If the system adopts carbon capture technology, G1 and G2 are converted into carbon capture power plants, if the system does not adopt it, G1 and G2 are conventional thermal power plants. Figure 11 shows the system. Table 1 shows the relevant parameters for the thermal plant and Table 2 shows the remaining parameters to be set. The dispatch quantities are solved using the CPLEX.

Comparison cases are set depending on whether the GRU wind power forecasts or from the Belgian grid are used.

Case 1: Consider the day-ahead dispatch of the Belgian grid with its wind power forecast (Most recent forecast) or GRU wind power forecast with carbon capture equipment.

Case 2: Consider the Belgian grid's own wind power forecasts (Most recent forecast) or GRU wind power forecasts, with the intra-day dispatch of carbon capture equipment.

Case 3: Dynamic dispatch using the Belgian grid's own wind power forecasts (Most recent forecast) or GRU wind power forecasts with carbon capture equipment.

4.2 Results and analysis

Figure 12 shows the results of the day-ahead dispatch with and without carbon capture devices. A shows thermal units 1 and two without carbon capture devices and B shows thermal units 1 and 2 with integrated carbon capture devices. The graphs show that after the retrofitting of carbon capture devices, there is a significant reduction in wind abandonment and a visible increase in the utilization of wind power. The analysis of the columns without carbon capture devices and the Belgian wind forecast column (with carbon capture devices) in Table 3 shows that the cost of the wind abandonment penalty is reduced by 69.032% with the installation of carbon capture devices. At the same time,

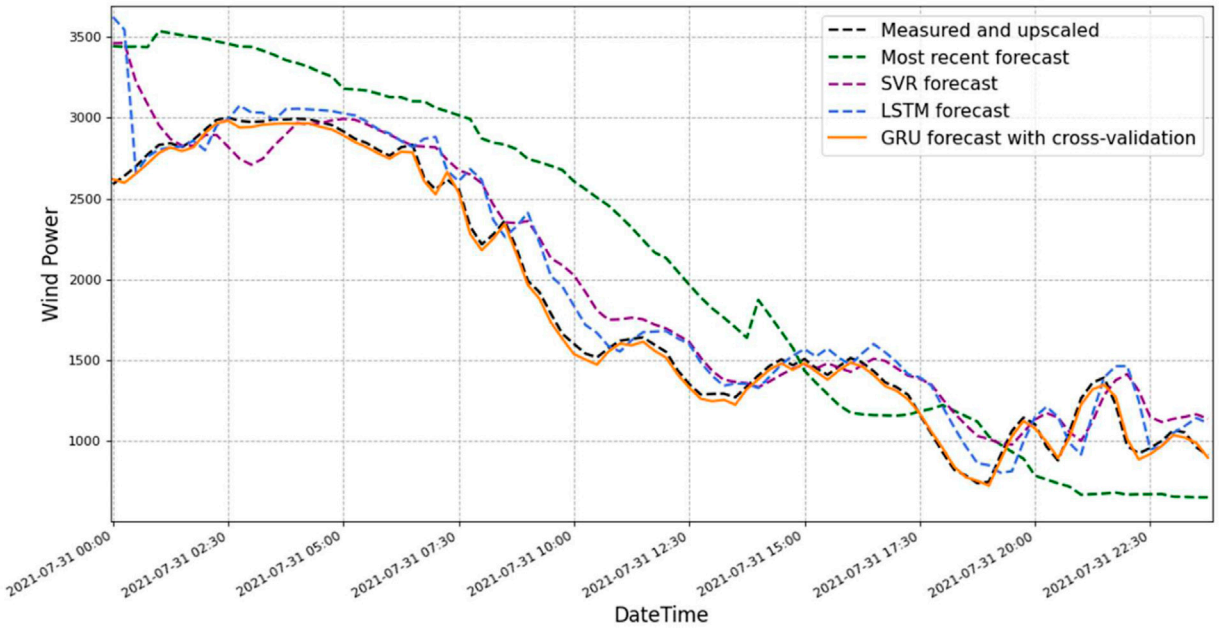

FIGURE 10
Wind power forecasting results (raw wind data\Irish grid forecasts\SVR, LSTM and GRU forecasts).

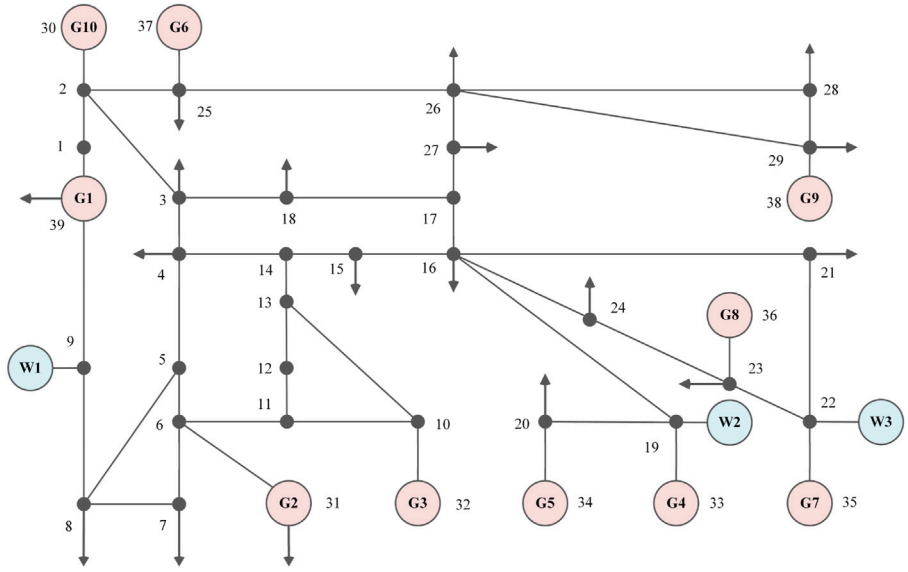

FIGURE 11
IEEE-39 node system.

the cost of carbon trading is reduced by 24.211%, and carbon emissions are reduced by 41.694% after the installation of carbon capture devices. Although the cost of running thermal power plants is higher with the addition of carbon capture devices, the total cost is reduced by 30.788%. This shows that carbon capture can reduce carbon emissions and at the same time satisfy the economy, helping to achieve low carbon economic dispatch of the power system.

TABLE 1 Thermal power unit parameters (Total of 10 thermal units; input parameters include operation, cost, climbing parameters and carbon capture intensity) (Shui et al., 2019).

Unit number	Maximum output	Minimum output	Start-stop costs	Cost parameter a	Cost parameter b	Cost parameter c	Minimum start/stop time	Unit climbing	Carbon emission intensity
1	455	200	31,500	0.00336	113.33	7000	6	200	0.9
2	455	150	35,000	0.00217	120.82	6790	5	200	0.92
3	130	30	3850	0.014	116.2	4900	5	80	0.99
4	130	25	3920	0.01477	115.5	4760	5	80	0.98
5	162	45	6300	0.02786	137.9	2450	5	100	1.02
6	80	20	1190	0.04984	155.82	2590	3	72	1.05
7	85	25	1820	0.00553	194.18	3360	3	80	1.06
8	55	10	210	0.02891	181.44	4620	1	60	1.12
9	55	10	210	0.01554	190.89	4655	1	60	1.15
10	55	10	210	0.01211	194.53	4690	1	60	1.1

TABLE 2 Other system parameters (Mainly system size parameters and carbon capture plant operating and cost parameters) (Yu et al., 2022).

Parameter name	Value
λ_B (Energy consumption per unit of carbon capture)/((MW·h)/t)	0.269
θ_B (Carbon Capture Efficiency)	0.9
η (Maximum operating condition)/%	120
M_{MEA} (MEA Moore's mass)/(g/mol)	61.08
M_{CO2}(CO_2 molar mass)/(g/mol)	44
θ (The amount of regeneration tower can be resolved)/(molCO2/molMEA)	0.24
C_R (Solution concentration)/%	30
σ_R (Solution density)/(t/m^3)	1.01
σ_T (Carbon trading price)/($/t)	120
λ_h (Carbon emission allowance factor)/(t/(MW·h))	0.7
μ_2 (Day-ahead wind power reserve factor)	0.2
ω (Net Residual Value Rate)/%	5
N_C(Depreciable life of liquid storage tank)/year	5
P_{CY}(Liquid storage tank unit price)/($/$m^3$)	300
V_{CY}(Reservoir volume)/m^3	60000*4
μ_1 (Day-ahead load standby factor)	0.05
C_{ZJ} (Total price of carbon capture equipment)/million $	165159.4
C_{GJ} (Total cost of retrofit of regenerative tower compressor expansion to 120% capacity)/million $	14264.3
N_T (Depreciable life of carbon capture equipment)/Year	15
σ_Q (Cost of wind abandonment penalty)/($/(MW·h))	210
λ_B (Energy consumption per unit of carbon capture)/((MW·h)/t)	0.269

As the load is supplied by the net thermal output and the grid power of wind power, it is only necessary to compare the net thermal output to analyze the system's wind abandonment situation. The net output of thermal units is shown in Figure 13. As can be seen from the graph, the different times of net thermal output are concentrated between 1:00 to 12:00, and the difference in net output during the corresponding period is the difference in the amount of wind abandoned with or without carbon capture devices.

Figure 14 shows a comparison of the dispatch results for case 1 (both with carbon capture units, using different wind power forecasts). As can be seen from the graph, when using GRU to forecast wind power, there is a certain degree of reduction in the amount of abandoned wind power due to the increased accuracy

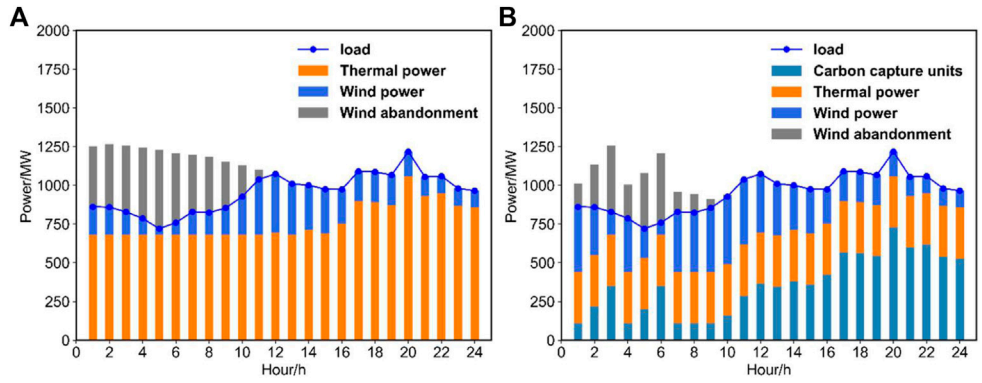

FIGURE 12
Day-ahead dispatch results with and without carbon capture devices ((**A**) is without carbon capture devices, (**B**) is with carbon capture devices).

TABLE 3 Day-ahead dispatching costs.

Costs	Without carbon capture	Belgian grid wind power forecast	GRU wind power forecast
Operating Costs of Thermal Power Units/$	711397	735595	751974
Carbon Trading Costs/$	383544	290683	192160
Wind Abandonment Penalty Costs/$	825835	255743	209170
Depreciation cost of storage fluid/$	0	47378	47379
Total Cost/$	1920776	1329401	1200684
Carbon Emissions/t	17746	10347	9605

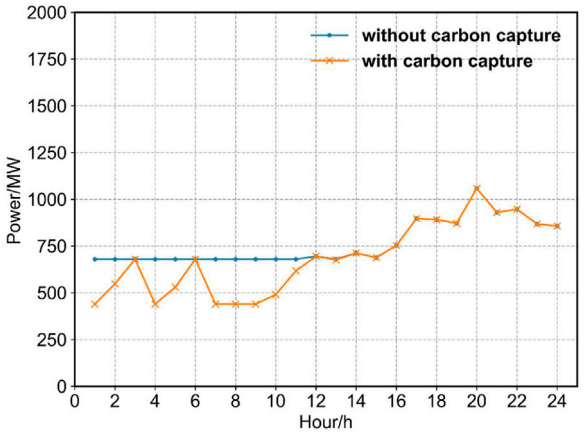

FIGURE 13
Comparison of the output of thermal power units with and without carbon capture devices.

of the forecast. As can be seen from Table 3, in the day-ahead dispatching phase, the carbon transaction cost, abandonment penalty cost, total cost, and carbon emissions are reduced by 166,206$, 11,547$, 177,753$ and 1479t respectively when using GRU to forecast wind power compared to using the Belgian grid to forecast wind power, a respective decrease of 23.293%, 83.644%, 24.439%, and 12.716%. This validates the advantages of the flexible operation of carbon capture units. At the same time, by using GRU to forecast wind power, carbon capture units can capture more CO2 and effectively improve wind power utilization. Overall, the improvement in the accuracy of wind power forecasting has been proven to have a positive impact on the reduction of carbon emissions and system economics.

In the day-ahead dispatch stage, carbon emissions depend mainly on the level of wind power consumption and the output of high-carbon units. As wind power does not emit carbon, the higher its utilization rate, the more thermal units will be replaced. At the same time, the amount of abandoned wind power decreases, the output of high-carbon thermal units decreases, and carbon emissions are reduced accordingly.

As shown in Figure 15, closely related to the net output of the thermal units is the carbon capture energy consumption. Unlike the split carbon capture unit, case 1 uses an integrated

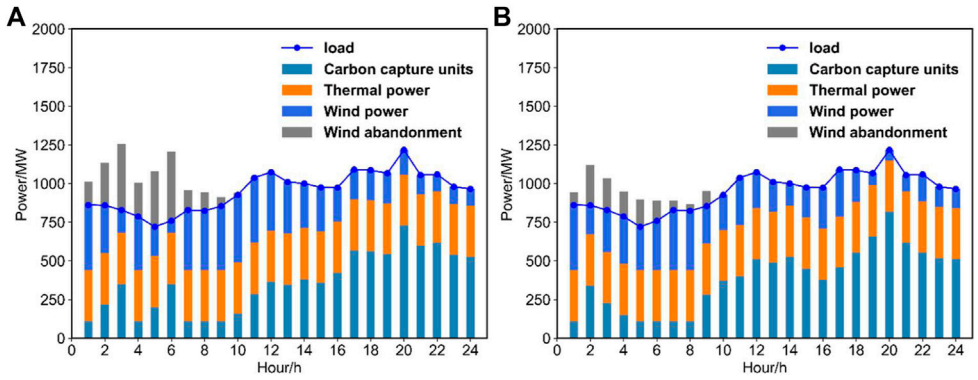

FIGURE 14
Comparison of dispatch results for case 1 ((**A**) considering grid forecast wind power in Belgium, (**B**) considering GRU forecast wind power).

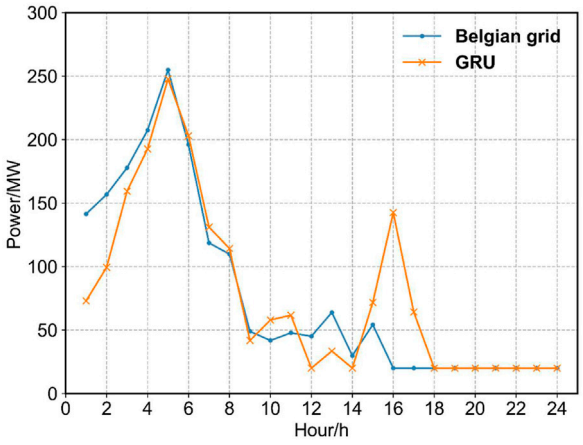

FIGURE 15
Comparison of carbon capture energy consumption using different forecast wind power in day-ahead dispatch.

carbon capture unit, where the processes of CO2 absorption and CO2 capture are not coupled, enabling a time-shifting of the carbon capture energy consumption, so that the energy consumption is higher in the low load periods and the lower limit of the net output of the carbon capture unit is lower than that of the split type. The carbon capture units G1 and G2 are on all hours, so there is no need to increase the net output to provide down-rotation reserves, which allows more wind power to be absorbed and reduces the carbon emissions of the system compared to not installing carbon capture devices. However, due to the low load, there is still a problem of wind abandonment and the low carbon capability needs to be further explored.

Figure 16 shows a comparison of the changes in the storage tanks of case 1, where A considers the Belgian grid forecast wind power and B considers the GRU forecast wind power. As can be seen from the graph, the carbon capture units release CO2 at low load times (2:00–9:00), which shows a decrease in the amount of liquid-rich tank storage and an increase in the amount of liquid-poor tank storage. During peak load hours (16:00–24:00), CO2 is stored, showing a rise in the amount of liquid stored in the rich tank and a fall in the amount of liquid stored in the lean tank. The reduced energy consumption of the carbon capture equipment processing enables energy time-shifting, laying the foundation for low carbon economic dispatch and further reducing carbon emissions with integrated carbon capture compared to split carbon capture. Compared to the dispatch carried out by the Belgian grid predicting wind power, the use of GRU predicts that wind power has a CO2 release during the small low load hours between 13:00 and 16:00.

Table 4 shows the cost table for the dispatch phase within case 2. Two scenarios are included: using the Belgian grid forecast or using the GRU forecast for wind power. Intraday dispatch does not take into account unit start-ups and shutdowns, so the costs include carbon trading costs, wind abandonment costs, lost load costs, and total costs. In the intraday scheduling phase, the total cost of using GRU wind forecasts is reduced by 177,753$ or 24.439% compared to using forecast wind. Carbon emissions are reduced by 1479t or 12.716%. The cost of the wind abandonment penalty is reduced by 11,547$, or 83.644%. It can be seen that the carbon capture system using GRU prediction wind power has the same advantages in terms of wind abandonment, cost, and carbon emissions in intra-day dispatch.

The intra-day dispatch is based on the start-up and shutdown of the units determined by the day-ahead dispatch, and the intra-day dispatch output is adjusted as follows. As can be seen from Figure 17, the same wind abandonment situation exists in case 2 intra-day dispatch

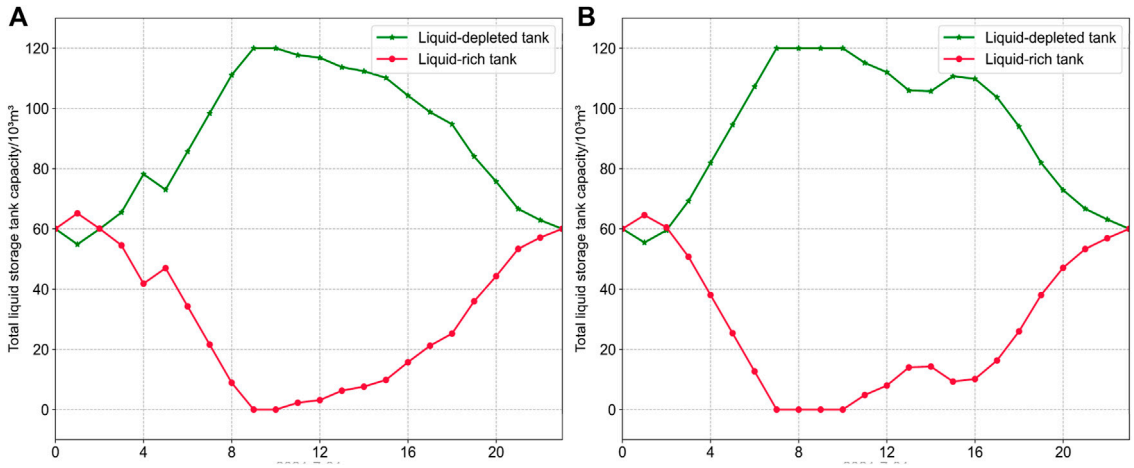

FIGURE 16
Comparison of reservoir changes in the day-ahead dispatch of Case 1 (**(A)** considering the Belgian grid forecast wind power, **(B)** considering the GRU forecast wind power).

TABLE 4 Intraday dispatching costs.

Costs	Belgian grid wind power forecast	GRU wind power forecast
Carbon Trading Costs/$	713539	547333
Wind Abandonment Penalty Costs/$	13805	2258
Lost Load Costs/$	0	0
Total Cost/$	727344	549591
Carbon Emissions/t	11631	10152

when using the Belgian grid forecast wind power for dispatch, with the abandonment time points mainly existing in the 0–20 period. This is because thermal power needs to reach a minimum output before it can be dispatched, and when thermal units start and stop, this can be seen as a sudden change in output power, and as the time scale shortens, due to the influence of creep. Combining all periods within a day, the remaining thermal units are adjusted less than the sudden change in thermal power caused by the start and stop of the thermal units, resulting in a wind abandonment and load loss situation. Systems containing carbon capture plants and using GRU to forecast wind power have stronger wind abandonment and load shedding characteristics.

Table 5 shows the dynamic dispatch stage cost table and Figure 18 shows the case 3 dynamic dispatch diagram. Intraday dispatch provides a reference point for the total output of the thermal plant for dynamic dispatch, which regulates the carbon capture energy consumption without changing the total output.

As can be seen from Table 5, the total cost of forecasting wind power using GRU is reduced by $134,983$ compared to the Belgian forecast of wind power in dynamic scheduling. Carbon emissions are reduced by 2395t or 19.867%. Loss of load costs is reduced by 6173$, or 73.218%. The cost of the wind abandonment penalty is reduced by 137,018$ or 18.540%. It is clear that in dynamic dispatch, the system using GRU to forecast wind power is more advantageous in terms of disposing of abandoned wind and dealing with load loss.

Figure 18 shows a graph of dynamically dispatched unit output. As can be seen from the graph, the improvement in prediction accuracy has led to greater involvement of carbon capture plants in the regulation of the 5min time scale, resulting in significant improvements in wind abandonment and load shedding, and demonstrating the effectiveness of the fast regulation characteristics of carbon capture plants. By regulating the carbon capture energy consumption to follow the changes in load and wind power, the carbon capture plant achieves the objective of absorbing the abandoned wind and reducing the lost load.

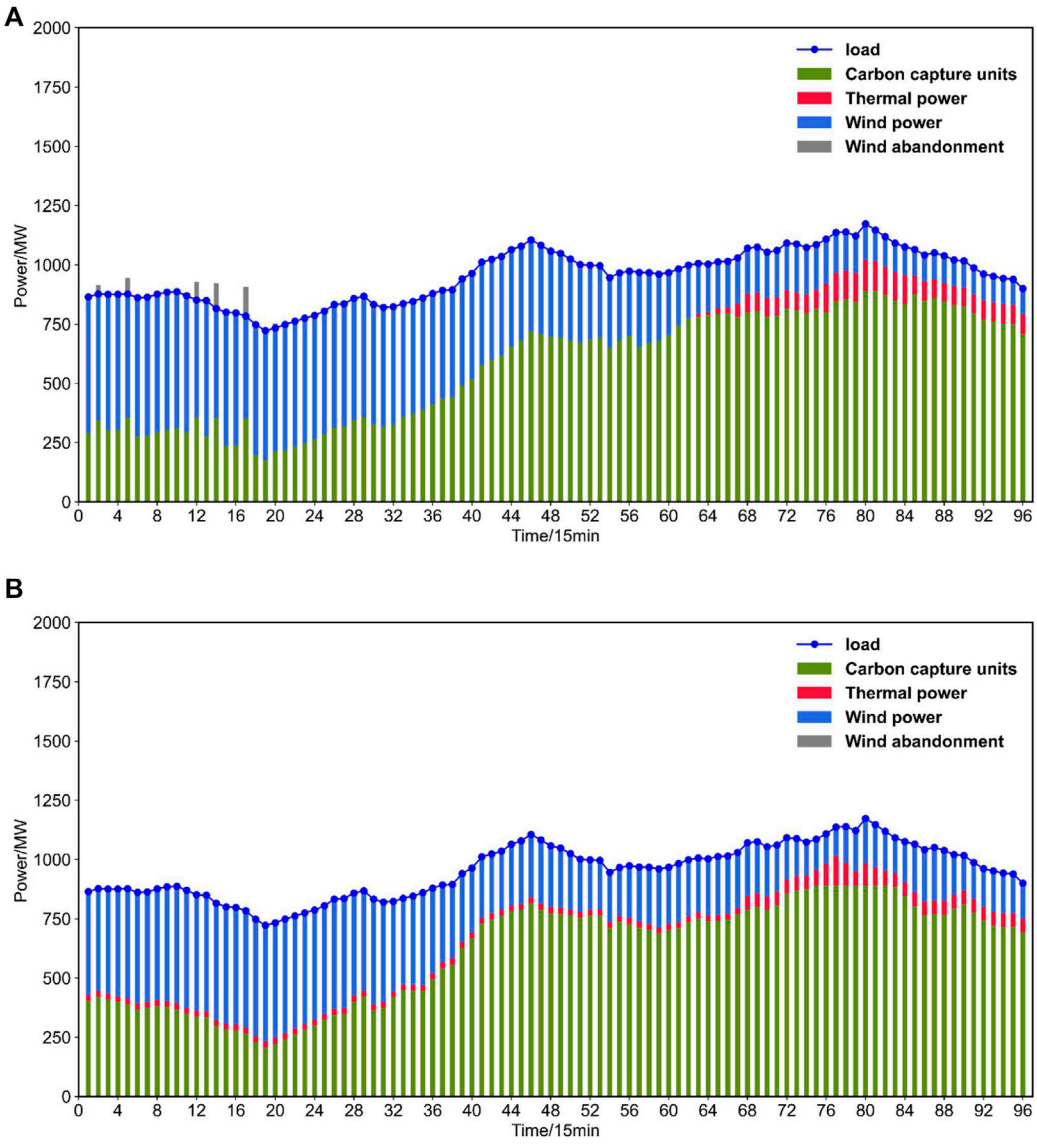

FIGURE 17
Intraday stage dispatch diagram ((**A**) considering Belgian grid forecast wind power, (**A**) considering GRU forecast wind power).

TABLE 5 Dynamic dispatching costs.

Costs	Belgian grid wind power forecast	GRU wind power forecast
Carbon Trading Costs/$	7586	621
Wind Abandonment Penalty Costs/$	739027	602009
Lost Load Costs/$	8431	2258
Total Cost/$	739872	604889
Carbon Emissions/t	12055	9660

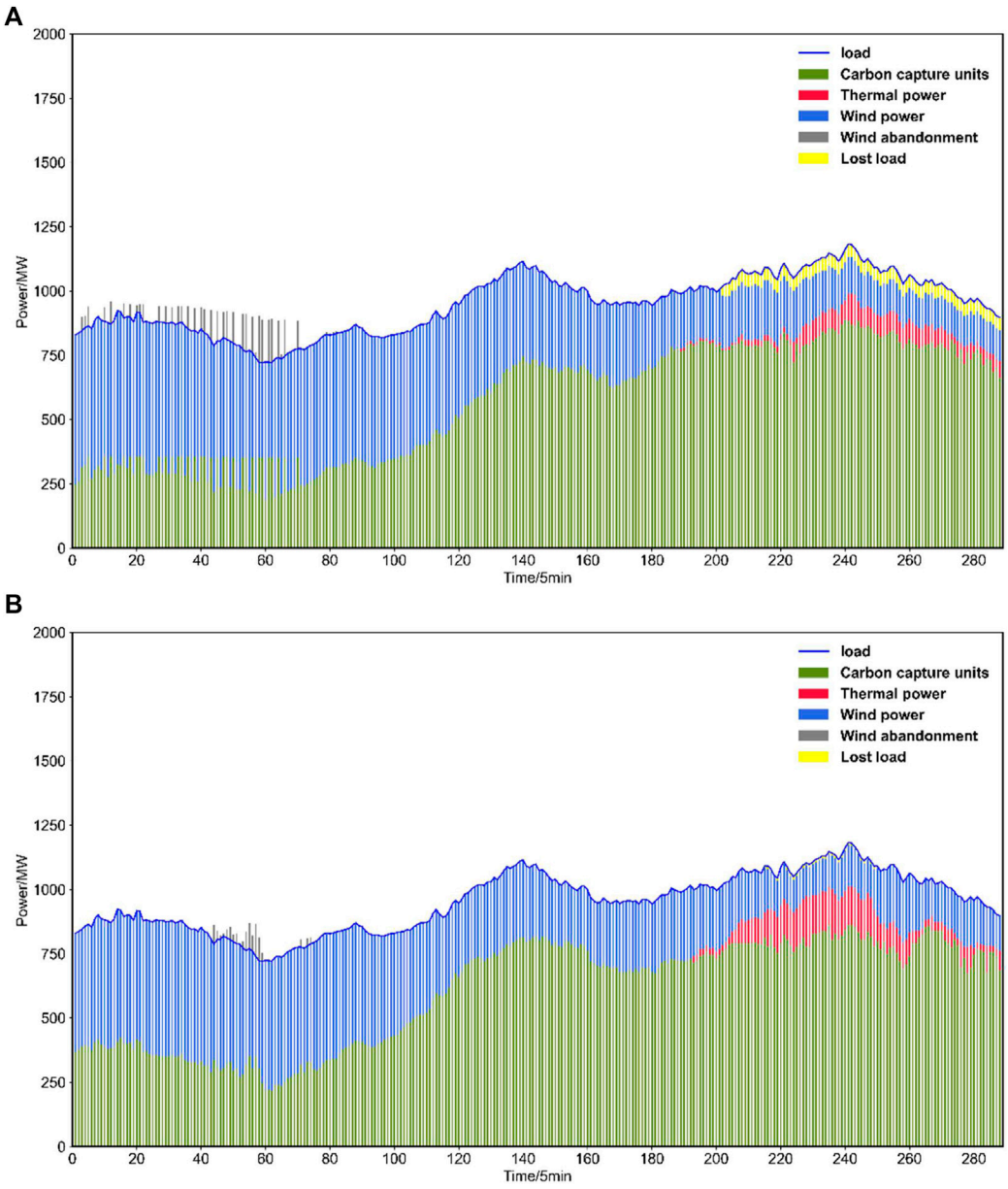

FIGURE 18
Dynamic dispatch diagram for case 3 ((**A**) considering Belgian forecast wind power, (**A**) considering GRU forecast wind power).

5 Conclusion

This paper constructs a multi-timescale optimal dispatch model that considers improving wind power forecasting accuracy while containing an integrated carbon capture plant and demonstrates the effectiveness of carbon capture plants in absorbing wind abandonment, coping with load loss situations, and reducing system costs, as shown in the following findings.

1) During day-ahead dispatch, the system with an integrated carbon capture plant has a 69.032% reduction in the cost of wind abandonment penalties relative to a system with only conventional plants, due to the deeper regulation range of the carbon capture plant. Carbon trading costs are reduced by 24.211% and carbon emissions are reduced by 41.694%. This demonstrates the effectiveness of carbon capture plants in improving wind power utilization and reducing carbon emissions.
2) In the intraday dispatch stage, the use of GRU to forecast wind power has led to an increase in forecast accuracy, which, when combined with carbon capture plants, can further exploit the low carbon performance of the system and improve economic efficiency. In the intra-day dispatch

stage, the system's dispatch flexibility can be improved to further reduce wind abandonment and achieve full utilization of source-side adjustable resources.

3) During dynamic dispatch, the system can respond to fluctuations in load and wind power in timely due to the fast regulation characteristics of the carbon capture plant and the improved accuracy of wind power forecasting. Its total cost is reduced by 134,983$ relative to a system that uses the Belgian grid forecast wind power. Carbon emissions were reduced by 2,395t or 19.867%. The cost of loss of load is reduced by 6173$, or 73.218%. The cost of wind abandonment penalties was reduced by 137,018$, or 18.540%. This justifies the improvement in forecasting accuracy and the use of multi-scale scheduling in dealing with wind abandonment and load loss.

Data availability statement

The original contributions presented in the study are included in the article/supplementary material, further inquiries can be directed to the corresponding author.

Author contributions

CD and YZ carried out the concepts, design, the definition of intellectual content, literature search, data acquisition, data analysis, and manuscript preparation. CD provided assistance for data acquisition, data analysis, and statistical analysis. YZ carried out literature search, data acquisition, and manuscript editing. GP and HZ performed manuscript review. All authors have read and approved the content of the manuscript and have made substantial contributions to all of the following: (1) the conception and design of the study, or acquisition of data, or analysis and interpretation of data, (2) drafting the manuscript or revising it critically for intellectual content, (3) final approval of the version to be submitted.

Conflict of interest

The authors declare that the research was conducted in the absence of any commercial or financial relationships that could be construed as a potential conflict of interest.

Publisher's note

All claims expressed in this article are solely those of the authors and do not necessarily represent those of their affiliated organizations, or those of the publisher, the editors and the reviewers. Any product that may be evaluated in this article, or claim that may be made by its manufacturer, is not guaranteed or endorsed by the publisher.

References

Chen, W., Qi, W., Li, Y., Z, J., Zhu, F., Xie, D., et al. (2021). Ultra-short-term wind power prediction based on bidirectional gated recurrent unit and transfer learning. *Front. Energy Res.* 9, 808116. doi:10.3389/fenrg.2021.808116

Chen, X., Huang, L., Zhang, X., He, S., Sheng, Z., Wang, Z., et al. (2021a). Robust optimal dispatching of wind fire energy storage system based on equilibrium optimization algorithm. *Front. Energy Res.* 9, 754908. doi:10.3389/fenrg.2021.754908

Chen, X., Zhang, X., Dong, M., Huang, L., Guo, Y., and He, S. (2021b). Deep learning-based prediction of wind power for multi-turbines in a wind farm. *Front. Energy Res.* 9. doi:10.3389/fenrg.2021.723775

Cheng, S., Teng, Y., Zuo, H., and Chen, Z. (2022). Power balance partition control based on topology characteristics of multi-source energy storage nodes. *Front. Energy Res.* 10, 843536, doi:10.3389/fenrg.2022.843536

Duan, J., Wang, P., Ma, W., Tian, X., Fang, S., Cheng, Y., et al. (2021). Short-term wind power forecasting using the hybrid model of improved variational mode decomposition and Correntropy Long Short -term memory neural network. *Energy* 214, 118980. doi:10.1016/j.energy.2020.118980

Fan, J. L., Wei, S., Shen, S., Xu, M., and Zhang, X. (2021). Geological storage potential of CO2 emissions for China's coal-fired power plants: A city-level analysis. *Int. J. Greenh. Gas Control* 106, 103278. doi:10.1016/j.ijggc.2021.103278

Fan, J. L., Wei, S., Yang, L., Wang, H., Zhong, P., and Zhang, X. (2019). Comparison of the LCOE between coal-fired power plants with CCS and main low-carbon generation technologies: Evidence from China. *Energy* 176, 143–155. doi:10.1016/j.energy.2019.04.003

Fan, J. L., Xu, M., Li, F., Yang, L., and Zhang, X. (2018). Carbon capture and storage (CCS) retrofit potential of coal-fired power plants in China: The technology lock-in and cost optimization perspective. *Appl. Energy* 229, 326–334. doi:10.1016/j.apenergy.2018.07.117

Farah, S., Aneela, Z., and Muhammad, M. (2021). A novel genetic LSTM model for wind power forecast. *Energy* 223, 120069. doi:10.1016/j.energy.2021.120069

Gao, Q., Zhang, X., Yang, M., Chen, X., Zhou, H., and Yang, Q. (2021). Fuzzy decision-based optimal energy dispatch for integrated energy systems with energy storage. *Front. Energy Res.* 9, 809024. doi:10.3389/fenrg.2021.809024

Han, H., Wei, T., Wu, C., Xu, X., Zang, H., Sun, G., et al. (2022). A low-carbon dispatch strategy for power systems considering flexible demand response and energy storage. *Front. Energy Res.* 10, 883602. doi:10.3389/fenrg.2022.883602

Han, L., Jing, H., Zhang, R., and Gao, Z. (2019). Wind power forecast based on improved Long Short Term Memory network. *Energy* 189, 116300. doi:10.1016/j.energy.2019.116300

Huang, X., Wang, K., Zhao, M., Huan, J., Yu, Y., Jiang, K., et al. (2022). Optimal dispatch and control strategy of integrated energy system considering multiple P2H to provide integrated demand response. *Front. Energy Res.* 9, 824255. doi:10.3389/fenrg.2021.824255

Huang, Y., Li, P., Zhang, X., Mu, B., Mao, X., and Li, Z. (2021). A power dispatch optimization method to enhance the resilience of renewable energy penetrated power networks. *Front. Phys.* 9. doi:10.3389/fphy.2021.743670

Jin, H., Teng, Y., Zhang, T., Wang, Z., and Deng, B. (2021). A locational marginal price-based partition optimal economic dispatch model of multi-energy systems. *Front. Energy Res.* 9. doi:10.3389/fenrg.2021.694983

Li, X., Wu, X., Gui, D., Hua, Y., and Guo, P. (2021). Power system planning based on CSP-CHP system to integrate variable renewable energy. *Energy* 232, 121064. doi:10.1016/j.energy.2021.121064

Liu, C., Wang, C., Yin, Y., Yang, P., and Jiang, H. (2022). Bi-level dispatch and control strategy based on model predictive control for community integrated energy system considering dynamic response performance. *Appl. Energy* 310, 118641. doi:10.1016/j.apenergy.2022.118641

Meng, Y., C, C., Huo, J., Zhang, Y., Murad, M. A. N. H., Xu, J., et al. (2022). Research on ultra-short-term prediction model of wind power based on attention mechanism and CNN-BiGRU combined. *Front. Energy Res.* 10. doi:10.3389/fenrg.2022.920835

Nie, Q., Zhang, L., Tong, Z., Dai, G., and Chai, J. (2022). Cost compensation method for PEVs participating in dynamic economic dispatch based on carbon trading mechanism. *Energy* 239, 121704. doi:10.1016/j.energy.2021.121704

Niu, Z., Yu, Z., Tang, W., Wu, Q., and Marek, R. (2020). Wind power forecasting using attention-based gated recurrent unit network. *Energy* 196, 117081. doi:10.1016/j.energy.2020.117081

Qian, T., Tang, W., and Wu, Q. (2020). A fully decentralized dual consensus method for carbon trading power dispatch with wind power. *Energy* 203, 117634. doi:10.1016/j.energy.2020.117634

Sahra, K., Mehdi, E., Soodabeh, S., and Hosein, M. S. (2022). A high-accuracy hybrid method for short-term wind power forecasting. *Energy* 238, 122020. doi:10.1016/j.energy.2021.122020

Shui, Y., Gao, H., Wang, L., Wei, Z., and Liu, J. (2019). A data-driven distributionally robust coordinated dispatch model for integrated power and heating systems considering wind power uncertainties. *Int. J. Electr. Power & Energy Syst.* 104, 255–258. doi:10.1016/j.ijepes.2018.07.008

Sun, Z., Zhao, M., Dong, Y., Cao, X., and Sun, H. (2021). Hybrid model with secondary decomposition, random forest algorithm, clustering analysis and long short memory network principal computing for short-term wind power forecasting on multiple scales. *Energy* 221, 119848. doi:10.1016/j.energy.2021.119848

Tanveer, A., and Zhang, D. (2022). A data-driven deep sequence-to-sequence long-short memory method along with a gated recurrent neural network for wind power forecasting. *Energy* 239, 122109. doi:10.1016/j.energy.2021.122109

Tian, H., Zhao, H., Liu, C., and Chen, J. (2022). Iterative linearization approach for optimal scheduling of multi-regional integrated energy system. *Front. Energy Res.* 10. doi:10.3389/fenrg.2022.828992

Wei, W., Hao, T., and Xu, T. (2022). Day-ahead economic dispatch of AC/DC hybrid distribution network based on cell-distributed management mode. *Front. Energy Res.* 10. doi:10.3389/fenrg.2022.832243

Xiang, Y., Wu, G., Shen, X., Ma, Y., Gou, J., Xu, W., et al. (2021). Low-carbon economic dispatch of electricity-gas systems. *Energy* 226, 120267. doi:10.1016/j.energy.2021.120267

Xie, H., Wang, W., Wang, W., and Tian, L. (2022). Optimal dispatching strategy of active distribution network for promoting local consumption of renewable energy. *Front. Energy Res.* 10. doi:10.3389/fenrg.2022.826141

Xing, Q., Cheng, M., Liu, S., Xiang, Q., Xie, H., and Chen, T. (2021). Multi-objective optimization and dispatch of distributed energy resources for renewable power utilization considering time-of-use tariff. *Front. Energy Res.* 9. doi:10.3389/fenrg.2021.647199

Yu, F., Chu, X., Sun, D., and Liu, X. (2022). Low-carbon economic dispatch strategy for renewable integrated power system incorporating carbon capture and storage technology. *Energy Rep.* 8, 251–258. doi:10.1016/j.egyr.2022.05.196

Zhang, G, G., Wang, W., Chen, Z., Li, R., and Niu, Y. (2022). Modeling and optimal dispatch of a carbon-cycle integrated energy system for low-carbon and economic operation. *Energy* 240, 122795. doi:10.1016/j.energy.2021.122795

Zhang, Z, Z., Du, J., Li, M., Guo, J., Xu, Z., and Li, W. (2022). Bi-level optimization dispatch of integrated-energy systems with P2G and carbon capture. *Front. Energy Res.* 9. doi:10.3389/fenrg.2021.784703

Zhu, X., Wu, J., and Liu, D. (2022). Robust unit commitment for minimizing wind spillage and load shedding with optimal DPFC. *Front. Energy Res.* 10. doi:10.3389/fenrg.2022.877042

Frontiers in
Energy Research

Advances and innovation in sustainable, reliable and affordable energy

Explores sustainable and environmental developments in energy. It focuses on technological advances supporting Sustainable Development Goal 7: access to affordable, reliable, sustainable and modern energy for all.

Discover the latest Research Topics

See more →

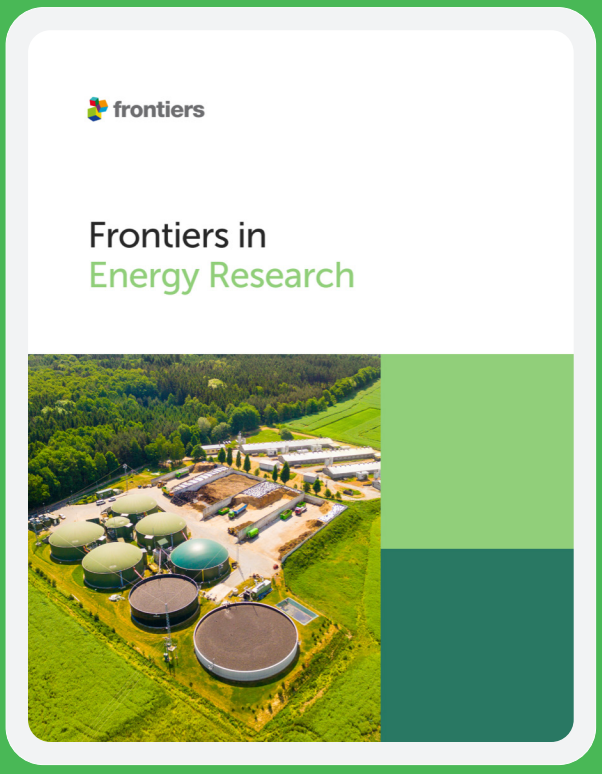

Frontiers

Avenue du Tribunal-Fédéral 34
1005 Lausanne, Switzerland
frontiersin.org

Contact us

+41 (0)21 510 17 00
frontiersin.org/about/contact